# Locomotion of Low-DoF Multi-legged Robots

by

Dan Zhao

A dissertation submitted in partial fulfillment
of the requirements for the degree of
Doctor of Philosophy
(Mechanical Engineering)
in the University of Michigan
2021

Doctoral Committee:

        Associate Professor Shai Revzen, Co-chair
        Assistant Professor K Alex Shorter, Co-chair
        Associate Professor Robert D. Gregg
        Assistant Professor Elliott J. Rouse

left side

right side

Leg tip trajectory
Leg slipping
BF origin trajectory
BF origin at φ = 0
Bodyframe at t=0
Bodyframe at t=6T
Fitted turning circle
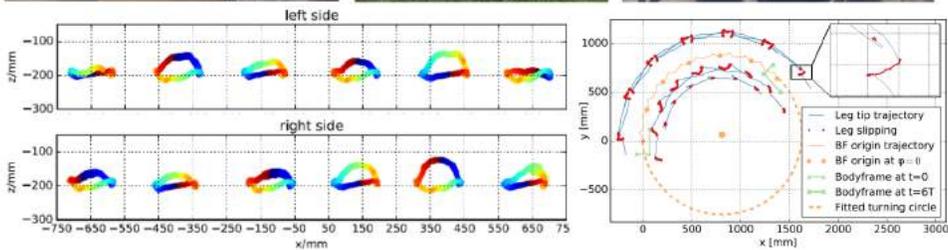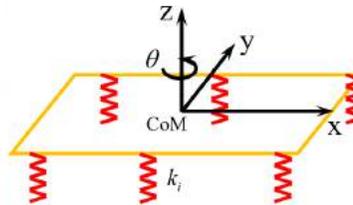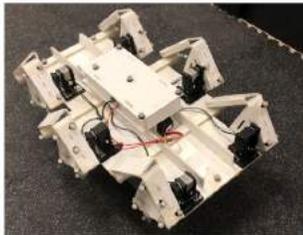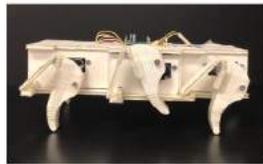
Dan Zhao

danzhaoy@umich.edu

ORCID iD: 0000-0003-0095-0818

DEDICATION

To my family.

ACKNOWLEDGMENTS

The work presented in this dissertation would not have been possible without the invaluable support from my advisor, my family, my lab colleagues, my committee, and my friends. Foremost, I thank my advisor Shai Revzen for his thoughtful mentorship. We both share great interests in robot design, and we have always worked together on the hands-on process of building, testing and debugging the robots, during which I learned and acquired a lot of knowledge and skills from him. Our conversations and discussions have always been inspiring and has opened my mind, this because of his broad knowledge and experience across many research disciplines. His advice has helped me understand both the philosophy and the value of scientific research. His training has taught me how to approach and think of engineering and scientific problems. His curiosity and passion towards unsolved problems has always inspired me to keep working on our research and to never give up even when faced with almost insurmountable difficulties. Therefore, I want to extent my sincerest appreciation to him for all his advice, effort and support he has given me. I would like to thank my co-chair K. Alex Shorter for his excellent advice in helping me to organize my dissertation so that it is coherent and understandable. His patience and assistance in listening to me practicing for my presentation is greatly appreciated.

I also would like to thank my lab colleagues for all their support while working together, and how they have all contributed to creating a warm and empathetic lab environment. George Council was the senior graduate student in our lab who has always helped me out with the electrical and programming problems I encountered when I was debugging my robots. I also enjoyed talking with him about many topics not limited to our research. It was always enjoyable and inspiring working with Brian Bittner in our research projects. Our journeys together to all the research events and conferences are all good memories and I treasure every single one of them. Matthew Kvalheim's enthusiasm towards mathematics has instilled my utmost respect and admiration for him. While I regard myself as leaning towards the experimental side of research, he has helped me to maintain my belief and focus in theoretical study. I thank Haotian Li for all his diligent efforts when helping me to motion track the endless robot locomotion experiments. It was a pleasure to cooperate with Vikram Sachdeva, Ziyou Wu, Arun Bishop, Yue Sun, Hao Luo, Marion Anderson, Erick Vega and all my other lab mates.

Finally, and most importantly, I thank all of the members of my family. I give my heartfelt thanks to my parents for raising me, for their sacrifices, and unconditional love and support, and for

TABLE OF CONTENTS

LIST OF FIGURES

LIST OF TABLES

ABSTRACT

Multi-legged robots inspired by insects and other arthropods have unique advantages when compared with bipedal and quadrupedal robots. Their sprawled posture provides stability, and allows them to utilize low-DoF legs which are easier to build and control. With low-DoF legs and multipleccontacts with the environment, low-DoF multi-legged robots are usually over constrained if no slipping is allowed. This makes them intrinsically different from the classic bipedal and quadrupedal robots which have high-DoF legs and fewer contacts with the environment. Here we study the unique characteristics of low-DoF multi-legged robots, in terms of design, mobility and modeling.

One key observation we prove is that 1-DoF multi-legged robots must slip to be able to steer in the plane. Slipping with multiple contacts makes it difficult to model these robots and their locomotion. Therefore, instead of relying on models, our primary strategy has been careful experimental study. We designed and built our own customized robots which are easily reconfigurable to accommodate a variety of research requirements. In this dissertation we present two robot platforms, BigAnt and Multipod, which demonstrate our design and fabrication methods for low-cost rapidly fabricated modular robotic platforms. BigAnt is a hexapedal robot with 1-DoF legs, whose chassis is constructed from foam board and fiber tape, and costs less than 20 USD in total; Multipod is a highly modular multi-legged robot that can be easily assembled to have different numbers of 2-DoF legs (4 to 12 legs discussed here). We conducted a detailed analysis of steering, including proposing a formal definition of steering gaits grounded in geometric mechanics, and demonstrated the intrinsic difference between legged steering and wheeled steering. We designed gaits for walking, steering, undulating, stair climbing, turning in place, and more, and experimentally tested all these gaits on our robot platforms with detailed motion tracking. Through the theoretical analyses and the experimental tests, we proved that allowing slipping is beneficial for improving the steering in our robots.

Where conventional modeling strategies struggle due to multi-contact slipping, we made a significant scientific discovery: that multi-legged locomotion with slipping is often geometric in the sense known from the study of low Reynolds number swimmers and non-holonomic wheeled snake robots which have continuous contact with the environment. We noted that motion can be geometric "on average", i.e. stride to stride, and can be truly instantaneously geometric. For each

of these we developed a data-driven modeling approach that allowed us to analyze the degree to which a motion is geometric, and applied the analysis to BigAnt and Multipod. These models can also be used for robot motion planning.

To explore the mechanism behind the geometric motion characteristics of these robots, we proposed a spring supported multi-legged model. We tested the simulation based on this model against experimental data for all the systems we studied: BigAnt, Multipod, Mechapod (a variant of 6-legged Multipod) and cockroaches. The model prediction results captures many key features of system velocity profiles, but still showed some systematic errors (which can be alleviated ad-hoc).

Our work shows the promise of low-DoF multi-legged robots as a class of robotic platforms that are easy to build and simulate, and have many of the mobility advantages of legged systems without the difficulties in stability and control that appear in robots with four or fewer legs.

CHAPTER 1

Introduction

1.1 Background and motivation

Most animals and mobile robots move through the world by moving parts of their body to generate reaction forces from the environment and thereby propel themselves. Legged locomotion focuses on that subset of locomotion that employs intermittent contact forces generated by dedicated organs, the "legs", for that propulsion. This is distinct from using fluid dynamic forces, as in fish swimming, or continuous contact forces, as in wheeled vehicles. Although wheeled vehicles are widely applied in human constructed environments, they usually have trouble dealing with complicated terrains like gaps, stairs, steep slopes, and many uneven terrains both natural and of human construction. Legged systems, on the other hand, have the morphology that has experienced hundreds of millions of years of evolution and possess the capability to exist and move almost anywhere on this planet. With such an advantage over wheeled vehicles, legged robots have attracted the public's attention and have become a popular research field for both scientific and engineering studies.

Among legged robots, multi-legged[1] robots are inspired by insects and other arthropods. Their multiple legs and sprawled posture provide extra advantages over bipedal and quadrupedal robots for moving on uneven terrains. With multiple legs supporting the body, stability issues that challenge bipedal and quadrupedal robots are no longer challenges for multi-legged robots. As long as the horizontal projection of CoM (center of mass) stays inside the polygon formed by the supporting legs, the multi-legged system with nonslip pinpoint contacts is statically stable. Multi-legged animals and robots usually have their legs sprawled outwards from their bodies. This sprawled posture offers them with additional stability to counter unexpected disturbance and provides them with possibilities for exceptional maneuverability on the horizontal plane, such as executing very tight turns at high speed. Multi-legged robots also have redundant legs. So even if one or two legs

---

[1]In this thesis, a multi-legged system is defined to have at least 6 legs in total and have at least 3 legs in contact with the environment at any given time.

are damaged or lost, they can still continue to move and finish the task. All these advantages offer multi-legged robots as good candidates for missions that require them to traverse uneven terrain with high mobility and reliability. For example, the ATHLETE (All-Terrain Hex-Limbed Extra Terrestrial Explorer) for lunar exploration [Hauser et al., 2006]; the military version of RHex built by Boston Dynamics for field scouting; the Little Crabster for underwater operations [Kim and Jun, 2014].

Another important feature of multi-legged robots is that they facilitate low-DoF[2] legs. Bipedal and quadrupedal robots usually have high-DoF legs to achieve required motion stability and agility. For instance, the bipedal robot Cassie (Agility Robotics) has 5 DoF per leg; The bipedal robot Atlas (Boston Dynamics) has 6 DoF per leg; The quadrupedal robots Spot (Boston Dynamics) and ANYmal (ANYbotics) have 3 DoF per leg. However, multi-legged robots do not require fully articulated legs for dynamic stability. Even with low-DoF legs, Multi-legged robots can still achieve stability and maneuverability, for example the RHex robot family [Saranli et al., 2001, Galloway et al., 2010] which have 1-DoF legs and the Sprawl robot family [McClung, 2006, Kim et al., 2006] which have 2-DoF legs. The myriapod millirobot in [Hoffman and Wood, 2011, 2012] also has 2 DoF per leg. Multi-legged robots can even mechanically couple legs into actuation groups to further reduce the total DoF of the system: VelociRoACH [Haldane and Fearing, 2014] has 2 motors in total controlling all 6 legs; OctoRoACH [Pullin et al., 2012] uses 2 motors to actuate all 8 legs; 1STAR [Zarrouk and Fearing, 2015] only has 1 motor operating all 6 legs. These robots have the average leg DoF of less than 1. The low-DoF legs offer extra advantages to Multi-legged robots. With all actuators concentrated in the body, such low-DoF Multi-legged robots have lighter legs which can swing much faster than fully articulated legs, which further boosts the speed of locomotion. They are also simpler to build and less complex to control compared with their fully articulated counterparts.

Low-DoF multi-legged robots are the research subjects we are interested to study in this dissertation. Previous researches usually focused on individual robot instances of this category to study their design, modeling and control. Here we try to obtain a better understanding of low-DoF multi-legged robots and their locomotion in general. To better state our motivation, legged systems are grouped into Figure 1.1 and they are classified by their leg DoF and number of contacts with the environment during alternating gaits[3]. We further propose a concept *Constraint Level* to describe a characteristic of legged systems by combining the influence of leg DoF and the influence of number of contacts with the environment. For systems with higher DoF legs and

---

[2]DoF is the abbreviation for *Degree of Freedom*. We use DoF to indicate the number of active joints on a robot leg, or the total number of actuation units on a robot. We note DoF < 3 as low-DoF and DoF ≥ 3 as high-DoF or fully articulated for a robot leg. At the same time, the robots with low-DoF legs are noted as low-DoF robots.

[3]Alternating gaits are the gaits that have half of all the legs in contact with the environment during stance phase. For example, the tripod gaits are the alternating gaits used by hexapedal animals and robots.
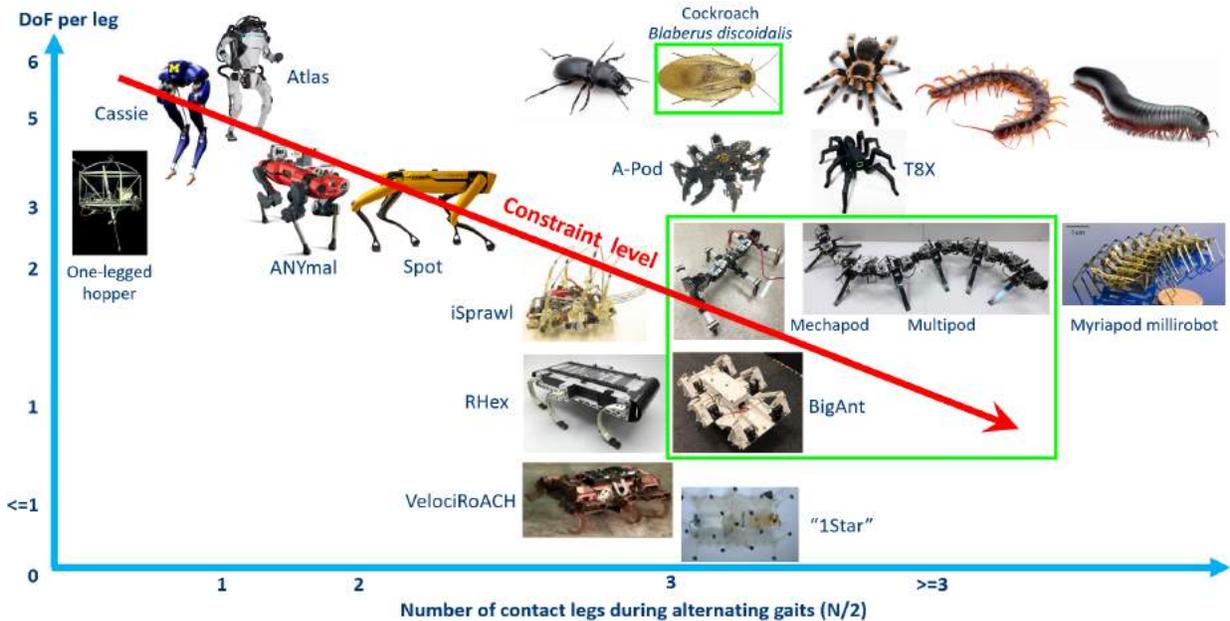
Figure 1.1: Legged system examples classified by their leg DoF and number of contacts with the environment during alternating gaits. The robots in the green box (BigAnt, Mechapod and Multipod) are the multi-legged robot platforms we built and tested for this dissertation. We also studied the motion of Cockroach *Blaberus discoidalis* which is marked out by a green box as well.

less contacts with the environment like bipedal robots Atlas and Cassie, their constraint level is low. For systems with lower DoF legs and more contacts with the environment like low-DoF multi-legged robots, their constraint level is high. Different locomotion possibilities are prescribed by different constraint levels. Legged systems with low constraint levels have high freedom of motion. They can accommodate many kinds of behaviors (gaits) with stance legs contacting the environment under holonomic constraints (no slip). However, legged systems with high constraint levels can only have limited motion if their stance legs are not allowed to slip (break the holonomic constraint). To visit a larger motion space and achieve better maneuverability[4], they must slip. This is also a key discovery from our experimental study and theoretical analysis of multi-legged locomotion, which will be further introduced in more detail in Chapter 2. When slip happens, the interaction between stance legs and the environment is no longer under holonomic constraints but governed by some nonholonomic constraints. Therefore, the constraint level is a trait of legged systems, which determines the necessity of slipping during their locomotion, or how much of their contact with environment falls into nonholonomic constraints given the same maneuverability requirement. It worth emphasizing that constraint level is a systemwise characteristic describing the necessity of breaking the holonomic constraints. Legged systems with higher constraint levels

---

[4]Maneuverability in this dissertation indicates the quality of moving freely in the space of horizontal plane or any environment surface the robot is moving on for more general cases.

have to slip to accommodate the given mobility requirement while systems with lower constraint levels do not have to slip, but they still possess the capacity to slip to further increase their mobility. For example, the cockroaches *Blaberus discoidalis* we tested have 6+ DoF per leg and can perform non-slip gaits for many kinds of motions, but they still slipped a lot in our experiments as shown in Figure 3.1.

For the low-DoF multi-legged robots we are interested in studying, they have high constraint levels thus they must slip. Slipping together with multiple contacts with the environment makes low-DoF multi-legged systems difficult to model. Classic modeling strategies for bipedal and quadrupedal robots usually assume that no slip happens or make nonslip as a control objective to fulfil. In these models, the interaction between the stance legs and the ground is just the unilateral holonomic constraints. For example, the famous template models SLIP (spring loaded inverted pendulum) and LLS (lateral leg spring) [Full and Koditschek, 1999, Holmes et al., 2006, Dickinson et al., 2000] assume there is no slip between supporting legs and the ground. Seipel and Holmes [2007] even group multiple contacting legs into one representative to focus on the template dynamics. Another conventional modeling strategy is the full body dynamics model that is popularly used for gait design/analysis and motion control/planning [Remy, 2011, Gregg et al., 2014, Fahmi et al., 2020, Gan et al., 2016]. Both modeling strategies provided significant scientific insights and sophisticated engineering applications for legged locomotion, but they did not include options to handle multi-legged contacts with slipping.

Legged robotic research relies heavily on models and model-based simulations for studying robot design, gait design/analysis and motion planning/control. However, currently no general modeling method is available for low-DoF multi-legged robots and their locomotion with slipping. Therefore, there are both technique and knowledge gaps in this field and these are what we are trying to contribute from this dissertation. To work towards this goal, we adopt the following research strategies: First, use real robot platforms to replace models for their technical functions and experimentally study multi-legged locomotion. After better understanding and knowledge are achieved through experimental studies, we then try to develop new general modeling strategies for low-DoF multi-legged robots.

1.2 Overview and contributions

1.2.1 Design

To experimentally study multi-legged locomotion, we first need reliable robot platforms to perform research tests. There are few commercial multi-legged robots available and robot platforms with fixed forms are also not adequate for a comprehensive study of multi-legged locomotion. Thus, we

need to build our own customized low-DoF multi-legged robots which are easily reconfigurable to accommodate to a variety of research requirements. This leads to the content of Chapter 2 of this dissertation.

In Chapter 2, we introduce our design and fabrication techniques of multi-legged robot platforms for our research. We adopted two strategies for our robots to achieve high reconfigurability. The first strategy is to make it easy to fully rebuild the robot platforms, and the second strategy is to introduce modularity to the robot design. Traditional design strategies usually require design iterations assisted by model-based simulations, while accurate models are not available for design or motion simulation in our study. To address this issue, we developed techniques for building multi-legged robots with very inexpensive material and very low time cost; such ensured that the fabrication of robot hardware was comparable to model construction in terms of time efficiency. Using this method, we can apply physical robots directly for design iteration tests and keep improving robot design until the design objective is achieved. Applying this strategy, we built the BigAnt robot (Figure 2.3i), a low-cost fast-fabricated hexapedal robot, of which the chassis is constructed of fiber tape and foam board and costs less than 20 USD in total. The whole robot can be built up within 5 hours including all the fabrication and assembling processes. After approximately 20 versions of rapid design iterations, the current BigAnt is a fully functional and robust robot platform which can perform many kinds of gaits and travel on outdoor uneven terrain despite its low fabrication costs. We also developed several variants of BigAnt for specialized applications, such as stair climbing, force sensing, walking on snow fields, education use, etc. Besides the design strategy, the fabrication technique and a useful robust robot platform, we also contribute to the low-DoF multi-legged robots field by introducing our insights and methods of designing 1-DoF leg trajectories as well as how to control leg motions on these trajectories to achieve better locomotion performance.

BigAnt as a hexapedal robot with 1-DoF legs does cover a substantial portion of our research requirements. For a more general study of multi-legged locomotion, we also built another family of robot platforms, Multipods (Figure 2.24), which have different structure morphology and leg DoF (2 DoF) comparing to BigAnt and RHex like robots. Multipod is a modular multi-legged robot that can be easily assembled to have different numbers of legs (4 to 12 legs currently). As a family of robot platforms, Multipod enables a large range of general multi-legged locomotion tests. We use Multipod to study how number of legs affect multi-legged locomotion. To make sure that Multipods with different numbers of legs take comparable behaviors, we also designed a family of undulatory gaits and performed them on Multipods in our experimental tests. In this way, we built a comprehensive data-set for multi-legged locomotion which has a 3-dimensional parameter space across 4 numbers of legs (6, 8, 10 and 12 legs), 26 kinds of undulatory gaits and 5 kinds of gait frequencies. This data set of Multipod motions can be used for a lot of general analyses and

studies for multi-legged locomotion. A significant portion of motion analysis in Chapter 4 of this dissertation is based on this data set.

1.2.2 Mobility

One general motivation of studying multi-legged locomotion is to make multi-legged robots as mobile as their animal counterparts. After the robot platforms were designed and fabricated, we further designed and tested different gaits on these robots. For example, the tripod walking gaits, turning in place gait, stair climbing gait, etc. for BigAnt; and the undulatory gaits for Multipod. Most of these gaits are straight walking gaits and are included in Chapter 2. For multi-legged locomotion, another important aspect of mobility is maneuverability, of which steering[5] is an essential part. Most previous research about multi-legged steering/turning methods are specific to their corresponding robot instances, and ignore the possibility of slipping. Prior to our work, the general foundation of low-DoF multi-legged steering was missing. Chapter 3 of this dissertation introduces our efforts to study the general issues pertaining to low-DoF multi-legged steering.

In Chapter 3, based largely on [Zhao and Revzen, 2020], we first analyzed and introduced the difference between wheeled steering and legged steering, showing that the principle of differential driving which is commonly used in wheeled systems, is non-trivial to use with legged systems. We then proposed a formal definition of steering gaits for legged locomotion from a geometric mechanics viewpoint, and further demonstrated how multi-legged morphology combined with low-DoF legs results in extra challenges for steering gaits. We proved that multi-legged steering has to slip with 1-DoF legs through theoretical analysis, and then analyzed the general strategy for low-DoF steering. Following the proposed steering strategy, we designed two kinds of steering gaits for multi-legged robots with 1-DoF legs and tested them on BigAnt. The experiment results were examined in terms of both steering and slipping. We showed that nonslip steering gaits do exist for a low-DoF multi-legged robot with 2 DoF legs, Mechapod (a hexapedal robot similar to 6 legged Multipod), and compared its best nonslip steering gait with other steering gaits we designed for it. The latter gaits with slipping easily outperformed the former nonslip gait in terms of steering. The experiment results from these two robot platforms and 4 kinds of steering gaits suggest that allowing slipping is beneficial when optimizing steering ability for low-DoF multi-legged robots.

1.2.3 Modeling

The experiment results from Chapter 3 confirmed our hypothesis that low-DoF multi-legged robots with high constraint levels need to slip for better mobility, which also raised the challenges of mod-

---

[5]General steering means changing the body orientation of system while moving forward/backward. A definition of steering for legged locomotion is introduced in Section 3.3.1

eling this kind of locomotion. However, there is also an important discovery from our experimental study that the steering performance, turning angle per gait cycle of BigAnt, is independent of its gait frequency. This result suggests that the steering motion of BigAnt is *geometric*[6], rather than dynamic as academics have traditionally assumed. While geometric motions were usually seen in systems like low Reynolds number swimmers and non-holonomic wheeled snake robots which have continuous contact with the environment.

In Chapter 4, we proposed the geometric analysis[7] methods for checking the geometric characteristics of a given periodic behavior for a given system. The proposed geometric analysis methods can be implemented both instantaneously and in average form based on the scientific and engineering requirements. We then extended our preliminary observation in Chapter 3 and performed a thorough geometric analysis on our multi-legged systems and their motions. The analysis results indicated that the tested BigAnt locomotion is geometric. Multipod locomotion is complicated by the wide parameter space. Different numbers of legs and different undulatory gaits lead to different levels of being geometric. The results show that most of Multipod locomotion is geometric on average while its instantaneously geometric property holds in a smaller gait frequency range with 10 and 12 legs. The results also suggest that with more legs, Multipod locomotion is closer to being geometric.

After confirming that multi-legged locomotion with slipping can be geometric, we developed data driven models associated with the geometric analysis. These data driven models can be extended to different gait frequencies behaviorwise and used for robot motion planning after some calibration trials. To explore the mechanism behind the geometric characteristics observed in multi-legged locomotion, we proposed a spring supported multi-legged model (noted as SSML) structure to model multi-legged systems from first principle physics. This model structure is systemwise and can be used to predict system motion generated by any gaits. We also analyzed the precondition and the feasible friction models that could make this model achieve geometric motion. The simulation based on this model was tested for all the systems we experimentally studied: BigAnt, Multipod, Mechapod and cockroach. The consequent prediction results did capture many key features of system velocity profiles, but still showed some systematic errors for CoM trajectory and system orientation which can be alleviated by corrections of constant offsets against angular velocity. In terms of computation efficiency, this model can be computed x50 times faster than the real time with Python code on a single core PC, thereby it possesses the potential to be used as an odometry model and embedded into the on-board computation units for real time control and

---

[6]"Geometric" is used as a terminology to describe the motion that the system speed in world frame is proportional to the speed of system shape change (eg. speed of leg joint rotation). A definition of *Geometric Motion* is given in Section 4.2.2.1

[7]We name the method of analyzing whether a behavior of a system is geometric as "Geometric Analysis" in this thesis. More details are introduced in Section 4.2.3

planning.

1.2.4 Summary and extension

In summary, the contribution of this dissertation is our study of the unique characteristics of low-DoF multi-legged locomotion, in terms of design, mobility and modeling.

The proposed concept of constraint level summarizes the general influence of the design morphology of legged systems on their locomotion. It provides a new perspective for classifying legged systems and identifies the intrinsic difference between legged systems with low constraint levels and legged systems with high constraint levels, and this new perspective is the necessity of allowing slipping. Our analysis about BigAnt leg trajectory design is applicable to all multi-legged robots with 1 DoF legs. The fabrication technique we developed in Chapter 2 can also be easily extended for building other multi-legged robots with low cost and low construction time. The data set of Multipod experiment results covers a sizeable range of low-DoF multi-legged locomotion. It has the geometric motions we discovered in Chapter 4 for high numbers of legs and low gait frequencies. There are also dynamic motions for Multipods with low numbers of legs and high gait frequencies. Geometric analysis is only one kind of study. More studies can be performed on this data set in future work exploring multi-legged locomotion.

For maneuverability, our proposed steering strategy is universal for low-DoF multi-legged robots. The two steering gaits we designed and tested for BigAnt can be used to steer other low-DoF multi-legged robots with slight modification of the details. The nonslip gait design method for Mechopod using 4-bar analysis can also be extended to many other low-DoF multi-legged robots with 2 DoF legs. The experiment results obtained from these steering motions provided evidence that slipping is a routine part of low-DoF multi-legged locomotion and benefits its steering performance. Slipping in multi-legged locomotion should be allocated more attention for both scientific research and the engineering goals associated with practical robot gait design and control.

Our geometric analysis methods can be easily applied to check whether or how close, a given periodic behavior of a given system is to being geometric. The result that multi-legged locomotion with slipping can be geometric is a meaningful scientific discovery and provides us with a new understanding of, and model for multi-legged locomotion. Due to their geometric nature, the data driven models for these tested multi-legged robots can be applied to different gait frequencies for different motion speeds without re-planning the motion path. Being geometric offers the advantage that planning and control of these multi-legged robots can be decoupled, while motion planning and control for bipedal and quadrupedal robots are usually coupled because of their highly dynamic characteristics.

The mechanism for multi-legged locomotion with slipping being geometric is still an open

8

question. Our proposed precondition, *fiction dominated assumption* (more details in Section 4.5.1), for the spring supported model is a hypothesis that could result in geometric motion for multi-legged systems. However, whether these tested motions satisfy this friction dominated assumption or not needs further verification. This is also the motivation for building the force sensing BigAnt variant (Section 2.2.8). We believe that the future projects that apply our proposed analysis and modeling technique combined with experimentally measured forces will reveal deeper knowledge about low-DoF multi-legged locomotion.

CHAPTER 2

Rapidly Fabricated Modular Multi-legged Robotic Platforms

2.1 Motivation and introduction

Legged robotic research has significant dependence on models and model based simulations for robot design, gait design/analysis and motion planning/control. However, currently there is no general modeling method for low-DoF multi-legged robots and their locomotion with slipping which are the topics we are interested in studying in this dissertation. Our strategy is using real robot platforms instead of imprecise models to experimentally study low-DoF multi-legged robots and their locomotion. Currently, there are almost no commercial robots available which are multi-legged in the sense of that term used here. Moreover, robot platforms designed with fixed structures and mechanisms[1] are hard to modify for different research proposes, thus they are inadequate for general study of multi-legged locomotion. This is the motivation behind the following information in this chapter.

To experimentally study low-DoF multi-legged locomotion in general, we need customized robot platforms that can meet a variety of research requirements. Our solution is to make the robot platforms easily reconfigurable. There are two approaches toward this objective. The first one is to construct the robot platforms so that they can be easily fully rebuilt. This approach requires special techniques to achieve low-cost fabrication in terms of both material and time given the limitations imposed by research funding and the time available. It also requires design strategies associated with the fabrication techniques to make the low-cost robot platforms fully functional. The second approach is to construct the robot platforms so that they are highly modular so components can be reused. Of course, these two approaches can also be combined to create more room for the robot platform to be easily reconfigurable. Therefore, rapidly fabricated modular multi-legged robot platforms are the design goals in this chapter of the dissertation.

---

[1]We usually use "Structure" to refer to rigid parts of a robot and use "Mechanism" to refer to articulated joints or parts of a robot.

Conventionally designed legged robots adopt classic mechanical manufacture techniques and ideologies. They contain many parts made of metal, carbon fiber, rubber, etc. for their structures and mechanisms, which make them durable but also expensive machines. Rebuilding them for quick design changes are costly engineering projects. That is also the reason why they rely heavily on model based simulation for their design and fabrication.

Some existing robot fabrication methods align with our goals. Wood et al. [2008] developed the Smart Composite Microstructure (SCM) fabrication technique for creating microrobots. SCM is widely applied to build the rigid structure and articulated mechanism for many microrobots such as RoACH [Hoover et al., 2008], VelociRoACH [Haldane and Fearing, 2014, Yun and Fearing, 2019], the myriapod millirobot [Hoffman and Wood, 2011, 2012], the flying at-scale robotic insect [Wood, 2008], etc.

In our lab, we are interested in creating meter-sized multi-legged robots. Just scaling up SCM designs geometrically by orders of magnitude is not a solution leading to functional mechanisms, since structural properties do not scale in a simple way. A combination of new materials and design concept must be made for larger scales. Inspired by SCM, our lab developed the plate and reinforced flexure (PARF) fabrication technique to rapidly fabricate low-cost, meter-scale robot platforms [Fitzner et al., 2017]. PARF uses inexpensive materials such as foam board, cardboard and corrugated plastics as rigid plates, and fiber-reinforced tape for construction of joints. We used servomotor modules that can be quickly disassembled and assembled from robot chassis (structure+mechanism) to actuate PARF mechanisms. The inexpensive fast-to-fabricate chassis and the easy-to-switch reusable modular actuation together enable us to conveniently rebuild our robot platforms to adapt to different research requirements.

We always prefer to add as much modularity as possible to our robot platforms for the convenience of reconfiguration. Many pure modular robots provide inspirations. For example, the self-reconfigurable modular robot in [Kamimura et al., 2001] and the soft origami-inspired modular robot in [Robertson et al., 2020]. We use the modular connector Modlock developed in [Davey et al., 2012] for adding modularity to our actuation. Modularity itself is also the key characteristic of the multi-legged robots that incorporate varying numbers of legs, especially for those with many legs. For example, the the myriapod millirobot in [Hoffman and Wood, 2011, 2012]; the centipede robot in [Masuda and Ito, 2014] and also the modular reconfigurable robot in [Sastra et al., 2008].

In this chapter, we introduce the two robot platforms we designed and built for our study of low-DoF multi-legged locomotion, which are BigAnt and Multipod. BigAnt is a low-cost fast-to-fabricate hexapedal robot that can be rebuilt easily. We present the design process of BigAnt including design strategy, design objective, detailed design/fabrication, modularity, techniques we developed that are associated with PARF, etc. We introduce a general gait design strategy for multi-legged robots with 1-DoF legs. We also present typical gait designs and test results for

BigAnt travelling in both the indoor and outdoor environments. Different variants of BigAnt for different specialized applications are then introduced. Multipod is a modular multi-legged robot that can be easily assembled with varying numbers of legs. We introduce the detailed design of its structure and mechanism. We present the undulatory gaits of Multipod for our study about how the number of legs affect multi-legged locomotion. The experiment results of all different numbers of legs, undulatory gaits and gait frequencies are summarized into a comprehensive data set for further analysis and modeling.

2.2 BigAnt: A Low-cost, Fast-to-fabricate Hexapod Robot

2.2.1 Design strategy and introduction

Building machines that can work reliably is always a challenging process. The iterations in the design and manufacture process are important steps for design improvements and all kinds of criteria checks. As depicted in Figure 2.1, traditional design strategies usually adopt many iterations relying on model-based simulations and less iterations from prototypes and real products. This is common for cases in which model-based simulation can provide sufficiently accurate evaluation and can be performed with low cost and over a short term, while prototypes and real products are costly to create. For example, the design of aircrafts and ships.
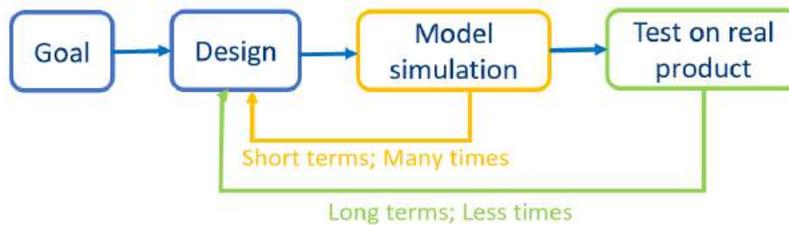
Figure 2.1: Traditional design iterations
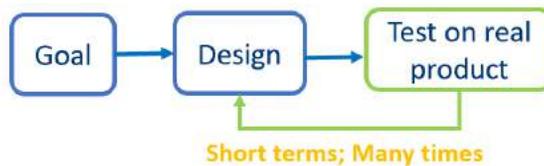
Figure 2.2: BigAnt design iterations

In the case of low-DoF multi-legged robots, there is no general modeling strategy, and the interactions between robot systems and the environment are difficult to be modeled accurately
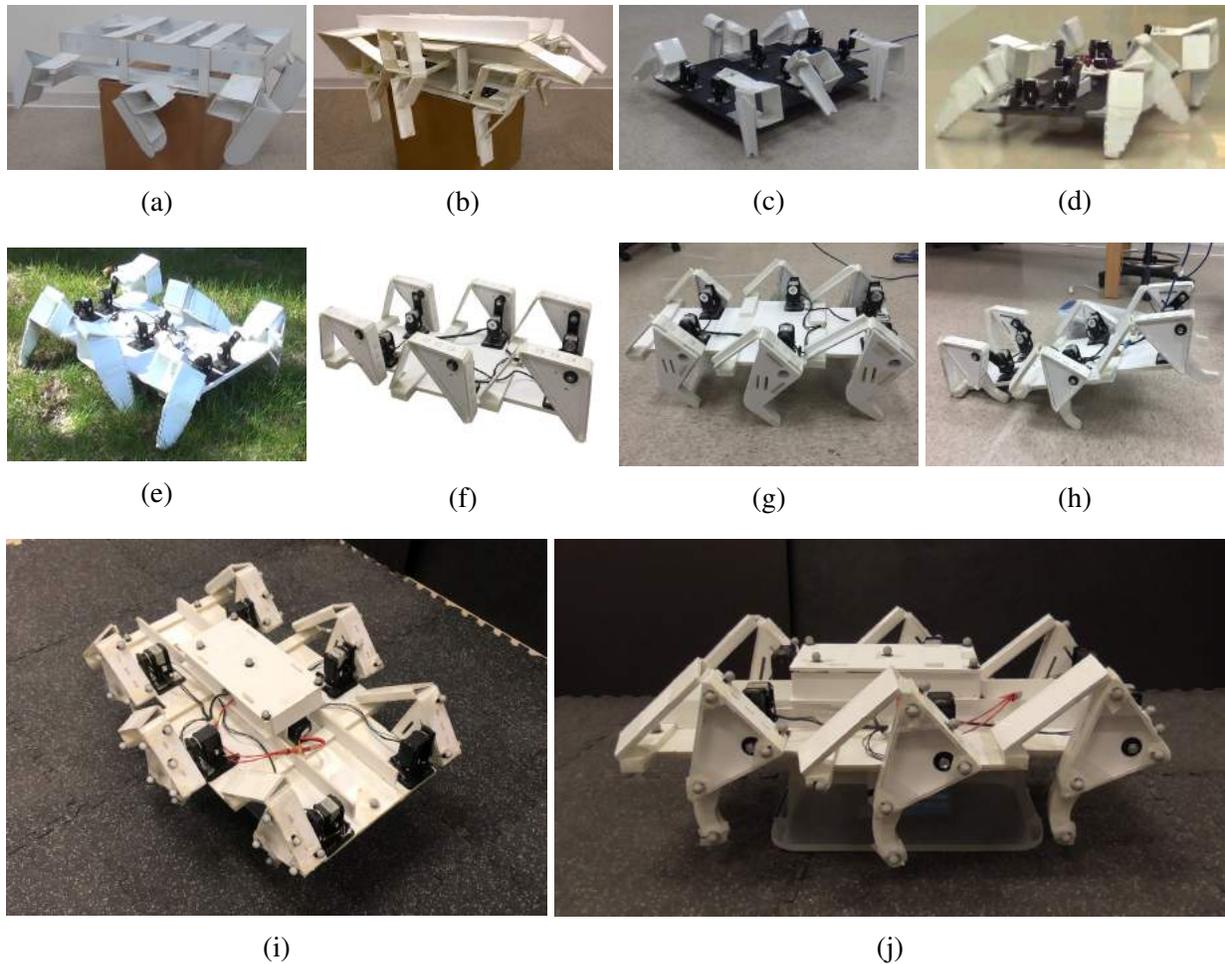
Figure 2.3: Milestone versions of BigAnt during design iterations. (a) and (b) were concept tests of drivetrain mechanisms. (c) was the first version capable of walking with a tether. (d) was the first version with power and control on board. (e) was the last prior version described in [Fitzner et al., 2017]. It the was also the first version we took to outdoor environment for tests. (f) was the first new version for the tests of the new drivetrain, after we found the problems faced by (e) in outdoor environments. (g) was an example version for the tests of leg shapes. (h) was the first version capable of climbing over obstacles higher than its hip height and is also the first version that succeeded in climbing stairs. (i) and (j) are the views of the newest design of BigAnt which is functional both indoors and outdoors and is widely used in our lab for multi-legged locomotion research.

for design iterations. Our strategy is to use real robot platforms directly for design iterations as expressed in Figure 2.2. The efficient design iterations are made possible as our robots can be rebuilt rapidly and inexpensively adopting the PARF fabrication technique and modular actuation. In this section, we present how we apply this design strategy to build low-DoF multi-legged robots.

13

BigAnt is a low-cost meter-sized[2] hexapod robot that can be fabricated rapidly and has been iteratively improved with many versions for both indoor and outdoor tasks. Its chassis can be manufactured with minimal tooling (a knife) and less than US$20 worth of materials: foam board (Elmer's Products Inc.) and fiber tape (3M Scotch #8959 fiber tape). With a laser cutter instead of the knife, BigAnt chassis can be fabricated and assembled with the actuation modules for a functional robot in fewer than 7 hours [3]. Thus, different versions of BigAnt structures and mechanisms can be tested and improved on a daily basis. There have been around 40 key design iterations in total for BigAnt, of which some milestone versions are presented in Figure 2.3.

Before the versions designed and tested in this dissertation, the prior versions of BigAnt were introduced in [Fitzner et al., 2017]. The latest prior version (shown in Figure 2.3e) could walk reliably during indoor tests. However, due to its relatively low foot clearance (≤ 4 cm), this version of BigAnt could not climb slopes or travel through terrains with centimeter-scale obstacles. The large sideways (lateral) leg motions at the swing phase also cause trouble for it to walk through the outdoor field with grass or vegetation. As aware of these drawbacks based on the observation from the previous outdoor tests and aiming for better locomotion performance, we continually improved BigAnt with quick design iterations and finally created the current version of BigAnt (Figures 2.3i and 2.3j).

Compared with the previous version (Figure 2.3e), the new BigAnt reported in this section achieves better locomotion performance with even fewer material types and material usage, and with even less fabrication time. Adopting the new design of both mechanism and structure, it can traverse through more complicated indoor and outdoor environment such as stairs, grass ramps, snow fields, etc. The high modularity of the new version further reduces the assembling and maintenance times and also provides the capability to switch between a variety of different applications.

2.2.2 Design objectives

With 6 motors for actuation, BigAnt is a typical low-DoF hexapod robot with 1 DoF per leg. There are two key parts for BigAnt design: the first key part is the drivetrain mechanism that can transfer the rotary outputs of the servo motors to the desired leg motions. The second key part is the base board structure that can hold and mount other parts. The baseline requirement is that these mechanisms and structures can be built with the PARF technique and be reliably functional. Besides this baseline requirement, we also integrate some other design goals and concepts as extra requirements into this new BigAnt design to make it even more efficient to iterate and possess

---

[2]The average dimension of different versions of BigAnt is around $0.9 \times 0.6 \times 0.2 [m]$ for its length, width and height.

[3]These material and time cost numbers vary from version to version. 20 USD and 7h are the highest numbers got from the prior versions of BigAnt introduced in [Fitzner et al., 2017]

more robust performance.

The first requirement is that the chassis should be designed with high modularity which facilitates BigAnt with extra reconfigurability. High modularity also offers the following detailed advantages: 1. It saves fabrication and assembling time and makes design iteration even faster and at a lower cost. 2. It facilitates easy repair and maintenance options. 3. It simplifies the branching out of variants for different applications. The second requirement is that the chassis design should be as simple as possible. Mechanical complexity is one of the major sources of failure and considerably increases the cost. Over complex mechanisms with PARF also accumulates joint errors and shortens the joint life span because of the relatively low stiffness and robustness if compared to metal parts. The leg designs of the prior versions of BigAnt (Figure 2.3e) exhibited some of these problems with complicated two-loop spatial linkages for the drivetrain mechanism. Having a simple chassis design also enables BigAnt to be fabricated more rapidly. The third requirement is that the chassis design should use as little material as possible. Restricted use of material includes both material types and material usage. This requirement directly supports our goal of making BigAnt construction even cheaper and more time efficient. We plan to fabricate the chassis only from two kinds of materials: a kind of foam board for rigid plates and a kind of fiber tape for flexure joints, while the prior versions in [Fitzner et al., 2017] required at least 5 kinds of materials, two for rigid plates and two for flexure joints with the assistance of one kind of hot glue.

All these extra requirements can not only offer positive contributions to BigAnt, but can also impose extra challenges to its design. Two of these challenges are, (a) how to achieve target drivetrain kinematics with simple mechanisms, and (b) how to maintain structure robustness with limited material type and usage. Adding modularity on top of these two is another challenge. All these challenges combined push us to think harder about the design. Simplicity vs. capability, reliability vs. low cost are the eternal balance considerations in mechanical designs, such considerations are even more relevant for the design of BigAnt. In summary, our general design objective for BigAnt to achieve a fully functional hexapedal robot with high modularity, despite the low cost and fast fabrication requirements.

2.2.3 Design of robot kinematics

Unlike multi-DoF (DoF ≥ 3) legs, the toe of 1-DoF leg can only occupy 1 dimensional manifold[4] instead of having full access to the 3D workspace. Then both the motion and force control of the actuation has to stay on this 1-dimensional manifold. This makes leg trajectory design the most important part for robots with 1-DoF legs, since it fully determines the leg motion by deciding both the the geometric properties and the kinematic properties of the toe trajectory, thereby determining

---

[4]We neglect the effects of leg deformation and assume the low-DoF leg is rigid for all our statements about leg trajectories.

15

the system locomotion. The geometric properties of the toe trajectory are the properties of the trajectory shape (locus), for example the trajectory clearance. The kinematic properties of the toe trajectory describe the relationship between the toe motion on the trajectory and the source motion from the actuator. In this dissertation, we use the *drive ratio* as the kinematic property of a designed leg trajectory. The drive ratio (noted as DR) here is defined as DR $=dv/d\omega$, where v is the toe speed on the 1-DoF trajectory and ω is the rotation speed of the motor shaft.

2.2.3.1 Feasible 1-DoF leg tip trajectory

For 1-DoF legs, there is no toe trajectory that achieves the best performance in every application case. The 1-DoF toe trajectory is often designed based on certain requirements. For example, the toe trajectory of the quadrupedal robot in [Liu and Ben-Tzvi, 2020] is designed for good trotting gait performance. The toe trajectory of the hexapedal robot in [Yun and Fearing, 2019] aims for sufficient clearance. Based on our study and tests of many versions of BigAnt designs, we find that the generally feasible toe trajectory for 1-DoF multi-legged robots should include the following geometric and kinematic properties.
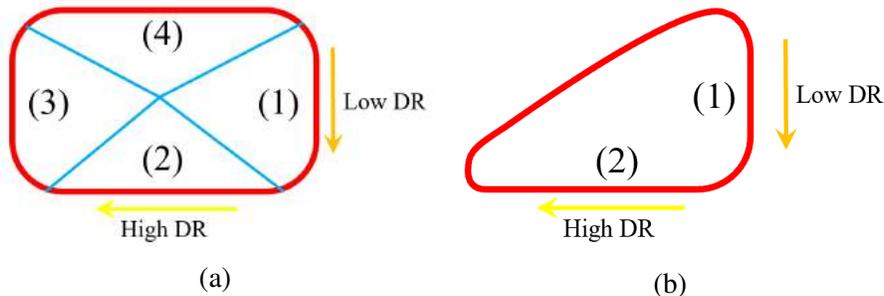
Figure 2.4: (a) A toe trajectory example that is generally feasible. DR here is noted for drive ratio. (b) Target trajectory for BigAnt drivetrain design. The toe trajectory is divided roughly into 4 regions based on motions in different directions.

First, the 1 DoF toe trajectory needs to have enough clearance when swinging down at its front part (region (1) in Figure 2.4a which we note as "push up") to provide the ability to climb over obstacles. Within region (1) of the toe trajectory, making the drive ratio small is necessary to fully utilize the torque of the actuation motor. If the drive ratio in region (1) is too large, the actuation motor may not generate enough torque to drive the supporting leg to push the robot body upwards against gravitational force.

Second, the trajectory needs to have a relatively flat backward stroke at its bottom part (region (2) in Figure 2.4a). Region (2) is where most of leg-ground interaction happens. The leg tip speed in this region along the trajectory (w.r.t the body frame) determines the upper bound of the CoM

16

speed that the whole system can achieve. A flattened contact motion in region (2) can also prevent robot CoM from oscillating too much in the vertical direction which causes motion instability and unnecessary waste of energy against gravity in those cases in which the robot is supposed to walk mostly on relatively flat surfaces. Within region (2) of the trajectory, the drive ratio is usually larger to offer a faster pushing-back motion, given that the motor output speed is identical. The reason why the drive ratio can be larger at region (2) of the trajectory is because the normal force against gravity is nearly perpendicular to the flat trajectory and can be mostly cancelled out by the constraint force of the kinematic structure rather than transferred into the joint space as resisting torque. Then all the motor torque is transferred into the force in the tangent direction of the trajectory which in region (2) only pushes along the flat stroke providing propelling force for the forward motion.

Region (3) on the trajectory is quite flexible since it is where the robot leg disengages from the ground and some other legs are usually already at regions (1) or (2) for the supporting. One special case that region (3) needs to be similar to region (1) is when the robot is required to have the same performance to walk backwards and to climb obstacles during the backward motion. The pure air-swing part (region (4)) possesses the most freedom since it has no interaction with the ground at all. Usually it only connects region (3) and region (1). However, it is still necessary to avoid sideways motions within regions (3) and (4) if the robot needs to walk through terrains similar to grass land. Otherwise the leg sideways motion combined with the swinging forward motion will push against the grass and waste energy. Such motions sometimes even result in the legs being trapped, similar to happened in the prior version of BigAnt (Figure 2.3e).

Generally, the connections between adjacent regions are required to be smooth for easy kinematic realization and smooth transitions between different contact conditions. Based on the above analysis of the useful and necessary properties of the 1 DoF trajectory, a generally feasible toe trajectory is depicted as in Figure 2.4a.

2.2.3.2 drivetrain design

Although Figure 2.4a provides an example of a 1-DoF toe trajectory that is generally feasible, it is not expected to be directly applied to any real robot. The final realistic toe trajectory must also compromise with the drivetrain and other kinematic performance requirements for specific low-DoF robots. For BigAnt design, we decided to avoid the complex drivetrain mechanism and aimed for a large stride length and high clearance. BigAnt is not required to have the same performance walking backwards as walking forwards, so the following trade-offs can be made for a simple drivetrain mechanism and full use of the robot baseboard space. We kept the properties of regions (1) and (2) in Figure 2.4a while removing region (3). Then the target toe trajectory becomes what is depicted in Figure 2.4b. We then use the drivetrain mechanisms that are as simple as possible to

generate trajectories which can approximate the target trajectory.
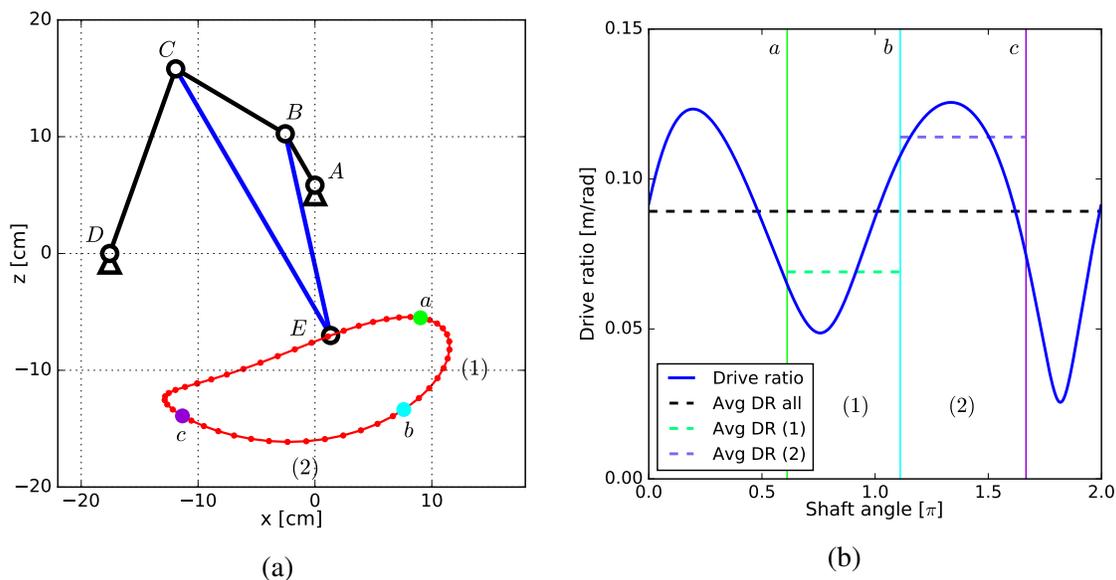
Figure 2.5: (a). BigAnt drivetrain mechanism and toe trajectory: A,B,C, and D are the rotational joints of a crank-rocker 4 bar linkage. The toe position E is a coupler point attached to the floating link BC. When the input crank AB rotates a full cycle, the motion of E generates the toe trajectory (red). The key points a, b and c mark out the key regions on the toe trajectory. (b). Drive ratio on the toe trajectory as a function of the shaft angle of input crank AB. The vertical lines that mark out region (1) and region(2) are the shaft angles corresponding to the key points on toe trajectory in Figure (a). The average drive ratios for different regions are depicted in the dash lines across the corresponding regions.

Apparently, the simplest drivetrain is directly driving the leg from the motor shaft like most RHex-like robots do, but it only generates a "circular"[5] toe trajectory. The second simplest 1-DoF mechanism is the 4-bar linkage mechanism which is prevalent and is also what we chose to use for the BigAnt drivetrain.

The final drivetrain mechanism and the corresponding toe trajectory that are designed for BigAnt in terms of general walking are shown in Figure 2.5a. The mechanism is a typical crank-rocker linkage with an augmented floating link structure transferring the rotary motion of the input crank to a 1-DoF output trajectory. The dimensions of the actuation module and base board space determine the length of input crank AB and positions of fixed joints A and D, leaving other links free to adjust. The final mechanism was chosen by exploring the dimension space of links $[BC, CD, BE, CE]$ for toe motion that is close to the target trajectory as in Figure 2.4b. We also

---

[5]This kind of direct drive generally results in circular shape toe trajectory. However, RHex-like robots usually adopt compliant C shape legs. The leg deformation and leg rolling contact with the ground during stance phase make the analysis of leg trajectory more complicated.

verified the drive ratio on this trajectory to make sure it is feasible. The result is presented in Figure 2.5b. It is clear that the drive ratio in region (1) is lower than the average value, while the drive ratio in region (2) is higher than the average value, offering BigAnt more force to push up in region (1) and a longer stride for moving forward in region (2) given the motor speed and torque remain constants.

2.2.3.3 Modularity analysis of the drivetrain
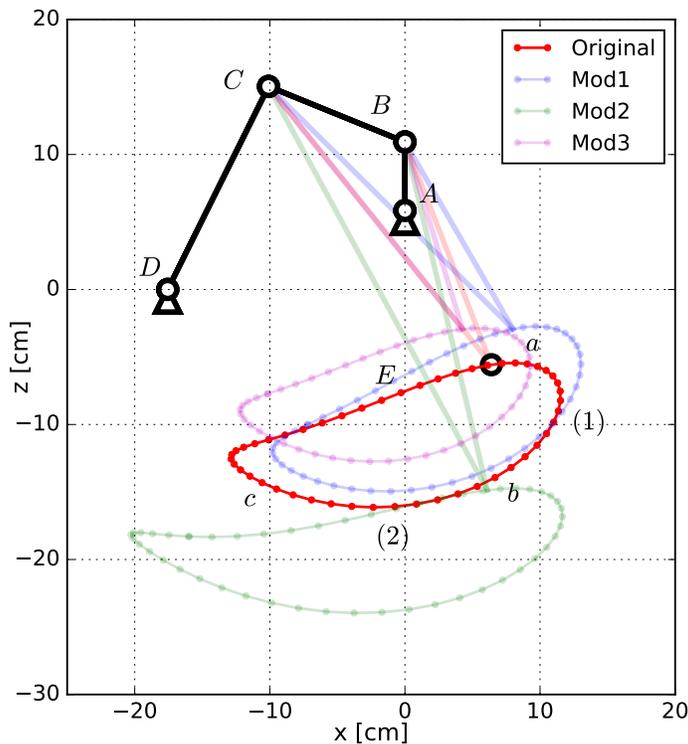
Figure 2.6: Toe trajectories for different modular cases: Original toe trajectory (red) is used as reference; Mod1 (blue) has extra clearance; Mod2 (green) has a higher drive ratio in region (2) for higher speed on flat ground; Mod3 (magenta) has a lower average drive ratio for a larger drive force.

Although Figure 2.5a provides a generally feasible toe trajectory for BigAnt, we still prefer the alternative, to quickly and easily adjust the toe trajectory for better performance in specific applications. That is where modularity helps. With high modularity, we can quickly switch to different toe trajectories for different applications.

In this section, we introduce how we embed modularity into the designed 4-bar mechanism. Since the crank link AB is determined by the actuation module and the rocker link CD has a fixed joint connected to the base board, they are not easy to switch, thus also not suitable for introducing

19

modularity. This leaves the float link BC and the coupler structure BCE as possible consideration. Even though the feasible dimension of link BC is quite constrained by the Grashof condition for guaranteeing that the mechanism is a crank-rocker, the position of the coupler point E is free. From a practical perspective, different E positions can provide a variety of toe trajectories for different applications. Changes of coupler structure BCE are also easier to achieve by physical structures than by using other parts of the drivetrain mechanism.

Figure 2.6 presents several toe trajectory examples generated by the E positions listed in Table 2.1. Each of these toe trajectories is able to provide better performance than others in certain circumstances. For example, toe trajectory of Mod1 which is designed for traveling through $10+$cm obstacles, has 14.3% more clearance than that of the original trajectory which is designed for general walking. Mod2 is designed for fast walking on flat ground. Its drive ratio in region 2 is increased by 26.8% from the original toe trajectory, making it walk almost 20% faster with the same shaft rotation speed. Mod3 is designed for traversing generally through terrains like grass land or granular media with a lower average drive ratio for more actuation force. It is worth noting that all the toe trajectories from different mods should be located under the base board to exploit the full use of their clearance and avoid of the interference with the base board. Moreover, we can still adjust the length of floating link BC on top of different choices of E positions for more options in a larger design space.

Table 2.1: Comparison of toe trajectory properties between different mods. The percentage changes are wrt. the values of the original toe trajectory properties. R(1) and R(2) are abbreviations of regions (1) and (2).

Cases	E pos.($|BE|,|CE|$)	Avg. DR	Avg. DR R(1)	Avg. DR R(2)	Clearance
Original	(17.7, 26.4) [cm]	8.92 [cm/rad]	6.94 [cm/rad]	11.4 [cm/rad]	10.7 [cm]
Mod1	(16.0, 25.5) [cm]	-2.15%	+0.38%	-0.38%	+14.3%
Mod2	(26.5, 34.0) [cm]	+23.8%	+13.9%	+26.8%	-13.7%
Mod3	(14.5, 23.0) [cm]	-10.8%	-7.93%	-11.6%	-7.62%

2.2.4 Mechanism and structure design

With the drivetrain mechanism and toe trajectory designed, the next step is to design the physical structure and mechanism to reliably achieve such kinematics. Besides, these physical structures and mechanisms should also be modular and as simple as possible based on our general design requirements mentioned in Section 2.2.2. In this section, we introduce the detailed leg design for BigAnt. For the designed drivetrain mechanism (Figure 2.5a), its joint A and input crank AB are existing parts of the actuation module, while all other joints and links need to be built from only

20

two kinds of materials: the plate material (Elmer's Products Inc. foam board $508 \times 762 \times 7$mm) and flexure material (3M Scotch #8959 fiber tape) with our customized PARF techniques.

2.2.4.1 Leg and hip design
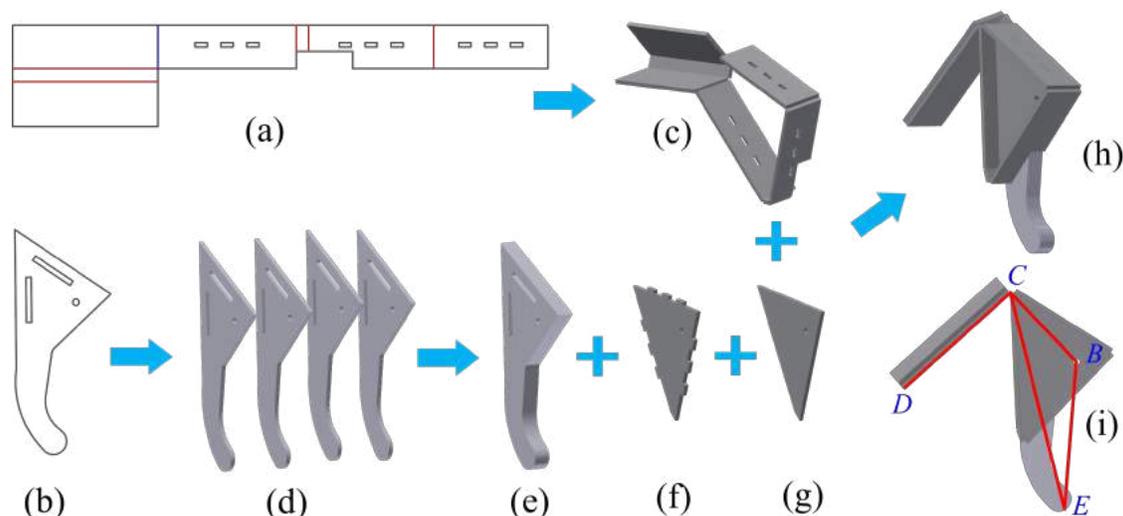
Figure 2.7: Leg and hip design of BigAnt: (a). 2D carving pattern for hip frame. (b). 2D carving pattern for leg part. (c). 3D structure of hip frame folded from (a). (d). 4 pieces of leg parts are sandwiched for construction of the leg. (e). BigAnt leg. (f). Supporting board for hip frame. (g). Positioning spacer for assembling leg into hip frame. (h). Hip-leg structure in 3D view. (i). The corresponding driven train mechanism depicted on the hip-leg structure.

To allow the floating link BC and coupler point E adjustable for modularity, we grouped them into one rigid part and call it "leg", which can be switched for different applications. The physical leg structure for real locomotion is not just a triangle like the coupler structure BCE in Figure 2.5a. The coupler point E can not be used as the only contacting part for the leg-environment interaction either. In reality, especially in field environments, when considering wear, motion smoothness and possible penetration contact with the environment, we usually design a curved surface as the contact region of a leg. The leg shape we designed for BigAnt general use is shown in Figure 2.7(b). This shape pattern is cut from foam board, and 4 sheets are sandwiched together by fiber tape to consist of a leg (Figures 2.7(d) and (e)). We use different leg shapes (Figure 2.7(b)) to achieve different coupler structures BCE (Figure 2.7(i)) for different applications as introduced in Figure 2.6.

The other part of the physical drivetrain mechanism consists of two rotation joints (C and D), a rigid link (CD) and a rigid frame for holding different kinds of legs. We call it the "hip frame". The main part of the hip frame is designed to be built from a single piece of foam board for fabrication

efficiency. The shape pattern of the hip frame part is shown in Figure 2.7(a). The blue and red lines are cut half way through for building PARF joints. When folded up, this shape pattern becomes an open frame (Figure 2.7(c)). With the supporting board (Figure 2.7(f)) enclosed, the open frame is transformed the complete hip frame for holding legs. The hip frame is designed to be a triangle for strength and stability. The mechanism link CD is reinforced with a triangular prism for the same reason.

When assembled together, the hip frame and the leg construct the main drivetrain mechanism and the ground interaction part (Figure 2.7(h)). The crank shaft from the actuation module drives this mechanism through the joint hole B in Figure 2.7(i) and generates the desired toe trajectory for BigAnt locomotion.

Here we also introduce the levels of physical modularity for BigAnt. Level 1 modularity refers to the part switching that does not require any tape removal. For instance, the leg switch only requires unscrewing the nuts on the actuation crank shaft at joint B. Level 2 modularity refers to the part switching that does not require tape removal from foam board surface. For instance, the switch of the whole hip-leg structure from the BigAnt base board belongs to the operation with the Level 2 modularity, since it only involves tape removal from other tape surfaces. It is worth noting that removing tape from a tape surface is easy and will not cause damage, while removing tape from a foam board may damage the surface.

2.2.4.2 Base board structure design

Base board design is the other key part of the BigAnt design besides the drivetrain mechanism introduced in the previous section. The base board of BigAnt holds the functionality of supporting and mounting leg-hip mechanisms, actuation modules, electrical components, and all other accessories like on board cameras, etc. Therefore, design of the base board mainly focuses on solving problems from following two aspects at the same time: (1). How to arrange the base board space and attach other units. (2). How to bear the load with limited material type and usage.

In terms of space arrangement, the first consideration is how to place the 6 hip-leg mechanisms. The trivial arrangement is setting 3 legs in a line on each side of a rectangular base board, similar to what is conduced in RHex family robots and the previous versions of BigAnt. However, this version of BigAnt is designed to maximize the step size subject to the dimension of foam boards and the work space of our laser printer. Thus to avoid interference between the consecutive legs, the base board shape is designed as shown in Figure 2.8(a) which places the middle legs slightly further from the base board center line. It is worth noting that we use a whole piece of foam board to carve for the main part of the base board to make full use of the material strength in this version. For other variants such as the water resistant version, we did conduct methods to connect the two pieces of planar material to a larger base board. For the space arrangement for other units, we
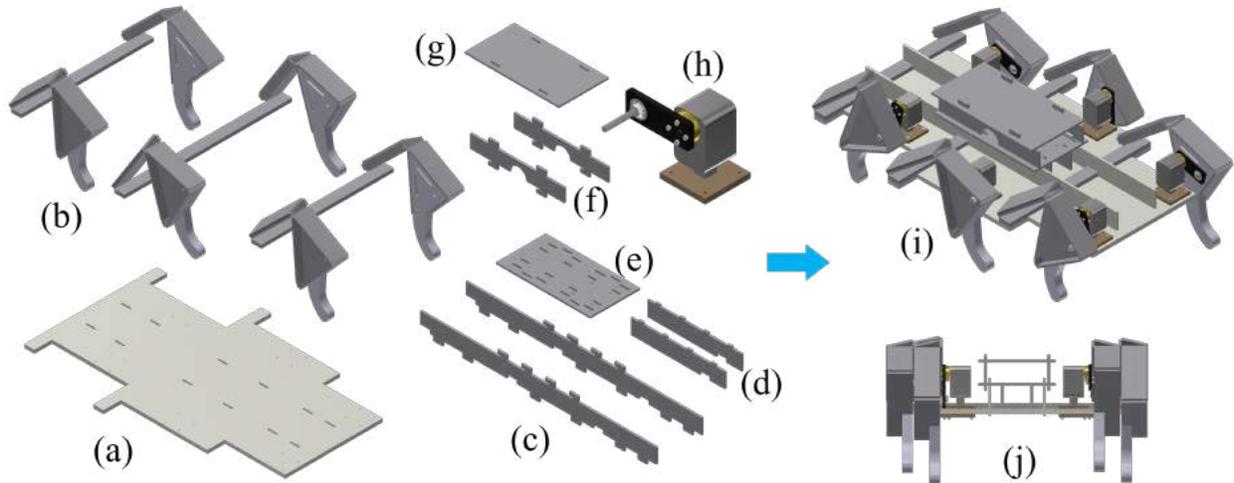
Figure 2.8: Base board design and assembly demo of BigAnt: (a). Base board part (x2 stacked). The notches on it are for the attachment of the sagittal ribs. The small holes are for the attachment of actuation modules. (b). Leg-hip structures that are attached to the lateral ribs. (c). Sagittal ribs. (d). Wall parts for the battery chamber. (e). Cover board 1. The notches are for the connection to sagittal ribs (c), the battery chamber walls (d) and the electrical chamber wall (f). The small holes are for the attachment of PCB boards. (f). Electrical chamber walls. (g). Cover board 2 for the electrical chamber. (h). CAD model of the actuation module which is magnified (x2) in dimension to the details. (i). The whole assembly of the BigAnt chassis with the actuation modules. (j). Front view of the BigAnt assembly showing the battery chamber (smaller one at bottom) and the electrical chamber(larger one on top).

mainly use rectangular chambers on the center line to hold them in position (Figure 2.8(j)).

With the base board shape and dimension determined from the space arrangement, the next design step is to ensure that the base board is strong enough to hold other units and support the whole system during locomotion with only quarter-inch foam board and tape. For the main base, we stack two pieces of base board part (Figure 2.8(a)) and fixed their edges together by fiber tape to increase its strength against bending. Three strips of fiber tape are wrapped around the main base in the lateral direction with tension to increase the stiffness. Two sets of reinforcement ribs are applied to further increase the structure strength of the base board. The first set contains 3 ribs taped to the main base along the lateral direction (Figure 2.8(b)). The second set consists of 2 sagittal ribs that are perpendicularly inserted into the main base (Figure 2.8(c)). The top parts of the 2 sagittal ribs are connected by the cover board 1 (Figure 2.8(e)) to increase the structure stability and provide space for the battery chamber. On top of cover board 1, another rectangular structure is built as the electrical chamber (Figure 2.8(j)).

As introduced in the previous section, the base board is also part of the drivetrain mechanism: it physically determines the positions of the fixed joints A and D referring Figure 2.5a. For attaching the leg-hip structures, the fixed joint D is not connected to the base board directly, while it is first

connected to the lateral ribs, then attached to the main base (Figure 2.8(b)). There are two reasons for such a design: First, it is easier to build a PARF joint D connecting leg-hip frame with lateral ribs since the triangular prism on link CD can only be fully closed after the construction of joint D. Smaller lateral ribs are easy to operate during the fabrication process than the whole main base. Second, such a design also brings extra modularity to BigAnt. The leg-hip structure with a lateral rib can be replaced together, if completely different kinematics are required and cannot be achieved by just switching the leg. Such a replacement does not require tape removal from the foam board surface but only needs to remove tape from tape surfaces. Thus, it introduces Level 2 modularity for BigAnt.

The other fixed joint A is determined by the actuation module (Figure 2.8(h)). The actuation modules are attached to the base board by the ModLock quick-locking connectors [Davey et al., 2012] which are pre-assembled to the base board by screws and bottom spacers. Joint A is located on the motor output shaft. Joint B is constructed by inserting the shaft screw of the crank into the joint hole on the leg. This assembling process physically closes the 4-bar linkage mechanism.

Figure 2.8 exhibits the base board design and the whole assembly of BigAnt. The base board structure is designed to be simple and robust. There are only 7 kinds of different parts in total for the construction of the base board. In summary, except for the actuation modules, all the chassis parts and assemblies of BigAnt are successfully designed to be built only from foam board and fiber tape.

2.2.5 Actuation and control

To make BigAnt a fully functional hexapedal robot for locomotion tests, the last design step is to add actuation, power circuit, and control board to the BigAnt assembly which we aforementioned. These actuation and control parts are also made modular and encapsulated for assembling convenience.

The motor of our actuation module (Figure 2.9a) is a high-end hobby servomotor (Dynamixel MX64, Robotis, Inc.). It is mounted to a ModLock base by screws for quick attachment to the robot base board. A customized laser-cut PBS crank is assembled to the motor output flange and holds a bolt with a skate board ball bearing for power transition to the chassis power train mechanism.

The control and communication architecture is one of the major changes compared to the previous versions of BigAnt. Previous control calculations were conducted on PC host. The control/sensing signals were sent through the Pololu Wixel module by radio wireless communication. To improve communication stability and operation range, we adopted a on-board calculation platform on the new BigAnt. The on-board unit we chose is Intel Edison which runs Linux and provides USB, serial as well as other interfaces to robot hardware. The communication for operation

<center>(a)</center>
<center>(b)</center>
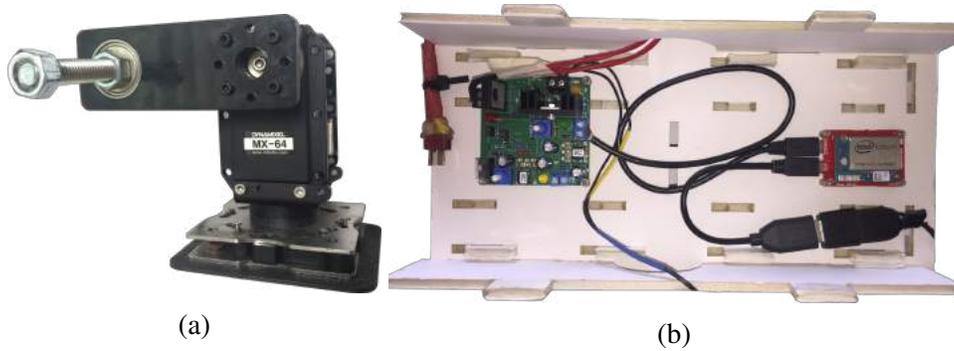
Figure 2.9: (a). Actuation module. (b). Power board (left) and Intel Edison unit (right) located inside the BigAnt electrical chamber.

commands and status feedback is achieved through a PC-hosted WiFi network by SSH protocol. This on-board calculating setup also provides the potential for fully autonomous operations of BigAnt. Figure 2.9b shows the Intel Edison unit attached to the cover board 1 in the electrical chamber of BigAnt.
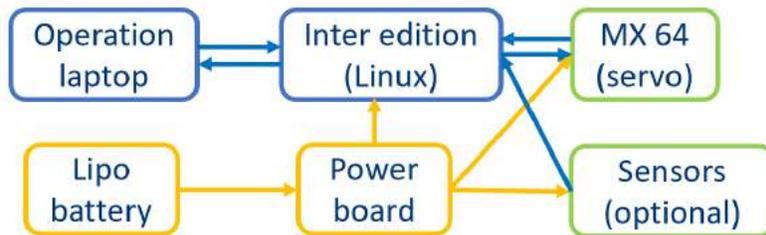
Figure 2.10: Control structure of BigAnt. The signal flow between two units is indicated by the orange arrows while the signal flow is indicated by the blue arrow.

BigAnt uses a 4-cell lithium polymer battery as its power source. We use a self-developed custom power board (Figure 2.9b) which passes through the 13.8-14.7V battery for motor drive, and also supplies regulated 5.5V for powering the Intel Edison unit and other digital devices. The detailed control structure of BigAnt is summarized in Figure 2.10.

2.2.6 Fabrication

In the above design sections, we focused on introducing the mechanism and structure design of the BigAnt chassis which are required to be built only from foam board and fiber tape. To successfully realize such a chassis for a robust robot platform with such low-cost materials in a limited time, a sophisticated technique and management of the fabrication are required. In this section, we will

<center>25</center>

introduce some detailed examples during the BigAnt fabrication process and report the material usage and the fabrication time.

2.2.6.1 Fabrication examples

The materials we used for the BigAnt chassis construction are: 1. Foam board (Elmer's Products Inc. $508 \times 762 \times 7$mm); 2. Fiber tape (3M Scotch #8959 fiber tape). The foam board can be cut either by knife for onsite construction and repair or by laser cutter for faster fabrication. The fiber tape is used with two kinds of width in the BigAnt fabrication: the original width from the tape roll (50 mm) and the half width (25 mm) by knife trim.

(1). Parts fabrication in batches by laser printer:
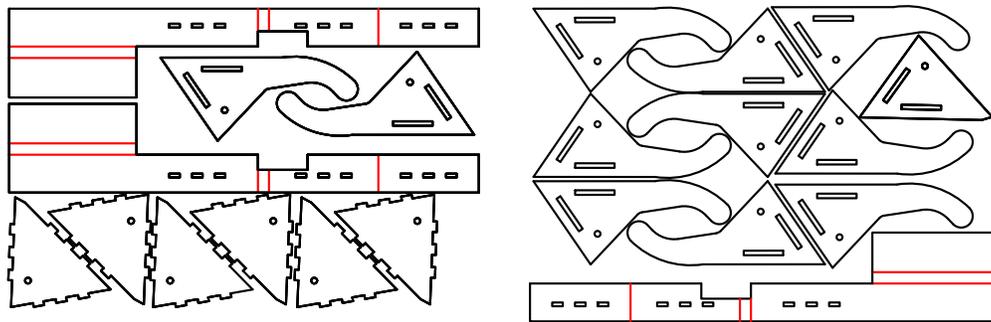
Figure 2.11: Examples of printing pattern clusters for parts fabrication.

In our lab environment, we used the laser printer (PLS6.150D Laser System, Universal Laser.) to cut parts from foam board. For efficiency of both material usage and fabrication time, parts were carefully arranged as pattern clusters to tightly fill a sheet of foam board as a batch (Figure 2.11). All batches of parts were then collected for further assembly.

(2). Joint fabrication:
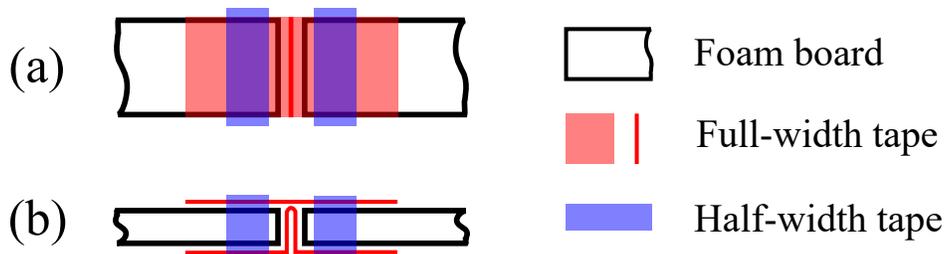
Figure 2.12: Joint fabrication

Joints built of foam board and fiber tape are the most important parts in the BigAnt chassis. They perform the role of connections for both mechanisms (eg. 4-bar linkage) and structures (eg.

reinforcement prism). Meanwhile, they are also more vulnerable than other parts because of the repeated fatigue damage during robot motion. Therefore, the joints need to be made strong and durable for a robust BigAnt. Figure 2.12 presents the detailed joint building technique we used for this version of BigAnt. The two joint parts were first connected by full-width fiber tape from both surfaces, then wrapped around by half-width tape in the perpendicular direction of the hinge to prevent peeling of foam board surface. This joint can rotate in a range of $[0, 180°]$.

(3). Tape the sandwich leg:

As introduced in Section 2.2.4.1, the BigAnt leg is constructed by sandwiching 4 leg part pieces. How to firmly connect the part pieces is the concern of the fabrication process here. The positioning notches offer the first level of connection when the tape is wrapped through them for positioning the leg sandwich (as shown as Step 1 in Figure 2.13). The distal end of the leg tip also needs a tape connection. It is worth noting that most of the contact with the ground happens in this region of the leg. The leg tip foam board will be easily damaged and worn-out if there is no protection. Thus, the fiber tape covering leg tip not only connects the sandwich but also protects the leg.
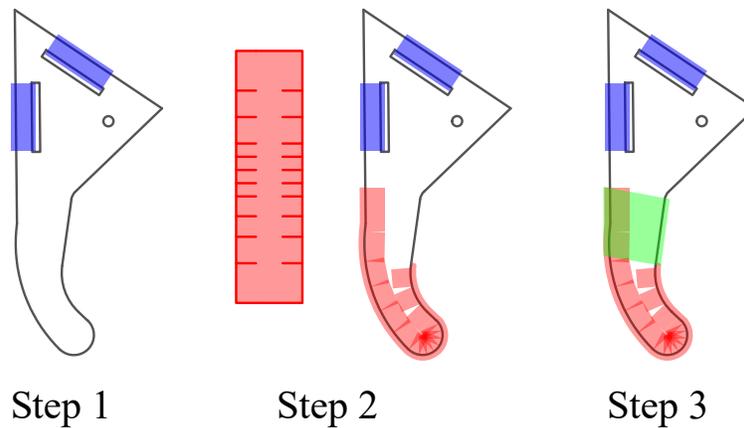
Figure 2.13: Sandwich leg fabrication steps. The tape adhere to the leg structure in the 3 steps that are indicated by the 3 colors.

Unlike taping the straight-line edges of the base board or the positioning notches, the tape on the curved leg edge cannot be directly attached. Otherwise, there will be wrinkles that decrease the tape adhesion force. To approximate the leg curve, we cut the two sides of the full-width tape into "fibers": small "fibers" for large curvature and large "fibers" for small curvature (as shown as Step 2 in Figure 2.13). When attached to the curved surface, the "fibers" will adhere the side surfaces one by one with overlapping to account for the distance changes along the radial direction. The last step for reinforcement of the sandwich structure is using tape to wrap around the leg across its straight-line edges (Step 3 in Figure 2.13). With the above introduced 3 steps, a robust sandwich leg assembly is fabricated.

(4). Tape assisted rib attachment:
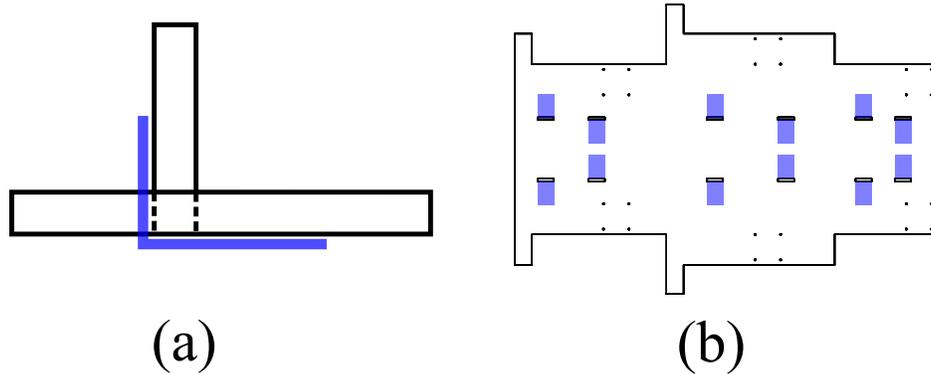
Figure 2.14: Tape assisted rib attachment. (a). Tape connects the sagittal rib side surface to the base board bottom surface. (b). Bottom view of the base board: tape direction switches along the rib to prevent the rib from tilting.

As introduced in Section 2.2.4.2, BigAnt adopts the ribs in lateral and sagittal directions to reinforce the base board structure. The lateral ribs are taped to the base board directly, while the sagittal ribs are inserted into the attachment notches on the base board perpendicularly. Even though the notch size is designed to be smaller than the thickness of the sagittal rib for an interference fit, the vibration during robot locomotion can still loosen the connection. To solve this problem, we use the half-width tape to assist the sagittal rib attachment. The tape are pre-attached to the rib teeth on their side surfaces and inserted together with the rib teeth into the base board. Then the tape are pre-loaded downwards and attached to the bottom surface of the base board as shown in Figure 2.14(a). It is worth noting that the taping direction alternates with the adjacent rib teeth for force balance. With this method, the sagittal ribs can be attached tightly to the base board without using any fastening component such as screws and nuts.

2.2.6.2 Material usage and fabrication time summary

The cost of fabricating the new BigAnt chassis is low. The total materials required are less than 7 sheets of foam board (Elmer's Products Inc. $508 \times 762 \times 7$mm) and less than 1 roll of fiber tape (3M Scotch #8959 fiber tape). The whole BigAnt robot can be built up within only 5 hours including all the fabrication and assembling processes. It is worth noting that the prior BigAnt chassis in [Fitzner et al., 2017] took 7 hours to build. With our new design and fabrication technique, the construction time is reduced by 29%.

2.2.7 Gaits design and locomotion tests

Despite its low cost and fast fabrication, BigAnt is a reliable hexapedal robot platform that has been frequently used in our research of multi-legged locomotion. In this section, we will introduce the general gait design for multi-legged robots with 1-DoF legs. We will then present the gait studies we performed on BigAnt and the corresponding experiment results. The BigAnt turning/steering gaits are intentionally excluded from this section and will be introduced in detail later in Chapter 3.

2.2.7.1 Gait design for robot with 1-DoF legs

Many multi-legged robots with 1-DoF legs adopt position/speed control for their actuation. For BigAnt, we also use the servo mode of its actuation motor to control the motor shaft motion, which is also the input of the drivetrain mechanism. The functions that map time to the motor shaft angle and angular speed are called the position profile and the speed profile of the actuation respectively. They are equivalent concepts for robot motion design with servo actuations, since the speed profile is the derivative of the position profile and one can be computed from the other.

For robots with 1-DoF legs, the leg tip trajectory can only occupy a 1-dimensional manifold. The motion of a robot leg is then fully determined by the position profile of its actuation through the drivetrain mechanism. The position profiles of all the actuations together determine the system motion. Therefore the gait design for the robots with 1-DoF legs is the design of the position profiles of all the actuations. Theoretically, the gait (actuation position profiles) has infinite options since it is a function into the N-dimension torus which we denote by $r(t) : \mathbb{R} \to \mathrm{T}^N$, where N is the number of 1 DoF legs with rotational actuations.

It is difficult to design a gait directly from the N-dimension function space given certain motion objectives. The two basic strategies for such gait design are to reduce the dimension and the order of the design space. To reduce the dimension of the gait function $r(t) = [r_1(t), r_2(t), \ldots, r_N(t)]$, the legs are usually grouped into different sets to generate motions with symmetry. For example, the classic tripod gait groups 3 legs into a motion set for the hexapedal walking, which has

$$r(t) = [r_1(t), r_2(t), r_1(t), r_2(t), r_1(t), r_2(t)] \tag{2.1}$$

where $r_1(t)$ is the actuation position profile of the left tripod legs (FL-MR-HL containing [F]ront-[L]eft, [M]iddle-[R]ight and [H]ind-[L]eft legs) and $r_2(t)$ is the actuation position profile of the right tripod legs (FR-ML-HR). Thus the original 6-dimensional gait space is reduced to be 2-dimensional. Besides grouping legs into legs sets, we can further reduce the gait space dimension by controlling some different leg sets to share the same motion pattern but with some position offsets. For example, by assigning the right tripod position profile to be $r_2(t) = r_1(t) + \pi$,

the tripod gait in Equation 2.1 is reduced to $r(t) = [r_1(t), r_1(t)+\pi, r_1(t), r_1(t)+\pi, r_1(t), r_1(t)+\pi]$ which is only 1-dimensional.

The other strategy is to reduce the order of the gait function $r(t) = [r_1(t), r_2(t), \ldots, r_N(t)]$. The actuation position profile $r_i(t) : \mathbb{R} \to \mathrm{S}$ is originally an arbitrary function which has infinite order. The method to reduce the design order of $r_i(t)$ is to parameterize it to be some basic low-order functions or their combinations. For example, the linear position profile $r_i(t) = kt$ only has 1 parameter k that needs to be designed; The Mth order Fourier series functions for approximating some periodic profile function $r_i(t)$ has $2M+1$ parameters that need to be determined. The famous Buehler clock developed for RHex in [Saranli et al., 2001] uses a piece-wise linear profile function for its gait, which is characterized by 4 parameters. We also use the Buehler clock for our BigAnt gait design. More details will be introduced in the next section.

In summary, grouping legs and adopting low-order profile functions based on the motion objectives are the basic strategies for gait design of low-DoF multi-legged robots.

2.2.7.2 Timing of 1-DoF trajectory and the Buehler clock design

For a 1-DoF leg, the leg tip trajectory is in a fixed locus (shape). Timing of the leg tip trajectory describes when and at what speed the leg tip arrives at some given point on the trajectory locus, which is an important representation of the leg motion. The motion objective usually can also be interpreted by some timing schedule on the leg trajectories. There are two important questions for the leg motion design: (1) which part of the leg tip trajectory should be in contact with the environment; (2) at what speed should the leg tip move during the contact. For example, a good contact part for the BigAnt normal walking gait should be in region (2) of its designed toe trajectory (Figure 2.5a), which is flatter in terms of curvature and has a larger drive ratio for propelling. We note the beginning of the contact as "touch-down" and note the end of the contact as "take-off". The selection of the take-off and touch-down points on the leg tip trajectories is a kind of timing planning for the leg motion. In the gait design for robots with 1-DoF legs, the motion objective and the actuation profiles are not explicitly connected, especially for those that have a drivetrain mechanism instead of directly driving the leg from the actuator. Timing planning on the leg trajectories is a bridge that helps to connect the motion objective with the actuation profiles. In this section, we demonstrate how to design a low-order actuation profile for the BigAnt tripod walking gait to achieve the target contact region on the leg tip trajectory.

The original Buehler clock for RHex [Saranli et al., 2001] was developed to regulate the timing on the leg trajectory. The rotation of a RHex leg is controlled to have two phases: the stance phase (equivalent to our contact region) and the flight phase (when the leg is swinging in the air). Legs must rotate slower during the stance compared to the leg motion during flight since the stance phase occupies less than half a full leg revolution and there must always be at least one tripod in

the stance phase. The Buehler clock of RHex provided a motor rotation profile that is a piece-wise linear function with a slow piece for stance and a fast piece for flight. This piece-wise linear function with two speed regions can also be used as a low-order profile function for the gait design of other multi-legged robots with 1 DoF legs. To simplify the Buehler clock formula for periodic gaits, the actuation position (motor shaft angle) profile $\psi(t)$ is rewritten as a function of phase ϕ as $\psi(\phi) : \mathsf{S}^1 \to \mathsf{S}^1$, where the phase is calculated from time as $\phi(t) = \exp(i2\pi t/T)$ and T is the gait period. We assume $\psi(0) = 0$ for further simplification, since the choice of zero phase can be arbitrary. Then the Buehler clock for a 1-DoF leg is characterized by 3 parameters: the beginning phase ϕ_s and the ending phase ϕ_e of the first linear region; the angle range $\Delta\psi_0$ of the first linear region, and has the following formula:

$$\psi(\phi) = \begin{cases} \omega_1\phi & \phi_s \le \phi < \phi_e \\ \omega_2\phi + \omega_1\phi_e & \text{Other phase} \end{cases} \tag{2.2}$$

where $\omega_1 = \Delta\psi_0/(\phi_e - \phi_s)$; $\omega_2 = (2\pi - \Delta\psi_0)/(2\pi - (\phi_e - \phi_s))$. Therefore, the design of the actuation profile function is now the design of the 3 parameters of the Buehler clock. The next step is to use the trajectory timing plan to determine these 3 parameters.

(a)

(b)
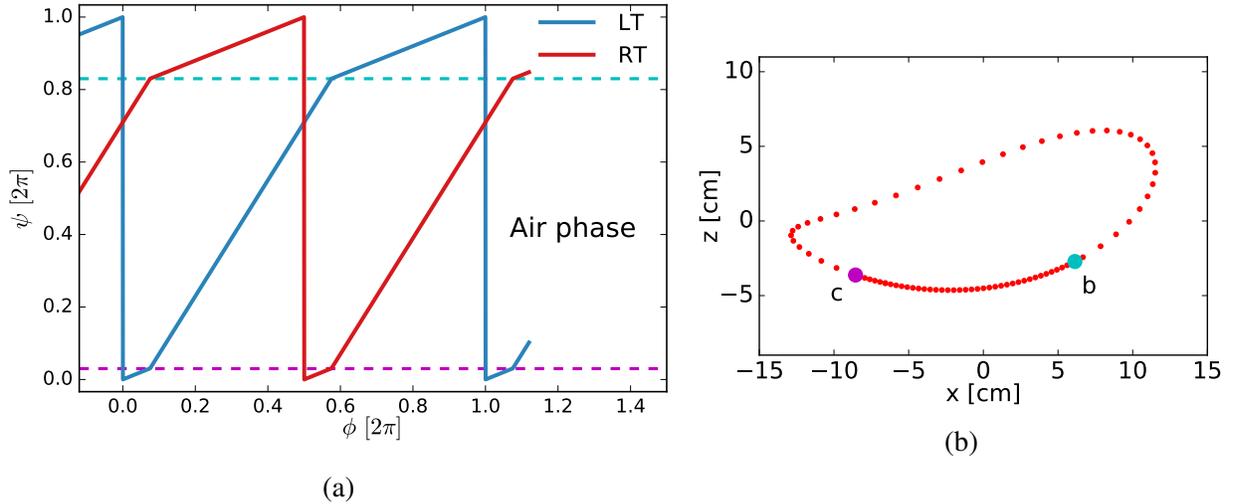
Figure 2.15: (a): The actuation profiles for the BigAnt tripod walking gait defined by the Buehler clock function. LT and RT are abbreviations for left tripod and right tripod. The two horizontal dashed lines exhibit the actuator shaft angles that correspond to the touch-down point b and the take-off point c on the leg tip trajectory as shown in (b). (b): The leg tip trajectory of the BigAnt walking gait depicted in (a), with sample points indicated at an equal phase (time) interval.

For normal walking, we adopted the timing plan that divides the leg trajectory into two regions: one region for contacting the environment (stance phase) and the other region for leg swinging in

the air (flight phase). The boundary of the two regions corresponds to the two key points on the leg tip trajectory: the "touch-down" and "take-off" points which we note as point b and point c respectively (Figure 2.17). For RHex like robots whose legs are directly driven by the actuator shafts, the "touch-down" and "take-off" points on the circular leg tip trajectory are directly represented by two shaft angles. While for robots with 1-DoF legs like BigAnt that are driven by some drivetrain mechanisms, an extra step needs to be taken to map these two points on the toe trajectory back to the two shaft angles which we note as ψ_s and ψ_e. With the "touch-down" point b and "take-off" point c selected on the leg tip trajectory, the last parameter from the timing plan is the duty factor P of the contact region (the ratio of the contact period over the whole gait cycle period). Without loss of generality, we assume the contact region corresponds to the first linear region in the Buehler clock and contains the zero shaft angle ($\psi(0) = 0$). Then the 3 parameters of the Buehler clock can be computed as: $\Delta\psi_0 = \psi_e - \psi_s$; $\phi_s = \psi_s/(\Delta\psi_0/2\pi P)$; $\phi_e = \psi_e/(\Delta\psi_0/2\pi P)$. Thus we achieve the actuation profile function of one leg or tripod.

It is worth noting that the above proposed contact region on the leg tip trajectory is just a timing plan. The realistic contact region of a leg during robot locomotion is determined by both the ground condition and the motion of the other legs. In the general scenario in which BigAnt walks on rigid flat ground with rigid toe trajectories and synchronized tripod legs grouping, the "touch-down" and "take-off" points on the toe trajectories are determined by the relative timing of the two tripods. The take-off of one tripod is at the same time as the touch-down of the other tripod since the supporting tripod is always the one with the lower vertical positions. This general case implies that the take-off point b and the touch-down point c should share the same vertical (world z axis) position. It also implies that the duty factor P of the contact region should be 0.5 since the stance period of one tripod equals to the flight period of the other tripod if the two tripods adopt the same Buehler clock pattern which is true for many hexapedal robots.

Based on the above analyses, we designed the BigAnt tripod walking gait as shown in Figure 2.15a. The left tripod adopts the Buehler clock formula $\psi(\phi)$ in Equation 2.2 with parameters designed as: $\Delta\psi_0 = 0.2[2\pi]$, $\phi_e = 0.075[2\pi]$ and $\phi_s = -0.425[2\pi]$. The zero shaft angle While the right tripod adopts the same Buehler clock pattern but with a half cycle offset: $\psi(\phi + pi)$. The consequent leg trajectory is depicted in Figure 2.15b. The leg tip trajectory has a slow contact region and a fast flight region. The contact region will be the real contact region during locomotion if the ground is flat. It is worth noting that if the legs are compliant, for instance the RHex legs, there can still be some period that all the legs are contacting the ground with the proposed tripod gaits, since the planned contact region can not be guaranteed because of the leg deformation.
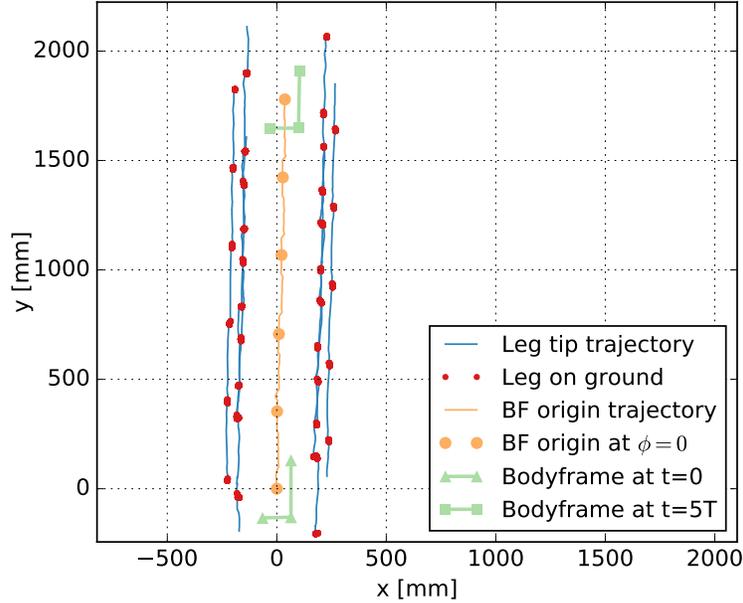
Figure 2.16: Test result of BigAnt tripod walking gait at gait frequency $f = 0.24Hz$. We plotted (left) leg tip trajectories (blue), with leg contact with the ground highlighted (red dots), and the trajectory of the body frame origin (yellow line) with the beginning of cycle indicated (yellow dots). We indicated the markers that define the body frame (light green) at the beginning (triangles) and end (squares) of this 5-stride trial.

2.2.7.3   Walking gait tests

We performed the tripod walking gait designed in Section 2.2.7.2 on BigAnt in our lab environment. The locomotion results were recorded using a reflective marker motion tracking system (10 Qualisys Oqus-310+ cameras at 120 fps, running QTM 2.17 build 4000, interfaced to custom SciPy 0.17.0 code using the Qualisys 1.9 Realtime API).

One example trial of BigAnt walking at gait frequency $f = 0.24Hz$ is presented in Figure 2.16. The body frame origin trajectory and the leg trajectories are all close to straight lines with very little sideways drifts after 5 gait cycles, indicating that the constructed BigAnt robot platform is in a good symmetric condition. From the motion tracked z position of each BigAnt leg tip, we learned at which part of the leg trajectories do the leg tips contact with the ground. The highlighted leg contacts all concentrate in forms of small dots in Figure 2.16, which suggests that little slipping happened during this tripod walking gait. If the legs have noticeable slip, the highlighted leg trajectories will be lines instead of being close to concentrated dots. That very little slipping is observed also implies that there is very little or no "double stance" (all six legs are in contact with the ground) time for the tested BigAnt motion. Otherwise, the speed difference of the two tripods at contact will push some legs to slip. This is also an indicator that the achieved BigAnt motion

33

gets a good match with our designed gait, since the "touch-down" and "take-off" of the two tripods took place at the right time as planned by the Buehler clock.

(a)

(b)
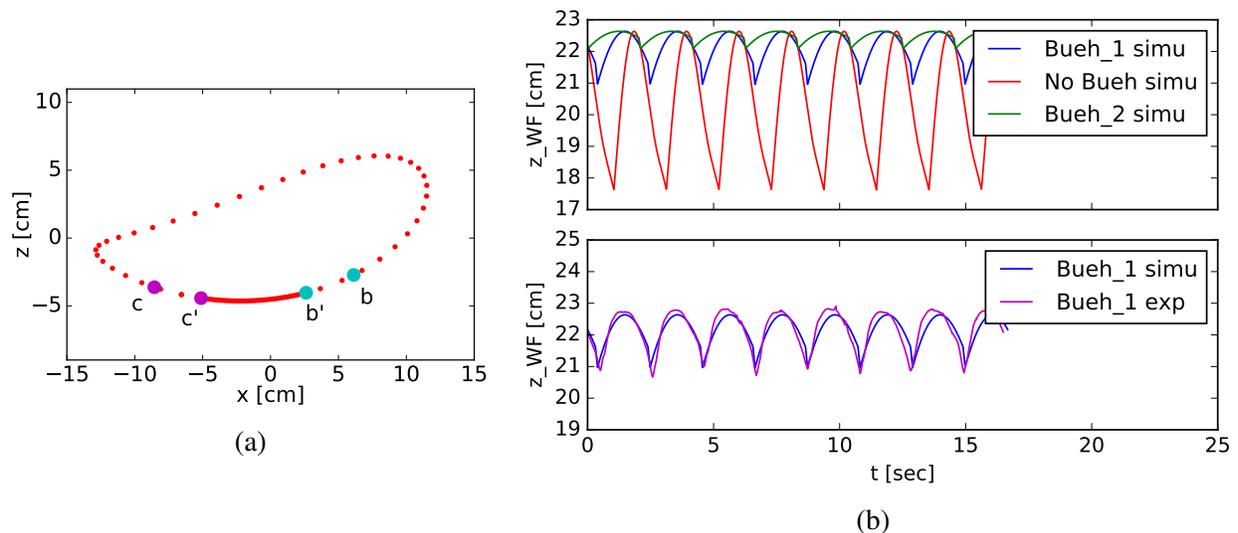
Figure 2.17: (a): Leg trajectory from Buehler clock II. The corresponding contact region $b'c'$ is compared with the contact region bc from Buehler clock I. The sample points on the trajectory are indicated at equal phase (time) intervals. (b). CoM z axis (vertical) positions vs. time in the locomotion generated by different actuation profiles in simulation and real robot experiment. The "No Bueh simu" case just adopted a linear actuation profile characterized by a single parameter: a constant shaft rotation speed. The experiment result (bottom subfigure) is from the same test trial as depicted in Figure 2.16.

In Section 2.2.7.2, we introduced how to plan the timing on the 1-DoF trajectory to determine the contact region. Such contact region planning that is achieved by the Buehler clock design reduces the parasite vertical oscillation when the robot system is walking on the horizontal plane. To exhibit the influence of the different contact regions, we designed another actuation profile for the BigAnt tripod walking gait which results in a smaller contact region $b'c'$ on the leg trajectory as depicted in Figure 2.17a. The original contact region bc is also marked on the trajectory for reference. We noted the original Buehler clock as Buehler clock I and noted the new Buehler clock as Buehler clock II. We then performed a kinematics simulation for BigAnt tripod walking gait adopting 3 different actuation profiles with the same gait period: Buehler clock I, Buehler clock II and a linear profile function with constant motor speed motion. The simulated system CoM z position in the world frame is presented in Figure 2.17b (top subfigure). To verify the accuracy of this kinematic simulation, the experiment result of the BigAnt gait adopting Buehler clock I is plotted along with the simulation result as a reference (Figure 2.17b bottom subfigure). The simulated CoM motion from the linear actuation profile exhibits a much larger vertical oscillation compared to those from the Buehler clock profiles. If directly applied to the real robot platform,

such a large vertical oscillation (5 cm, almost half of the leg trajectory clearance) will waste a lot of the battery energy and cause extra unnecessary impact damage to the robot structure. The Buehler clock II does generate even less vertical oscillation than Buehler clock I, but it does so by sacrificing the stride length as shown in Figure 2.17a; there is a trade-off. A strategy that worked well for us was to set an upper bound on acceptable vertical oscillations, and search for maximal stride length within that bound. It is worth nothing that these results and analyses again supports our hypothesis about the 1-DoF leg trajectory that a flat contact region is generally helpful for low-DoF multi-legged locomotion.

2.2.7.4 Turning in place gait

In this section, we introduce a turning in place gait designed for BigAnt.
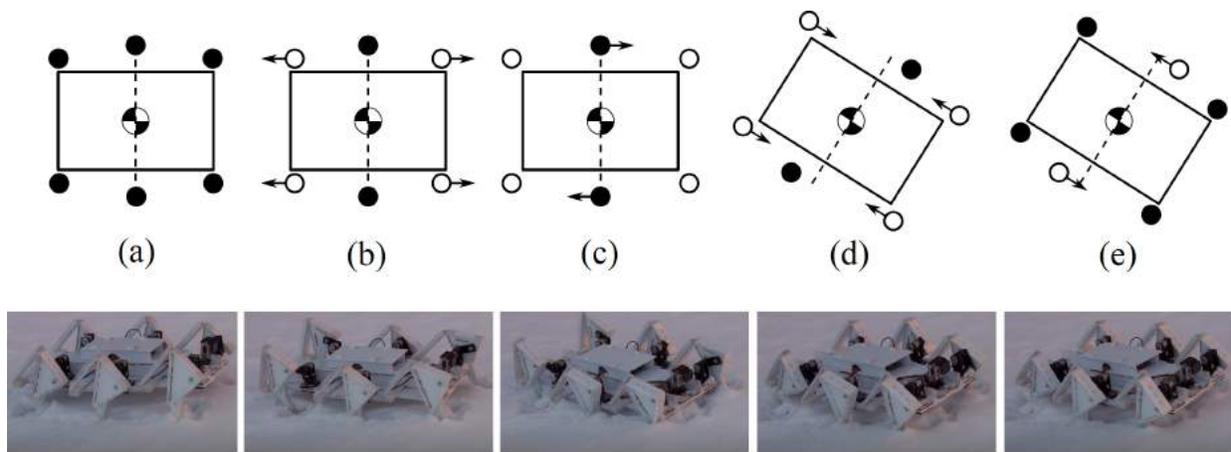
Figure 2.18: Demo of BigAnt turning in place gait: gait procedures (top) and a trial of gait test on BigAnt in snow field (bottom). (a): all 6 legs stand on the ground; (b): Front and hind legs are raising up at the same time, leaving the middle legs supporting the robot; (c): The supporting middle legs perform skew motions to rotate the robot; (d): Front and hind legs drop down together to the original position in (a) for supporting. (e): Middle legs move back to the original position in (a). After step (e), the robot returns to the original configuration as in (a), but with its orientation changed.

The details of the turning in place gait are presented in Figure 2.18. For robots like BigAnt that have 1 DoF leg trajectories parallel to the robot sagittal plane, turning in place results in sideways (in direction perpendicular to the initial sagittal plane) motions for all legs. Such sideways leg motions resist the turning-in-place motion if the corresponding legs are contacting with the ground. The essence of this gait is to use the middle legs which have minimal sideways motion to support the body and generate the turn. The legs are grouped by front, middle and hind leg pairs. Each of the leg groups is driven by a piece-wise linear position profile. It is worth noting that this gait

is a dynamic gait; the speed of execution matters. In steps (b), (c) and (d) (Figure 2.18), the leg motions need be tuned to ensure that the middle legs are always supporting the robot while the front and hind legs are (as much as possible) in the air. We tuned the gait in the lab on a flat rigid floor to get BigAnt well balanced in steps (b), (c) and (d). However, the results in uneven outdoor environments can be different, since the balance of the two-leg-supported steps (b), (c) and (d) cannot be completely guaranteed, and either the front pair or the hind pair may contact the ground. Despite this, in most of the cases BigAnt can still change its orientation with this gait, since most of the weight is on the middle legs and the motion of the middle legs still dominates in rotating the system, while forcing the front or hind legs to slip (see bottom row of Figure 2.18; BigAnt was performing a turning in place gait in the snow).

2.2.7.5 Outdoor tests

Even though BigAnt is low-cost and fabricated rapidly, it is a fully functional hexapedal robot. One of our design objectives for BigAnt is to ensure its capability to traverse the uneven outdoor environments. The prior BigAnt (Figure 2.3e) failed to walk on the flat grass land because of its low leg trajectory clearance and extra sideways motion in flight phase. With the new design, our BigAnt successfully travelled through the grass field, grass ramp, hip-high obstacles/curbs and even the Wave Field[6]. Figure 2.19 demonstrates BigAnt climbing over a bump in the wave field. More motion examples can be found in this media link.

Figure 2.19: BigAnt outdoor tests on the grass wave field.

2.2.8   Variants of BigAnt

With our proposed design strategy, design objectives, design/fabrication techniques, and some iterations of real robot tests, this version of BigAnt we achieved is proved to be a reliable multi-legged robot platform. Its kinematics design, chassis design and fabrication techniques make it a paradigm and a master branch version for BigAnt evolution. We further developed many variants

---

[6]The Wave Field is an earthen sculpture on the North Campus of University of Michigan

of BigAnt based on this master branch version for specialized tasks and tests. In this section, we will introduce some variant examples of the BigAnt family robots.

2.2.8.1 Water resistant BigAnt

In BigAnt outdoor tests, we observed that some parts of the BigAnt structures and mechanisms are slightly weakened by water when it walks on wet grass fields. It is an issue with the foam board material. The strength and stiffness of foam board decrease when they are wet. The two surface layers of foam board are also more vulnerable to peeling when they are wet, which further weakens the mechanism joints. To solve this problem with BigAnt chassis and to improve BigAnt's ability to perform outdoors tasks, we developed a water resistant variant of BigAnt.

The primary changes for this variant are from the material and the material related structure design. We use the corrugated plastic board for this variant to replace the foam board for the function of the rigid plate in PARF. Besides water resistance, the biggest difference between corrugated plastic board and foam board is the homogeneity of the material properties. Foam board possesses uniform mechanical properties along all their tangential directions. However, corrugated plastic boards are stronger and stiffer in the direction along their ridge cells and weaker and softer in the direction perpendicular to their ridge cells. Therefore, we adjusted the structure design and fabrication accordingly to ensure that all the potential loads are covered by some corrugated plastic boards in their strong directions. For example, the base board parts were laser cut from two corrugated plastic boards from two directions and stacked together to resist the bending from both saggital and lateral directions. We also designed extra ribs to connect and reinforce the robot base board. With such material change, structure design and fabrication adjustments, we achieved a water resistant BigAnt which is functional as the original foam board version. Figure 2.20 demonstrates the BigAnt water resistant variant operating in outdoor snow environments. It was climbing over a bump in the wave field covered by 10+ cm depth of snow. More motion details for this test can be found in this media link.

Figure 2.20: Outdoor test of the water resistant BigAnt on the wave field that is covered by 10+ cm depth of snow.

2.2.8.2 Stair climbing BigAnt

A big challenge for meter-scale multi-legged robots to move in human constructed environments is to climb the stairs which are designed for humans. Almost all stairs have step heights that are higher than the BigAnt hip. Climbing hip-high obstacles is also a challenge for legged system in general. This issue is more problematic for robots with low-DoF legs.

Figure 2.21: BigAnt climbing stairs (left). The distance sensor that is integrated into the BigAnt stair climbing variant (right).

We designed a gait for BigAnt to tilt up its body and sit on its hind and middle legs. In this way, the front legs are raised up high enough to step on the first stair and then initiate the climbing process. Such a climbing gait is an open loop gait that can drive BigAnt to climb 4 to 6 stair steps before it fails to further climb. This is because the robot is not perfectly symmetric, and the accumulated errors will gradually change the spots where the legs land on the stairs and finally cause some legs to miss a stair or become trapped between stair steps. To solve this issue, extra sensing for feedback loops could be used to correct BigAnt motions during stair climbing. Therefore, we built a stair climbing variant of BigAnt by integrating a sensor on each of the BigAnt legs. To maintain the tradition of being low cost, the sensors on this BigAnt variant are inexpensive (Pololu Sharp GP2Y0A41SK0F Analog Distance Sensor; around 10 USD each). Figure 2.21 shows the BigAnt stair climbing variant and how we attach the distance sensor to the BigAnt leg. These distance sensors provide feedback information about the distance between the BigAnt leg and the stair surfaces. However, the distances measured from such sensors are only accurate when the sensor face is parallel to the target surface, while the robot motion generates a varying angle between the sensor and the stair surfaces during the climbing process. Thus, the sensor output voltage cannot be mapped to the real distance between the robot legs and each of the stairs. Instead, we tried to identify the features in such sensor signals which correspond to the leg contact with the stair and use this information to correct BigAnt motion. Stair climbing is an ongoing

project for BigAnt.

2.2.8.3 Force sensing BigAnt

BigAnt robot platforms are widely used in our lab for multi-legged locomotion study. Currently, all our analysis and models of the robot locomotion are based on the motion data measured by the motion tracking system in experimental tests. The information of the ground reaction force (GRF) during leg-ground interaction would further improve our understanding of multi-legged locomotion. For example, there can be static indeterminacy in Multi-legged locomotion: with multiple contacts there can be internal forces with zero net acceleration introduced, so the forces cannot be observed from body motions.

Conventional force sensors are usually torque sensors that are installed to the robot actuation joints or strain gauges that are attached to the compliant components of the robot structure. All these sensors need further modeling processes of the robot to estimate the GRF. There are also dedicated treadmills that can directly measure the GRF of robots or humans that are walking on them. These force sensing treadmills work for heavy bipedal or quadrupedal robots that usually have only 1 or 2 legs contacting the treadmill surface. For our multi-legged robots that are relatively light, these force sensing treadmills are not capable of identifying the GRF on each leg. Their high cost also limits the appropriateness of their application. Another drawback of adopting force sensing treadmills to the study of multi-legged locomotion is that they limited the surface which multi-legged robots can walk on for GRF studies. The multiple contacts of multi-legged robots are complicated and sensitive to the ground conditions. For example, some analyses require the GRF of robots walking on surfaces with different friction conditions.
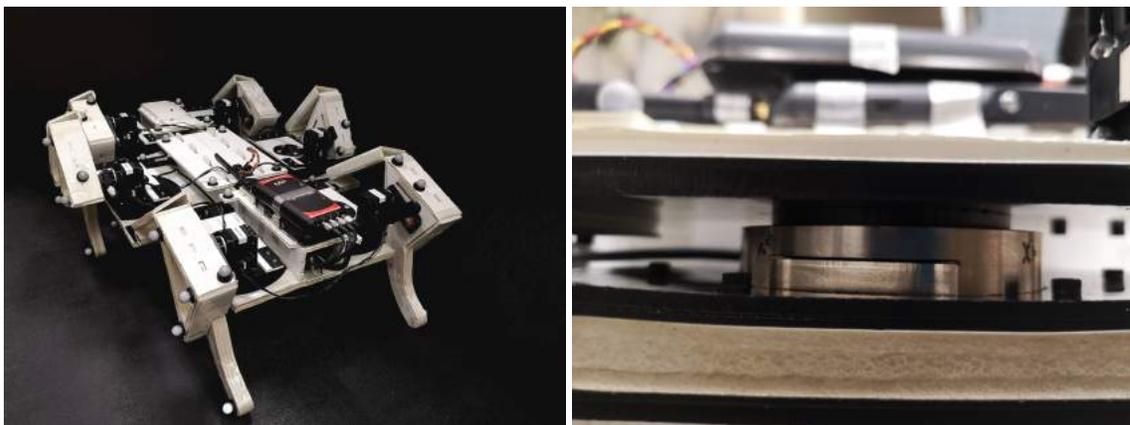
Figure 2.22: Force sensing BigAnt (left); The force transducer connecting the leg-actuation module to the base board.

Based on the objective of measuring the GRFs for low-DoF multi-legged robots, we (with Yue

Sun, a former student in our lab) designed and built a force sensing variant of BigAnt as shown in Figure 2.22. It adopts 6 force transducers (ATI Industrial Automation gamma SI-130-10) which can measure forces and torques in all the 3 axes of the transducer reference frame. To simplify the process of calculating the GRFs from the measured raw force information, we modified the connection structure between the BigAnt legs and the base board. The drivetrain mechanism and the actuation module of each leg are constructed on an isolated "leg base" connected to the base board by a force transducer. In this way, the forces between the leg modules and the base board can be directly measured. It is worth noting that the force transducers and their accessories are heavy components compare to other parts of BigAnt and require stiffer and stronger structures than the original BigAnt. Therefore, we adopted some more kinds of materials for constructing the BigAnt base board and the leg-actuation module, such as thicker foam board and two kinds of ABS plastic boards, to achieve the strength and stiffness requirements. This force sensing variant of BigAnt is now operational for measuring GRFs in BigAnt locomotion tests.

2.2.8.4   A small version of BigAnt: MediumAnt
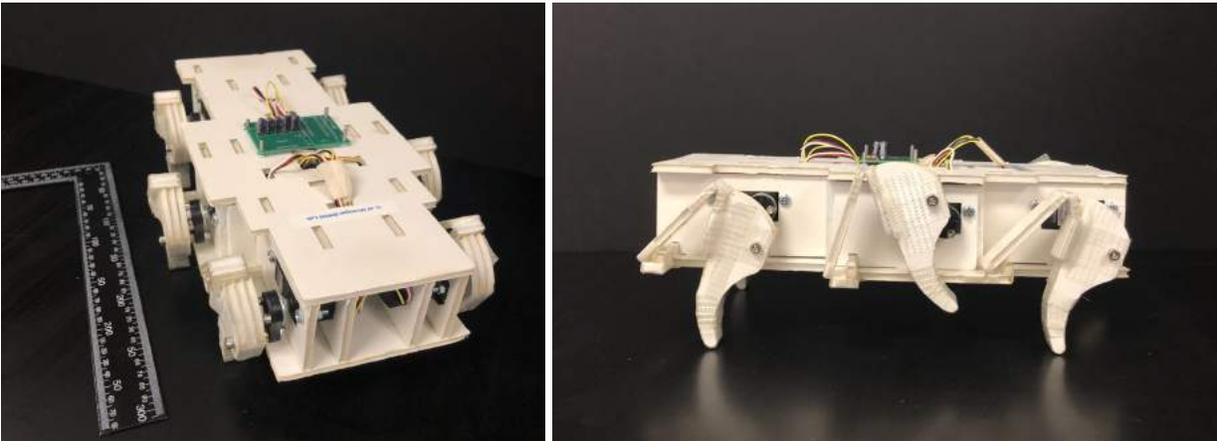
Figure 2.23: The small variant of BigAnt: MediumAnt

The current version of BigAnt has proved to be a robust design. We we (with Huo Luo, a former student in our lab) extended this design to a smaller variant of BigAnt, named as MediumAnt, for education and potential entertainment use. The MediumAnt (Figure 2.23) is the size of a notebook. Its chassis is also made from only foam board and fiber tape, and adopts the same 4 bar mechanism as its drivetrain but with scaled down dimensions. We also changed the original leg-hip design to a simpler structure, since the strength-to-load ratio increases as the robot size decreases. Simple structures for the MediumAnt legs are enough for its locomotion. The base board of MediumAnt was designed to hold servo motors and batteries as an encapsulated structure. Besides the smaller

size, MediumAnt is low cost, with less than 250 USD for all of the materials, servo motors, control and communication units. This makes MediumAnt an affordable robot platform for education and entertainment applications.

2.3   Multipod: A highly modular multi-legged robot with adjustable numbers of legs

BigAnt can be easily rebuilt and has many modular components. It is applied in our research as the subject of the multi-legged robots with 1 DoF legs. For the general study of low-DoF multi-legged locomotion, we also need robot platforms with 2 DoF legs and robot platforms that possess more than 6 legs. Therefore, we combine these two motivations together and build the Multipod robot which is a modular multi-legged robot that can be easily assembled for different numbers of legs. It also has effectively 2 DoF per leg and so this enables us to incorporate a more general range of low-DoF multi-legged robots and their locomotion in our study.

2.3.1   Design

2.3.1.1   Basic structure

The Multipod design is inspired by the previously studied "centipede robot" [Sastra et al., 2008, 2012]. Figure 2.24 demonstrates our 12-legged Multipod and a sketch of its actuation structure. The basic structure unit of Multipod is its modular leg segment which has 3 servos (high-end hobby servomotors, Dynamixel MX106, Robotis, Inc.) actuating the 3 joints which are usually 2 yaw joints and 1 roll joint for our study.

All the actuation servos are built into the Modlock modules [Davey et al., 2012] which enable the quick construction of the Multipod modular leg segment. By connecting several modular leg segments again using Modlock connectors, the Multipod can be easily assembled into the robot platform with the desired numbers of legs. In each modular leg segment, there is also a pair of spring legs that are coupled by the same base mount and attached to the roll joint. The base mount can adjust the leg length and stiffness by controlling how much length the leaf spring is extended out.

With this modular structure, Multipod possesses an articulated spine instead of a rigid body similar to the BigAnt and RHex structure. All the actuation units are also concentrated in this articulated spine. Such morphology of Multipod can be regarded as a snake robot augmented with legs.

41
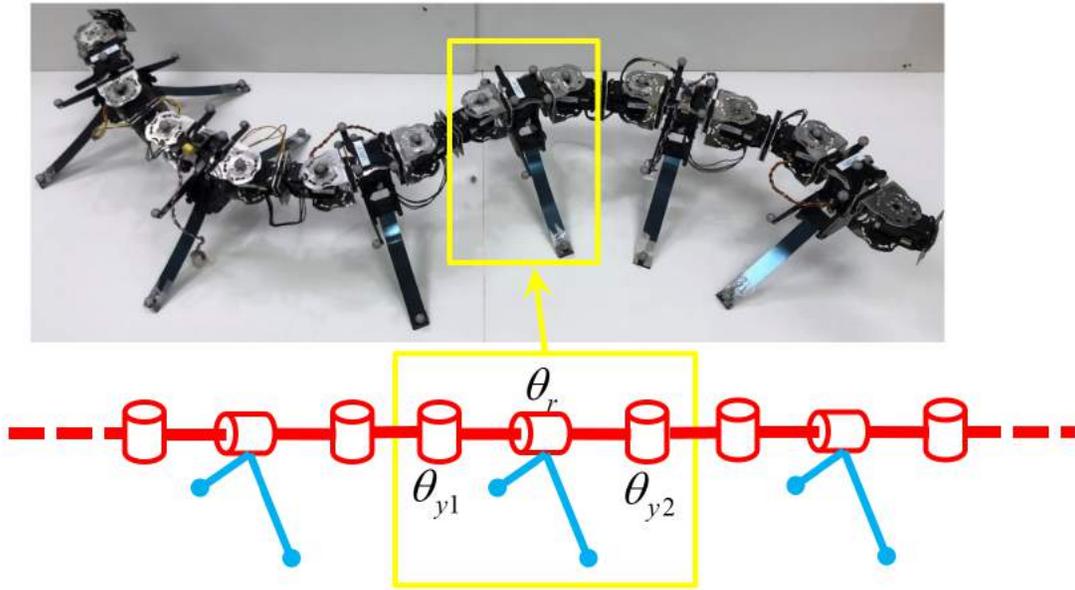
Figure 2.24: Multipod robot (top); A sketch of Multipod (bottom) that exhibits its basic structure: Each modular leg segment has 3 servos actuating 2 yaw joints and 1 roll joint. The corresponding actuation angles are noted as θ_{y1}, θ_r and θ_{y2} respectively. There is a pair of spring legs attached to the roll joint. Each leg segment is 26 cm long.

2.3.1.2 Leg segment modes and DoF analysis

Each modular leg segment of Multipod can possess two modes that can be differentiated by the joint type combinations. As introduced in the previous section, the Multipod leg segment usually adopts two yaw joints and one roll joint as show in Figure 2.25a. We refer to this kind of leg segment as the YRY (yaw-roll-yaw) mode. With high modularity, the Multipod leg segment can have another joint combination as demonstrated in Figure 2.25b, which has one pitch joint, one roll joint and one yaw joint. We refer to this kind of leg segment as YRP (yaw-roll-pitch) mode. It is also worth noting that the roll joint in each leg segment only moves the leg pair, while it does not change the spine shape as the yaw and pitch joint do.

A Multipod robot with full YRY leg segments is exhibited in Figure 2.24 while a Multipod robot with full YRP leg segments is exhibited in Figure 2.24 The YRY leg segment is adopted for Multipod walking on relatively flat ground. It provides more freedom for the spine to bend in the yaw direction compared to YRP leg segments, and this enables Multipod to perform nonslip gaits which will be introduced in detail in Section 3.6.1. The YRP leg segment is designed to add both pitch and roll motion freedom to Multipod. This enables the Multipod spine to bend both "up-and-down" and "left-to-right", and could augment the Multipod's potential to travel through uneven terrains or climb stairs. It is worth noting that we can still mix different modes of leg segments for
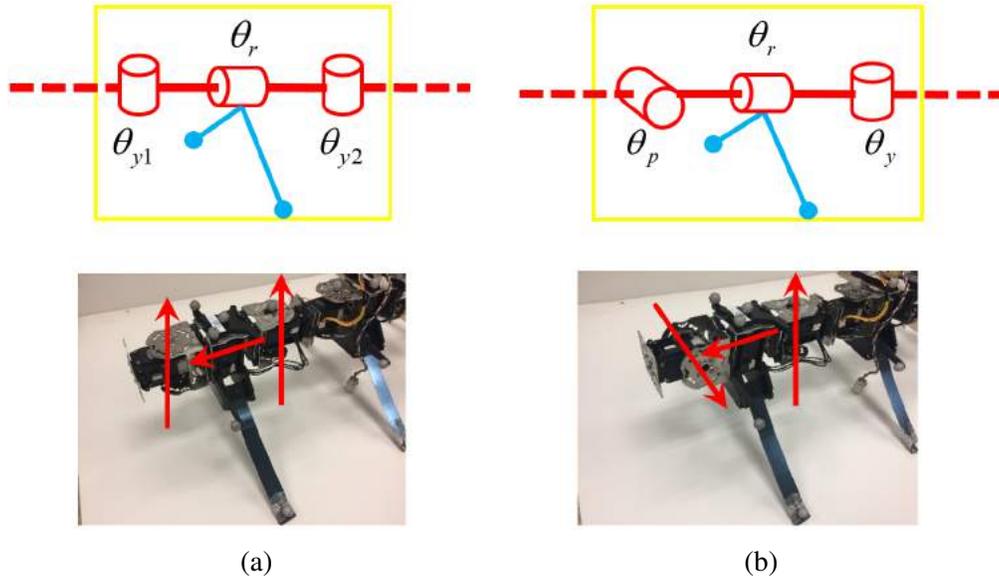
Figure 2.25: The modular leg segments of Multipod with actuation structure sketches on the top row and the robot examples on the bottom row. (a): YRY (yaw-roll-yaw) mode. Its corresponding actuation angles are noted as θ_{y1}, θ_r and θ_{y2}. (b): YRP (yaw-roll-pitch) mode. Its corresponding actuation angles are noted as θ_y, θ_r and θ_p.

an asymmetric robot morphology, even though such setups require more complicated gait design to achieve good mobility.

Figure 2.26: 12-legged Multipod with YRP leg segments.

Most of the legged robots have a rigid body base with their legs extended out from this body base like a tree graph, such as RHex, Spot, Cassie. The leg DoF of robots with this kind of morphology is apparent. However, the DoF on each leg of Multipod is not a question with obvious answers. If we consider the leg DoF in an average sense, there are 3 actuation joints on each leg segment which is shared by a pair of 2 legs, so Multipod has an average of 1.5 DoF per leg. However, this kind of average DoF analysis does not reflect the true mobility of Multipod. For

example, if we check the leg segments at the one end of the Multipod spine, there is a joint moving freely in the air and only two joints connecting the legs with other parts of the robot, so the leg segments on the two ends of Multipod have averagely 1 DoF per leg.

Here we propose an analysis aspect for thinking about the DoF of each Multipod leg. We place a reference frame on one pair of legs and then check the motion DoF of the consecutive leg pair wrt. the reference leg pair. There are 4 joints between any two leg pairs, so the motion DoF of the consecutive leg pair wrt. the reference leg pair is 4. From this perspective, each leg pair has 2 DoF. However, the 2 DoF for each leg pair do not mean that each leg has 1 DoF, since the two legs in a leg pair are physically coupled together. The 2 DoF for each leg pair enables both leg tips to occupy a 2-dimensional manifold. For example, when Multipod is adopting a kind of alternating gait, there is only one leg contacting the ground while the other leg of the leg pair is in the air. Only the leg motion in contact with ground affects the system locomotion. The contact leg possesses the 2 DoF of this leg pair, so it is effectively a 2 DoF leg. In summary, as long as the designed gaits for Multipod do not require both two legs in one leg pair to contact the ground at the same time, Multipod is a multi-legged robot platform with effectively 2-DoF legs.

2.3.2 Undulatory gaits

Multipod, as a multi-legged robot platforms with adjustable numbers of 2-DoF legs, is capable to perform a variety of gaits for its mobility and for multi-legged locomotion studies. In this section, we focus on introducing a family of undulatory gaits we designed for Multipod.

Undulatory gait is a general kind of motions that are usually adopted by animals such as centipedes, millipedes, snakes, etc. Their robot counterparts also use this kind of gaits for their locomotion. The key characteristic of undulatory gaits is that all of the legs or segmented body parts behave in the same motion pattern with a constant phase offset between the adjacent segments. From a simpler perspective, undulatory gaits drive the system to behave like a mechanical wave in the local reference frame. Therefore, the undulatory gaits can be easily extended from systems with a low number of segments to the same type of systems with more segments. One of our motivations for creating Multipod is to study how the number of legs affect multi-legged locomotion. Thus, the only changeable parameter should be the number of legs. Undulatory gait is a good choice for this research objective, since it is easy to perform on Multipod and also makes it reasonable to compare the motions of Multipods with different numbers of legs.

In most of our locomotion tests, we use Multipod robots with YRY leg segments. The corresponding undulatory gait we designed has the following formula for the actuation joint inputs:

$$\theta_{y_1} = \theta_{y10} \cos(2\pi ft + i\Delta\phi) \tag{2.3}$$

$$\theta_r = \theta_{r0} \sin(2\pi ft + i\Delta\phi) \tag{2.4}$$

$$\theta_{y_2} = \theta_{y20} \cos(2\pi ft + i\Delta\phi) \tag{2.5}$$

where θ_{y_1}, θ_r and θ_{y_2} are the joint angle inputs as depicted in Figure 2.25a; θ_{y10}, θ_{r0} and θ_{y20} are parameters that control the joint motion amplitudes; f is the gait frequency; t is the time; $i = 1, 2, \ldots, N/2$ is the leg segment index (N is the total number of legs); $\Delta\phi$ is the phase offset between adjacent leg segments. These gait parameters determines the detailed undulatory behaviors that Multipod performs. Figure 2.27 presents an example of 12-legged YRY Multipod walking with undulatory gait introduced above.
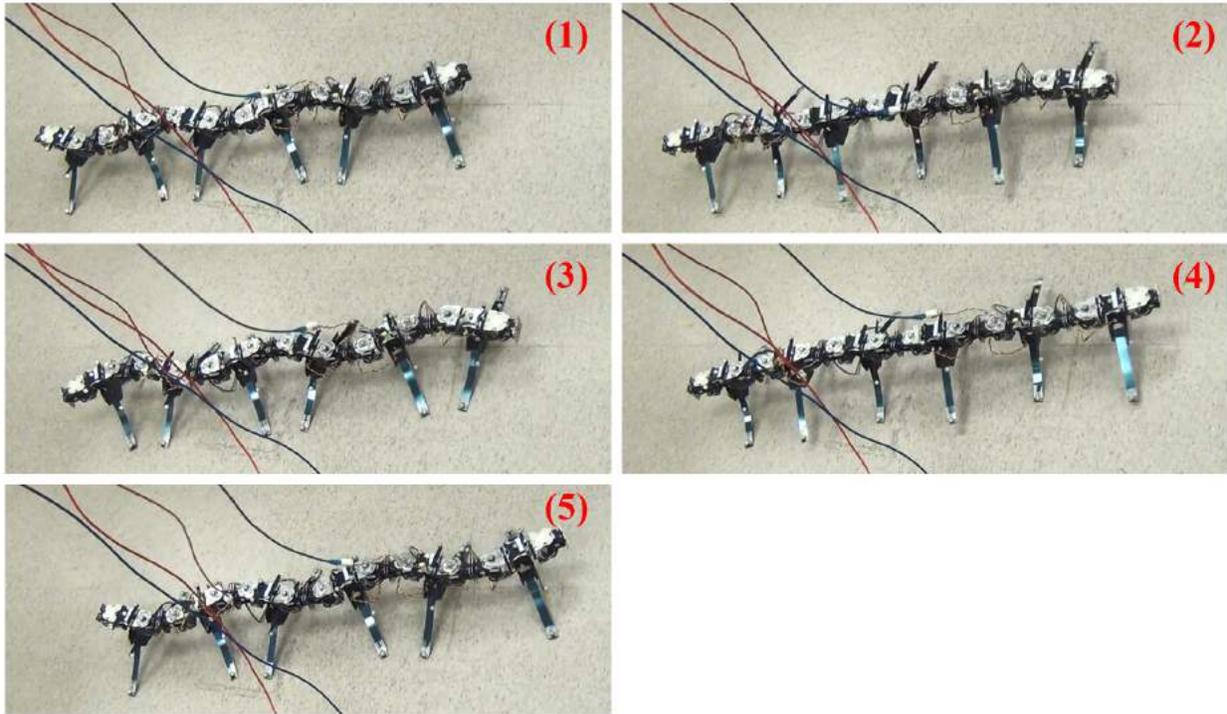
Figure 2.27: Undulatory gait example for 12-legged Multipod with YRY leg segments: Multipod is walking from left to right in the order of (1) - (5).

For Multipod robots with YRP leg segments, the undulatory gait we designed has the following formula for the actuation joint inputs:

$$\theta_y = \theta_{y0} \cos(2\pi f t + i\Delta\phi) \tag{2.6}$$

$$\theta_r = \theta_{r0} \sin(2\pi f t + i\Delta\phi) \tag{2.7}$$

$$\theta_p = \theta_{p0} \cos(2(2\pi f t + i\Delta\phi)) \tag{2.8}$$

where θ_y, θ_r and θ_p are the joint angle inputs as depicted in Figure 2.25b; θ_{y0}, θ_{r0} and θ_{p0} are parameters that control the joint motion amplitudes. These undulatory gait parameters for YRP Multipods need more tuning and testing. Otherwise, there could be interference between Multipod parts or overloaded joint servomotors during its locomotion. Meanwhile, the YRY Multipods are more stable, adopting the proposed undulatory gaits with a wide range of gait parameters. Figure 2.28 presents an example of 12-legged YRP Multipod walking with undulatory gait introduced above. More undulatory gait examples with different numbers of legs can be found in this media link.
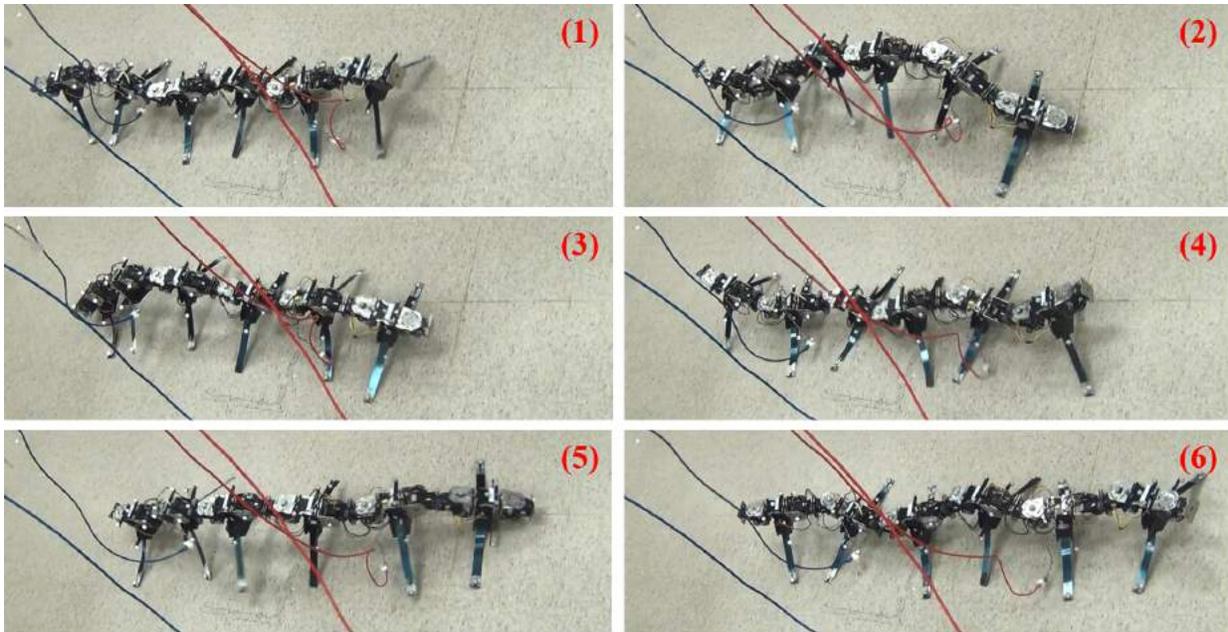
Figure 2.28: Undulatory gait example for 12-legged Multipod with YRP leg segments: Multipod is walking from left to right in the order of (1) - (6).

2.3.3 Locomotion experiments

To experimentally study the influence of the number of legs on multi-legged locomotion, we perform a family of undulatory gaits on Multipod robots with 4 to 12 legs. The Multipod robots are

assembled into the YRY mode for their modular leg segments The undulatory gaits performed have the actuation profiles in the forms of Equation 2.4.

2.3.3.1 Gait parameters selection and experiment setup

For the convenience of gait parameter tuning and for the motion symmetry of Multipod when walking both forwards and backwards, we assigned the same motion amplitude θ_{y0} to the two yaw joints on each leg segment, leading to $\theta_{y10} = \theta_{y20} = \theta_{y0}$. The detailed amplitude values for the gaits were selected and tuned during the experiment tests. We chose the standard alternating gait ($\Delta\phi = \pi$) as the reference baseline gait for the parameter selection tests. The yaw joints control the leg swing motion in the front/back direction and determine the "width" of the Multipod leg tip trajectory if observed from the side view. We maximize the yaw amplitude θ_{y0} to increase step size, limited by when consecutive segments interfere with each other. The roll joints control the leg swing motion in the up/down direction and determines the "height" of the Multipod leg tip trajectory if observed from the side view. The roll amplitude θ_{r0} is then selected based on the following two requirements: (1). Every leg pair should have a flight phase rather than continually contacting the ground. (2). The robot configuration can be held still by all the servomotors when the system CoM reaches its peak positions during the undulatory motion. The first requirement defines the lower bound of the roll amplitude θ_{r0}, since roll amplitude below this bound causes some pairs of legs to be in contact with the ground all the time. The second requirement defines the upper bound of the roll amplitude, since roll amplitude above this bound indicates some servomotor is overloaded during system locomotion. The feasible roll amplitudes should be within these two boundaries for all the tested numbers of legs adopting the reference alternating gait.
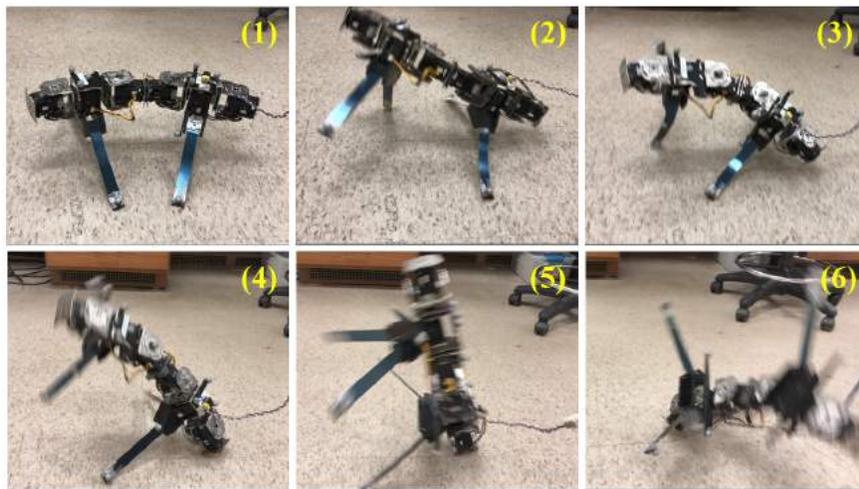
Figure 2.29: 4-legged Multipod failed to walk with the undulatory gait parameters that generate stable gaits for other numbers of legs (6 to 12).

47

The parameter-selection tests with the standard alternating gaits were performed on Multipod robots with 4 to 12 legs. Among all numbers of legs, the 4-legged Multipod showed different behaviors compared to the Multipod robots with 6 or more legs. As demonstrated in Figure 2.29, the 4-legged Multipod lost its stability as long as one or more of its legs have flight phase, which violated the lower bound requirement of the roll amplitude. This observation also supports our hypothesis that a 4 legged robot is intrinsically different to a multi-legged robot that possesses at least 6 legs. We then used the Multipod robots with 6 to 12 legs for our experiments. Based on the parameter-selection tests and requirements, the final selected roll amplitude θ_{r0} is 25 degrees and the final selected yaw amplitude θ_{y0} is 20 degrees for the undulatory gaits.

To obtain a more general study about how the number of legs affect multi-legged locomotion, the experiment tests of the alternating gait are insufficient. We adopted a list of 26 phase offsets $\Delta\phi$ (from 0.2π to 1.8π) to cover almost the whole range of the undulatory gaits that are represented by Equation 2.4. It is worth noting that the undulatory gait with the phase offsets within $[-0.2\pi, 0.2\pi]$ only drives Multipod to oscillate in one place (travel zero distance) rather than generating observable locomotion. That is the reason why we selected the phase offset range as $[0.2\pi, 1.8\pi]$. We chose this family of undulatory gaits as the test gaits for our Multipod experiments. Moreover, only one kind of gait frequency does not provide adequate locomotion samples. We also performed each of kind of undulatory gaits with 5 different gait frequencies: $f = [0.3, 0.6, 1.2, 2.4, 3.0]Hz$. In summary, the Multipod experiments possess a 3-dimensional parameter space with 4 kinds of numbers of legs ([6,8,10,12] legs), 26 kinds of undulatory gaits and 5 kinds of gait frequencies. Therefore, there are in total of 520 ($4 \times 26 \times 5$) trials in our Multipod experiments. For each test trial, Multipod walks 5 gait cycles forwards and 5 gait cycles backwards.

2.3.3.2 Data set and preliminary results

To record the Multipod motions in the experiments, we attach reflective markers on different parts of Multipod (Figure 2.30a) and apply the motion tracking system (the same setting as the BigAnt experiments introduced in section 2.2.7.3) to capture the robot's motion. The position of each marker is measured by the motion tracking system and represented as a 3D vector which indicates its xyz coordinates in the world frame. Figure 2.30b exhibits the positions of all the tracked Multipod markers on the world frame xy plane at any given instant. During the Multipod locomotion, every marker generates a 3D time series. Therefore, the result data for each experiment trial is a $3N_m \times N_t$ matrix, where N_m is the total number of markers and N_t is the number of time series samples. We collected the result data matrices for all the 520 trials of experiments we performed with Multipod to construct a rich data set which includes Multipod locomotion with 4 kinds of numbers of legs, 26 kinds of undulatory gaits and 5 kinds of gait frequencies.

This data set contains a significant amount of Multipod locomotion information in which we

(a)

(b)
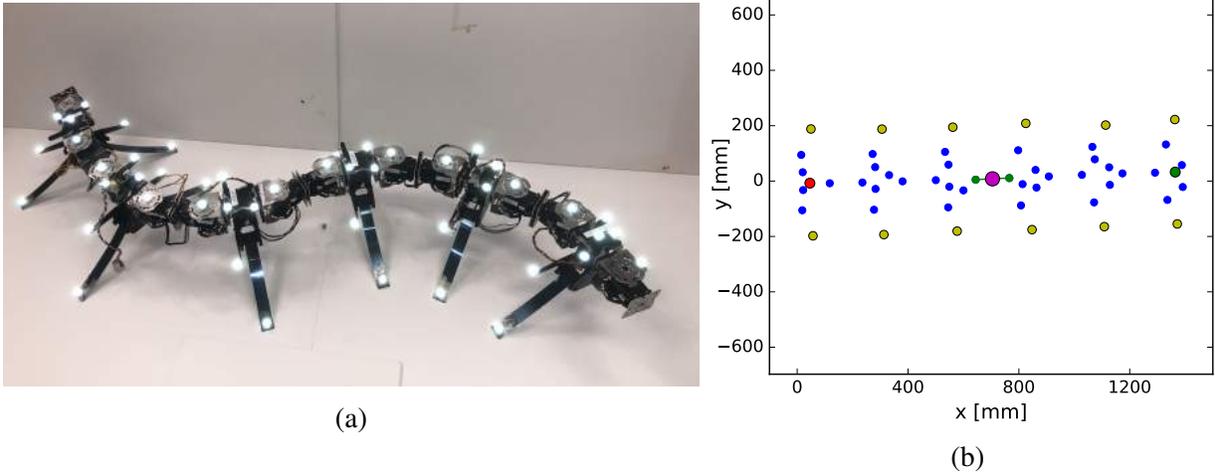
Figure 2.30: (a): 12-legged Multipod with marker setup highlighted under a flashlight; (b): Plotted marker positions data from the motion tracking system.

can perform a lot of analyses and studies. In this section, we introduce some examples of the preliminary analysis.

BigAnt has relatively rigid legs and drivetrain mechanism/structure, its 1 DoF leg tip trajectory from the experiments is almost the same as the designed trajectory. Meanwhile, the detailed Multipod leg tip trajectories remain unknown without experiment tests, even though we can tune the trajectory "width" and "height" by adjusting the joint motion amplitudes using our mechanical intuition. We can also construct kinematic models to simulate the Multipod trajectory, but the simulated results still can not include the leg tip motion affected by the spring leg compliance. The first preliminary analysis example in the Multipod experiment data set is to check the Multipod leg trajectories. The raw leg position time series are leg tip trajectories in the world frame. They need to be transformed into some body frame to become the regular leg tip trajectory that we generally refer to. We define the *body frame*[7] of Multipod as the following conventions: The body frame origin is defined to be the midpoint of center point C_h of the head (first) leg segment and the center point C_t of the tail (last) leg segment (there are two makers at C_h and C_t); The body frame x axis direction is defined to be the direction of vector $C_t C_h$; The body frame z axis direction is defined to be the direction of the world frame z axis; The body frame y axis is then the cross product of the body frame z axis with the x axis. With this body frame convention, we can get the Multipod body frame trajectories as exhibited in Figure 2.31a. It shows that the leg tip trajectories of the two legs in the same leg segment are similar but not symmetric, especially when observed from the

---

[7]Although this may seem to be obvious for BigAnt for RHex, defining a body frame for e.g. a slithering snake or Multipod is non-trivial and has significant computational implications [Hatton and Choset, 2011]
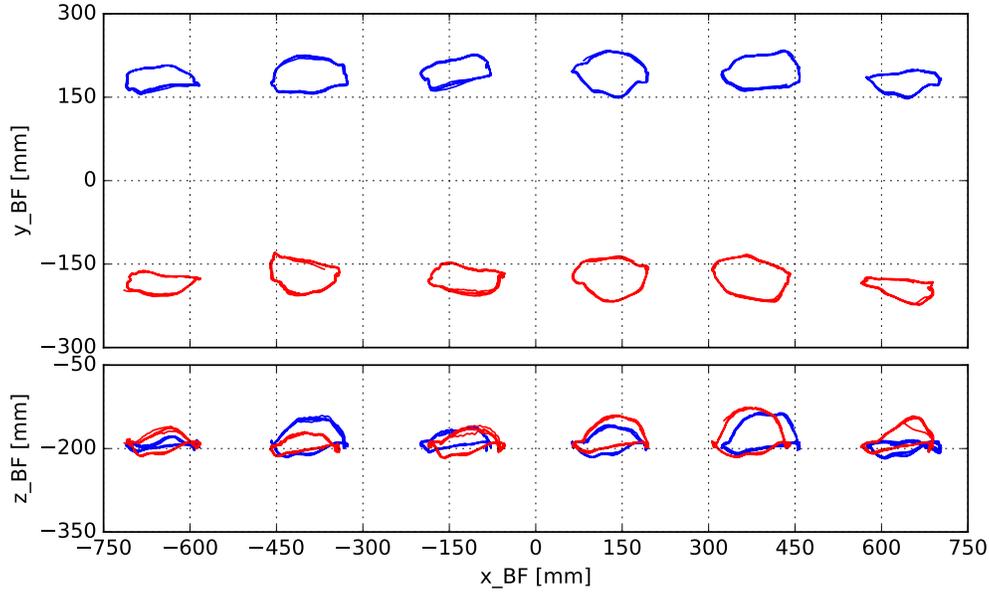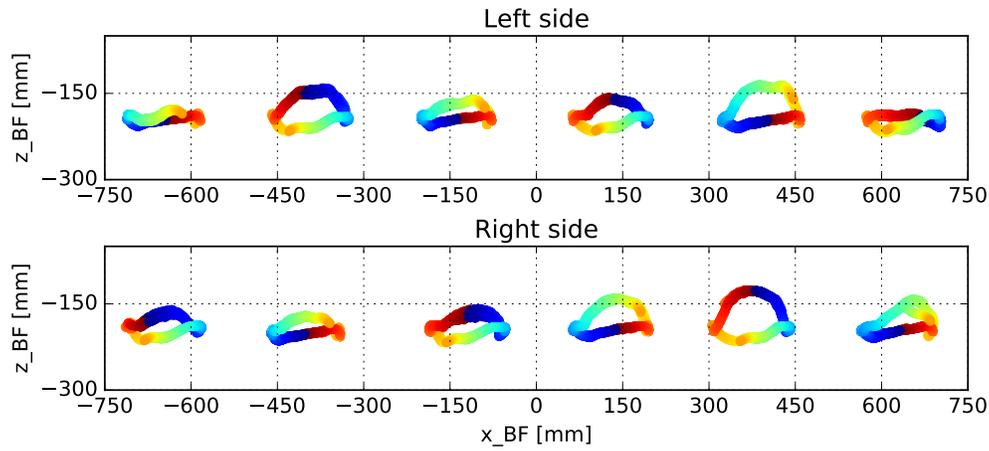
Figure 2.31: (a): Leg tip trajectories of the 12-legged Multipod taking the undulatory gait with phase offset $\Delta\phi = \pi$ at gait frequency $f = 0.3Hz$. The subplot at the top is from the top view while the subplot at the bottom is from the side view. (b): Leg tip trajectories in (a) colored to indicate the timing by the global phase. The global phase increases from dark blue to dark red clockwise. The point that connects dark red to dark blue corresponds to the zero global phase.

side view. This observation indicates that the Multipod robot is not perfectly symmetric. The leg tip trajectories on the same side from the different leg segments are also different. To further check the timing on the these leg trajectories, we color them with the same color map that indicates the system global phase. The global phase is achieved from the time variable t and frequency variable

50

f in Equation 2.4. The phase colored leg trajectories are depicted in Figure 2.31b.

(a)

(b)

(c)
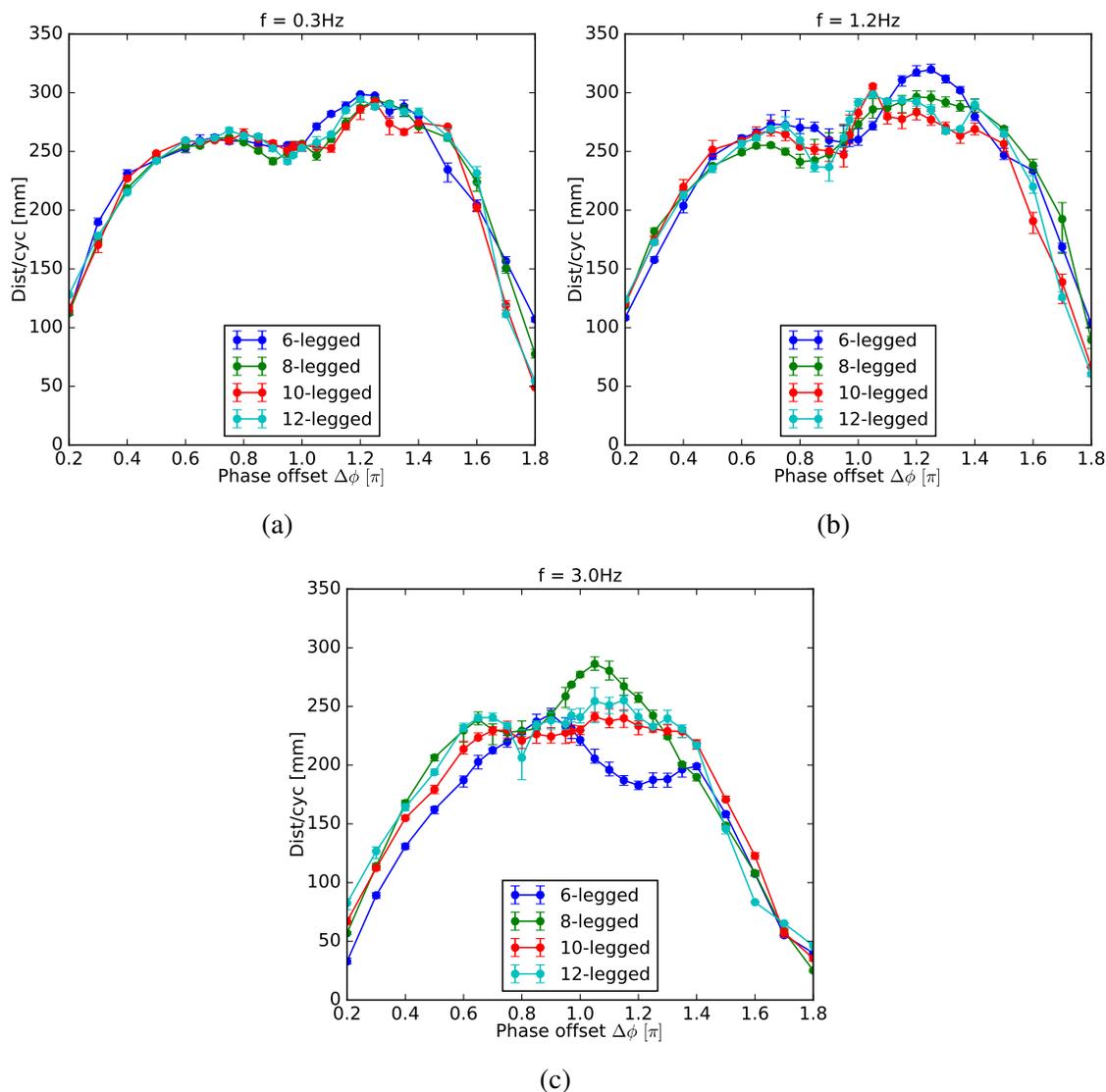
Figure 2.32: Distance travelled per gait cycle by the Multipod body frame origin vs. the undulatory phase offset for [6,8,10,12] legged Multipod walking in 3 gait frequencies: 0.3 Hz (a), 1.2 Hz (b) and 3.0 Hz (c).

Another preliminary analysis example is to check the Multipods' locomotion speeds with different undulatory gait parameters and numbers of legs. To compare the locomotion from different gait frequencies, we chose a normalized speed variable, distance travelled by the body frame origin per gait cycle (noted as dis/cyc), as the locomotion property to be analyzed. The dis/cyc can be calculated from the locomotion speed v as v/f. The calculation results of dis/cyc for all 4 different numbers of legs, 26 undulatory gaits and 3 gait frequencies are presented in Figure 2.32. We can see that the dis/cyc property of Multipod is primarily influenced by the phase offset of the undu-

latory gaits for all numbers of legs and gait frequencies. At the lowest gait frequency $f = 0.3Hz$ (Figure 2.32a), dist/cyc of the Multipod locomotion with different numbers of legs are quite similar for almost all the undulatory gaits. As gait frequency increases, dist/cyc from different numbers of legs begins to diverge: At $f = 1.2Hz$ (Figure 2.32b), the dist/cyc of the 6-legged Multipod is slightly different with other cases at phase offset from 1.1π to 1.4π; at $f = 3.0Hz$ (Figure 2.32b), the dist/cyc of both the 6-legged and 8-legged Multipod exhibit noticeable difference from each other and also from 10-legged and 12 legged cases. Our preliminary hypothesis about such observations is that: dist/cyc is a general locomotion property for Multipod shared by different numbers of legs; the sharing of this property is affected by the gait frequency; the Multipod robots with less legs are easier to be influenced than these with more legs. A more thorough study of the Multipod locomotion will be introduced in Chapter 4.

2.4   Conclusion and discussion

The key motivation of this chapter is to achieve low-DoF multi-legged robot platforms that can be used to experimentally study low-DoF multi-legged locomotion in a general way. The strategy we proposed to cover a variety of research requirements is to make the robot platforms easily reconfigurable. We applied this strategy from two aspects: (1) making the robot platforms easy to be fully rebuilt; (2) introduce as much as possible modularity to the robot design. Based on these objectives, we deigned and built two robot platforms for our study of low-DoF multi-legged locomotion.

BigAnt is a low-cost fast-fabricated hexapedal robot that can be rebuilt easily. We also embedded a noticeable amount of modularity to BigAnt to further increase its reconfigurability for different research and application requirements. As a robot whose chassis is only constructed from a kind of foam board and a kind of fiber tape, BigAnt proved itself to be a functional and robust multi-legged robot platform in both indoor and outdoor tests. The current BigAnt has also been used as a master version for the creations of many variants to solve the specialized problems, such as the water resistant BigAnt, stair climbing BigAnt, force sensing BigAnt and MediumAnt (the smaller version of BigAnt). Our proposed design and fabrication techniques for BigAnt can be extended to the development for other low-DoF multi-legged robot platforms or the early-stage prototypes of legged robots in general. For example, the general feasible 1-DoF trajectory can be directly applied as a reference for other multi-legged robots with 1 DoF legs. The design and fabrication techniques of building robot chassis from inexpensive materials rapidly are also good paradigms of constructing robot prototypes. An interesting observation we would like to share from our BigAnt design study is that it took us around 15 hours to construct a 3D CAD model for BigAnt, while it only took us less than 5 hours to both fabricate all BigAnt parts and finish the

whole assembling process. Such fast and inexpensive fabrication techniques enable our iterative design strategy for building low-DoF multi-legged robots. Even though the interaction between low-DoF multi-legged robots and the environment is difficult to model precisely, especially when these robots are walking on uneven terrains, we can still perform real robot tests to evaluate the design performance and make improvements during the design iterations.

Besides the robot design and fabrication methods, we also introduced the essence of the gait design for multi-legged robots with 1 DoF legs, which is the design of the actuation profiles. We further introduced the general strategies to reduce the order and the dimension of the design space for the actuation profiles. By grouping the legs and adopting low order profile functions, the gait designs for multi-legged robots are reduced to gait parameter selection problems. Moreover, we proposed a new perspective to analyze the gait design for 1 DoF legs. With fixed leg trajectory locus (shape), timing on 1 DoF leg trajectories connects the motion objectives with the detailed actuation profiles. We explained in detail how to design the Buehler clock to regulate the timing on the leg trajectory to further determine the contact region. This method is generally useful for multi-legged robots with relatively rigid 1-DoF leg trajectories. It is worth emphasizing that the Buehler clock is just one low-order actuation profile. We can adopt more knot points on a piecewise linear profile to generate more complicated speed region combinations rather than just two speed regions regulated by the Buehler clock. We can even add the inverse function of the drivetrain mechanism to the actuation profile functions to achieve even more precise timing or speed control on the 1 DoF leg trajectories.

Another low-DoF multi-legged robot we constructed is Multipod. The primary motivation of Multipod is to study how the number of legs affects multi-legged locomotion. Therefore, Multipod is designed to be a modular multi-legged robot that can be easily assembled for different numbers of legs. It also has effectively 2 DoF per leg and enables us to cover a more general range of low-DoF multi-legged robots and their locomotion. The reconfigurability of Multipod is from its high modularity. We introduced its basic structure and how its modularity enables it to easily achieve different numbers of legs and different modes of leg segments (YRY and YRP). The leg DoF for Multipod which as an articulated spine is not apparent. We proposed a method to analyze its leg DoF and demonstrated how its legs are effectively 2 DoF. A family of undulatory gaits were designed for Multipod with both the YRY and YRP leg segments. These undulatory gaits can be easily extended to the Multipod robots with different numbers of legs and make the locomotion comparable between different numbers of legs. Thus they are the experiment gaits for our study of in influence pf the number of legs. It is worth noting that there are many other gait options for Multipod. This is one of our future research directions. For example, the steering gaits for Multipod; the gaits that can enable Multipod to walk on uneven terrains with the YRP leg segment mode. These are both interesting and meaningful research projects.

With the formula of the undulatory gaits determined, we selected feasible gait parameters, the roll and yaw motion amplitudes, for the formal experimental study of number of legs as an influence through the preliminary experiment tests with the standard alternating gait. The preliminary tests revealed the difference between the 4 legged Multipod with other Multipods with no less than 6 legs. To cover an adequate range of undulatory locomotion, we performed 26 kinds of undulatory gaits on the Multipod robots with 4 kinds of numbers of legs in 5 kinds of gait frequencies. The motion tracking results of these total 520 test trials are organized into a comprehensive data set for the study of multi-legged locomotion. In this chapter, we also performed some preliminary analysis on this data set. We checked the body frame leg trajectories of Multipod and compared the distance travelled per gait cycle by the Multipod body frame origin during their undulatory locomotion. The dist/cyc turned out to be an interesting property that remains the same across different numbers of legs regardless of the undulatory gait phase offsets as long as the gait frequency is low. We also observed that with more legs, the similarity of dist/cyc between different numbers of legs is easy to be preserved into the higher gait frequency range. More detailed analyses about these different types of Multipod locomotion and more insights about the dist/cyc property will be demonstrated in Chapter 4.

CHAPTER 3

Maneuverability and Slipping of Low-DoF Multi-legged Robots

3.1 Motivation and introduction

This chapter is based largely on our paper [Zhao and Revzen, 2020].

Thanks to their sprawled posture and multi-legged support, stability is not as hard to achieve for multi-legged robots as it is for bipeds and quadrupeds. A general research goal and a key engineering challenge with hexapods have been to produce insect-like mobility and agility, of which maneuverability is an important part. Maneuverability for locomotion in this dissertation indicates the quality of moving freely in the horizontal plane.

Steering (turning while translating) is an essential component of maneuverability. However, the mechanisms of multi-legged steering are not always clear, especially for robots with underactuated (low-DoF) legs. Before our work here, we were aware of no agreed upon theoretical definition for steering in general. Many previously published steering and turning methods are specific to a robot design, and cannot be easily applied to other robots in general, and low-DoF multi-legged robots in particular. If we are interested in legs that actually exhibit 1-DoF motion, many studies could not be classified as "real" low-DoF steering, since they used leg deformation to generate asymmetry, which makes the legs able to visit a configuration space which has dimension larger than 1. The turning gaits of VelociRoACH [Haldane and Fearing, 2014] and 1STAR [Zarrouk and Fearing, 2015] are typical examples of such methods. Also, almost all previous studies have missed or ignored a key phenomenon – slipping. In our experimental tests of steering/turning behavior of both insects and robots, a large fraction of leg motions were "slipping".

To better understand the modeling and control of low-DoF multi-legged robots we first analyze and introduce the distinction between wheeled steering and legged steering to show that the differential driving method for wheeled steering is non-trivial to use for legged steering. We then propose a formal definition of steering for legged systems from a geometric mechanics viewpoint,

and show why steering is challenging for low-DoF multi-legged robots. We also prove that multi-legged steering has to slip with 1-DoF legs and analyze the general strategy for low-DoF steering. Following the proposed general strategy, we design and experimentally test two kinds of steering gaits for BigAnt. The experiment results are studied in terms of both steering and slipping. We also demonstrate that non-slip gaits do exist for Mechapod (a hexapedal robot similar to 6 legged Multipod) which has 2-DoF legs, but their steering performance are much worse than the gaits we designed which allow for slipping. All the presented experiment results demonstrate the importance of allowing for slipping to occur intentionally when optimizing steering ability, and in turn suggest that conventional non-slip contact models might miss significant parts of the steering performance envelope.

3.2   Background

Unlike bipedal and most quadrupedal vertebrates, insects have legs sprawled outward in fore-aft and lateral directions, which offers them additional stability and exceptional maneuverability in horizontal plane, making them able to execute very tight turns at high speeds [McClung, 2006]. Even with similar sprawled structure, achieving such maneuverability in hexapedal robots is challenging. Getting better understanding of the steering behaviors is an essential part of improving maneuverability. One approach is to study animal turning behavior and build models and hypothesis that would inspire robot gait design. The other approach to studying steering behavior in robots is to directly test proposed steering gaits on robot platforms and further explore the experimental results to explain and improve the achieved gaits. In this section, we summarize some previous research from the aspects of these two approaches.

3.2.1   Maneuverability in biological hexapods

Franklin et al. [1981] discovered two principal methods the cockroach *Blattella germanica* used to turn: increasing step frequency or step length of legs on one side of the body relative to the other, where the step length change was achieved by changing either the leg arc swing magnitude or functional length of the legs. Some extreme changes of step length like pivoting one leg in place or even moving one leg backwards were observed in bee turning by Zolotov et al. [1975]. Jindrich and Full [1999] measured the full dynamics of turning in the cockroach *Blaberus discoidalis* and analyzed the contributions of each leg to turning, concluding that turning dynamics can be characterized as a minor modification of straight-ahead running. To describe motion of cockroaches in the horizontal plane, several models were developed by Schmitt and Holmes [2000], Seipel et al. [2004], Proctor and Holmes [2008]. Our own study of running *Blaberus discoidalis* cockroaches
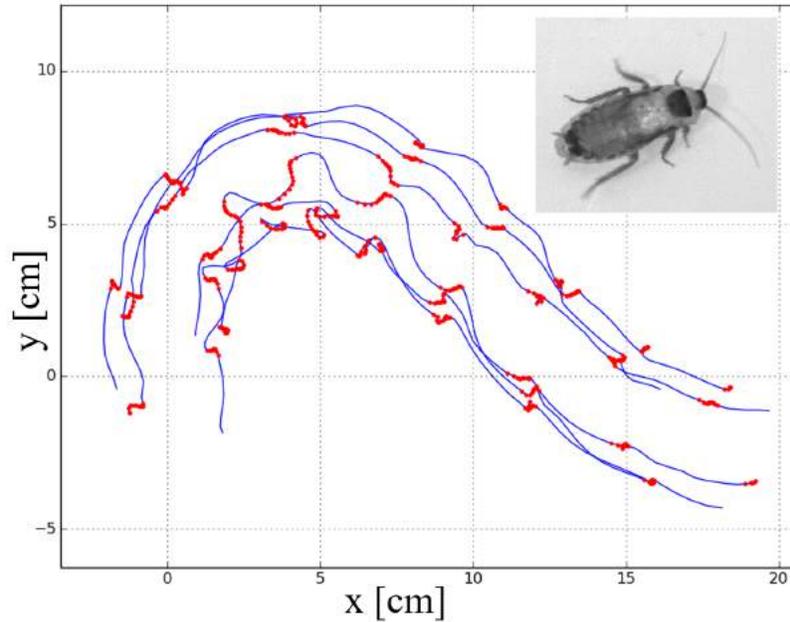
Figure 3.1: Cockroaches slip while running. We recorded 24 trials of *Blaberus discoidalis* running at 15-77cm/s on foamcore [Elmer's 900803 Foam Board]. On average, front, middle, and hind legs slipped 18%, 15%, 16% of their total travel distance. We show the tarsus (foot) trajectories recorded in the world frame while moving forward relative to the body (blue), and while moving backward (red). Note: synchronized side-view videos suggest that feet moving back with respect to the body are in contact with the ground.

[Sachdeva et al., 2018] observed that a large fraction of cockroach foot motions are "slipping" in the sense that the feet are moving with respect to the ground while in contact with it as shown in Figure. 3.1. It seems that the cockroaches exhibit far less non-slip ground contact than assumed in previous published locomotion models.

3.2.2 Maneuverability in hexapod robots

For fully actuated hexapod robots (active DoF per leg ≥ 3) inverse kinematics has been used to plan footholds for precise quasi-static steering [Roy and Pratihar, 2014, Duan et al., 2009]. However, multi-legged robots do not require fully articulated legs for dynamic stability. Even with 1-DoF or 2 DoF legs, hexapedal robots can still achieve stability and maneuverability — for example the RHex robot family [Saranli et al., 2001, Galloway et al., 2010] and the Sprawl robot family [Mc-Clung, 2006, Kim et al., 2006]. Several investigators have looked at maneuverability of hexapods: McClung [2006] did a thorough investigation of the dynamic maneuverability of Sprawlettes (2 DoF per leg) and identified effective parameters that can be used for steering. Many interesting turning methods were also tested and studied on the RoACH family of rapidly-prototyped palm-

size robots [Pullin et al., 2012, Haldane and Fearing, 2014, Zarrouk and Fearing, 2015]. For Oc-
toRoACH, Pullin et al. [2012] applied a differential speed method for dynamic turning by driving
legs on different sides with a different frequency. Haldane and Fearing [2014] demonstrate that
oscillations in height and roll angle determine VelociRoACH's turning behavior and developed a
steering gait for VelociRoACH controlled by phase offset between the left and right sets of legs.
1STAR in [Zarrouk and Fearing, 2015] claimed to be the first steerable robot with only one actu-
ator; it generated rotation by continuously accelerating and decelerating the legs resulting in the
compliance disparity between alternate stance tripods. Zarrouk et al. [2015] also summarized the
turning performance of these three palm-size robots and other famous multi-legged robots. There
were also hexapedal robots which adopted assistant structures to generate turning motion, such as
TAYLRoACH using a inertial tail [Kohut et al., 2013a] and SailRoACH using an air dynamic sail
[Kohut et al., 2013b]. This strategy is out of our research scope which focuses on steering by gaits,
but these two examples are interesting methods that worth mentioning.

3.3 Basic definition and strategy

3.3.1 Definition of steering with a periodic gait

Legged systems (animals and robots both) typically move using a *periodic gait*[1]: a cyclic shape-
change which produces (at least on average) a motion through the world. The shape-change can
be represented by the leg motions in the body frame of the system. Thus, each leg is repeating the
same motions every period of a periodic gait, and the body is thereby propelled in a similar way
each cycle.

For moving on a horizontal plane, we typically desire robots to allow us to control position
and heading. We will refer (by slight abuse of terminology) to the rigid body motion generated (at
least on average) by a single period of a periodic gait as the *holonomy* of that gait. The framework
of geometric mechanics provides a precise language for describing how holonomies arise from
periodic shape changes [Marsden and Ostrowski, 1998, Bloch et al., 2005]. The partitioning of
configuration into body frame and (body) shape is so intuitive that most of the time we assume
its validity without careful examination, however, as a technical point, we note that geometric
mechanics shows that when the mechanics of a system are governed by a Lagrangian symmetric
under the Lie group $SE(2)$, i.e. when the mechanics are the same in all positions and orientations
on a plane, the symmetry always induces a principal fiber-bundle structure allowing a configuration
q of the system to be represented in terms of a *body frame*[2] pose g in the world, and a *shape* b of

---

[1]Some authors conflate the term "gait" with "periodic gait"; the definition and discussion of non-periodic gaits is
outside the scope of this manuscript.

[2]Although this may seem to childishly obvious, defining a body frame for e.g. a slithering snake, is non-trivial and

the robot.

The instantaneous configuration $q = (g, b)$ is an element in the overall configuration space $Q = G \times B$. The shape space B is typically a compact manifold in $\mathbb{R}^k$ for some $k > 1$, and represents the possible shapes of the body, with the current shape being $b \in B$. The instantaneous body frame $g \in G$ is an element of the group G, which for horizonal motions is the group of rigid body motions in the plane, $\mathsf{SE}(2)$.
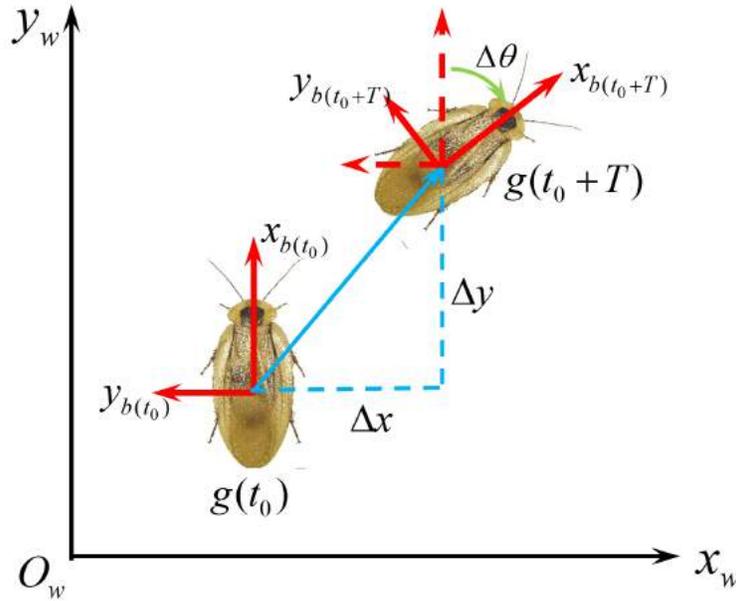
Figure 3.2: Coordinate frames for definition of steering

Executing a cyclic shape change does not, in general, correspond with a cycle in body frames. While the shape starts and ends the same over a cycle, the body frame changes, constituting motion.

Consider a system moving using a periodic gait with period T, and configuration given by $(b(t), g(t)) \in B \times G$. The body shape $b(t)$ must also be periodic with period T. The holonomy of this gait would be $\Delta g := g(t + T)(g(t))^{-1}$, and is the same for all choices of t. The theory of geometric mechanics tells us that $g(t)$ is completely defined by knowing $g(0)$, $\dot{g}(0)$ and $b(t)$. To capture the fact that the gait is defined by a *periodic* $b(t)$ we will take the domain of $b(\cdot)$ to be the unit circle $\mathsf{S}^1 \subset \mathbb{C}$. Instead of thinking of $b(\cdot)$ as a function of t, we shall take $b(\phi)$, $\phi \in \mathsf{S}^1$, and $\phi(t) = \exp(i2\pi t/T)$.

A holonomy in our case is a rigid body motion and can be represented in homogenous coordinates (see Equation 3.1), where $\Delta\theta$ is the orientation change; and Δx and Δy are the translation

has significant computational implications [Hatton and Choset, 2011]

of body frame origin as shown in Figure 3.2.

$$\Delta g = \begin{bmatrix} \cos(\Delta\theta) & -\sin(\Delta\theta) & \Delta x \\ \sin(\Delta\theta) & \cos(\Delta\theta) & \Delta y \\ 0 & 0 & 1 \end{bmatrix} \qquad (3.1)$$

We define *steering* to be the ability to select the rotational component $\Delta\theta$ of the holonomy Δg within an interval around 0 by employing a one-parameter family of periodic gaits. Thus, a steering gait is a function: $b(\phi, s) : S^1 \times [-\theta_m, \theta_m] \to B$, such that the holonomy $\Delta g(s)$ for the gait $b(\cdot, s)$ has a rotational part $\Delta\theta$ equal to s. We further require that the map $\Delta g(s)$ be continuous in s, i.e. small changes in steering parameter lead to small changes in the resulting holonomy. The astute reader may note that we have omitted the discussion of T and its potential dependence on s. For now, we will assume that a steering gait has a common period T used for all choices s. However, it should be noted that if the motion is in practice "geometric", as we will later claim, the holonomy is in fact independent of the choice of T, making this issue moot.

Steering and turning are two terms we often see used in describing locomotion. We use the terms "steer" and "turn" to refer to different phenomena: turning is the rotational component of the body frame; steering is the ability to do so continuously with magnitudes of turn in an interval containing 0 (pure translation) while at the same time also translating. Thus, one can "turn in place", but not "steer in place". More interestingly, a robot might have some acheivable discrete translation-rotation motions available, i.e. the ability to "move and turn", without the ability to steer. This can happen, for example, by doing two full steps on one side of the body, while taking one full step on the other side.

3.3.2 Phase constraints limit periodic gaits

It should be noted that repeated motions of individual legs do not, on their own, make a periodic gait. To be periodic, the motion of all legs together must be periodic. Thus, if one considers each leg as an independent subsystem executing a periodic motion, the periodicity of body motion implies a constant phase difference constraint between the "sub-system phases" [Revzen et al., 2008] of the respective legs.

To illustrate why this phase constraint has important implications, let us compare a legged system to a typical wheeled vehicle with wheels on both sides of an axle. When the vehicle turns by an angle, the left and right wheels incur a permanent phase shift representing the difference between the arc lengths travelled by the two sides. It is for this reason that wheeled vehicles have a "differential" in their axle. Because the wheels are symmetric under their axis of rotation, they are symmetric under phase change, and this phase shift is of no consequence for future motions;

to the best of our knowledge its only use is the chalk marks made for parking enforcement, which use this phase difference to detect if a car has moved.

In legged systems, such shifts could produce significant changes in motion. For example, the difference between trotting, pronking, and pacing in quadruped gaits is primarily having a different, yet constant, difference between the sub-system phases of the legs [Wilshin et al., 2017]. Not only do different gaits have corresponding phase constraints, there typically are phase differences that do not generate viable gaits. For example, there can be phase differences which place no leg to support the body over a period of time, resulting in the robot body falling on the ground. To support the body, legs of a multi-legged robot must maintain their phase differences within a limited viable range. For example, many hexapods can maintain quasi-static balance by ensuring that at all times there is a set of legs contacting the ground at points which surround the horizontal projection of the Center of Mass (COM) — a constraint that can be formulated in terms of phase locking.

3.3.3 The geometry of steering strategies

Each periodic gait $b(\cdot, s)$ embeds the circle S^1 in the shape space B. Thus $b(\cdot, s)$ is described entirely in terms of a geometric object – its image in B, comprising a 1-dimensional collection of body shapes (see Figure 3.3 (a)) – and the rate at which these shapes are adopted. In those cases where the physics create a "principal kinematic system", that rate information has no bearing on the resulting holonomy, and the gait can be thought of as a purely geometric entity – a loop in shape space. Changing holonomy to steer must therefore require changing this loop (e.g. to Figure 3.3 (b)).
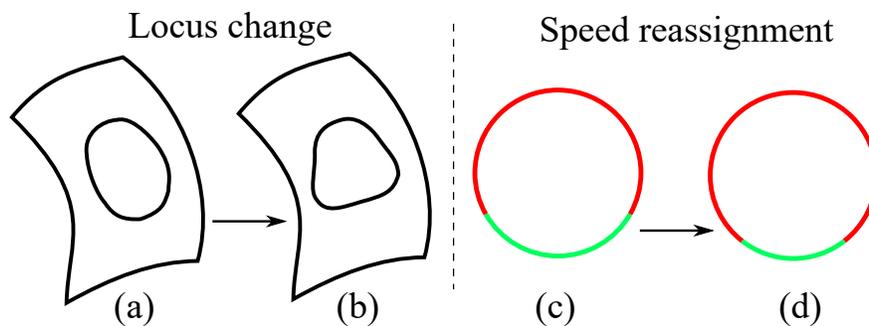
Figure 3.3: Illustration of gaits and gait change. Gaits occupy a loop in shape space (a) since they are an image of the circle S^1. To modulate a gait we may change that image in shape space (b). Alternatively, a gait can be viewed as a combination of each leg trajectory cycle. For a leg trajectory cycle (c,d) with fast (red) and slow (green) segments, a gait can be modulated by changing which parts of the cycle are executed at which speed ((c) vs. (d)).

3.3.3.1 Changing timing to steer

Consider the the case of a robot with 1-DoF legs. Each leg is mechanically constrained to a fixed 1-dimensional track; the only change available to such a leg is changing its timing, e.g. changing the duration it spends moving slowly vs. moving quickly in a given cycle (Figure 3.3 (c) and (d)). Even though the shape of the physical motion of each leg cannot change, and only its rate moving along its cycle can by modulated, this is not equivalent to being restricted to merely changing the rate of a fixed gait. The key difference is that when changing the rate of a gait, all legs change rate precisely the same way together. Even with 1-DoF legs, when the rates of individual legs along their cycles is modulated differently in different legs, the resulting shape-space loop is *geometrically* different (Figure 3.3 (b)). However, because of the phase constraints (see sec. 3.3.2) that need to be maintained, the rate modulation of individual legs must integrate to an integer number of cycles after a period. Typically, that integral will be 0, implying that all legs executed the same number of steps. While some legs can be "sped up" relative to other legs, they must then also be "slowed down" to resyncronize the legs at the end of the cycle.

3.3.3.2 The special case of bilateral symmetry in the plane

Consider a system (animal or robot) which is bilaterally symmetric. This implies the existence of a symmetry map $S : B \to B$ and an associated $\hat{S} : \mathfrak{se}(2) \to \mathfrak{se}(2)$ which map body shape to its mirror image, and body velocities to their mirror images. Both of these maps must be involutions, i.e. $S(S(b)) = b$ and $\hat{S}^2 = I$. Furthermore, in the case of planar motion in particular, regardless of the choice of body symmetry axis, the operator $\hat{S}$ flips the sign on rotational velocities.

It is quite common for bilaterally symmetric organisms to employ "symmetric gaits" for translation, i.e. $S(b(\phi, 0)) = b(-\phi, 0)$ (note: $-\phi = \exp(i\pi)\phi$, the phase after a half-cycle). In such gaits the cycle of body motions consists of two mirror image halves; the first half cycle is the mirror image of the second half cycle.

The associated body frame velocities $g^{-1}\dot{g}$ satisfy $\hat{S} \cdot g^{-1}(\phi)\dot{g}(\phi) = g^{-1}(-\phi)\dot{g}(-\phi)$, i.e. they too are mirrored after half a cycle, and therefore the rotational velocities too are mirrored. In both 3D and 2D, the rotational part of motion is unaffected by translation, i.e. one can compute the total rotation of a sequence of rigid body motions without knowing the translation. This corresponds to the algebraic property of both groups being semidirect products $\mathsf{SE}(3) = \mathsf{SO}(3) \ltimes (\mathbb{R}^3, +)$ and $\mathsf{SE}(2) = \mathsf{SO}(2) \ltimes (\mathbb{R}^2, +)$. In the special case of 2D, $\mathsf{SO}(2)$ is commutative, and therefore the rotations occurring in the second half of the gait cycle perfectly cancel those occurring in the first half, leading to a pure translation.

Thus it is a special feature of 2D planar motion (and of 2D planar motion only!) that symmetric gaits always produce a net translation with no rotation. Many organisms and robot designers

employ this feature to produce translation from legged systems[3].

It further follows that by introducing a parametric change in one half of the cycle, one is likely to introduce a net rotation, and that by introducing the self-same parametric change in the other half cycle containing the mirrored portion of the motion, one may introduce a rotation of the same magnitude but opposite sign. Then such parametric asymmetry makes the original symmetric gait a steering gait.

As humans it is hard for us to conceive of any other way to produce translational motion and to modulate it by steering, since bilateral symmetry is so ingrained in our morphology. Still, we must exercise caution in assuming all legged systems must use this approach. For example, horses use a "rotary gallop" gait which is not bilaterally symmetric when moving at high speeds; therefore they are likely to use non-mirror strategies for steering left and steering right.

3.3.4   Performance criteria for steering

Existing literature suggests different performance metrics for quantifying steering. McClung [2006] suggest the metric of $v\dot{\theta}$ that combines the angular turning rate $\dot{\theta}$ with forward speed v. This metric is dimensional, and gives a natural advantage to high-speed running robots with dynamic steering gaits. Zarrouk et al. [2015] used the metric of average heading change per step, which is estimated from the average turning rate and the step rate, to summarize the turning performance of a dozen of famous multi-legged robot platforms. We will use a similar metric – the turning angle per cycle in $[deg/cyc]$ – and also use a geometric measure of turning, the turning radius in $[mm]$.

Compared with the metric of turning angle per step in Zarrouk et al. [2015], turning angle per gait cycle can be applied to more cases, as the notion of "step" is only meaningful for in symmetric gaits. Typically in steering the two steps in one gait cycle have noticeably different turning angle, making turning angle per step bimodally distributed.

Turning radius is a world-frame measure which represents how sharp a turn the steering gait can achieve, and is thus an important parameter for motion planning.

3.4   Multi-legged steering with low DoF legs

From this section on we restrict our attention to multi-legged systems which have sufficient friction with the ground to justify the claim that COM momentum (known as "group momentum" in

---

[3]The naive reader might assume that the translation created by a symmetric gait must be along the axis of symmetry; this is untrue. Rather, the set of translation directions acheivable is itself symmetric; every gait that lists to left has a partner that lists to the right by the same angle.

geometric mechanics) dissipates quickly[4]. Typically, this would be the consequence of having 3 or more point contacts with the environment at all times; if contacts can support torques, fewer contacts than 3 might suffice. Our assumption rules out discussion of highly dynamic gaits with low duty cycles, and the gaits of bipeds, and the more rapid gaits of quadrupeds.

We will discuss legs with 1 or 2 DoF, where by DoF we only include active DoF-s that can be directly controlled. Passive DoF, like the deformations of elastic legs, are not included. In this, the issues facing low-DoF multi-legged robots are the converse of those facing the typical bipedal or quadrupedal robot: the former are over-constrained with respect to the ground, whereas the latter are under-constrained.

3.4.1   Steering with these conditions is hard

To futher illustrate the importance of the investigation we conducted, consider the conditions for multi-legged low DoF steering. Removing any one component of "multi + legged + low DoF + steering" produces an easier to solve problem.

If "legged" is not a requirement: Many wheeled vehicle have low DoF multi-contacts with ground, but such contacts are continuous. The continuous symmetry of the wheels allows them to have arbitrarily accumulated phase from the phase difference introduced with steering. This implies that wheeled vehicles switch within an $N-1$ dimensional family of functionally identical periodic gaits (N number of wheels), one for each possible choice of phase differences between the wheels. In that sense, wheels or treads solve a different, far easier problem.

If "multi-" is not a requirement: For bipedal robots with low DoF legs, only one leg is touching the ground for most of the time. Bipedalism creates substantial problems in controlling an under-actuated, unstable plant. For bipedal robots, the bigger challenge is to maintain heading and stability – a single pin-joint contact, or even a toe and heel pair of contacts, often generate heading and orientation changes that can be exploited for steering. It should also be mentioned that with only two legs, 3 DoF per leg requires 6 motors, i.e. a device of comparable mechanical and electrical complexity to a hexapod with low DoF legs.

If "low-DoF" is not a requirement: As soon as each leg has 3 or more DoF, foot placement can be arbitrarily controlled within a volume, making the body frame fully locally controllable in a kinematic sense. At the cost of this extra complexity, steering becomes much easier, at least at the low speeds we consider here.

It is also important to notice that these conditions do not make locomotion uniformly difficult; we have only identified these difficulties in the case of steering. If the robot is not required to allow the heading to be continuously controlled while moving, making the robot bilaterally symmetric

---

[4]By "quickly" we mean that we are in the domain where the recent results of Kvalheim et al. [2019] apply, implying that the equations of motion can be written in an approximately geometric form (*ibid*).

allows one to exploit the trick described in section 3.3.3.2 to translate without rotation. In particular, in the case of hexapod robots, a designer may use the alternating tripod gait. In such a gait, the three feet in contact with the ground form a triangle under the center-of-mass and translate relative to the body without changing the shape of the triangle. This uniquely defines the motion of the body frame, and given bilateral symmetry, allows for a walking gait with zero heading change.

From these examples, we can see that multi-legged steering with low-DoF legs is particularly hard. Solving this problem would allow us to use multi-legged robots with a mechanical and electrical complexity lower than that of today's popular bipeds and quadrupeds.

3.4.2   1-DoF steering creates conflicting constraints

To be able to translate using a set of non-slip foot contacts, those foot contacts must themselves translate as a rigid set of points in the body frame while in stance. This geometric constraint must be designed into the motion of any set of legs used for non-slip motion. Note that this geometric constraint is necessary, but not sufficient to make a gait have no slip: accelerations or gravitational force components can be large enough to break a contact outside its friction cone and cause it to slip anyway. The gaits we describe are slow enough, and stable enough where all slipping is caused by incompatible foot motions.

(a) Steering   (b) Translating
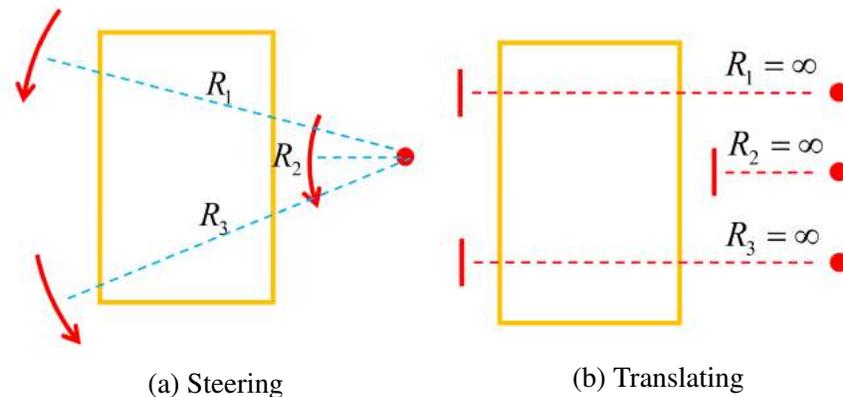
Figure 3.4: Leg strokes in the body frame for a tripod of legs, assuming non-slip motion while steering (3.4a) and while translating without heading change (3.4b). Note that leg strokes needed for non-slip steering and noslip translation have incompatible 2D projections in the body frame, and thus cannot be the result of the same 1-DoF motion.

The problem of incompatible foot motions becomes starkly clear when considering a robot with 1-DoF legs (see Figure 3.4). The feet of 1-DoF legs follow a 1-dimensional path in the body frame. Whichever feet support the body while translating (we assume a tripod in Figure 3.4), they must follow identical paths in the body frame. Whichever feet support the body while steering

65

along some arc, the feet must follow different paths from each other because they are at different radii from the center of rotation. Since the legs are assumed 1-DoF, each individual leg can only follow one path – showing that allowing a range of turning radii creates conflicting constraints on the 1-DoF path of the feet.

Naively, one might assume that hexapedal robots with 1-DoF legs moving parallel to the body would have trouble steering and turning. In practice, direction changes merely force the robots break the non-slip constraint. For example, RHex is highly maneuverable [Johnson, 2013] and turns easily, but it does so with considerable slipping.

3.5   Steering of hexapod with 1 DoF legs: BigAnt
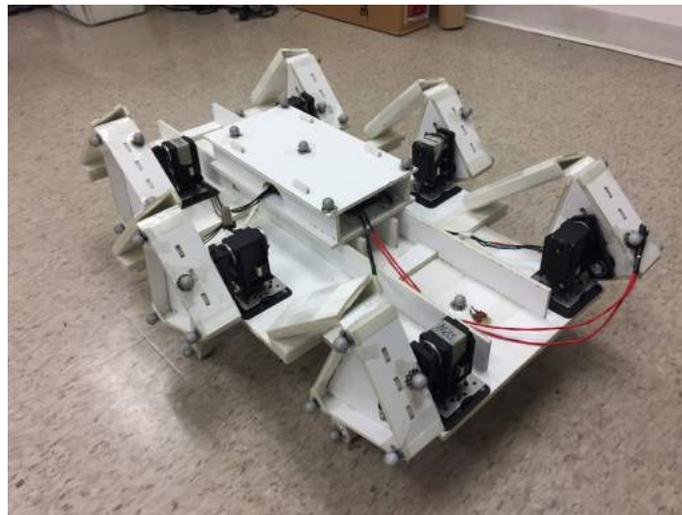
Figure 3.5: BigAnt used for steering gait tests.

The steering tests for multi-legged robot with 1-DoF legs were conducted on the BigAnt robot. The design and development of BigAnt is introduced in Chapter 2, and only summarized briefly here. Its chassis structure and mechanisms were manufactured using the PARF (plate and reinforced flexure) technique [Fitzner et al., 2017, Miller et al., 2015] developed in our lab. Using PARF, the chassis of BigAnt can be manufactured with minimal tooling (a knife) and less than US$20 worth of materials (Elmer's Products Inc. foam board $508 \times 762 \times 7$mm and 3M Scotch #8959 fiber tape). With a laser cutter instead of the knife, the chassis can be fabricated within 7 hours, which includes 30 minutes assembly. The fast and inexpensive turnaround allowed the design of BigAnt to be iterated quickly. Instead of simulating each re-design we used experiments to directly measure and iteratively improve the robot (see Figure 3.5 for version used here).

Like the RHex family of robots [Galloway et al., 2010, Saranli et al., 2001], BigAnt has six

1-DOF legs. Each leg is actuated by a servo motor (Robotis Dynamixel MX64), but rather than directly rotating a leg like RHex robots do, the legs of BigAnt are driven through a 4-bar mechanism. The leg trajectory was chosen by exploring the space of possible 4-bar designs for motions with a flattened backward stroke and a high clearance when swinging forward (see Figure 3.7a). While other linkages exist that could produce a flatter back stroke, those require significant additional complexity or larger dimensions compared with current 4-bar design. The BigAnt leg is highly modularized, making it easy to both replace worn out legs, and install custom leg geometries for different applications.

3.5.1 Steering gaits design

While the 4-bar linkage defines the geometry and position-dependent gearing ratio of BigAnt legs, the instantaneous position of the leg along its ovoid path is under (conventional PID based) servo control. If all six legs are driven at constant angular speed as two anti-phase tripods of legs ("left tripod" FL-MR-HL containing [F]ront-[L]eft, [M]iddle-[R]ight and [H]ind-[L]eft legs; and the "right tripod" FR-ML-HR), the robot exhibits substantial up-down motions representing parasitic work against gravity. To obtain a smoother motion, we scheduled the motion of the the the shaft angles ψ_k $k \in \{\text{FL}, \text{FR}, \text{ML}, \text{MR}, \text{HL}, \text{HR}\}$ as a function of leg phase ϕ_k using a two-speed schedule: a (typically) fast "aerial phase", and a (typically) slow "ground contact phase" (see Figure 3.6). To our knowledge, this idea comes from work done by M. Buehler on the RHex robot, and is sometimes referred to as a "Buehler Clock" in the RHex literature. The Buehler clock is defined by 4 parameters. Often these are the "sweep" angle through which the leg moves in ground contact, a "duty cycle" defining the fraction of the cycle in ground contact, the stance angle "offset" away from vertical, and the phase at midstance. Because the choice of zero phase is arbitrary, we always chose the liftoff phase to be 0, leading to a Buehler clock defined by only 3 parameters.

3.5.1.1 Steering gait I: timing regulation of mid legs

We designed our gaits by tweaking these three gait parameters at a moderate gait frequency ($\sim$ $0.2\,\text{Hz}$) until the robot was both moving reliably and hardly bouncing up and down. We then introduced steering control by modulating the functions ψ_{ML} and ψ_{MR} with a steering input s. The overall phase change of such a modulation must be 0; it is therefore a periodic function of phase. We chose an obvious candidate $-\cos(2\pi\,\phi)$ which we used to advance/retard the phase of one middle leg, and retard/advance the phase of the other middle leg in an anti-symmetric way. Letting
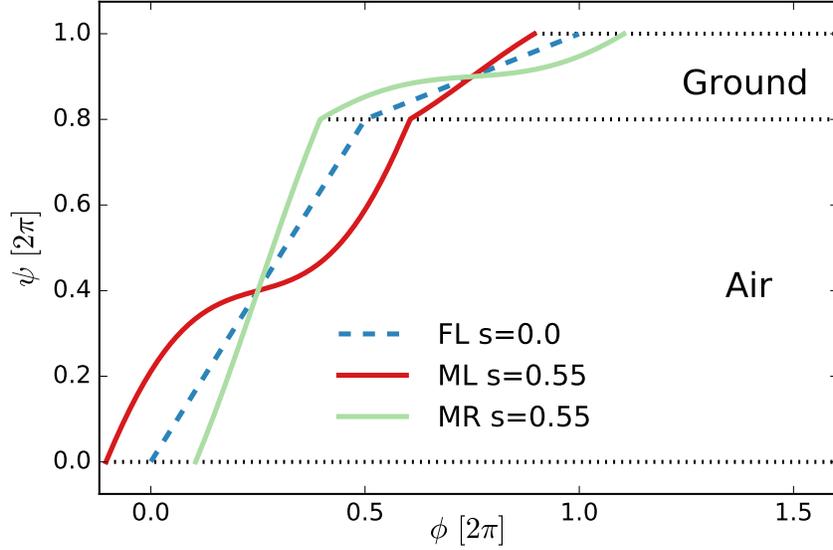
Figure 3.6: BigAnt joint angle output as a function of local phase ϕ within a gait cycle. When moving straight, the phase to joint angle relationship is a "Buelher clock" consisting of a fast constant speed phase for aerial motion and a slow constant speed phase during expected ground contact(dashed blue line). With a steering input of $s = 0.55$ (see Equation 3.2), the mid left leg motion (red) and mid right leg motion (green) are modulated in opposite ways, generating a steering motion to the right.

(a) No steering

(b) ML, $s = 0.55$

(c) MR, $s = 0.55$
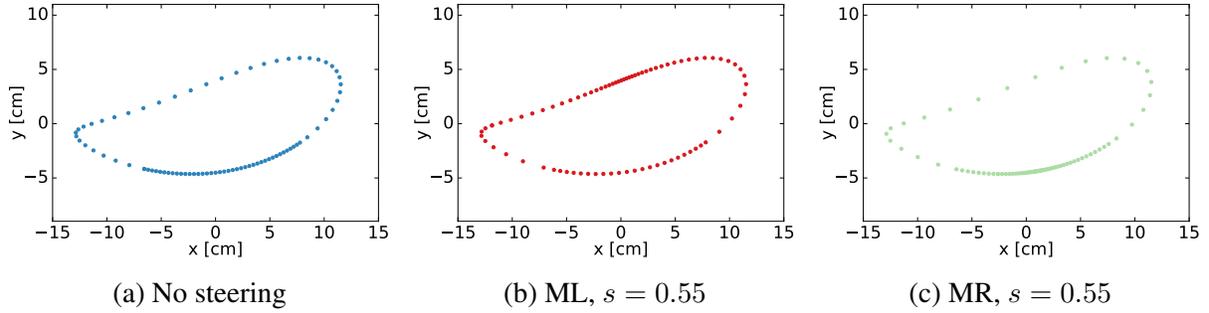
Figure 3.7: Leg trajectory in the body frame, with points indicated at equal phase intervals. Without steering (a) a clear Buehler clock effect is visible. With steering at $s = 0.55$, the timing of ML (b) and MR (c) becomes different, even though the shape of the trajectory is the same.

$b(\phi) : \phi \mapsto \psi$ be the Buehler clock function chosen, our shaft angles were:

$$
\begin{aligned}
\psi_{\text{FL}} = \psi_{\text{HL}} &:= b(\phi) \\
\psi_{\text{FR}} = \psi_{\text{HR}} &:= b(\phi + 1/2) \\
\psi_{\text{ML}} &:= b(1/2 + \phi + s\,k_s \cos(2\pi\,\phi)) \\
\psi_{\text{MR}} &:= b(\phi - s\,k_s \cos(2\pi\,\phi))
\end{aligned}
\tag{3.2}
$$

where $k_s := 0.24$ is a constant gain adjusting sensitivity. The shaft angles with steering modulation of $s = 0.55$ are shown in Figure 3.6. The corresponding leg trajectories at Figure 3.7b and Figure 3.7c give us an explicit view of how the mid right leg is slowed down at ground contact and how the mid left leg is sped up at the same part of trajectory. With such modulated tripod gait, we can now steer BigAnt by changing the input parameter s to different values.

The strategy of steering by modulating middle legs is itself bio-inspired, and based on the strategies cockroaches often use for turning [Jindrich and Full, 1999].

3.5.1.2 Steering gait II: by Buehler Clock modulation

As introduced in Section 2.2.7.2, we can determine the contact regions of the leg trajectories by designing the Buehler Clock functions for the actuation profiles. For BigAnt tripod gaits, if the legs (leg) on one side have a larger contact region and the leg (legs) on the other side has a smaller contact region, BigAnt will turn in the direction of the side with the smaller contact region. This turning mechanism can be used for steering BigAnt, by applying different Buehler Clocks on the two sides of the body.

(a)

(b)
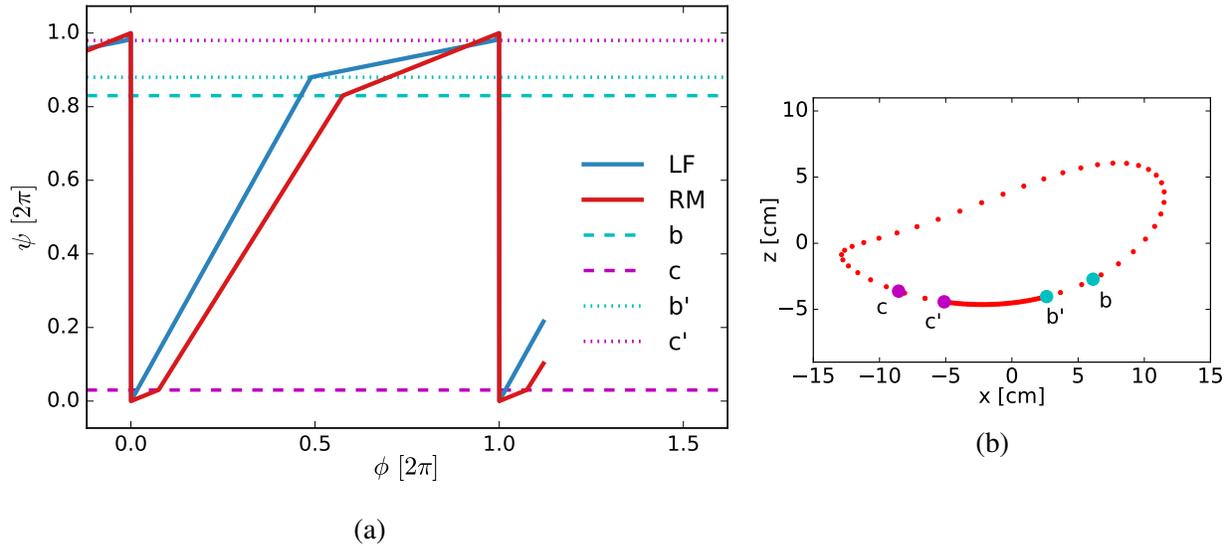
Figure 3.8: (a): Actuation profile of the modulated Buehler Clock $\psi^S(\phi, s = -0.1)$ compared to the original Buehler Clock $\psi^L(\phi)$. The horizontal lines indicate that "take-off" and "touch-down" points depicted in (b). (b): BigAnt leg tip trajectory with the larger contact region bc and the smaller contact region $b'c'$ highlighted for comparison. The sample intervals are based on Buehler Clock $\psi^S(\phi, s = -0.1)$

We chose to modulate the original tripod walking gaits we designed for BigAnt in Section 2.2.7.2. The corresponding Buehler Clock is written in the form of Equation 2.2. We use the

superscript L (S) to indicate the larger (smaller) contact region Buehler clock parameters. We kept the original parameters of Buehler clock I for $\psi^L(\phi)$), i.e.: $\Delta\psi_0^L = 0.2$, $\phi_e^L = 0.075$, $\phi_s^L = -0.425$ (with "take-off" and "touch-down" angle as $\psi_e^L = 0.03$, $\psi_s^L = -0.17$). For the legs with the smaller contact region we used: $\Delta\psi_0^S = \Delta\psi_0^L - |s|$, $\psi_e^S = \psi_s^L - 1/2|s|$

$$\phi_s^S = \begin{cases} P\psi_e^S/\Delta\psi_0^S & \psi_e^S \geq 0 \\ (1-P)/\psi_e^S/(1-\Delta\psi_0^S) & \psi_e^S < 0 \end{cases} \tag{3.3}$$

where s is the steering parameter; P is the duty factor (which in this case is 0.5, i.e. half a cycle). We define the positive steering parameter s for the right turning by making the left side legs adopt $\psi^L(\phi)$ while making the right side legs adopt $\psi^S(\phi, s)$. We define the negative steering parameter s for the left turning by making the right side legs adopt $\psi^L(\phi)$ while making the left side legs adopt $\psi^S(\phi, s)$. Figure 3.8a exhibits the result actuation profiles for the left tripod with steering parameter $s = -0.1$. The corresponding larger contact region on the FL and FR legs and the smaller contact region on the ML leg are depicted in Figure 3.8b. It is worth noting that with some large steering parameters s, there could be a reverse drive on the Buehler Clock $\psi^S(\phi, s)$ for sharp turns.

3.5.2 Steering tests

To verify our analysis about low-DoF multi-legged steering and measure slipping behavior during steering, we used two types of robot platforms that have different morphology and different effective DoF per leg (1-DoF and 2-DoF) for our experiments. We tested both robots on two substrates – a relatively slippery linoleum floor, and higher friction interlocking rubber tiles (C9 interlocking fitness mat; Target Inc 2015). We tried a variety of steering parameters and speeds. All the locomotion results were recorded using a reflective marker motion tracking system (10 Qualisys Oqus-310+ cameras at 120 fps, running QTM 2.17 build 4000, interfaced to custom SciPy 0.17.0 code using the Qualisys 1.9 Realtime API)

3.5.2.1 Steering gait I test results

We tested the steering gait introduced in the previous subsection on BigAnt with different steering input parameters and recorded the motion using Qualysis motion capture systems. Figure 3.9 shows an example of BigAnt walking on our lab floor; we provide detailed plots and statistics for this trial which consisted of 6 strides at gait frequency $f = 0.22\,\mathrm{Hz}$ and steering input $s = 0.75$. Results from other trials were quite similar, and so we do not provide such details from every trial. We collected a total of $N = 39$ trials, $N_s = 225$ strides, total time of ~ 1800 seconds at $120\,\mathrm{fps}$
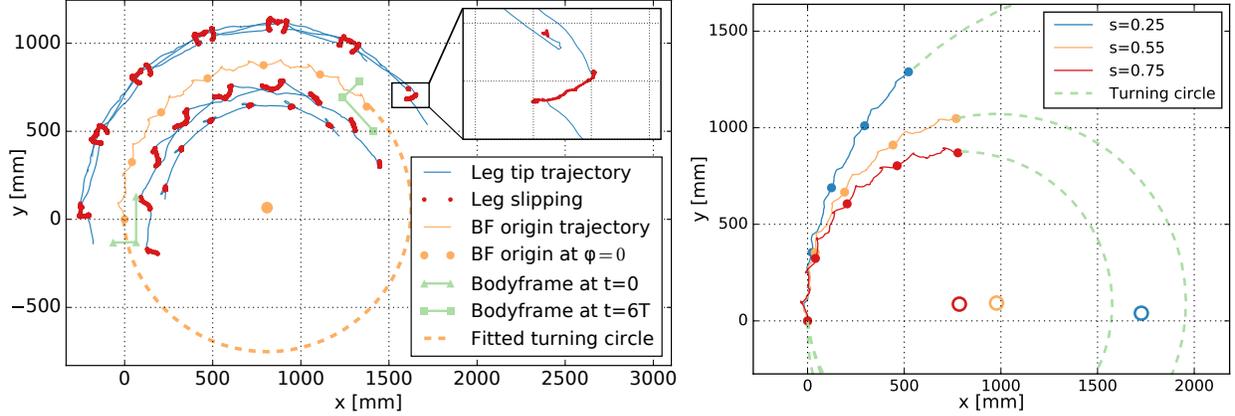
Figure 3.9: BigAnt motion in world frame (left) and Steering results at different values of s (right). For gait frequency $f = 0.22$ Hz; steering input $s = 0.75$, we plotted (left) leg tip trajectories (blue), with slipping highlighted (red dots; magnified in inset), and the trajectory of the body frame origin O (yellow line) with the beginning of cycle indicated (yellow dots). We indicated the markers that define the body frame (light green) at the beginning (triangles) and end (squares) of this 6 stride trial. To estimate turning radius we fit a circular arc (dotted yellow) to the body frame origin. In this trial, BigAnt turns $23°$/cyc and the turning radius is 818 mm. Exploring other values of s (right) we plotted the motion of the body frame origin at different values of the steering parameter s (teal, yellow, red for 0.25, 0.55, 0.75 resp.), while leaving all other gait parameters unchanged. To each trial of 4 strides we fitted a circular arc (dashed green) and indicated the center of rotation (teal, yellow, red circles). Results suggest a clear parametric dependence of turning radius on steering parameter value.

for a total of $N_f = 2.16 \times 10^5$ frames of data, using $N_r = 3$ similarly constructed robots.

Additionally, we collected various metrics of slipping: (1) the slipping distance; (2) the "slipping ratio" of slipping distance to total leg motion distance. A slipping ratio of 0 indicates a non-slip gait; a slipping ratio of 100% represents a leg that always remains in contact with the ground and is never in static friction. The average slipping ratio for the trial (Figure 3.9) we examined in details is 20.6%. To better understand the kind of slipping taking place, we separate slip into two components: slipping in the direction tangent to the arc the robot is moving along, and slipping in the direction radial relative to this arc. For the slip in each components, we compute both the time-averaged absolute value, and the time-averaged value (see table3.1).

We also examined the foot motions with respect to the body frame. Our expectation was that foot motions are, for all practical purposes, rigidly dictated. Therefore, regardless of the value of s or which of the 6 identical (up to mirror image) legs we observe, we should see the same trajectory for the foot in the body frame (see Figure 3.10(b)(c)(d)).

To get more details about how the interaction between leg and ground results in such steering behavior, we plotted world frame z motion vs. body frame x (see Figure 3.10(a)(e)). These two

Table 3.1: Slipping by leg for $s = 0.75$, $f = 0.22$ Hz. Motion capture error bounds were ± 3.5 mm at 99th percentile of error

	FL	ML	HL	FR	MR	HR	Mean
Slip/cyc [mm]	98	48	119	115	60	133	95
Slip ratio [%]	18.7	9.6	22.1	28.7	13.8	30.9	20.6
Abs. tangent [mm/cyc]	45	40	66	97	52	96	66
Abs. radial [mm/cyc]	79	18	81	49	20	77	54
Avg. tangent [mm/cyc]	-9	26	31	25	-5	35	17
Avg. radial [mm/cyc]	-47	5	44	-12	2	38	5

subfigures show a longer stroke in ground contact for all left legs, compatible with the observation that the robot turned to the right.

3.5.2.2 Steering gait II test results

We tested the steering gait II with 7 steering parameters on BigAnt with the same motion tracking system as in 3.5.2.1. Each steering parameter was tested 3 times. The motion results in the world frame are plotted in Figure 3.11, and indicate that the steering parameter controlled the turning rate. The quantitative results are presented in Table 3.2.

We also plotted the leg trajectories in the world frame for a steering trial (see Figure 3.11). The results indicate that the legs slipped a noticeable amount when BigAnt was adopting the steering gait II. The similar body frame trajectory check was done and presented in Figure 3.12, which verifies that the BigAnt leg is still follow the design the trajectories. It also shows the left side legs remained larger contact regions while the right side legs achieved smaller contact region from the modulated Buehler clock.

Table 3.2: Statistics of BigAnt adopting the steering gait II with differential steering parameters as the cases shown in Figure 3.11

Steering input	$s = -0.3$	$s = -0.2$	$s = -0.1$	$s = 0$	$s = 0.1$	$s = 0.2$	$s = 0.3$
Ang/cyc mean [deg]	-29.2	-22.6	-10.5	0.6	11.5	23.4	32.5
Ang/cyc std. [deg]	0.7	1.6	1.1	1.0	1.2	1.2	1.1

3.5.3 Steering and slipping

At this point it should become quite clear that while BigAnt is not hard to steer with our choice of steering gait (see Figure 3.9 for steering with different inputs of s), the actual mechanical interac-
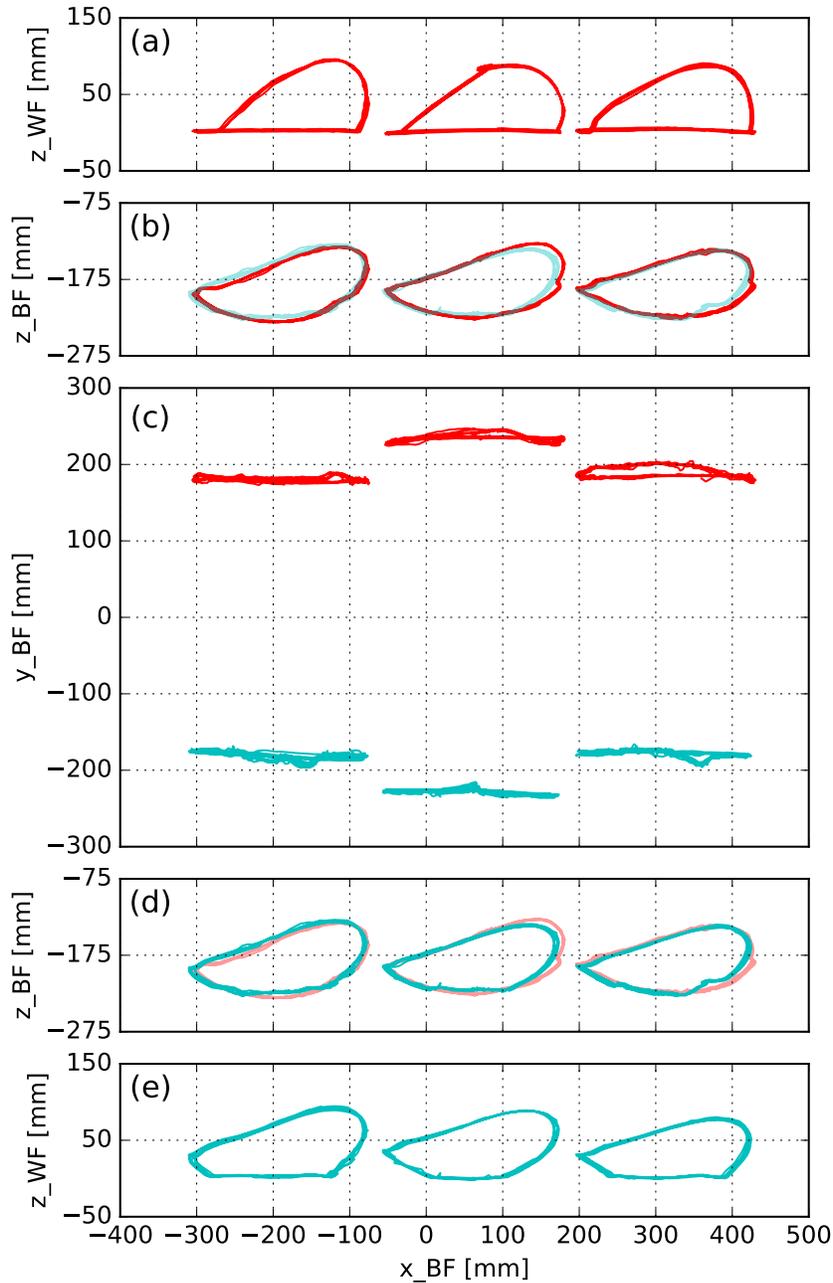
Figure 3.10: BigAnt foot motion in the body and wold frames. We show horizontal (x, y) projection (c) and saggital (x, z) projections (a)(b)(d)(e) with side of the leg indicated by color (left - red; right - teal). In the body frame (b)(d), the contralateral leg is also shown (transparent) to highlight that motions are symmetric in the body frame. Viewed with world frame z (0 is ground), the left legs (a) have a longer ground stroke than the right legs (e). This highlights the counter-intuitive notion that actual ground strokes can be quite different even with identically shaped trajectories, thanks to timing and slipping.
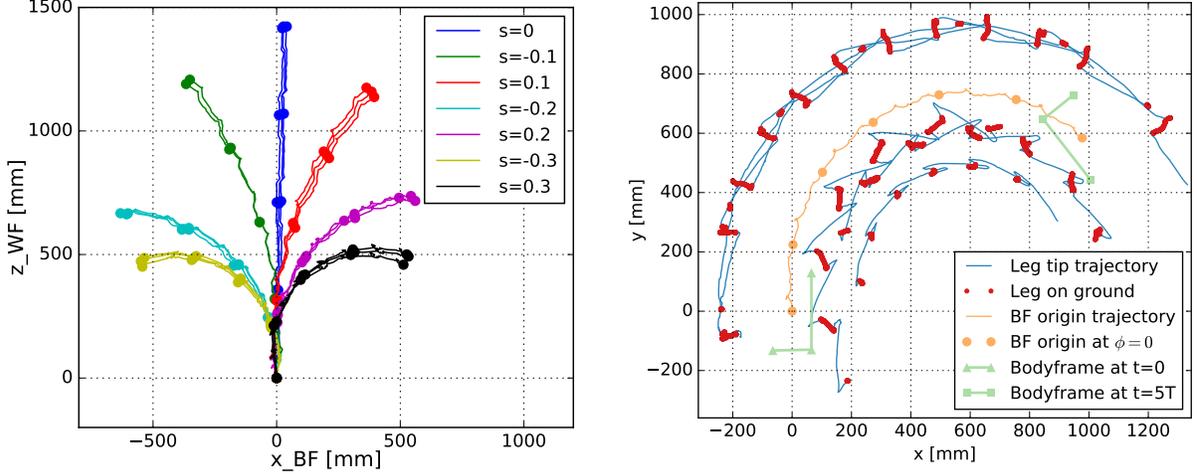
Figure 3.11: BigAnt motion in the world frame when adopting the steering gait II at gait frequency $f = 0.24Hz$. Left: The body frame origin trajectories of BigAnt with different steering parameters. Right: The robot walked 6 cycles with steering parameter $s = 0.1$. We plotted the trajectories of the feet (solid hairine blue), and highlighted their positions on the ground (red dots). We also plotted the motion of the body frame (green), indicating start position (green triangles), end position (green squares), position at start of each cycle (yellow circle), position over time (yellow line), and best-fit circular arc (dashed thick yellow line). In this trial, BigAnt turns $11.5°/\text{cyc}$.

tion that produces steering from the modulation of ψ_{ML} and ψ_{MR} with s is not at all obvious.

To better understand how BigAnt actually steers we conducted a multi-robot, multi-parameter study, summarized in Figure 3.13. We compared the results taken from 3 independently constructed copies of the BigAnt robot, over a variety of gait frequencies, and on both low friction and high friction substrates. The purpose of this comparison was to establish whether it was in fact s which controlled the steering behaviors, or whether we merely created systems whose multi-contact interaction too complex for us to understand in some idiosyncratic way.

Since the experimental datasets are of slightly different sizes, and there is no reason to assume the parameters we measure are normally distributed, we used non-parametric methods for our statistical analysis. Each grouping of parameters was represented by a bootstrap sample of size 1000; this size was chosen because all groupings were at least of this size. The use of bootstraps facilitates homoscedasticity of the box-plots we use to represent the results, and allows the spread to be meaningfully compared across groupings. The results show that s reliably governed steering across all 3 robots, and produced statistically indistinguishable outcomes with them. They further show that once the influence of s is removed, neither gait frequency nor substrate friction have a detectable influence on the rate of turning. This suggests a very peculiar physics: one that is geometric by its independence from time parameterization, includes significant slipping, and yet is nearly independent of the magnitude of the friction coefficients that govern this slipping.
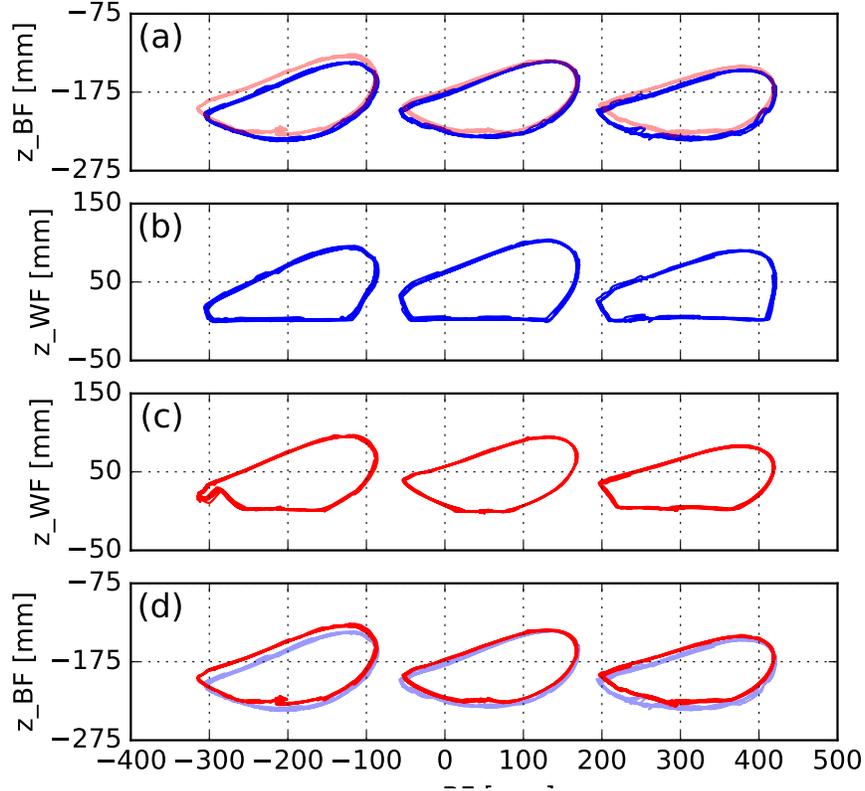
Figure 3.12: BigAnt foot motion in the body and wold frames when adopting steering gait II with steering parameter $s = 0.1$ and gait frequency $f = 0.24Hz$. We show saggital (x, z) projections (a)(b)(c)(d) with side of the leg indicated by color (left - blue; right - red). In the body frame (a)(d), the contralateral leg is also shown (transparent) to highlight that motions are symmetric in the body frame. Viewed with world frame z (0 is ground), the left legs (b) have a longer ground stroke than the right legs (c).

To gain further insight into how such a counter-intuitive outcome might appear, we analyzed several slipping metrics of individual legs at different values of the steering parameter s, holding the remaining parameters constant. These results are in Figure 3.14, and come from the $f = 0.22$ Hz trials with robot R1.

From Figure 3.14a we observe that the slip ratio, which equals total distance slipped divided by total distance traveled, clearly increases with s. The change is expressed mostly in the tangent direction, where legs of the left tripod (FL,MR,HL) are retarded more with higher s, and legs of the right tripod (FR,ML,HR) are advanced. These changes are straight-forward to anticipate from Equation 3.2. The radial directions harbors a surprise: FL and HL respond to changes in s quite strongly and with opposite sign, but their symmetric counter-parts FR and HR do not. This suggests that during left tripod stances with large s, FL moves radially in (right) and HL moves radially out (left), whereas in right tripod stances little to no radial motion is observed.
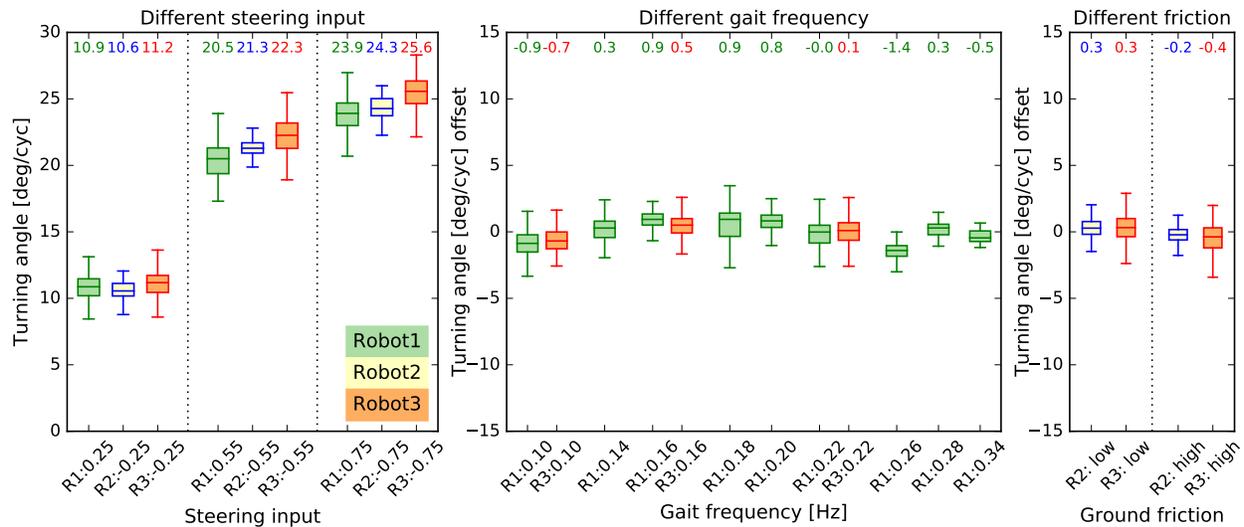
Figure 3.13: Turning rate dependencies on various parameters. To show dependence (or lack thereof) of turning rate on various parameters, we binned data according to the parameter value and collected a bootstrap sample of size 1000, making the spread of the various box-plots meaningful for comparison. We also present the numerical mean values of each box plot (number above box-plot). First, we group data by which of the 3 comparable robots (R1, R2, R3; green, yellow with blue frame, orange) we took data from, and at what value of the steering parameter s that trial was running (0.25, 0.55, 0.75 parts of the left sub-plot). Results show a clear dependence of turning rate ω on s, which is consistent among all 3 robots. Since the influence of s and robot ID r dominated variability in ω, we subtracted the average $\langle\omega\rangle(s, r)$ from ω to examine the data for any additional effects of gait frequency ($0.10\,\text{Hz}$ to $0.34\,\text{Hz}$ middle subplot), or ground-to-foot friction coefficient (right subplot). Results fail to reject the null for these potential influences. Together, these results suggest that s alone governs the turning rate for each robot, and does so reliably for all the robots of this type we built.

76

(a) Slip ratio   (b) Average slip, tangent [mm]   (c) Average slip, radial [mm]
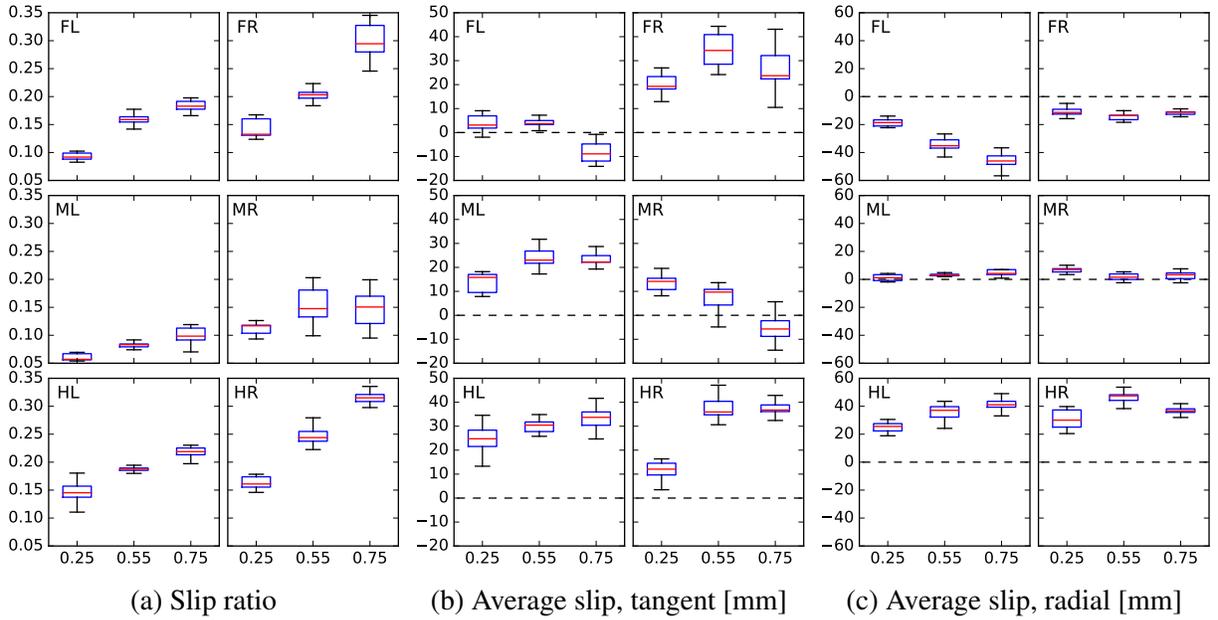
Figure 3.14: BigAnt slipping metrics, by leg and steering parameter value. We collected the slipping metrics for BigAnt platform R1 with $f = 0.22\,\mathrm{Hz}$, partitioned by $s = 0.25$, 0.55, and 0.75. We present the ratio of slipping distance to travel distance (a); average distance slipped tangent to direction of motion along the turning arc (b); and average distance slipped radial to turning arc and thus perpendicular to direction of motion (c). Slipping in (b) is non-productive for locomotion; slipping in (c) is necessary to rotate the robot around its axis. Each metric is presented separately for each of the robot's legs. We created each box-plot by evaluating the metric by a bootstrap sample of 100 period-long windows from the relevant slice of the dataset. Note that with this gait the robot arcs to the right.
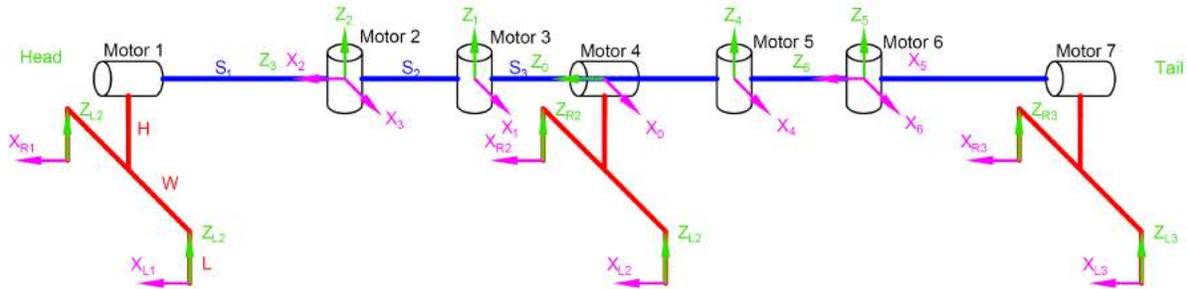
Figure 3.15: Mechapod is actuated by 7 highly geared down servo motors (Dynamixel MX106 and MX64): 4 of them are on the spine controlling the spine yaw motion (Motor 2,3,5,6); the other 3 controls leg roll motion (Motor 1,4,7). The 3 pairs of legs are coupled by spring steels which offer compliance to the robot.

3.6 Steering of hexapod with 2 DoF legs: Mechapod

To explore the relationship of slipping and steering with 2-DoF legs, we used the "Mechapod" robot, a hexapedal robot derived from a previously studied "centipede robot" [Sastra et al., 2008, 2012]. Centipede attempted to be the first modular robot to exhibit a dyanmic gait with aerial (ballistic) phases using geared-down, conventional servo motors. Mechapod consists of an articulated spine with 7 motor modules, connected to 3 elastic legs that extend side-to-side (see Figure 3.15).

Defining a body frame for shape-changing robots can be a non-trivial [Hatton and Choset, 2011]. Following previous work [Sastra et al., 2012], we associate a body frame with Mechapod by taking the line connecting the center of one end-module ("front") with the center of the opposite end-module ("back") as the X axis, and constraining the center of the middle module to the Y axis. Similar to Multipod leg DoF as introduced in Section 2.3.1.2, Mechapod also has effective 2 DoF per leg.

3.6.1 Mechapod non-slip steering gaits

We considered the problem of introducing steering into the alternating tripod gait used for rapid motion with the Mechapod. When engaging in this gait, the roll motors in the front, middle, and hind modules are typically set to the same fixed angle with alternating signs. Under the assumption that this angle is small, its cosine is nearly constant. This allowed us to plan the motion of the 3D robot in terms of its 2D horizontal projection, which consists of two 4-bar linkages tied together. Each 4-bar has one DoF allowing the robot to move while maintaining non-slip contact with the ground. The idea of embedding such a 4-bar linkage to allow non-slip motion was an insight of the original "centipede robot" designer (S. Sastra of [Sastra et al., 2008]; see Figure 3.16).

We construct a periodic 4-bar gait as follows (refer to Figure 3.17). Assuming a cycle with
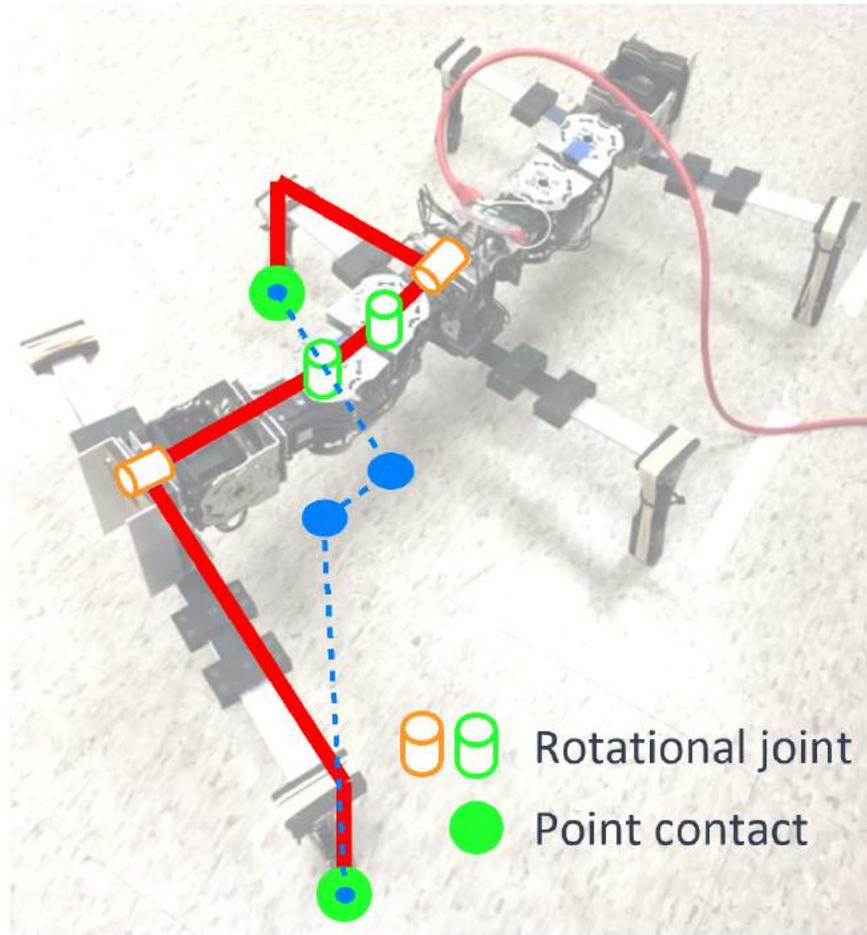
Figure 3.16: Overlay showing how Mechapod contains a 4-bar linkage. When the roll motors (orange cylinders) are activated and holding stationary at equal angles, the robot can be standing on a tripod (here FL,MR,HL) with presumed point contacts at the feet (green dots for FL,MR). The projection of the robot on the horizontal is then a 4-bar linkage (blue dots and dashed lines).
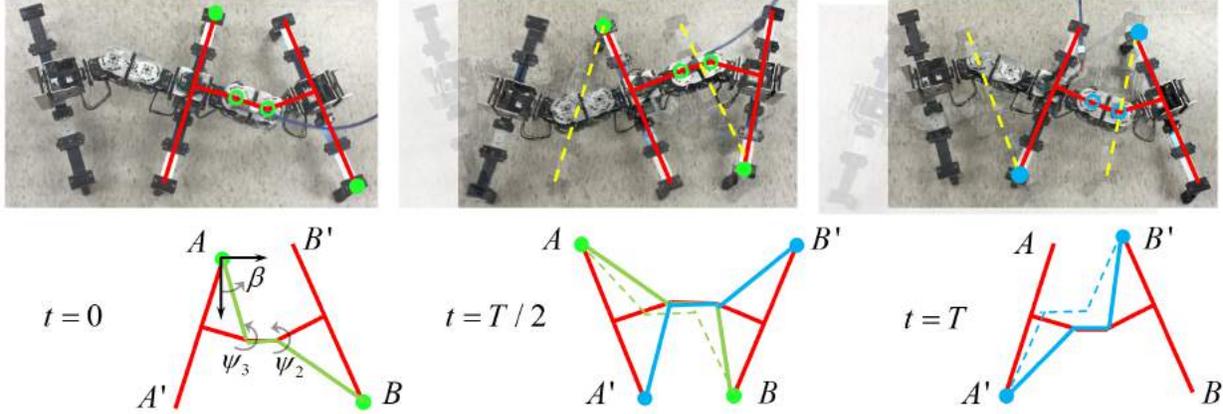
Figure 3.17: Mechapod locomotion can be represented by the motion of two 4-bar linkages. We show 2 consecutive steps of Mechapod walking left to right (top row; 3 photos of double stance configuration). We indicate the skeleton of the front half (red lines; open circles for motors) and the previous leg positions (dashed yellow). Supporting legs in first step (solid green circles) and in second step (solid blue circles) show the pivots of the abstracted 4-bar (bottom row). The first step 4-bar (green) and the second step 4-bar (blue) share link lengths and there is a well defined relationship between the angles of the links before and after the support switch for a fixed value of spine motor angles ψ_2, ψ_3. We denote the locations of the feet by A, B, A', B', and by β the sweep angle of the A–A' leg. Since this is a kinematic model, we may arbitrarily choose the switchover time to be mid-cycle at $t = T/2$.

period T, we take $t = 0$ as start of support for one tripod, and $t = T/2$ as switch to support by the other tripod. At time $t = T$, the robot configuration needs to cycle back to the same configuration as that at time $t = 0$ to have a periodic solution, so distances between foot locations must satisfy $|AB(0)| = |AB(T)|$ and $|A'B'(0)| = |A'B'(T)|$. With the non-slip constraint, the supporting legs are pinned to the ground. During the first step ($0 \leq t \leq T/2$), feet A, B are on the ground; during the second step ($T/2 \leq t \leq T$), feet A', B' are on the ground. Thus $|AB(0)| = |AB(T/2)|$ and $|A'B'(T/2)| = |A'B'(T)|$; together with the previous equalities, this gives:

$$|AB(0)| = |AB(T/2)| \qquad\qquad |A'B'(0)| = |A'B'(T/2)| \qquad (3.4)$$

Assuming we start a step with $[\beta(0), \psi_2(0), \psi_3(0)]$ at $t = 0$, and by definition $\beta(0) := 0$, the 4-bar structure dictates the distances $|AB|$ and $|A'B'|$ as a function of β, and through $\beta(t)$ as a function of t. The solution of Equation 3.4 thus uniquely selects possible values of $\beta(T/2)$ as an implicit function of the initial $\psi_2(0), \psi_3(0)$. This implies that by exhaustively scanning choices of these initial values we can discover all possible non-slip Mechapod gaits. We performed such an analysis, showing $\beta(T)$ as a result of initial values $\psi_2(0), \psi_3(0)$, also taking into account to forbid
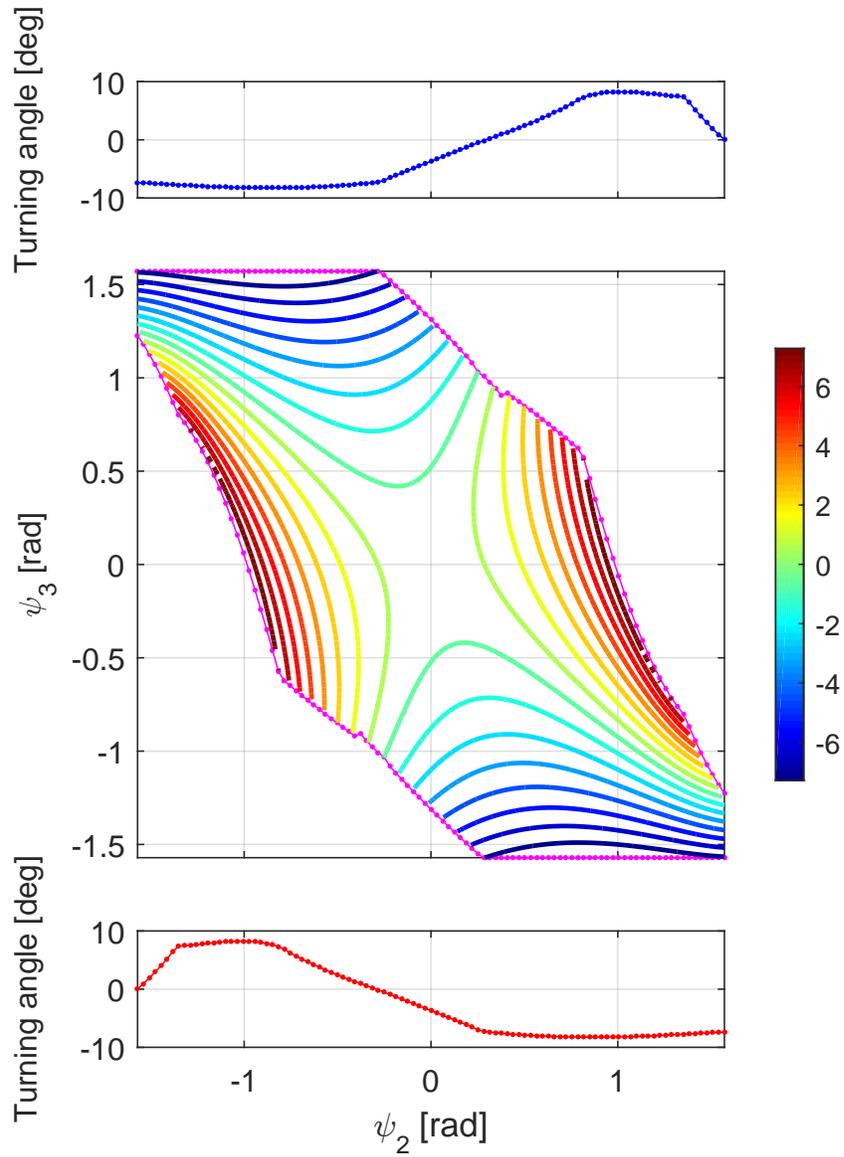
Figure 3.18: $\beta(T)$ for all non-slip gaits of Mechapod. The overall turn $\beta(T)$ (colored contours, center subplot) after a cycle of non-slip motion for feasible non-slip gaits, and its value on the two boundaries of the feasible range (magenta dots in center; top and bottom graphs), which also show the extremal values.
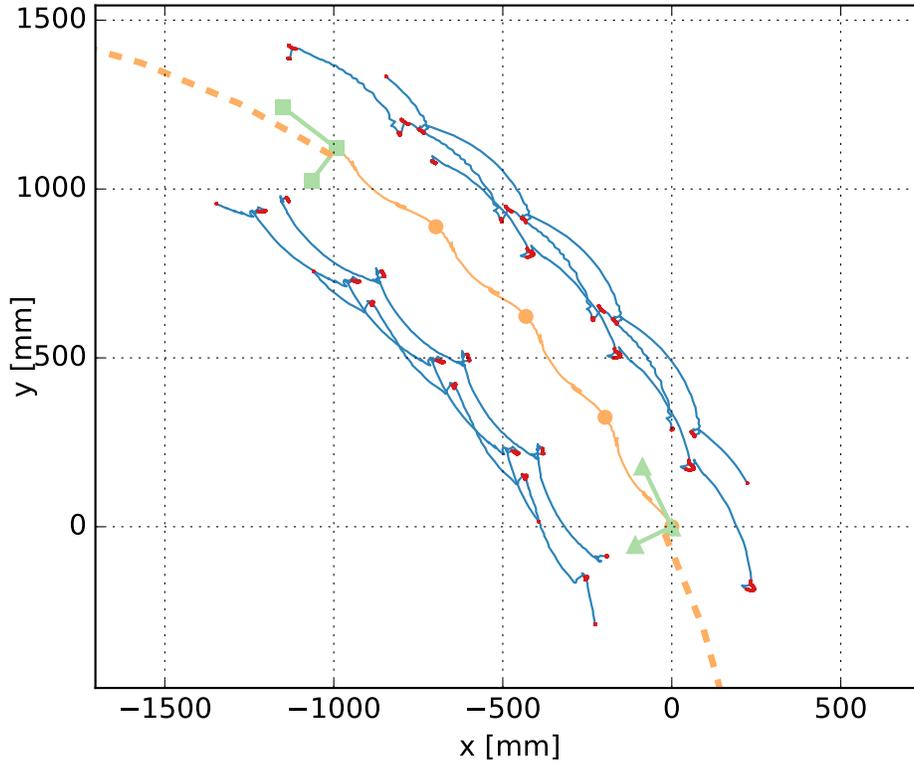
Figure 3.19: Mechapod maximal predicted turning rate non-slip gait. We plotted the trajectories of the feet (solid hairine blue), and highlighted their positions on the ground (red dots). We also plotted the motion of the body frame (green), indicating start position (green triangles), end position (green squares), position at start of each cycle (yellow circle), position over time (yellow line), and best-fit circular arc (dashed thick yellow line). The robot walked 4 cycles at a frequency of 0.33 Hz. Results show that feet do in fact hardly slip at all. In this trial, Mechapod turns $8.0°/\text{cyc}$ and the turning radius is 2692mm

poses that would cause self-interference (see Figure 3.18). The maximal turning rate this analysis predicted was $8.09°/\text{cyc}$, given the dimensions of the physical Mechapod.

We tested the maximal non-slip turning gait going forward and back on the robot (total of $N = 34$ trials, $N_s = 136$ strides, $N_f = 6.12 \times 10^4$ frames of data; see one such trial in Figure 3.19). Going forward, the robot averaged $6.7°/\text{cyc}$ turning, and going back $9.6°/\text{cyc}$. Thus, on average this gait produced $8.15°/\text{cyc}$ of turning while steering – a very close correspondence to the theoretical prediction of $8.09°/\text{cyc}$. The turning angle difference between forward and backward motion comes from the fact that Mechapod is not perfectly symmetric. Examining the foot motions in the robot body frame (see Figure 3.20) shows that right tripod stance trajectories closely follow the concentric arcs expected from the theoretical analysis in Figure 3.4, whereas left tripod stance motions are far less arced. The robot turned strongly to the left in right tripod steps, and then turned a little back to the right in left tripod steps.
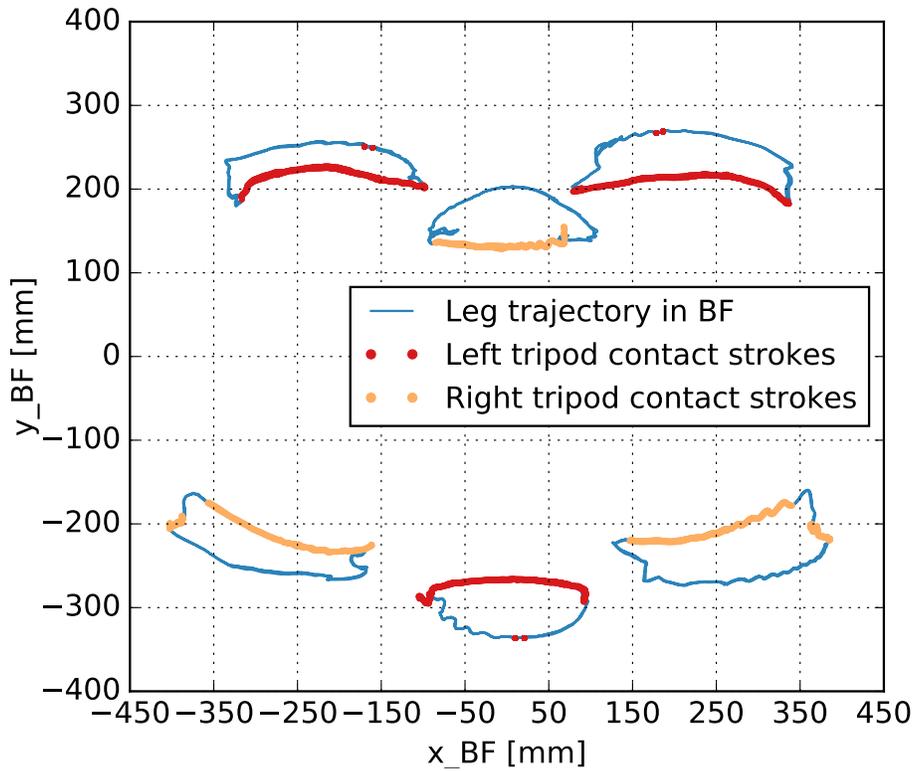
Figure 3.20: Mechapod body frame foot motions from the trial shown in Figure 3.19. Robot moves to the right. We dermined ground contact frames based on the vertical height of the feet from motion tracking. Since the legs are highly elastic, the feet did bounce in an out of contact as shown.

We note an additional complication of using this method to produce non-slip steering: to steer we need a parametric family of gaits controlled by a steering parameter $-1 \leq s \leq 1$ (here ± 1 chosen as limits wlog). This requires being able to solve $\psi_2(t, s)$ and $\psi_3(t, s)$ such that for every value of s we obtain a non-slip motion – thus solving the 4-bar kinematics in real-time. We must then also choose a family of non-slip gaits such that $[\psi_2(0, s), \psi_3(0, s)]$ traces a path from the extremal left turn at $s = -1$, through a no-turning gait at $s = 0$, and finally to e.g. $s = 1$ for the extremal right turn. Ideally, this path should be chosen such that the turn angle is proportional to s. While of these additional steps are straightforward to implement, the goal of the current investigation was to compare non-slip steering and steering which employs slipping.

3.6.2 Mechapod steering gaits with slipping

As an alternative to producing a non-slip steering gait, we explored steering the tripod gait with various modulations. The gait we employed was of the form:

$$
\begin{aligned}
\psi_1 = -\psi_4 = \psi_7 &:= A_{\text{roll}} \sin(\phi) \\
\psi_2 = -\psi_6 &:= A_{\text{yaw1}} \cos(\phi) \\
\psi_3 = -\psi_5 &:= A_{\text{yaw2}} \cos(\phi)
\end{aligned}
\tag{3.5}
$$

We then introduced two types of modulation "spine twist" where all roll motors were given a constant offset to the same side causing the robot to lean to one side, and "spine bend" where all yaw motors were given a constant offset to the same side causing the neutral shape of the spine to be bent along an arc (see Figure 3.21). These modulations were introduced as follows: the updated motor angles $\psi_i'(\phi, s)$ were given by $\psi_i'(\phi, s) = k_{\text{twist}}s + \psi_i(\phi)$ for $i \in \{1, 4, 7\}$, and $\psi_i'(\phi, s) = k_{\text{bend}}s + \psi_i(\phi)$ for $i \in \{2, 3, 5, 6\}$. This allowed us to introduce various combinations of bending and twisting, and test their efficacy at producing steering.

As expected, making either k_{twist} or k_{bend} non-zero produced reliable steering gaits. We presented various combinations of bending and twisting in [Zhao and Revzen, 2016, Zhao et al., 2015]. The effect of bending ($k_{\text{bend}} > 0$) followed intuition quite well – when the spine was bent, the robot turned around a center of rotation on the inside of the average arc of the spine (although not around the center of the spine's arc). Twisting ($k_{\text{twist}} > 0$) produced even better steering performance, where leaning to the left caused the robot to steer right; the mechanism of this steering result remains somewhat unclear.

We investigated the twist-based steering gait for the Mechapod using similar analyses to those used for BigAnt (see figs. 3.23, 3.22, and 3.23). Table 3.3 gives the corresponding quantitative steering performance and slipping metrics.
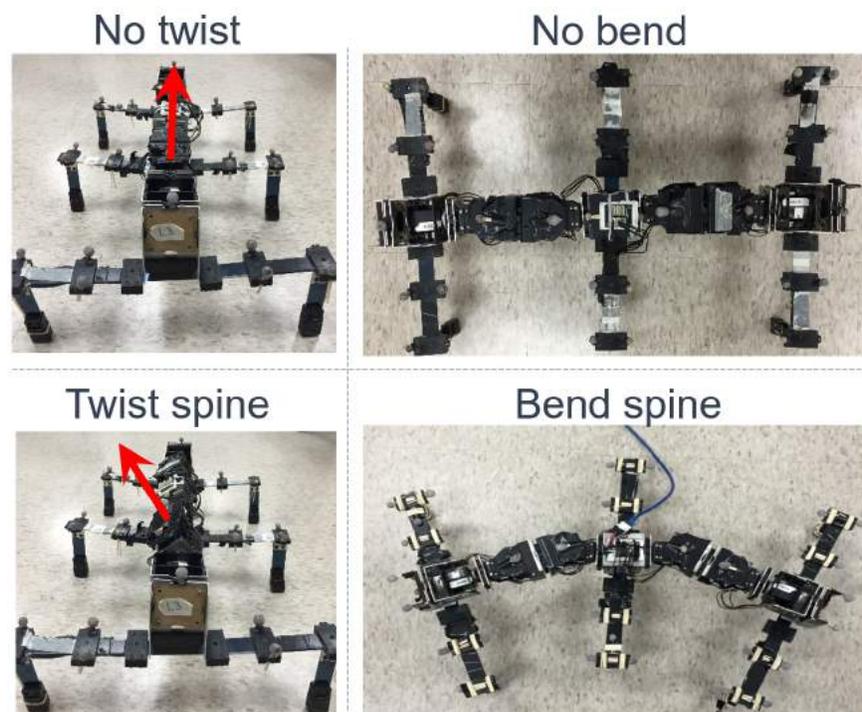
Figure 3.21: Mechapod neutral position and its modulation for steering. When the Mechapod is moving without turning, its shape oscillates around the shapes shown in the top row. By adding spine twist, the spine leans on average (bottom left); by adding spine bend, the spine is arced on average (bottom right).
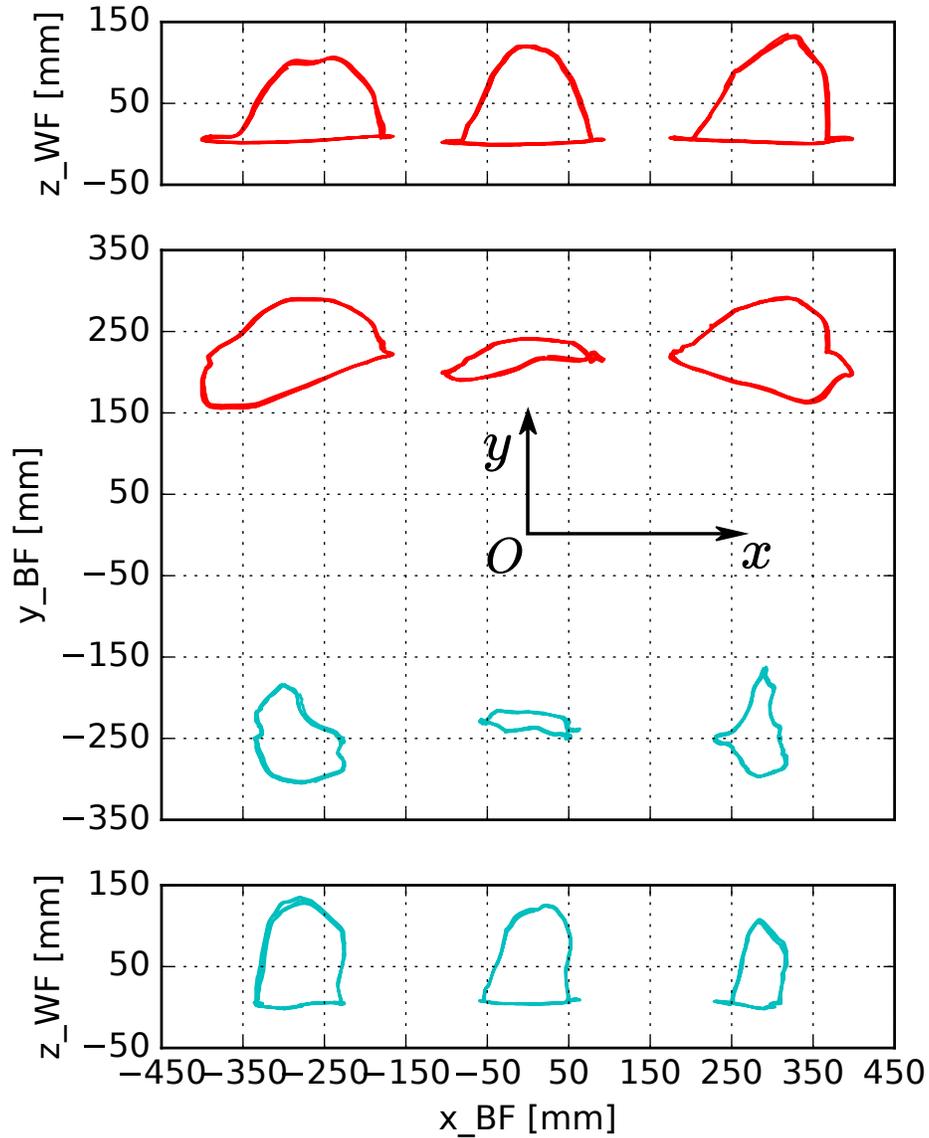
Figure 3.22: Foot motions in body frame x, y and world z for trial in Figure 3.23. We plotted the motion of the left legs (top subplot, red in middle subplot), and the right legs (bottom subplot, teal in middle subplot). The twist-based steering gait produced shorter ground strokes on the right than on the left, commensurate with a turn to the right.
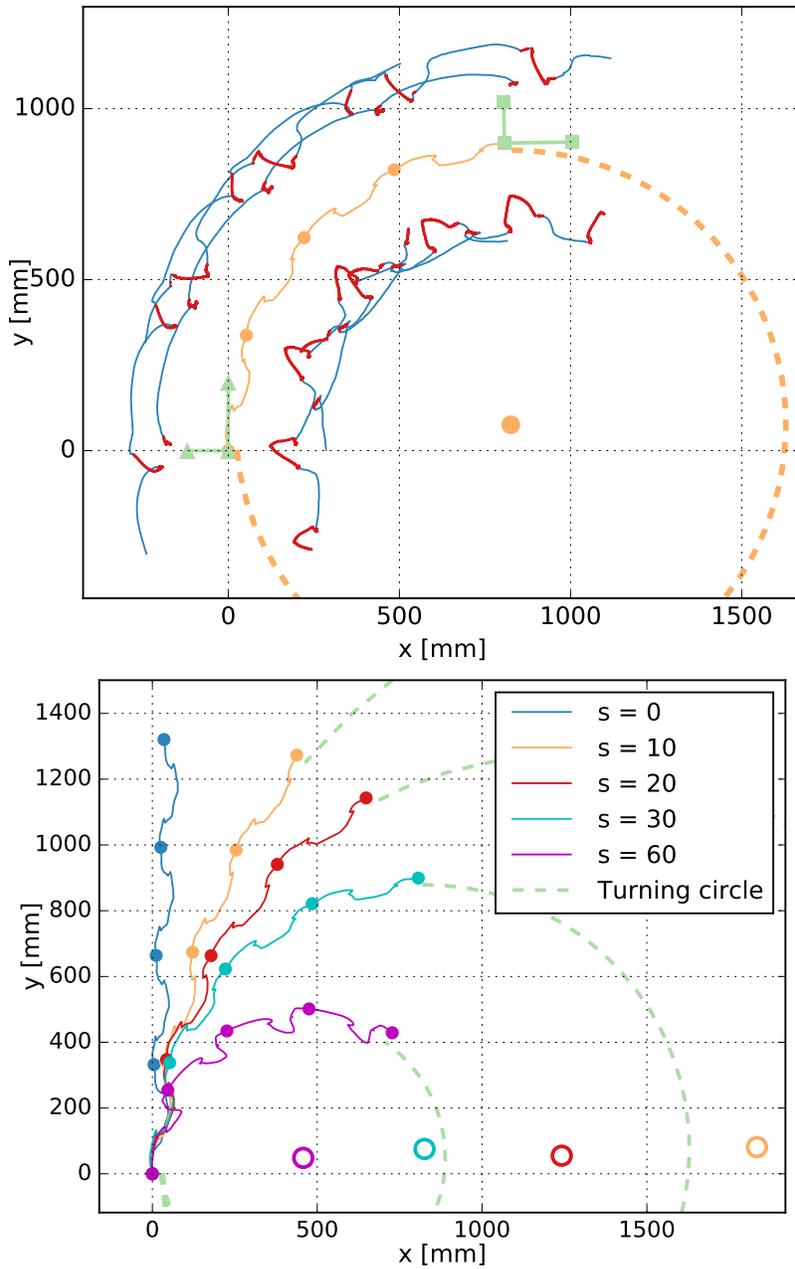
Figure 3.23: Mechapod motions with $k_{\text{twist}} = 1, k_{\text{bend}} = 0, s = 30°$ (left) and twist gait on low friction surface, for $s = 0, 10, 20, 30, 60[°]$ (right).We plotted the trajectories of the feet (solid hairine blue), and highlighted their positions on the ground (red dots). We also plotted the motion of the body frame (green), indicating start position (green triangles), end position (green squares), position at start of each cycle (yellow circle), position over time (yellow line), and best-fit circular arc (dashed thick yellow line). The robot walked 4 cycles at a frequency of $0.33\,\text{Hz}$ and turned $22.3°/\text{cyc}$, for a turning radius of $860\,\text{mm}$. Results show that feet slipped a great deal. For other values of $s = 0, 10, 20, 30, 60[°]$ we plotted (right) location of body frame (solid) with COM after each cycle (solid circles), best fit turning arc (green dashed) and center of rotation (open circle).

Table 3.3: Steering and slipping results for trials in Figure 3.23. Slip in this table are averaged by leg then by gait cycle.

s [°]	°/cyc	R [mm]	Slip [mm/cyc]	Slip ratio
10	8.1	1802	129	26.5%
20	14.2	1312	133	26.9%
30	22.3	860	138	29.2%
60	32.8	437	186	36.2%

The largst twist steering parameter we used was $s = 60°$. With this value, the Mechapod turned approximately $33°/$cyc, about $\times 4$ better than the best non-slip steering performance. This turning rate is far better than BigAnt and the robots investigated by Zarrouk et al. [2015]. It is also worth noting the slip ratios at approximately 36%, almost double that of cockroaches.

3.7 Conclusion and discussion

Multi-legged robots are not in common use, despite their inherent stability and the mechanical robustness that can be achieved with three or more legs contacting the ground at once. Two factors that might be limiting their deployment are the mechanical complexity of building many multi-DoF legs, and the difficulty in understanding and planning for the multi-contact regimes that arise when these robot morphologies are employed. The first factor can be addressed by using legs with only 1 or 2 DoF each, and this category of robots was the topic of our study here. We presented two hexapedal robots with 6 and 7 motors respectively. The 6 motor BigAnt has 1-DoF legs; the 7 motor Mechapod has, for all practical purposes, 2-DoF legs.

Under the assumption that we wish, at minimum, to steer the robots on a horizontal plane, we showed how these appealing low-complexity morphologies raise unique problems related to multi-legged locomotion in general, and underactuation in particular. We showed that for the robots in question, there exist natural ways to produce steering, and illuminated some of the special relationship between bilateral symmetry and steering. We showed that the best steering gaits we produced do not obey the non-slip contact conditions robot designers usually employ in planning. For the BigAnt, non-slip conditions would have precluded turning altogether. For the Mechapod, non-slip gaits do exist, but under-perform *ad-hoc* steering gaits we tried by a factor of $\times 4$.

The careful examination of mechanism of turning in both BigAnt and Mechapod lead to some surprising results. The relationship between Mechapod shape modulation and steering outcome proved difficult to elucidate. More interestingly, BigAnt motions proved to be independent of speed and friction coefficient, suggesting that a geometric theory similar to that which governs slithering

snake robots [Gong et al., 2016] might be applicable. An initial foray into how the viscous-friction-like relationships of geometric mechanics arise from simple Coulomb friction models can be found in our recent publication Wu et al. [2019].

Taken together this evidence suggests that design of multi-legged robot gaits raises some new issues related to phase, but effective solutions for steering are not hard to find, and do not require the full complexity of 3 or more DoF per leg. The key issue is that steering gaits, and by extension, other high-performance maneuvers, must assume that slipping will invariably take place, and be an integral part of the planned motion. This does not, however, imply that multi-legged maneuvers require knowledge of friction coefficients or planning in the full phase space, as some might have assumed. At least for our robots, it seems that some kind of geometric mechanics theory is lurking just around the corner, and with it we will be able to reap the benefits of simple and robust multi-legged robot morphologies.

One obvious important direction of future investigation is developing and validating physics codes for multi-legged locomotion which can handle the persistent slipping that we have discovered to be necessary for effectively steering our robots. Besides building better models that include slipping, another interesting approach is to explore the potential of non-slip gaits with low-DoF legs. We have shown that Mechapod can have non-slip steering gaits with only 7 motors; perhaps other low DoF per leg designs can be produced which have better steering performance. Yet another important direction to explore is the high-speed limit: how do the approaches we studied here extend as robots move faster, inertia plays a larger role, and power rather than torque limits the motors?

CHAPTER 4

Geometric Analysis and Modeling of Multi-legged Locomotion

4.1   Motivation and contribution

In a study of a complicated system and its behavior, people usually try to construct a model to represent the original subject. Models are usually built based on direct observations, summarized characteristics, first principle physics and math, or structure/parameter identifications. A good model can then be used to analyze and predict the behavior of the original system. For robots, models are useful for the planning and control of their motions. Therefore, the basic motivation of this chapter is to explore methods that can be used to model multi-legged locomotion for better planning and control of multi-legged robots.

Conventional models for legged locomotion, especially for bipedal and quadrupedal robots, usually assume that no slipping happens between the robot's foot and the ground for their motion analysis and control. This assumption or control objective is reasonable for such under-constrained systems with high-DoF legs but a low number of contacts with the environment, since they have enough motion freedom to avoid slipping as slipping itself can cause motion instability within such systems. However, from our studies in previous chapters, we showed that slipping happens and is also inevitable for low-DoF multi-legged locomotion for improving its maneuverability on the 2D horizontal plane.

Besides slipping, another challenge for modeling low-DoF multi-legged robots is their multiple contacts with the environment during locomotion. Realistic leg-ground contact alone can be a complicated problem regarding collision and slipping [Remy, 2017]. Multiple contacts plus slipping makes this issue even more severe since the distribution of internal forces between multiple supporting legs is usually impossible to calculat from previous motion and actuation forces. In other words, which legs will slip and the extent to which they slip are both hard to calculate from history states and current inputs, which makes it very difficult to predict robot motion. One possible solution is full state force sensing on each robot foot to measure the 6-dimensional force

wrench at ground contact, which can be then fed into full body dynamics to calculate robot acceleration. However, this kind of sensing is usually hard to implement and measuring accuracy is also hard to guarantee, especially for low-DoF multi-legged robots which need legs that are simple and light in construction. In conclusion, modeling multi-legged locomotion is a challenging problem and research about this topic could fill an important gap in this area.

Despite the modeling challenge from multi-contact and slipping, we still see hope from our experimental study of multi-legged locomotion. By examining the locomotion characteristics of different multi-legged systems from cockroaches to our robots, we find that even though there is slipping involved, these multi-legged motions turned out to be surprisingly geometric[1] rather than dynamic as has been traditionally understood. For example, from the BigAnt steering summary Figure. 3.13, we saw that turning angle per gait cycle (a geometric property) does not depend on gait frequencies nor the ground friction condition. Previously, geometric motions were usually observed in the systems like low Reynolds number swimmers and non-holonomic wheeled snake robots which have continuous contact with the environment. Legged locomotion with piecewise holonomic constraints (no slip condition) can also be geometric. As far as we aware, this is the first time people have observed geometric motion for legged locomotion with slipping on solid surfaces. These geometric characteristics provide us with a new perspective to understand and model multi-legged locomotion with slipping.

In this chapter, we first introduce some background about conventional models for legged systems and basic foundations about geometric motion. I then refer to our geometric analysis for the locomotion results from experimental studies of multi-legged systems. Two modeling strategies inspired by geometric characteristics are then demonstrated: one is for data driven geometric models and the other is for models built from first principle physics. Model based simulation results are also included in these sections.

4.2   Background and introduction

4.2.1   Classical models of legged locomotion

Classic modeling strategies for bipedal and quadrupedal animals and robots usually assume that no slip happens or make nonslip a control objective. In these models, the interaction between the stance legs and the ground is a unilateral holonomic constraints. For example, the famous animal template models SLIP (spring loaded inverted pendulum) and LLS (lateral leg spring) [Full and Koditschek, 1999, Holmes et al., 2006, Dickinson et al., 2000] assumed there was no slip be-

---

[1]"Geometric" is used as a terminology here to describe the system motion that is governed by first order equation, ie. system speed in world frame is proportional to the speed of system shape change(eg. speed of leg joint rotation).

tween supporting legs and the ground. Seipel and Holmes [2007] did consider slipping in their CT-SLIP model, but it has only one contact by grouping multiple contacting legs into one. Proctor and Holmes [2018], Proctor et al. [2010], Kukillaya et al. [2009] adopted a simplified rigid body model which included all 6 legs of cockroaches but did not consider leg slipping. Roboticists have access to precise rigid body models of the parts of their robot, and that is popularly used for gait design/analysis and motion control/planning [Remy, 2011, Gregg et al., 2014, Fahmi et al., 2020, Gan et al., 2016]. Both modeling strategies provided significant scientific insights and sophisticated engineering applications for legged locomotion, but did not consider multi-legged contacts with slipping.

4.2.2 Geometric mechanics and modeling

4.2.2.1 Introduction of geometric mechanics

In the field of geometric mechanics, the motion equations of nonholonomic systems are constructed in a *reduced form* using dynamic constraints and group symmetries [Bloch et al., 1996, Cendra et al., 2001]. The dynamic constraints are usually derived from Lagrangian or Hamiltonian conservation laws, while group symmetries typically extend from the homogeneity of the environment to remove the dependence of robot dynamics on the robot position in the environment. In the case that the symmetry group is the group of rigid transformations, the symmetry expresses the fact that a system's interactions with a uniform environment do not depend on its position and orientation in that environment. The system motion equations can then be written in the form of a *reconstruction equation* [Ostrowski and Burdick, 1998]:

$$g^{-1}\dot{g} = A(r)\dot{r} + \mathrm{I}^{-1}(r)p \tag{4.1}$$

$$\dot{p} = f(r, \dot{r}, p) \tag{4.2}$$

where $g \in \mathsf{SE}(2)$ or $g \in \mathsf{SE}(3)$ is the group of rigid transformations; $g^{-1}\dot{g}$ then represents the velocity of the system's body frame of reference; r is the internal shape w.r.t. the body frame; p is the generalized momentum; $\mathrm{I}^{-1}(r)$ is usually called momentum distribution function. There are other similar forms of *reconstruction equation* with detailed expression for function $f(r, \dot{r}, \dot{p})$ in certain application circumstances developed by the geometric mechanics community ([Bloch et al., 1996, Cendra et al., 2001, Ostrowski and Burdick, 1998, Shammas et al., 2007]). *Reconstruction equation* is a formal tool for us to express the intuition that symmetry in the environment should allow motion equations to be written relative to the body frame. It also suggests that the influence on body frame motions can be separated into two factors: a kinematic contribution ($A(r)\dot{r}$) and a

momentum contribution $(\mathrm{I}^{-1}(r)p)$. Especially, in the case that one of these factors dominates the other, we can achieve strong insights about the key features of the locomotion for modeling.

A subsequent reduction based on the reconstruction equation can be achieved for zero momentum systems. With momentum gone, the motion equation further downgrades into a *mechanical connection* [Marsden and Ostrowski, 1998] that linearly maps internal shape velocities to body velocities of the system:

$$g^{-1}\dot{g} = A(r)\dot{r} \tag{4.3}$$

where $A(r)$ is the *local connection*. Equation 4.3 is also called *kinematic reconstruction equation* by some people. We prefer to calling Equation 4.3 *geometric connection equation* to emphasize that we use it to define whether a system motion is geometric. Based on how the zero-momentum condition is achieved, this class of systems includes: (1) systems with no initial momentum operating under momentum conservation laws, such as the floating astronaut in Marsden and Ostrowski [1998], the pivoting dynamic robot in Shammas et al. [2007] and the high Reynolds swimmer in Hatton and Choset [2013]; (2) systems with linear nonholonomic velocity constraints[2] and their momentum variables are totally annihilated by the constraints, such as the snake robot in Shammas et al. [2007]; (3) systems with non-conservative forces that are large enough to dominate system dynamics and "quickly" dissipate the momentum to zero, such as the small swimmers in low Reynolds environments [Hatton and Choset, 2013].

These geometric mechanics tools were primarily used to study the motion of nonholonomic systems such as the rolling disk [Bloch et al., 1996], snakeboard [Ostrowski and Burdick, 1998, Ostrowski, 1996], and a variety of wheeled snake-like robots [Ostrowski and Burdick, 1998, Shammas et al., 2007] and multi-linked serpent-like swimmers [Hatton and Choset, 2013, Dai et al., 2016, Bittner et al., 2018]. The common feature shared by all these systems is that they all have continuous contact with the environment, while we discovered that multi-legged locomotion with slipping which has discontinuous contact with environment can also be geometric. Parallel to our studies, there is a research project about using geometric mechanics technique to model a quadrupedal robot walking on granular media [Aydin et al., 2017].

4.2.2.2 Modeling geometric systems

We define systems whose motion can be described by Equation 4.3 to be geometric systems. The body velocities of these systems are linearly mapped from their internal shape velocities. The key point of modeling such systems is to determine the *local connection $A(r)$*.

---

[2]Usually defined as "Pfaffian constraints". For systems with environmental symmetries, Pfaffian constraints are often expressed in the body frame. (e.g., no sideways slipping for wheels)

For low Reynolds number swimmers, Hatton and Choset [2013] assumed the drag forces on each swimmer link are linear functions of the body velocities and used force/moment balance to calculate the local connection. For high Reynolds number swimmers, Hatton and Choset [2013] adopted the momentum conservation law to obtain the geometric reconstruction Equation. In a study of tetrapod locomotion on granular media, Aydin et al. [2017] applied the resistive force theory for granular media to numerically approximate the local connections by differentiating the force balance equation.

While the systems we mentioned above are non-holonomic, it should be noted that holonomic or piecewise holononic systems are always geometric [Revzen et al., 2021]. The connection naturally arises from the Jacobian matrix which is the derivative of body frame position w.r.t. shape (or configuration, for classical robot systems). For example, examine the ability of a robotic manipulator to move and orient its own center of mass[3]. There is typically a map $F : \mathcal{Q} \to \mathsf{SE}(3)$ from the configuration parameters describing the shape of the robot $r \in \mathcal{Q}$, to the body frame $g \in \mathsf{SE}(3)$ given by $g = F(r)$. The geometric motion in this case can be studied using the Jacobian J_F of F. The "local connection" $A_F(r) := (F(r))^{-1}J_F(r)$ follows by deriving the body velocity $v_b \in \mathfrak{se}(3)$: $A_F(r)\dot{r} = v_b = (F(r))^{-1}J_F(r)\dot{r}$ (where we assumed notation a standard matrix Lie group representation for $\mathsf{SE}(3)$).

For piecewise holonomic systems such as fully actuated legged robots with non-slip gaits, there exists an $F[c] : \mathcal{Q} \to \mathsf{SE}(3)$ for every continuous set of contacts $c \in C$ out of a finite set of contact combinations C. If any one of the contact combinations is maintained, no locomotion is possible because of holonomy. However locomotion is possible, because the change in contacts involves a change of $F[c]$. Here the local connection allows for a concise and precise representation using $A_{F[c]}(r) := (F[c](r))^{-1}J_{F[c]}(r)$. This function has a jump discontinuity when c changes, but it allow us to model locomotion using the equation $g^{-1}\dot{g} = A_{F[c]}(r)\dot{r}$, which produces continuous solutions in the body frame g. In essence, piecewise holonomic motions have a local connection comprising pieces, each of which is derived from the Jacobian of a different set of holonomic constraints.

4.2.3 Geometric analysis of motion

The systems introduced in previous sections are mostly models with assumptions (linked bar swimmers) and real systems with apparent constraints and behavior patterns (snake board and wheeled snake-like robots). Their geometric characteristics are usually discussed systemwise. However, the multi-legged systems we are studying are real robot platforms which have variable behaviors

---

[3]We tacitly assume a CoM attached "body frame"; the proper selection of such a frame is non-trivial Hatton and Choset [2011].

and complicated interactions with the environment. For example, some gait patterns are intrinsically dynamic, such as the BigAnt turn in place gait introduced in Section 2.2.7.4 which has two legs supporting the robot body. Also, some gaits can lead to geometric motions in lower gait frequencies, while they result in more dynamic motions in higher gait frequencies when momentum influence starts to dominate. Therefore, the geometric characteristics of multi-legged systems need to be studied behaviorwise instead of systemwise. We name the method of analyzing whether a behavior of a system is geometric as "Geometric Analysis" in this thesis. Based on detailed engineering application purpose, the geometric analysis is performed in two ways: instantaneous geometric analysis and average geometric analysis.

4.2.3.1 Instantaneous geometric analysis and phase driven model

A behavior for legged systems is also referred as a gait. As introduced in Section 3.3.1, a gait can be represented as a function $r(t)$ which maps time to system shape space. For real experiments, the tested behavior inputs are functions $r(t)$, which come from a low-dimensional parameter space and therefore span low dimensional manifolds in the full shape space. Our tested behaviors on multi-legged robots are all periodic gaits as introduced in previous sections, and so both system body velocity $V_B = g^{-1}\dot{g}$ and shape inputs $r(t)$ can be written as functions of system phase ϕ. Furthermore, the geometric connection equation Equation 4.3. can be written in the following form:

$$g^{-1}\dot{g} = A(r(\phi(t)))\frac{dr}{d\phi}f \qquad (4.4)$$

where $f = d\phi/dt$ is the gait frequency. Therefore, to check whether the in-cycle system motion is strictly geometric, we can compare whether the normalized body velocity $V_{BNorm}(\phi) = V_B(\phi)/f = g^{-1}\dot{g}/f$ is the same phase signal[4] for different gait frequencies f. We name this check as the instantaneous geometric analysis and name $V_{BNorm}(\phi)$ as the phase driven geometric model for a periodic gait $r(\phi)$. The phase driven geometric model is a kind of data driven model from experiment results. The performance of the phase driven model evaluated on test trials is also used as a quantitative metric to assess how close the system motion is to instantaneous geometric.

As introduced in Chapter 3, the motion of multi-legged robots we care most about is the planar motion on the 2D horizontal plane ($g \in \mathsf{SE}(2)$). In this case, the body velocity can be written as a 3-dimensional vector: $V_B(\phi) = [V_{Bx}(\phi), V_{By}(\phi), V_{B\theta}(\phi)]$, whose 3 coordinates correspond to system CoM velocity V_{CoM} projected to body frame x and y axes, and the angular velocity $\dot{\theta}$ of body frame respectively. Since we always place the body frame x axis in the direction from robot/animal tail to head (sagittal direction) and body frame y axis in the system from right to left

---

[4]The phase signal here is equivalent to the time series signal of body velocity aligned by system phase ϕ

(lateral direction), V_{Bx} then represents forward/back velocity and V_{By} represents lateral velocity w.r.t. the system body frame.

4.2.3.2 Average geometric analysis and mean value model

When planning robot motion to navigate through the environment, we usually run the robot in integer numbers of gait cycles and use the motion generated by a gait cycle as a unit motion step. In this case, it is useful to know whether this unit motion step is independent of gait frequency. If so, the planning problem will be much easier. The system motion Δg in 2D case after a gait cycle can be written as:

$$\Delta g = g(\phi + 2\pi)g(\phi)^{-1} = \begin{bmatrix} \cos(\Delta\theta) & -\sin(\Delta\theta) & \Delta x \\ \sin(\Delta\theta) & \cos(\Delta\theta) & \Delta y \\ 0 & 0 & 1 \end{bmatrix} \tag{4.5}$$

Here the system motion is represented as the displacement and rotation angle in world frame as Δx, Δy and $\Delta\theta$, as depicted in Figure. 3.2. We name the analysis to check whether Δg stays the same for different gait frequencies f as *average geometric analysis*.

For analysis of experiment data, we use *geometric properties*: distance travelled per gait cycle by system CoM (we use *dist/cyc* for abbreviation) and turning angle of the body frame per gait cycle (we use *ang/cyc* for abbreviation). Dist/cyc is equivalent to $\sqrt{\Delta x^2 + \Delta y^2}$ and can be directly sampled from system CoM trajectories in the world frame. Ang/cyc is $\Delta\theta$ and can be calculated from body frame pose change. For experiment tests of a gait pattern $r(\phi)$ with different gait frequencies $\{f_i\}$, there is a list of {dist/cyc} and a list of {ang/cyc}. If elements in each list are the same or close to each other, the locomotion generated by the gait pattern is regarded as geometric on average. The mean value of each list is then defined as the mean value model of this gait pattern, which is also the unit motion step for motion planning. The mean value model is also a kind of data driven model.

4.2.3.3 Discussion of geometric analysis

Geometric analysis is proposed to check whether the system motion from experiment tests is geometric. Real experiment data does not give perfect geometric motion because of residual dynamic effects and other kind of noises. We are checking how close the locomotion is to being geometric. The data driven model itself is both a result and a tool. It is a result that can be used to predict motion in planning, while it is also a tool to check how geometric the motion is by evaluating the model prediction errors. When the prediction errors from these data driven models are smaller than some thresholds, we regard the tested motion to be "geometric".

Being instantaneously geometric means that the motion fulfils the definition of geometric motion in Equation 4.3 and 4.4. It directly implies the motion being geometric on average, but it is more complicated to perform and needs velocity calculation from experiment sensing data. Being geometric on average is a necessary condition for being instantaneously/strictly geometric but it is not a sufficient condition. However, it is easier to perform by statistics analysis directly from the experiment position results and can act as a quick pre-check for further instantaneous geometric analysis. An average geometric analysis is also adequate for motion planning purposes in navigating through large environments.

Different gait patterns $r(\phi)$ lead to locomotions that have different levels of being geometric. For instance, some can stay in a geometric region with a larger frequency range while some can only stay in a geometric region with a smaller frequency range. Based on the zero-momentum condition applied to the reconstruction equation as introduced in Section 4.2.2.1, there exists some gait frequency limit within which any multi-contact gait pattern $r(\phi)$ in the shape space can lead to geometric motion. The geometric properties can then be discussed as being close to fully systemwise but this gait frequency limit could be too small to be used for realistic motion planning.

4.3 Average geometric analysis

As introduced in Section 4.2.3, geometric motion can be interpreted from two aspects: instantaneously geometric or geometric on average. In many cases, geometric on average properties are enough for motion planning of mobile robots which usually navigates through a much larger environment space than the robot shape space. The key geometric property examined in this section for analyzing geometric phenomena is dist/cyc. Constant dist/cyc for a range of gait frequencies directly leads to the linear relationship between average system body velocity and average shape velocity (equivalent to gait frequency), which indicates the system translational motion is geometric on average.

In this section, we introduce the average geometric property analysis for multi-legged systems we tested: BigAnt, Multipod and cockroach, to check whether their motion can be regarded as geometric on average.

4.3.1 Average geometric analysis for BigAnt robot

In this section of analyzing BigAnt motion, we also examined another geometric property besides dist/cyc, which is the turning angle (orientation change) per gait cycle (we use ang/cyc for abbreviation). Similar to dist/cyc, constant ang/cyc for a range of gait frequencies directly leads to the linear relationship between average system body angular velocity and shape velocity, which
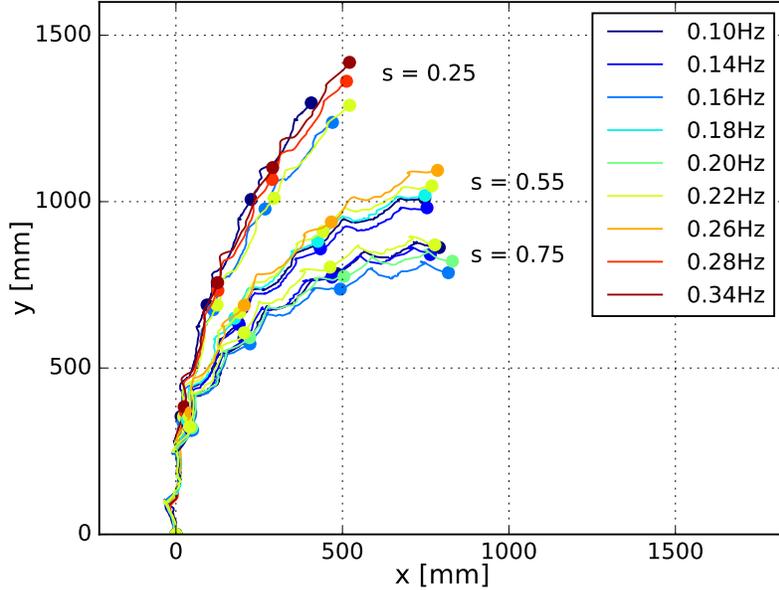
Figure 4.1: CoM trajectories of BigAnt for 3 different steering inputs (s=0.25,0.55,0.75 as labeled) and 9 different gait frequencies shown in different colors (gait frequency increases as color changes from cold to warm). Within each CoM trajectory, the beginning and the end of each gait cycle are highlighted by dot markers. 4 cycles of gait were recorded for each trial.

Table 4.1: Statistics mean and RMSE (Root Mean Square Error) of dist/cyc compared to the mean value model for all BigAnt test trials (75 samples for each steering input).

Steering input	$s = 0.25$	$s = 0.55$	$s = 0.75$
Dist/cyc mean [mm]	361	347	327
Dist/cyc RMSE [mm]	19	11	8.5
Relative RMSE	5.2%	3.3%	2.6%

indicates the system rotation motion is geometric on average.

In Section 3.5.3, when we experimentally tested BigAnt steering gaits, we observed that ang/cyc of BigAnt motion is close to constant and does not depend on gait frequencies from Figure 3.13, which shows BigAnt rotation motion in these tests is close to geometric on average. This observation is also an important motivation for us to start to look at multi-legged locomotion from a geometric mechanics perspective.

Here we investigate the 15 trials of steering tests performed on Robot 1 in Figure 3.13. The detailed parameter setup is summarized in the caption of Figure 4.1. The gait inputs for each steering parameter took the same shaft angle-phase profile (as shown in Figure 3.6), but were run in different frequencies. From Figure 4.1 which depicts BigAnt CoM trajectories of these tests, we can see that the BigAnt motion mainly depended on the 3 steering parameters (3 cluster branches)

Table 4.2: Statistics mean and RMSE (Root Mean Square Error) of ang/cyc compared to the mean value model for all BigAnt test trials (75 samples for each steering input).

Steering input	$s = 0.25$	$s = 0.55$	$s = 0.75$
Ang/cyc mean [deg]	10.9	20.3	23.7
Ang/cyc RMSE [deg]	0.9	1.2	1.2
Relative RMSE	8.7%	6.0%	5.2%

while the gait frequency had limited influence (difference within each branch). The final CoM positions with the same steering input but different gait frequencies may seem slightly diverged from each other, but we also need to acknowledge that experimental data is exposed to noises and the final position is the accumulation of 4 gait cycles. If the system is perfectly geometric with the ideal experiment condition, the final positions of different gait frequencies should be the same.

Beside qualitative observations of CoM trajectories, we also perform quantitative analysis about the geometric properties of dist/cyc and ang/cyc for these BigAnt motions. The corresponding results are presented in Figure.4.2. Both of these two geometric properties show very small change w.r.t. gait frequency for all 3 steering inputs. Dist/cyc indicates a tiny uptrend which may come from the small residual inertial effect as gait frequency increases, while turning angle per cycle almost stays the same within a 3.5x frequency range (0.10-0.34 Hz).

We consider a model to be the mean value of the geometric property given certain steering gaits. For all gait frequencies, the relative errors of dist/cyc and ang/cyc from the mean value model prediction (labeled above each boxplot bin in Figure 4.2) are mostly within $\pm 6\%$. More statistics analysis for the mean value model are recorded in Table 4.1 and Table 4.2, which also indicate that the errors are small. Based on all these analyses, we can conclude that the geometric properties: dist/cyc and ang/cyc of the tested BigAnt motion are close to constants. In other words, the BigAnt motion is close to geometric on average in both translation and rotation, i.e. the whole SE(2) planar motion group.

4.3.2 Average geometric analysis for Multipod robots

In the previous section, the analysis showed that the BigAnt steering motion is geometric on average. We also investigated whether such kind of geometric motions can be observed in many other multi-legged systems. For this purpose, the Multipod data set we obtained in Section 2.3.3.2 is analyzed in this section. The Multipod data set contains locomotion behaviors of the Multipod family robots with 6,8,10,12 legs taking 26 kinds of undulatory gaits in 5 gait frequencies ([0.3, 0.6, 1.2, 2.4, 3.0] Hz). Thus, there are a total of 520 ($4 \times 5 \times 26$) experiment trials in the whole Multipod data set. Moreover, Multipod also has a different morphology: it has an articulated spine with
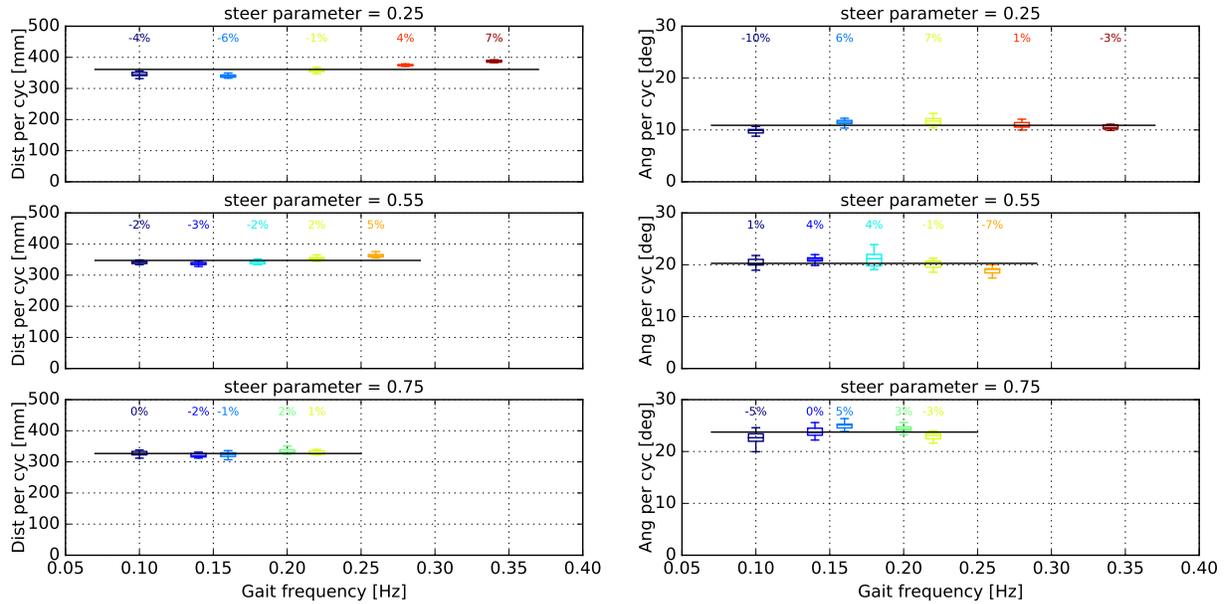
Figure 4.2: Geometric analysis of BigAnt motion: dist/cyc (left) and ang/cyc (right). We randomly bootstrapped 15 samples by a one-period time window on the motion tracked CoM trajectory and body frame orientation to gather the statistics of dist/cyc and ang/cyc respectively for each trial of the test. The statistics of each trial is then represented in a boxplot bin vs. the corresponding gait frequency (the same coloration as Figure 4.1). The statistics mean of dist/cyc and ang/cyc for each steering input is plotted as a horizontal line for reference purposes. To further check the dependence of these two geometric properties wrt. gait frequency, the relative error between the mean of each boxplot bin and the global mean (black horizontal line) is labeled above the corresponding boxplot bin.

compliant legs, while BigAnt has a trunk body attached with 1 DoF rigid legs. All these greatly extend our study scope of multi-legged locomotion. Multipod slips a lot too, which excludes it from piecewise holonomic and makes it the slipping legged system we are interested in. One trial of Multipod motion in the world frame is shown in Figure 4.3 which has slipping part highlighted on the leg trajectories.

For the detailed analysis, we continue checking the geometric property dist/cyc. This time, the analysis of ang/cyc is omitted since all the Multipod motion is walking in a straight line while there is very little turning effect. Besides dist/cyc, we also report a slip ratio[5] of each trial of Multipod motion to show how much the system slips. Slip ratio itself is not an explicit geometric property such as dist/cyc and ang/cyc, but a slip ratio can reveal some implicit information about the robot motion and offer rationale to some motion mechanism.

Figure 4.4 shows two examples of the average geometric analysis for Multipod. The first

---

[5]The term of slip ratio is defined as all the slip distance divided by all the distance travelled by all the legs of the system in the world frame
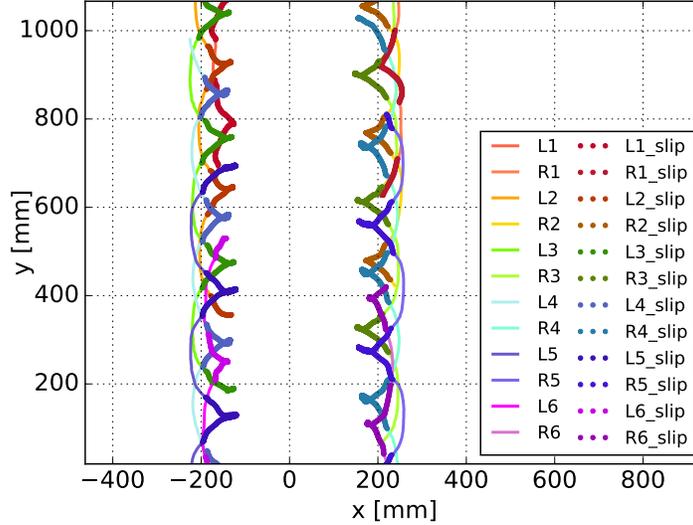
Figure 4.3: World frame leg trajectories of one trial of test from Multipod data set: leg number = 12; phase offset of the undulatory gait $\Delta\phi = 1.35\pi$; gait frequency $f = 0.3Hz$ (refer to Equation 2.4 for detailed gait profile). The slipping parts on the leg trajectories are highlighted by thicker markers with a slightly darker color. Li and Ri in the legend refers to number i th left leg and i th right leg, counting from head to tail.

observation is that Multipod slips significantly in both examples, with the slip ratio larger than 40%. For the motion in the first example (12 legged Multipod taking undulatory gait with 1.20π phase offset), the dist/cyc property is close to a constant value throughout all of the first 4 gait frequencies ([0.3,0.6,1.2,2.4] Hz) and starts to diverge at the highest gait frequency of 3.0 Hz. While for the motion in the other example (10 legged Multipod taking undulatory gait with 1.05π phase offset), the dist/cyc property is close to a constant value for the first two gait frequencies ([0.3,0.6] Hz) and start to diverge from the third gait frequency. These two analysis examples suggest that different Multipod robots (leg numbers) with different undulatory gaits have different levels of average geometric motion. For some behavior, the geometric motion can be kept in a wider frequency range, while for others, the geometric motion can only be achieved in a smaller frequency range.

To further assess the geometric motion for the whole data set of Multipod, the same analysis as in the above examples are performed for all tested trials and the results are summarized in Figure 4.5, which depicts the dist/cyc mean vs. phase offset, RMSE vs. phase offset and the sorted RMSE for the mean value models of different frequency groups. The result RMSE presents no obvious pattern w.r.t the phase offset, so we reorganized these results in a sorted order to compare the influence from leg numbers and frequency groups. The influence of frequency groups on the prediction performance matches our intuition that the Multipod motion in a lower frequency range is more geometric while the motion in higher frequency is more dynamic. Combining the analyzed
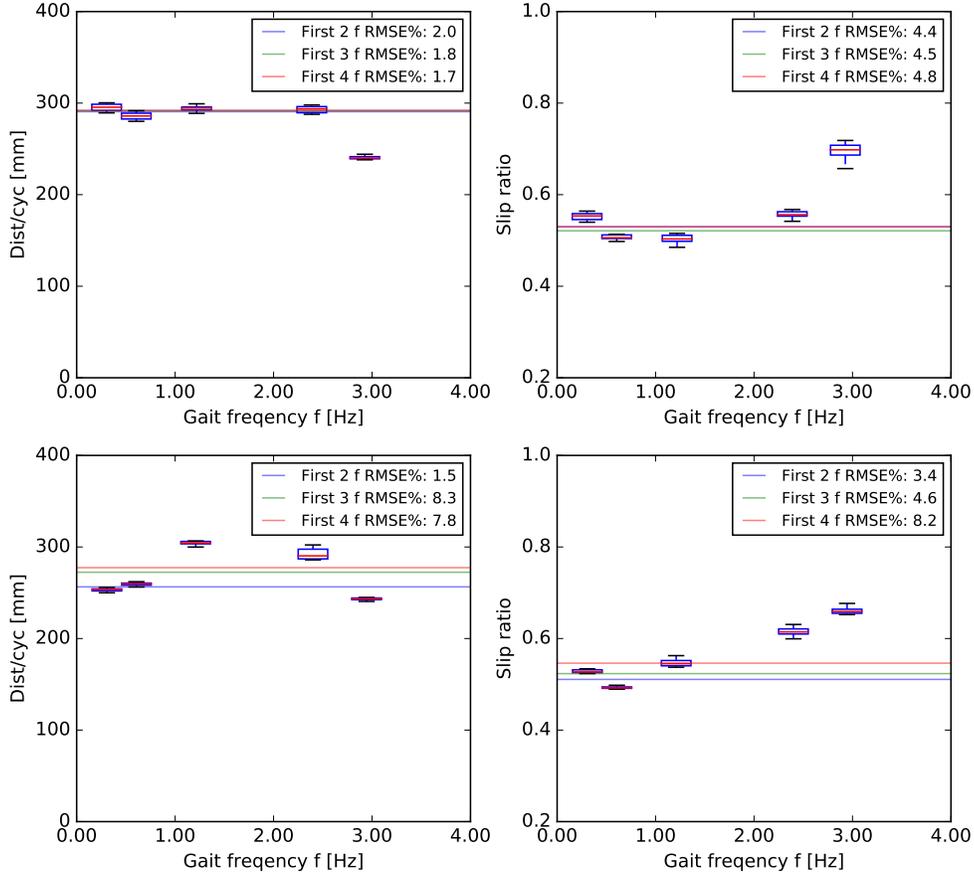
Figure 4.4: Geometric analysis examples of Multipod motion for dist/cyc (left column) and slip ratio (right column). The two rows correspond to the two example trial sets: 12 legged Multipod taking undulatory gait with 1.2π phase offset (top row); 10 legged Multipod taking undulatory gait with 1.05π phase offset (bottom row). Each set contains 5 test trials with 5 different gait frequencies ($f = [0.3, 0.6, 1.2, 2.4, 3.0]$ Hz). We randomly bootstrapped 15 samples by a one-period time window on the motion tracked CoM trajectory and leg trajectories to obtain the statistics of dist/cyc and slip ratio respectively for each test trial. The sampled statistics of each trial is then represented in a boxplot bin positioned by its corresponding gait frequency. The statistics means of dist/cyc and slip ratio that grouped by different gait frequencies, are plotted as horizontal lines: the blue line is the mean of samples from the first two boxplot bins; the green line is the mean of samples from the first three boxplot bins; the red line is the mean of samples from the first four boxplot bins. The relative root mean squared error (RMSE%) of each mean value model is also labeled in the figure legend for reference. The samples from the highest frequency (3.0 Hz) case are not included in any mean value model, since they behaves very differently from all other cases ([0.3,0.6,1.2,2.4] Hz) throughout the data set and we consider them to be out of the geometric region.

results in Table 4.3 and Figure 4.5, we can conclude that with more legs, the tested Multipod locomotion is closer to being geometric on average and can keep such geometric property in a larger frequency range.
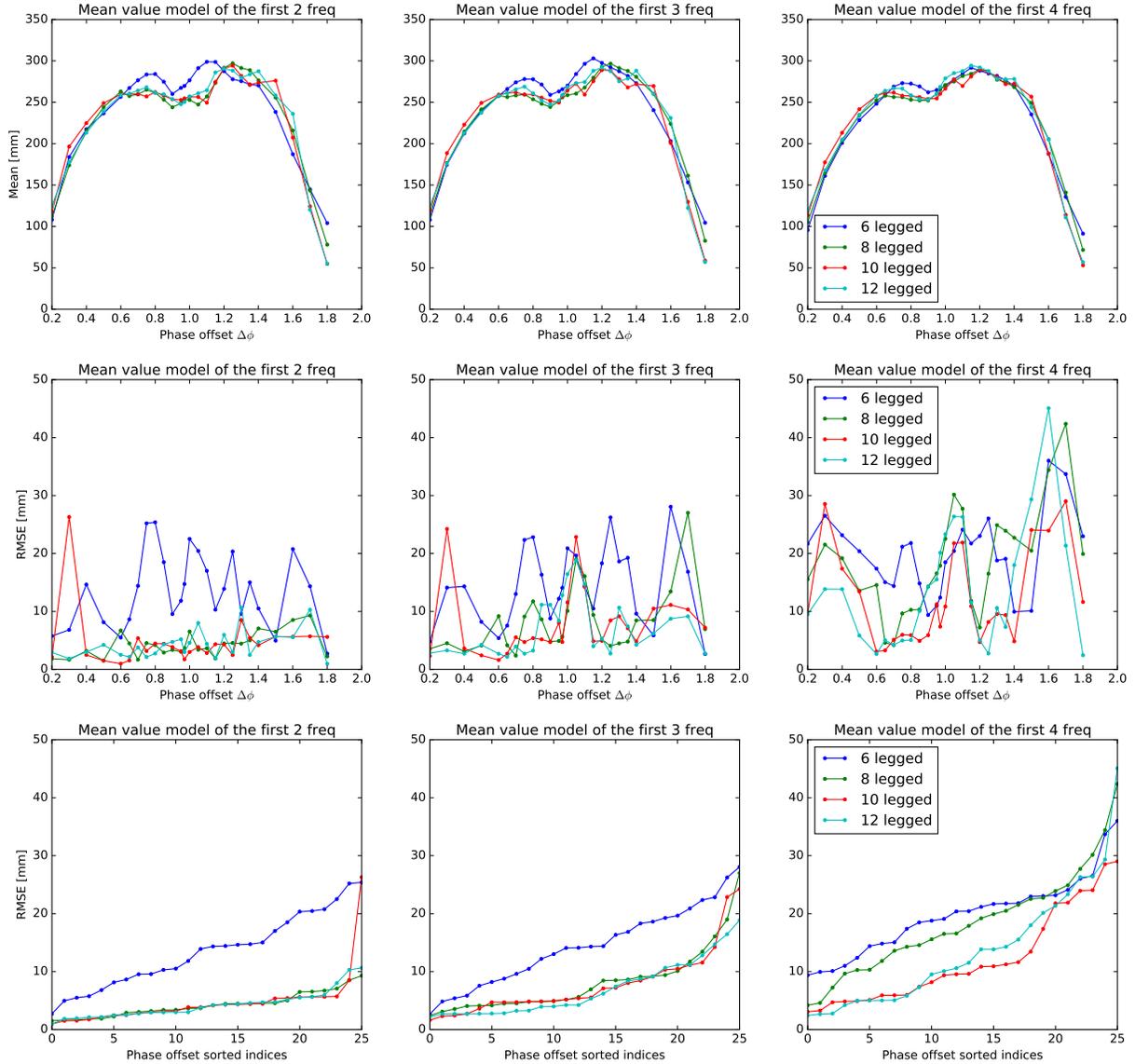
Figure 4.5: Average geometric motion analysis of Multipod. We compared the prediction error of the model trained on data from the 1,2, and 3 lowest gait frequencies (columns). For each class of models we plotted the mean motion (top row) and the RMSE of prediction (middle row) at each of the gaits studied (horizontal axis "phase offset"), for each number of legs (line and marker color). To make it easier to assess how good the models were overall, we sorted the RMSE value into increasing order (bottom row). Results show that 8, 10, and 12 legs are very close to geometric at the lowest two frequencies, and continue to be similar when the third frequency is added to the dataset. The 6 legged robot does not follow the model as well, although its worst-case error is still only about 30%. We conclude that with more legs, the Multipod becomes closer to being geometric.

Besides the above analysis based on the mean value model assessment for each test trial, we summarized all samples of dist/cyc and slip ratio for all leg numbers, all undulatory gaits and all

103

Table 4.3: Number of Multipod test trials that can be considered to be geometric on average by the standard of having their relative RMSE under 5%. Each number is out of 26 (undulatory gaits) for a given leg number and the mean value model of a given frequency group.

	6 legged	8 legged	10 legged	12 legged
First 2 frequencies	12	25	24	25
First 3 frequencies	12	21	20	22
First 4 frequencies	5	7	16	13
Marginal mean	9.7	17.7	20	20

gait frequencies in one figure (Figure. 4.6) for a global analysis of the full data set. In this figure, both the dist/cyc and the slip ratio show their main dependence on the undulatory gait phase offset. We can also see that Multipod robots slip a lot (with at least 40% slip ratio) with all the undulatory gaits. The dist/cyc offset boxplots stay in similar range when the gait frequency is scaled by x8 times (from 0.3 Hz to 2.4 Hz), and they only started to decrease at x10 times frequency (3.0 Hz). This observation of dist/cyc statistics again supports our conclusion that tested Multipod robots are very close to being geometric on average. The variance of dist/cyc statistics gradually increases with gait frequency while it gradually decreases with leg numbers, which further verifies our intuition that higher gait frequency makes the system more dynamic and our hypothesis that more legs make the system motion closer to geometric. One last interesting observation pertains to the clear negative correlation between dist/cyc and slip ratio in our Multipod tests, thus indicating that the more Mulipod slips, the less distance it moves per gait cycle using undulatory gaits. This may seem trivial, but it actually verifies that the motion geometric property changes when leg slip condition changes.

4.3.3 Average geometric analysis for Cockroach

Cockroach is the animal system we studied in this project. Even though it has at least 5 DoF on each leg, the cockroach still presented significant slipping during its locomotion in our tests. Many previous research studies have shown that cockroaches are highly dynamic and adopted the non-slip assumption to build dynamic models. Here we are interested in investigating the cockroach slipping motion we observed, and checking whether or not and to what extent, this motion can be regarded as geometric.

We placed cockroaches *Blaberus discoidalis* on foam boards [Elmer's 900803] for free running with an observed speed range of 15-77cm/s. 24 trials of cockroach motion were recorded by a high-speed camera and then transferred into raw motion data of body and foot locations by each video frame using the tool developed by Revzen [2009]. One example of tracked cockroach foot
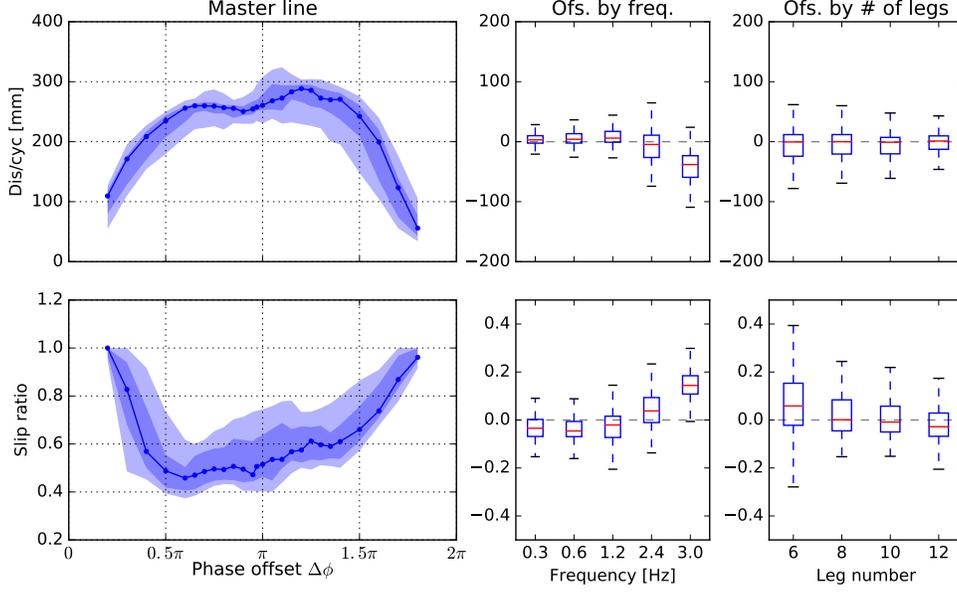
Figure 4.6: Summary of all Multipod tested motions in the data set regarding dist/cyc (top row) and slip ratio (bottom row). The dist/cyc and slip ratio samples for each test trial are calculated using the same bootstrapping method introduced in the caption of Figure. 4.4. Therefore, the full sample set of each property is a data matrix D with dimension equal to $[4, 5, 26, 15]$ (4 leg numbers; 5 gait frequencies; 26 phase offsets; 15 bootstrapping samples). The ribbon plots in the first column are the two properties vs. undulatory gait phase offset for all different leg numbers and gait frequencies (with D reshaped into $[4 \times 5 \times 15, 26]$ for the ribbon plot). The master line (solid dotted line in the middle: $D_{med}[1, 26]$) are the median of the data distribution ($[4 \times 5 \times 15]$) at given phase offset, while the ribbons cover $\pm 25\%$ (darker blue) and $\pm 45\%$ (lighter blue) of the distribution variations from the median master line by gait frequency and leg number influence. All these variations are then regrouped as offsets ($D_{ofs} = D - D_{med}$ with dimensions $[4, 5, 26, 15]$) from the master lines, and binned into boxplots by gait frequencies (middle column; D_{ofs} is reshaped into $[4 \times 26 \times 15, 5]$) and leg numbers (right column; D_{ofs} is reshaped into $[5 \times 26 \times 15, 4]$) respectively.

trajectories is shown in Figure 3.1. Within all these tests, cockroach front, middle, and hind legs slipped 18%, 15%, 16% of their total travel distance on average [Zhao and Revzen, 2020].

To check whether tested cockroaches have geometric motion, examining the geometric properties alone is not sufficient since we do not have full control authority over the animal systems as we do over the robot systems. For instance, many quadrupedal animals (dogs, horses) take a different gait pattern (galloping) at higher gait frequencies for higher moving speed compared to the lower speed gait pattern (trotting). Therefore, we first need to check whether the tested cockroaches were adopting the same or similar gait pattern at observed gait frequencies. Body frame leg positions are plotted out in Figure 4.7 for such checks. The tests show that our tested cockroaches actually took a very close tripod gait pattern for both low-speed tertile to high-speed tertile, which enables our further analysis on the geometric properties of cockroach motion.
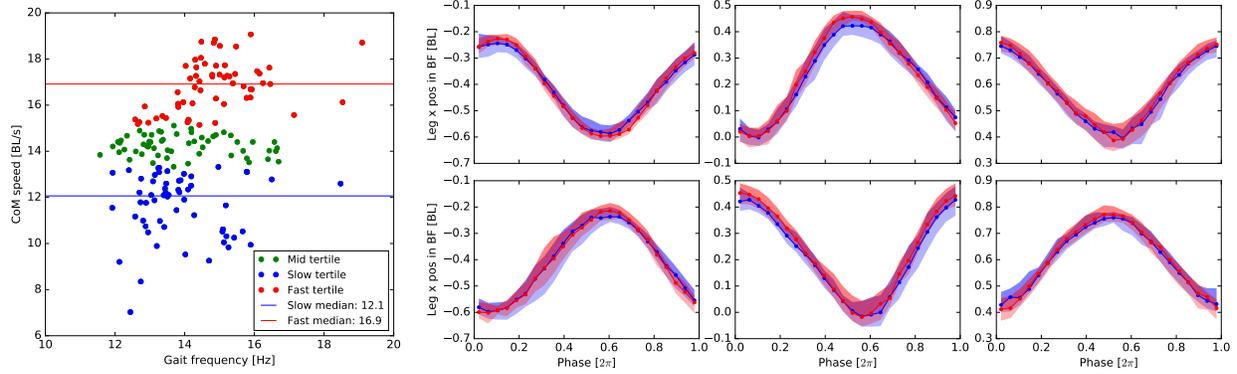
Figure 4.7: Cockroach gait pattern check. Left: cockroach CoM speed vs. gait frequency. All the samples are partitioned into even 3 tertiles by 33% and 66% percentile division lines of the corresponding speeds. The medians of slow and fast tertiles are marked out in horizontal lines with their value labeled in the legend. The ratio of the fast tertile median to the slow tertile median is 1.4x. Right: ribbon plots of leg x positions in the body frame vs. global phase for the slow sample tertile (blue) and the fast sample tertile (red) defined by the figure on the left. Each ribbon plot consists of 25 sample bins divided evenly by the global phase. In each ribbon, the center solid line consists of the median of each sample bin, while the ribbon covers data from 25% to 75% percentile of the sample bin. The ribbons are very close to each other for all 6 legs, which verifies that the gait patterns of the two tertiles are very close. The mean of the ratios between the two median lines of all leg x positions is 1.02, for a quantitative reference. The leg y positions of the two tertiles are also very close, which are omitted for plotting.

To check whether the tested cockroach has geometric motion, we analyze the same geometric property as that of BigAnt and Multipod: CoM traveled distance per gait cycle (dist/cyc). Since the tested cockroaches were different individual subjects, we use body length as a normalized unit for dist/cyc. We also analyze the slip ratio of cockroach motion wrt. gait frequency. This time ang/cyc property is omitted, since the cockroach was running freely and presented almost random turning behaviors. We then focus on analyzing the translational motion.

The corresponding results are presented in Figure. 4.8, from which we can see that the distribution of dist/cyc and slip ratio did not show obvious dependence on gait frequency. Applying the mean value models for dist/cyc and slip ratio, the prediction statistics are recorded in Table. 4.4. The RMS error to mean prediction ratio is around 16%, which is not as good as the result achieved of BigAnt and Multipod. These results imply that the tested cockroach locomotion is complicated and average geometric property alone is not adequate to represent its translational motion.

Although this analysis does not provide strong enough evidence to support the hypothesis that tested cockroach locomotion is geometric on average, it does introduce a method and provide an example pertaining to how to check the geometric property of the motion of an animal subject. This analysis also shows some interesting observations relevant to geometric motion: (1). Tested
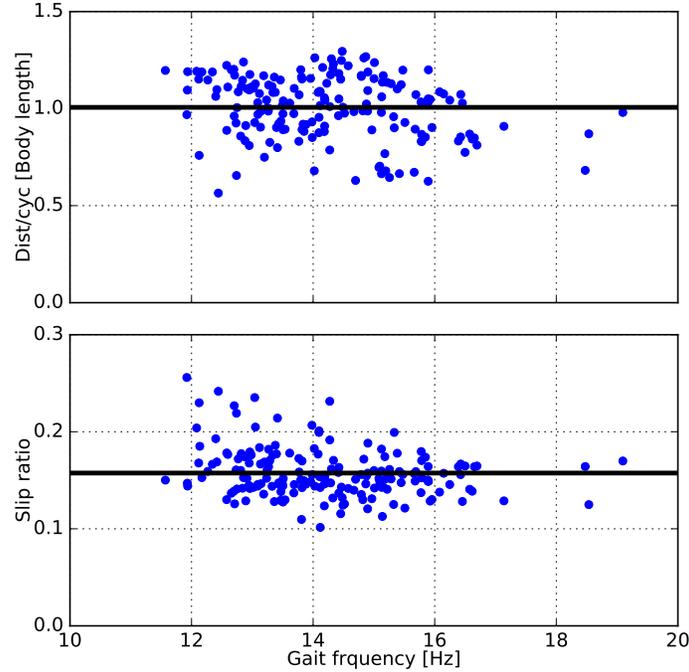
Figure 4.8: Geometric analysis of cockroach: dist/cyc (top) and slip ratio (bottom). Every point in this plot is the result from one gait cycle of one test trial. Gait cycles are divided by the global phase with phase zero fixed to the Poincaré section defined at the mean x position of the front left leg trajectory in the body frame. Unlike robot motions, free running cockroaches have different gait period time even in the same test trial. That is why the cockroach data set has many gait frequencies. The mean of dist/cyc and slip ratio is plotted as a horizontal line for reference purposes.

cockroaches do not increase step size to increase movement speed. As introduced in the Figure 4.7 caption, the speed ratio between the fast and slow tertile median is 1.4, while the shape ratio is 1.0. (2). Tested cockroaches constantly slip at all observed gait frequencies and do not try to reduce slip ratio when increasing gait frequency.

4.4 Instantaneous geometric analysis

For precise motion planning, being geometric on average is not enough. For instance, when the robot is required to perform a small motion in less than a gait cycle, cycle-based properties such as dict/cyc and ang/cyc can not make precise predictions to represent such small motions. To solve this problem, we need to further investigate the system motion within a gait cycle and check whether the body velocity is linearly related to the shape velocity at any instant of time. That is to check whether the motion is strictly geometric according to Equation 4.3 or Equation 4.4

Table 4.4: Statistics mean and RMSE (Root Mean Square Error) of dist/cyc [Body length] and slip ratio [%] compared to the mean value model for all test trials of cockroach.

Prediction statistics	Mean	RMSE	Relative RMSE
Dist/cyc	1.01	0.16	16.1%
Slip ratio	15.7	2.5	16.2%

4.4.1 Instantaneous geometric analysis and phase driven model for BigAnt
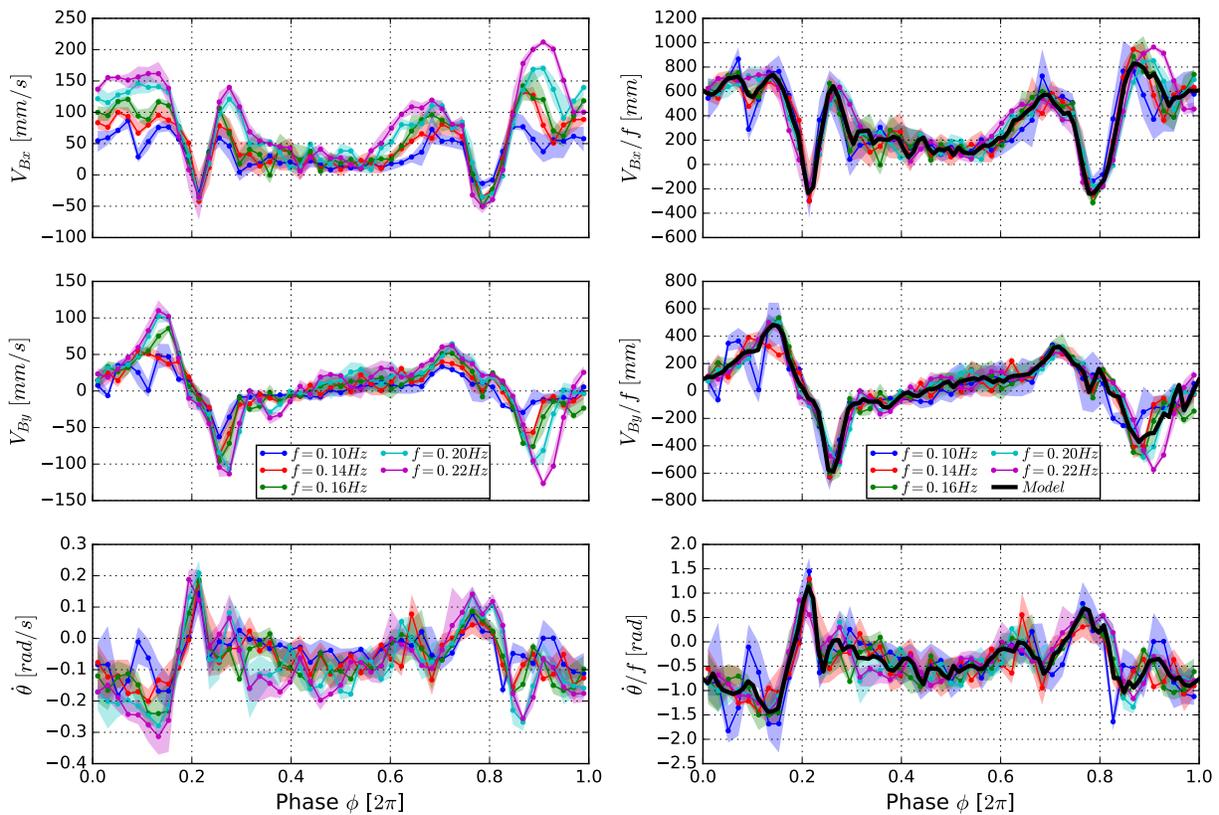
Figure 4.9: Instantaneous geometric analysis of BigAnt. The analyzed data set comes from the test trials in Figure 4.1 with steering input $s = 0.75$ taking 5 gait frequencies labeled in this figure legend. The left column plots are body velocities $V_B = [V_{Bx}, V_{By}, V_{B\theta}]$ vs. system phase ϕ. The right column plots are the normalized body velocities $V_{BNorm} = V_B/f$ vs. system phase ϕ. Each ribbon plot for a test trial consists of 50 sample bins divided evenly by the system phase. The center solid line connects the median of the data samples in each sample bin, while the ribbon covers data from 25% to 75% percentile of the data samples in each sample bin. The black lines on the left column plots are the phase driven models of $V_{BNorm}(\phi)$ fitted from all the normalized body velocities from different gait frequencies using Fourier series regression.

For instantaneous geometric analysis of BigAnt motion, we investigated the experiment tests

shown in Figure 4.1 with steering input $s = 0.75$ taking 5 gait frequencies. Figure 4.9 summarizes the results of body velocity V_B and normalized body velocity V_{BNorm}. From this figure, we can see that body velocities share very similar patterns with different amplitudes that resulted from different gait frequencies. After normalizing the body velocities, V_{BNorm} of different test trials are positioned at almost the same phase signal with little variance, even in doubled frequency range (0.10 to 0.22 Hz), showing the tested BigAnt motions are close to being instantaneously geometric. A phase driven model $V_{BNorm}(\phi)$ is also calculated by Fourier series regression across the normalized body velocities of all 5 tested trials, and also shown in Figure 4.9 with black lines.

$$\hat{V}_B(\phi) = f V_{BNorm}(\phi) \tag{4.6}$$

To evaluate the performance of this phase driven model, the predicted body velocity $\hat{V}_B(\phi)$ is calculated by Equation 4.6. The prediction error is summarized in Table 4.5, which can be used as a quantitative metric to assess how close the tested BigAnt motion is to being instantaneously geometric. However, significantly, the reported RMSE is from comparing the prediction with the experimentally measured data, thus it is also affected by noises and inconsistency between gait cycles while the robot walks through the environment which is also not perfectly symmetric. To compare the non-geometric effect with other error sources, we also report the RMSE of the Fourier series model fitted from each individual test trial as a reference showing the noises and inconsistency between gait cycles. We can see that the extra error by applying the geometric phase driven model is relatively small, so we can conclude that these tested BigAnt motions are close to being instantaneously/strictly geometric.

Table 4.5: Result of BigAnt phase driven model. For each test trial in Figure 4.1 with steering input $s = 0.75$, we present the RMSE (Root Mean Square Error) of the body velocity prediction $\hat{V}_B(\phi)$ (components in rows; gait frequency in columns) indicating the quality of the out-of-sample prediction for body velocity. This cannot reasonably be expected to do better than a Fourier Series model trained to each specific trial, and so the prediction ability of these trial-specific models (RMSE in parenthesis) serves to contextualize the magnitude of the geometric model's RMSE.

	0.10 Hz	0.14 Hz	0.16 Hz	0.20 Hz	0.22 Hz
RMSE of V_{Bx} [mm/s]	20 (16)	22 (20)	20 (17)	22 (15)	31 (21)
RMSE of V_{By} [mm/s]	15 (11)	15 (12)	15 (13)	17 (12)	22 (15)
RMSE of $V_{B\theta}$ [rad/s]	0.06 (0.05)	0.06 (0.05)	0.06 (0.05)	0.07 (0.05)	0.08 (0.06)

4.4.2 Instantaneous geometric analysis & phase driven model for Multipod

Besides the analysis of the BigAnt robot, we also investigated the instantaneous geometric property of Multipod robot for its whole data set with different leg numbers, different undulatory gaits and different gait frequencies. Here, we will introduce some typical analysis examples in detail as shown in Figure 4.10.

As previously mentioned, all tested Multipod motions are walking straight (in body x axis direction), so we focus on analyzing V_{Bx}. From Figure 4.10, we can see that body velocity V_{Bx} increases as gait frequency f increases within x8 frequency range (from $0.3Hz$ to $2.4Hz$). V_{Bx} seems saturated after $f = 2.4Hz$ and barely increases as shown in the cases with $f = 3.0Hz$. For the normalized body velocities $V_{BxNorm} = V_{Bx}/f$, they are sensitive wrt. to all varying parameters ($f, \Delta\phi$, and leg number). V_{BxNorm} has larger in-cycle oscillation with lower gait frequency, smaller leg number and phase offsets $\Delta\phi$ closer to π.

We should note that V_{BNorm} from different gait frequencies will be exactly the same phase signal as if the motion is strictly geometric in perfect experiment condition. As depicted in the figure examples, normalized body velocities of the Multipod only stay close between the two lowest gait frequencies (x2 frequency range from $f = 0.3Hz$ to $f = 0.6Hz$), while these normalized body velocities show different phase signals pattern after x4 frequency (from $f = 1.2Hz$ to $f = 3.0Hz$). This shows that the tested Multipod motion is close to instantaneously geometric only for the first two gait frequencies, even though the average geometric property can be preserved in a larger frequency range. This observation also aligns with our intuition and previous average geometric analysis that slower motion is closer to be geometric than faster motion. Therefore, we use the lowest frequency case as the baseline geometric reference and fit a phase driven model from its normalized body velocity by Fourier series regression, which is exhibited as a black line in Figure 4.10.

To quantitatively assess how close the locomotion cases of the first two gait frequencies are to instantaneous geometric, the above phase driven model is evaluated on the motion data with $f = 0.6Hz$ for all leg numbers and phase offsets. The result prediction RMSEs are reported in Figure 4.11, from which we can see that Multipod robots with additional legs have obviously smaller prediction errors conveying that more legs make the Multipod motion closer to instantaneously/strictly geometric. From all above analyses, we can conclude that 10-legged and 12-legged Multipod is almost instantaneously/strictly geometric at gait frequencies from $0.3Hz$ to $0.6Hz$ with all tested undulatory gaits.
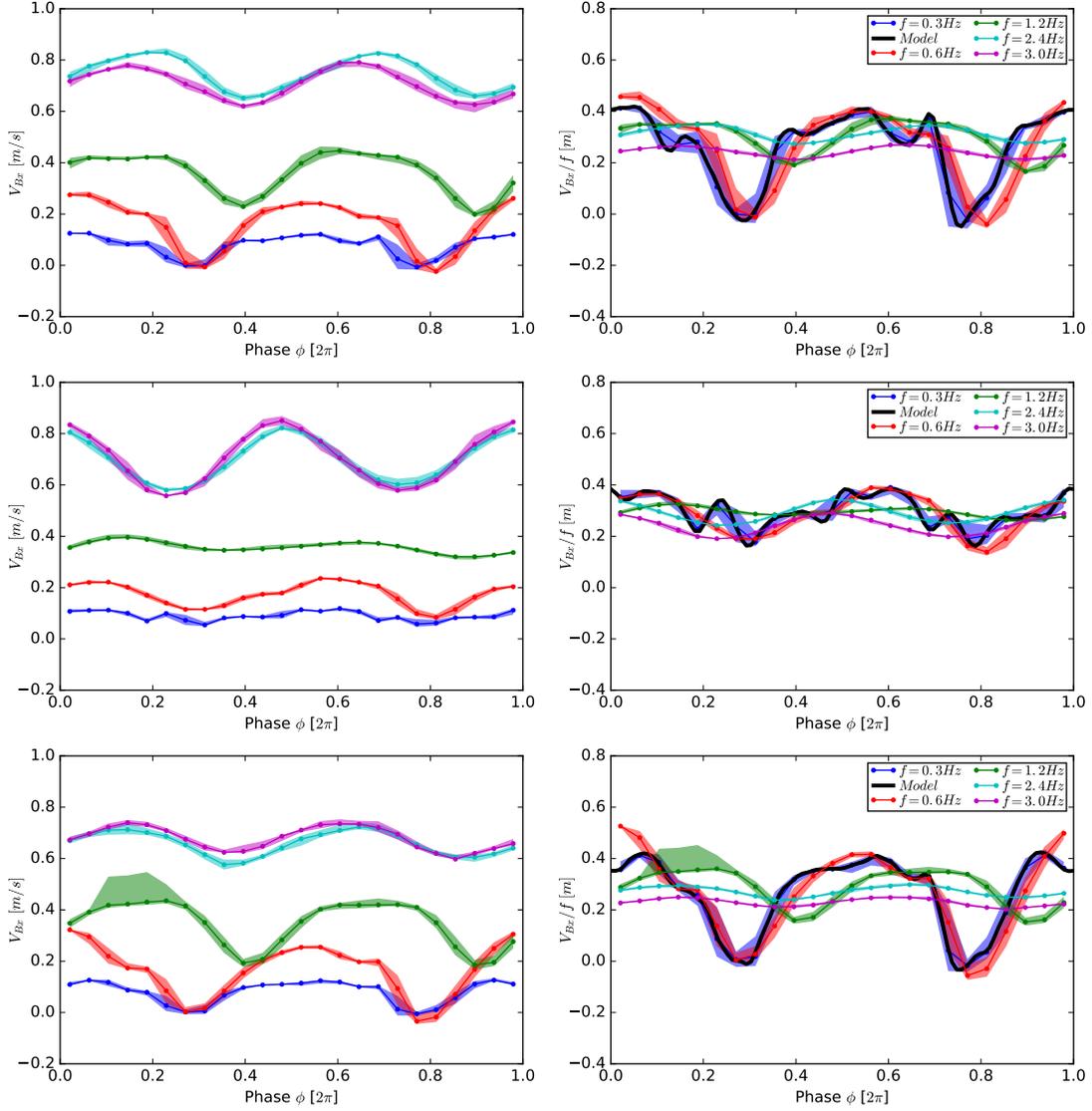
Figure 4.10: Instantaneous geometric analysis examples of the Multipod motion for body velocity V_{Bx} vs. phase ϕ (left column) and normalized body velocity V_{Bx}/f vs. phase ϕ (right column). The three rows correspond to the three example trial sets: 12-legged Multipod taking undulatory gait with 1.0π phase offset (top row); 12-legged Multipod taking undulatory gait with 1.2π phase offset (middle row); 10-legged Multipod taking undulatory gait with 1.0π phase offset (bottom row). Each trial set contains 5 test trials with 5 different gait frequencies ($f = [0.3, 0.6, 1.2, 2.4, 3.0]$ Hz). Each ribbon plot for a test trial consists of 25 sample bins divided evenly by the system phase ϕ. The center solid line connects the median of the data samples in each sample bin, while the ribbon covers data from 15% to 85% percentile of the data samples in each sample bin. The black lines on the left column plots are the phase driven models of $V_{BxNorm}(\phi)$ fitted from the normalized body velocity with gait frequency $f = 0.3Hz$ using Fourier series regression.
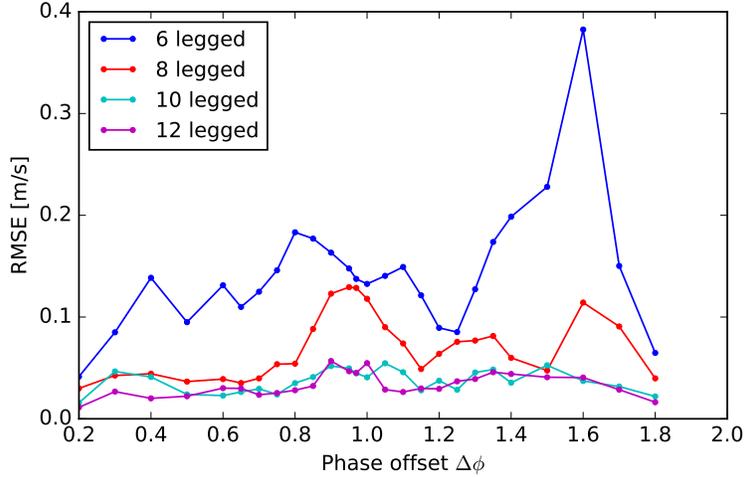
Figure 4.11: RMSE of the Multipod data driven models vs. undulatory gait phase offsets for all numbers of legs: Each phase driven model is fitted from normalized body velocity V_{Bx}/f of the test trial with the lowest gait frequency ($f = 0.3Hz$). The phase driven models are then applied to predict the body velocities of test trials with gait frequency $f = 0.6Hz$ and the corresponding RMSE are calculated and plotted in Figure

4.5   A Model for multi-legged locomotion with slipping

With the previous average and instantaneous geometric analysis, we find our experimentally tested Multi-legged locomotion is geometric. Such a characteristic provides a strategy to model the complicated low-DoF Multi-legged systems. The data driven models such as mean value models of geometric properties (dist/cyc and ang/cyc) and phase driven models have been tested for geometric analysis. They also showed capability to predict system motions adopting certain gaits with different gait frequencies. Based on these analyses and test results, some follow-up questions emerge: 1. Why are these tested multi-legged locomotion geometric? 2. What are the possible physics behind these phenomena?

In this section, we will try to explore the answers to these two questions by carrying out physical assumptions and checking these assumptions using models built from first principle physics.

4.5.1   Model assumption of friction dominated locomotion

The dynamic characteristics of mechanical systems mainly comes from the inertia effect. For multi-legged systems to exhibit geometric motion, the inertia effect should be dominated by other non-holonomic constraint forces such as introduced in Section 4.2.2.1. Here we assume that the observed multi-legged locomotion with slipping is in the *Friction Dominated Case*. We define *Friction Dominated Case* as the case that: friction/damping effect from leg-ground contact is dom-

$$r = \{(x_i(t), y_i(t), z_i(t))\}_{i=1,..,6}$$

$$\dot{g} = (\omega, v_x, v_y)$$

Friction Dominated
Multi-legged Model

$$g^{-1}\dot{g} = -A(r)\dot{r}$$
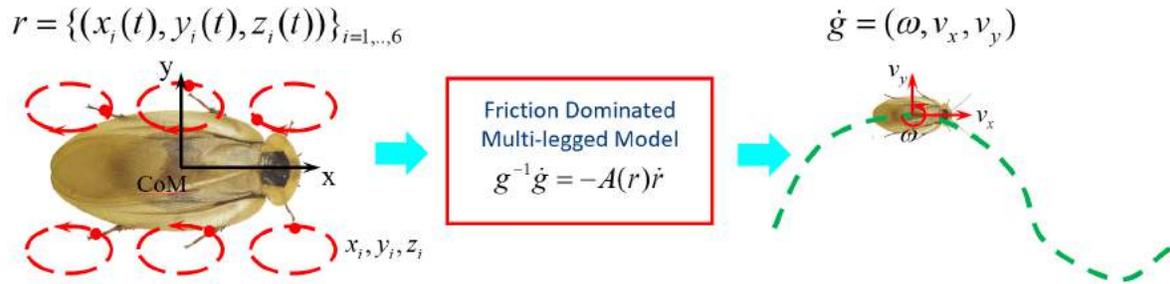
Figure 4.12: Goal model structure.

inating system force conditions, such that the ratio of inertia force to friction/damping force is small enough to be neglected. With this assumption, the dynamic mode from inertia effect can be dissipated fast enough and the whole system motion is quasi-static[6]. This friction dominated assumption is similar to the low Reynolds number condition for small swimmers which leads to the zero-momentum condition. All the momentum related terms in original reconstruction equation (4.2) can then be omitted and result in the geometric connection equation (4.3).

Our goal in this section is to build a geometric connection model for Multi-legged locomotion with slipping from first principle physics based on the friction dominated assumption. The model takes egocentric leg motions (shape and shape velocity inputs) and computes body velocity as demonstrated in Figure 4.12.

4.5.2   Model construction
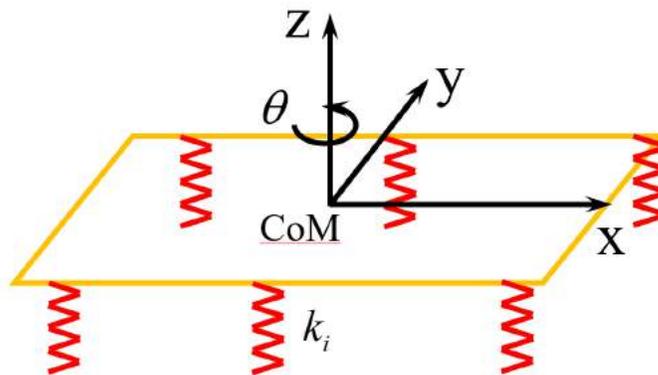
Figure 4.13: Spring supported multi-legged model.

Based on the friction dominated assumption, our next step is to construct a physical model

[6]The system is still moving but the forces applied on the system are always balanced with net force equals to zero

113

which has linear local connection structure. Here, we allocate given a multi-legged system with N legs (or other contacts), indexed by $j = 1 \ldots N$. The time varying foot positions in the body frame of reference are given by $q_j \in \mathbb{R}^3$. The body frame location is given by a time varying rigid body motion $g \in \mathsf{SE}(3)$. Body frame pose g wrt. world frame reference has the following form:

$$g = \begin{bmatrix} \mathrm{R} & p_0 \\ 0 & 1 \end{bmatrix} \tag{4.7}$$

where $\mathrm{R} \in \mathsf{SO}(3)$ is rotation matrix between the body frame and world frame; $p_0 = [p_{0,x}, p_{0,y}, p_{0,z}]$ is the position of the body frame origin in the world frame. In the model we are constructing, we assume a simplified form for g to only focus on the system motion on horizontal 2D plane:

$$g = \begin{bmatrix} \cos\theta & -\sin\theta & p_{0,x} \\ \sin\theta & \cos\theta & p_{0,y} \\ 0 & 0 & 1 \end{bmatrix} \tag{4.8}$$

To simplify the notation for position and velocity calculation, we further note the 2D rotation matrix $\mathrm{R}(\theta)$ and the skew matrix S of angular velocity $\dot\theta$ as following:

$$\mathrm{R}(\theta) = \begin{bmatrix} \cos\theta & -\sin\theta \\ \sin\theta & \cos\theta \end{bmatrix} \qquad \mathrm{S} = \begin{bmatrix} 0 & -1 \\ 1 & 0 \end{bmatrix} \tag{4.9}$$

We can then calculate the leg position and velocity in the world frame XY plane:

$$p_{j,xy} = p_{0,xy} + \mathrm{R}(\theta) q_{j,xy} \tag{4.10}$$

$$\dot{p}_{j,xy} = \dot{p}_{0,xy} + \mathrm{R}(\theta)\dot{q}_{j,xy} + \dot{\theta}\mathrm{S}\mathrm{R}(\theta)q_{j,xy} \tag{4.11}$$

It worth noting that the body frame velocity is originally in matrix form as:

$$g^{-1}\dot{g} = \begin{bmatrix} 0 & -\dot\theta & V_{Bx} \\ \dot\theta & 0 & V_{By} \\ 0 & 0 & 0 \end{bmatrix} \tag{4.12}$$

For convenience, we note it in vector form as used in previous sections:

$$g^{-1}\dot{g} = V_B = [V_{Bx}, V_{By}, \dot\theta]^{\mathrm{T}} \tag{4.13}$$

Body frame origin velocity in body frame $[V_{Bx}, V_{By}]$ can also be transferred into the world frame as:

$$\dot{p}_{0,xy} = \begin{bmatrix} v_x \\ v_y \end{bmatrix} = \mathrm{R}(\theta) \begin{bmatrix} V_{Bx} \\ V_{By} \end{bmatrix} \tag{4.14}$$

4.5.2.1 Contact legs and normal forces

With the focus on the system motion in the XY plane, the calculation of z axis motion is decoupled out and used only to determine the contact leg indices and the normal force on each supporting leg. Combining all these assumptions, we propose a model which possesses the structure exhibited in Figure 4.13. In this model, each leg is assumed as a vertical spring attached to the system "base board" (body frame XY plane). The attaching point of each leg spring moves along the foot trajectory projected into the body frame XY plane: $(q_{j,xy}(t))$. The rest length $l_{j,0}$ of each leg spring changes vertically with the normalized foot z position which is defined in Equation 4.15. Since $q_{j,z}(t)$ is always negative (the foot tip is always beneath the base board), the rest length $l_{j,0}$ is then regulated into the range of $(0, 1]$.

$$l_{j,0} = -q_{j,z} / \max \{|q_{i,z}(t)|, i = 1 \dots N\} \tag{4.15}$$

The stiffness of each leg spring is noted as k_j, which is a hyper-parameter that requires tuning during simulation. The compression amount Δl_j and the normal force $F_{j,z}$ of each leg spring is calculated as:

$$\Delta l_j = l_{j,0} - p_{0,z} \tag{4.16}$$

$$F_{j,z} = \begin{cases} k_j \Delta l_j & \Delta l_j > 0 \\ 0 & \Delta l_j \leq 0 \end{cases} \tag{4.17}$$

where $p_{0,z}$ is the z axis position of body frame origin in world frame and should always be positive. $p_{0,z}$ can then be calculated from the z axis force balance resulted from the friction dominated assumption:

$$\sum_{j=1}^{N} F_{j,z} - Mg = 0 \tag{4.18}$$

This calculation can be implemented explicitly without equation solving procedures for computation efficiency. The detailed calculation is presented in Algorithm 1.

Algorithm 1 Contact leg indices and normal force calculation

1: $L \leftarrow [l_{1,0}, l_{2,0} \ldots, l_{N,0}]$ ▷ Initiate rest length list for all leg springs
2: $K \leftarrow [k_1, k_2 \ldots, k_N]$ ▷ Initiate stiffness list for all leg springs
3: $s \leftarrow argsort(L)$ ▷ Get index list that sorts L from longest to shortest rest length
4: $p_{0,z} \leftarrow L[s[1]]$ ▷ Initiate $p_{0,z}$ with the longest rest length
5: $k_T \leftarrow K[s[1]]$ ▷ Initiate the total stiffness k_T of all contact legs
6: $F_T \leftarrow 0$ ▷ Initiate the total normal force F_T of all contact legs
7: $Flag \leftarrow 0$ ▷ Flag variable which indicates whether all legs are contact legs
8: **for** $i = [2, \ldots, N]$ **do**   ▷ Loop through all other sorted leg indices
9:     $\Delta z \leftarrow p_{0,z} - L[s[i]]$ ▷ Find how much $p_{0,z}$ moves down for next contact
10:     $F_T \leftarrow F_T + k_T \Delta z$ ▷ Accumulate the total normal force
11:     **if** $F_T > Mg$ **then**   ▷ Check whether current contact legs can fully support system weight
12:         $Flag \leftarrow 1$ ▷ Update flag to indicate not all legs are contact legs
13:         **break**   ▷ Break the loop
14:     $p_{0,z} \leftarrow L[s[i]]$ ▷ Update $p_{0,z}$ with the next longest rest length
15:     $k_T \leftarrow k_T + K[s[i]]$ ▷ Update the total stiffness with the next leg spring added
16: **if** $Flag = 1$ **then**   ▷ For the case that not all legs are contact legs
17:     $\Delta z \leftarrow (Mg - (F_T - k_T \Delta z))/k_T$ ▷ Calculate the balance position
18:     $p_{0,z} \leftarrow p_{0,z} - \Delta z$ ▷ Update $p_{0,z}$
19: **else**   ▷ For the case that all legs are contact legs
20:     $\Delta z \leftarrow (Mg - F_T)/k_T$ ▷ Calculate the balance position
21:     $p_{0,z} \leftarrow p_{0,z} - \Delta z$ ▷ Update $p_{0,z}$
22: **return** $p_{0,z}$

4.5.2.2 Tangent forces and planar motion

With $p_{0,z}$ calculations completed, the normal forces and contact leg indices are determined by Equation 4.17. The next step is to compute the system motion in the world frame XY plane. Note that we need to model Multi-legged locomotion with slipping, so the key assumption we are making here is about the contact friction model. Friction itself is a complicated problem and there are many friction models for different applications. Most of the friction models are functions of relative velocity and normal force between two contact objects: $F_f(\dot{x}, F_N)$. Here we use this general friction formula to represent any friction model for the propose of introducing our multi-legged model structure. Detailed friction model choice will be discussed in the following section.

Given the general friction model, the friction force on each contact leg (indexed by i) in the world frame XY plane can be calculated as:

$$F_{i,xy} = F_f(\dot{p}_{i,xy}, F_{i,z})$$ (4.19)

where we use the index i to vary only over legs which are in contact with the ground and note the total contact leg number as N_i. With the tangent force on each leg, we can also calculate the moment around the body frame z axis exerted by each leg as:

$$M_{i,z} = \mathrm{R}(\theta) q_{i,xy} \times F_{i,xy}$$ (4.20)

By substituting the $\dot{p}_{j,xy}$ of Equation 4.11 into Equation 4.19 and further into Equation 4.20, we get the tangent force $F_{i,xy}$ and z axis moment $M_{i,z}$ of each leg as functions of the shape inputs $(q_{j,xy}, \dot{q}_{j,xy})$, the calculated normal force $F_{i,z}$ from $q_{j,z}$, and the unknown system planar motion $(\dot{p}_{0,xy}, \dot{\theta}, \theta)$. The body frame orientation variable θ can be updated by an initial value $\theta(0)$ and $\dot{\theta}$ in the numerical simulation, so we can consider there are only 3 unknown variables $[\dot{p}_{0,x}, \dot{p}_{0,y}, \dot{\theta}]$.

From the friction dominated assumption, we also calculated the XY plane force and moment balance as:

$$\sum_{i=1}^{N_i} F_{i,x} = 0$$ (4.21)

$$\sum_{i=1}^{N_i} F_{i,y} = 0$$ (4.22)

$$\sum_{i=1}^{N_i} M_{i,z} = 0$$ (4.23)

Therefore, we have 3 equations to solve the 3 unknowns $[\dot{p}_{0,x}, \dot{p}_{0,y}, \dot{\theta}]$ for the system planar

motion in numerical simulation.

4.5.2.3   Friction model and local connection

With the general model structure introduced, here we will introduce our choice of friction model. The classic Coulomb friction model and viscous friction model for slipping has formulas as follows if considered for each leg:

$$F_{j,xy} = -\mu_j F_{j,z} \frac{\dot{p}_{j,xy}}{\|\dot{p}_{j,xy}\|} \tag{4.24}$$

$$F_{j,xy} = -c_j \dot{p}_{j,xy} \tag{4.25}$$

where μ_j and c_j are Coulomb friction and viscous friction coefficients respectively. Coulomb friction force is linearly related to the normal force and has direction opposite to the relative motion velocity between leg and ground. Viscous friction force is linearly related to the scale of the relative motion velocity between leg and ground, and it also has the opposite direction to the relative velocity. Each model is functional within certain circumstances, and they have their individual limitations. For Coulomb friction model, the biggest issue is the singularity problem at $\dot{p}_{k,xy} = 0$. It has no explicit formula at this static case, and its friction force can only be determined by the outside net force exerted on the leg. For our tested multi-legged locomotion, despite the high slipping ratio, there may still be some contact legs that do not slip at some instances during the motion. Thus, Coulomb friction model on its own is insufficient for our goal model which requires an explicit force formula for all leg contacts. Viscous friction model can provide explicit force equal to 0 at $\dot{p}_{k,xy} = 0$ and its friction force only relays on leg speed, while we also know that the leg tangent force is affected by the normal force at most dry mechanical contacts. In conclusion, either friction model on their own is inadequate for our multi-legged model.

To solve this problem, we proposed (Zhao et al. [2018], Zhao and Revzen [2021]) a contact friction model that combines Coulomb friction and viscous friction features:

$$F_{j,xy} = -\mu_j F_{j,z} \dot{p}_{j,xy} \tag{4.26}$$

By this composited friction model, we make the friction force scaled by both the normal force and the relative velocity to the ground. This assumption is an ansatz for us to have an explicit friction formula for each leg, which leads to overall geometric results. We further test this model in simulation and present its performance compared to the experiment ground truth.

With this model, $F_{j,xy}$ is linearly related to $F_{j,z}$, so the contact leg index is implicitly included by Equation 4.17 and there is no need to use a different index notion. By substituting $\dot{p}_{j,xy}$ in

Equation 4.11 into Equation 4.26, the tangent force of each leg is expressed as:

$$F_{j,xy} = -\mu_j F_{j,z} \dot{p}_{0,xy} - \mu_j F_{j,z} \mathrm{R}(\theta) \dot{q}_{j,xy} - \mu_j F_{j,z} \mathrm{SR}(\theta) q_{j,xy} \dot{\theta} \tag{4.27}$$

Note that $F_{j,xy}$ is the physical vector of leg tangent force represented in the world frame. We can also represent the leg tangent force in the body frame noted as $F_{j,xy}^B$:

$$F_{j,xy}^B = \mathrm{R}(-\theta) F_{j,xy} = -\mu_j F_{j,z} \dot{p}_{0,xy}^B - \mu_j F_{j,z} \dot{q}_{j,xy} - \mu_j F_{j,z} \mathrm{S} q_{j,xy} \dot{\theta} \tag{4.28}$$

where we use $\dot{p}_{0,xy}^B$ to note for $\mathrm{R}(-\theta)\dot{p}_{0,xy}$, which is exactly the body velocity $[V_{Bx}, V_{By}]^{\mathrm{T}}$. The moment around the body frame z axis exerted by each leg in Equation 4.20 can also be written as:

$$M_{j,z} = q_{j,xy} \times (\mathrm{R}(-\theta) F_{j,xy}) = q_{j,xy} \times F_{j,xy}^B \tag{4.29}$$

With $F_{j,xy}^B$ Equation 4.28 plugged in, the moment is exhibited in explicit form:

$$M_{j,z} = +\mu_j F_{j,z} q_{j,y} V_{Bx} - \mu_j F_{j,z} q_{j,x} V_{By} - \mu_j F_{j,z} (q_{j,x}^2 + q_{j,y}^2) \dot{\theta} - \mu_j F_{j,z} (q_{j,x} \dot{q}_{j,y} - q_{j,y} \dot{q}_{j,x}) \tag{4.30}$$

From the friction dominated assumption, the force and moment balance is represented in the body frame as:

$$\sum_{j=1}^{N} F_{j,xy}^B = -\left(\sum_{j=1}^{N} \mu_j F_{j,z}\right) \begin{bmatrix} V_{Bx} \\ V_{By} \end{bmatrix} - \mathrm{S}\left(\sum_{j=1}^{N} \mu_j F_{j,z} q_{j,xy}\right) \dot{\theta} - \sum_{j=1}^{N} \mu_j F_{j,z} \dot{q}_{j,xy} = \begin{bmatrix} 0 \\ 0 \end{bmatrix} \tag{4.31}$$

$$\sum_{j=1}^{N} M_{j,z} = \left(\sum_{j=1}^{N} \mu_j F_{j,z} q_{j,y}\right) V_{Bx} - \left(\sum_{j=1}^{N} \mu_j F_{j,z} q_{j,x}\right) V_{By} -$$
$$\left(\sum_{j=1}^{N} \mu_j F_{j,z} (q_{j,x}^2 + q_{j,y}^2)\right) \dot{\theta} - \left(\sum_{j=1}^{N} \mu_j F_{j,z} (q_{j,x} \dot{q}_{j,y} - q_{j,y} \dot{q}_{j,x})\right) = 0 \tag{4.32}$$

Therefore, there are 3 linear equations for the 3 unknown motion variables $[V_{Bx}, V_{By}, \dot{\theta}]$. We can further write the equation solution into matrix form:

119

$$
\begin{bmatrix} V_{Bx} \\ V_{By} \\ \dot{\theta} \end{bmatrix} = -
\begin{bmatrix}
\sum_{j=1}^{N} \mu_j F_{j,z} & 0 & -\sum_{j=1}^{N} \mu_j F_{j,z} q_{j,y} \\
0 & \sum_{j=1}^{N} \mu_j F_{j,z} & \sum_{j=1}^{N} \mu_j F_{j,z} q_{j,x} \\
-\sum_{j=1}^{N} \mu_j F_{j,z} q_{j,y} & \sum_{j=1}^{N} \mu_j F_{j,z} q_{j,x} & \sum_{j=1}^{N} \mu_j F_{j,z}(q_{j,x}^2 + q_{j,y}^2)
\end{bmatrix}^{-1}
$$
$$
\begin{bmatrix}
\mu_1 F_{1,z}, \cdots, \mu_N F_{N,z} & 0, \cdots, 0 & \mathbf{0} \\
0, \cdots, 0 & \mu_1 F_{1,z}, \cdots, \mu_N F_{N,z} & \mathbf{0} \\
-\mu_1 F_{1,z} q_{1,y}, \cdots, -\mu_N F_{N,z} q_{N,y} & \mu_1 F_{1,z} q_{1,x}, \cdots, \mu_N F_{N,z} q_{N,x} & \mathbf{0}
\end{bmatrix}
\begin{bmatrix} \dot{Q}_x \\ \dot{Q}_y \\ \dot{Q}_z \end{bmatrix} \quad (4.33)
$$

where $\dot{Q}_x = \dot{q}_{1,x}, \dot{q}_{2,x}, \dots, \dot{q}_{N,x}$, $\dot{Q}_y = \dot{q}_{1,y}, \dot{q}_{2,y}, \dots, \dot{q}_{N,y}$ and $\dot{Q}_z = \dot{q}_{1,z}, \dot{q}_{2,z}, \dots, \dot{q}_{N,z}$ are the matrix blocks representing system shape velocity which is exactly $\dot{r}$ in Equation 4.3. For notation convenience, we note the above matrix equation as: $V_B = -\mathrm{C}^{-1}\mathrm{D}\dot{r}$. Note that $F_{j,z}$ is a function of body frame leg z positions $\{q_{j,z}, j = 1, \dots N\}$, then C and D are just matrix functions of system shape $r = \{[q_{j,x}, q_{j,y}, q_{j,z}]\}$ with friction model coefficients $\{\mu_j\}$. Therefore, the system equation (Equation 4.33) we derived from our friction model has the classic geometric connection form of $g^{-1}\dot{g} = A(r)\dot{r}$.

4.5.3 Model and simulation discussion

Inspired by our discovery that multi-legged locomotion with slipping can be geometric, we proposed the spring supported model structure and Coulomb-viscous combined friction model in the previous section, which leads to an explicit geometric connection form. Following are some details that are worth further introduction and discussion.

4.5.3.1 Model structure and normal force calculation

First, although the spring supported multi-legged model structure shown in Figure 4.13 looks similar to the classic SLIP model, they have some intrinsic differences. Our model focuses on the system motion on the 2D horizontal plane while classic SLIP model focuses on system motion on the vertical plane. The springs in our model are assumed to be vertical all the time and there is no active/passive swing motion during the gait. The motions of the springs are induced from the planar motions of the attaching points, while the spring rest lengths are regulated by the original body frame leg z positions to fulfil our assumption of ignorable pitch and roll motion. Unlike the springs in SLIP model, the springs in our model are not introduced to match or determine the dynamics during walking. They are solely used to determine the force distribution among the supporting legs given z axis force balance based on leg z positions in the body frame.

It should be noted that the model structure is designed for multi-legged systems which have

at least 3 supporting legs at any given time and usually have a leg number $N \geq 6$. For static or quasi-static mechanical systems with 3 supports, the 3 normal forces can be solved by the 3 balance equations: $\sum F_z = 0, \sum M_x = 0, \sum M_y = 0$ with no need of leg springs. For static or quasi-static mechanical systems with more than 3 supports, material properties need to be included to determine the normal force distribution. That is the reason why we introduced leg springs into our model structure. We assume that the spring-supported multi-legged system has $N_i \geq 3$ supporting legs and the base board which the leg springs are attached to is rigid. Assuming the small pitch and roll angles of the base board, we can then represent the compression amount of each leg spring Δl_i as following:

$$\Delta l_i = -\Delta z_0 - \alpha_x q_{i,y} + \alpha_y q_{i,x} \tag{4.34}$$

where $-\Delta z_0$ is the dropped distance of the body frame origin; α_x and α_y are the small angles in which the baseboard is rotated around body frame x and y axis respectively; $q_{i,x}$ and $q_{i,y}$ are still leg positions in the body frame as used previously. This equation is applicable for all N_i supporting legs and the normal forces can be calculated from $F_{i,z} = k_i \Delta l_i$. Therefore, by introducing 3 more unknown variables ($\Delta z_0, \alpha_x, \alpha_y$), we gain N_i more equations. With the original 3 force/moment balance equations, there are total of $N_i + 3$ equations for the $N_i + 3$ unknowns: N_i normal forces $\{F_{i,z}\}$ plus 3 parameter variables $\Delta z_0, \alpha_x, \alpha_y$.

In our model structure we can also embed this kind of method. However, it needs to solve equations and interactively determine the contact leg index $\{i\}$. Compared to the simplified version of this method as introduced in previous section 4.5.2.1, the overall computation requirement for the algorithm will be much larger and extra tuning will also be needed for calculation with real experiment data. That is why we selected the simplified version by ignoring the roll and pitch motion together with the moment balance thereby aiming to construct a simple model that can assist robot real-time planning and control.

4.5.3.2 Leg spring stiffness

Besides the calculation method, the normal force distribution is also affected by the hyper parameters $\{k_j\}$, which are the stiffness for leg springs and need tuning during simulation. For example, in the extreme case that k_0 of the longest leg spring ($j = 0$) is large enough, this leg will be the only supporting leg based on the method that only considers z axis force balance. Obviously, that is impossible for quasi-static balance and the system will fall over, and further break the assumption of the small enough pitch and roll. To avoid this kind of problem, we always add an assertion in Algorithm. 1 to check whether there are at least 3 contact legs at any time step. In the simulations for checking real experiment data, we usually tune the leg stiffness $\{k_j\}$ to ensure that there are

half of the total legs ($N_i = N/2$) contacting the ground when the robot is conducting alternating gaits. It is worth noting that we also use leg z positions in the body frame to regulate the leg spring lengths as explained in Equation 4.15. So, the rest length differences between ground truth supporting legs are small for all tested gaits, thereby ensuring that the search of feasible $\{k_j\}$ is not difficult in terms of the correct contact leg indices.

In summary, the first criteria for tuning $\{k_j\}$ is to ensure that the calculated contact leg indices are correct. The feasible leg spring stiffness $\{k_j\}$ is in a relatively wide range. For detailed choice of hyper-parameters $\{k_j\}$, we usually test different stiffnesses in the feasible range and select the $\{k_j\}$ which gives the best match to the ground truth system motion. An optimization loop could also be applied to search for the best stiffness parameters.

In most cases, we assume that the leg springs share the same stiffness parameter k. It is easier for both hand tuning and optimization, and works well for symmetric contact legs layout (8-legged and 12-legged). For the 6-legged case, the tripod contact layout is not symmetric: there is one leg on one side and two legs on the other side. If the 3 supporting leg springs have the same rest length $l_{j,0}$ and the body frame original is at the center of supporting triangle, the z axis force balance alone will result in evenly distributed normal forces, while the full force/moment balance will result in that the middle supporting leg on one side has the normal force equal to the twice of the normal force of the front or hind leg on the other side. For this asymmetric supporting layout, we usually assign larger stiffness k_j to the middle legs for the compensation of lacking moment balance when hand tuning $\{k_j\}$ or setting initial values for optimization.

One last key point we need to emphasize is that both the normal force calculation method and the stiffness parameter choice in this model structure can determine the contact leg indices and normal force distribution. They then further affect the connection coefficient matrices in Equation 4.33. However, they do not change whether the model is geometric or not. The underlying geometric structure is primarily determined by the friction model during leg contact which is introduced in the next section.

4.5.3.3 Friction models and geometric structure

The spring supported model structure we proposed is a framework that can use different friction models as introduced in Section 4.5.2.2. We do not regard Equation 4.33 as the only connection model for the model structure, but a promising candidate that is worth further checking with experimental data. Here we discuss how different friction models will perform in our model structure for simulation and what is the factor that leads to explicit geometric connection.

As introduced in the previous section, our composited friction model in Equation 4.26 can result in an explicit geometric connection formula exhibited in Equation 4.33. If we use the classic viscous friction model, we can achieve a similar geometric connection Equation The only differ-

ence is that the normal force variable of each leg $F_{j,z}$ in Equation 4.33 will downgrade into an indicator variable Ind_j that solely indicates whether the leg is in contact with the ground:

$$Ind_j = \begin{cases} 1 & F_{j,z} > 0 \\ 0 & F_{j,z} = 0 \end{cases} \tag{4.35}$$

If the classic Coulomb friction model is adopted by assuming that all of the legs are slipping at all time, we can still write the resultant motion equation in similar form as Equation 4.33. But all the normal force terms $F_{j,z}$ have to be replaced by $F_{j,z}/\|\dot{p}_{j,xy}\|$. In this case, the motion equation is no longer a geometric connection equation, since there are shape velocity related terms $\{\dot{p}_{j,xy}\}$ in the coefficient matrices.

In summary of the above discussion, to make our spring supported model structure achieve an explicit geometric connection, the contact friction model should have the following form:

$$F_{j,xy} = H_j \dot{p}_{j,xy} \tag{4.36}$$

where H_j is a coefficient variable which does not depend on the leg velocity $\dot{p}_{j,xy}$. For more general cases, H_j can also be a matrix modeling forces that are generated by a wheel, skate, claw, or otherwise non-isotropic frictional contact. As long as H_j is independent with the leg velocity $\dot{p}_{j,xy}$, the friction model and the sping-supported model structure will lead to an explicit geometric connection.

Even though the classic Coulomb friction cannot result in an explicit geometric connection, we were still curious to see whether it can offer good simulation performance in our spring-supported model structure with the assumption that all supporting legs are slipping. However, the simulation test with Coulomb friction model (Equation 4.24) runs much slower than the simulation with viscous friction model or our composited friction model. It also results in a lot of prediction outliers close to infinity. This kind of numerical instability exists when there are supporting legs with velocities that are equal or close to zero. We use the following simple example to explain this issue. Given that a hexapedal robot walks straight forward (no turning) with a tripod gait and non-slip contact with ground, the supporting legs have velocities in the body frame expressed as $\dot{q}_{i,xy} = [-v, 0]$. As a consequence of the holonomic constraint from the no slip condition, the body frame origin (CoM) will have velocity in the world frame as $\dot{p}_{0,xy} = [v, 0]$ assuming the body frame x axis is in the same direction of the world frame x axis. In the above scenario, if Coulomb friction model is adopted to solve the body frame velocity $\dot{p}_{0,x}$ from shape velocity inputs $\dot{q}_{i,x}$, we have the force balance in x axis as follows:

$$\sum_{i=1}^{N_i} F_{i,x} = \sum_{i=i}^{N_i} \mu_i F_{i,z} \frac{\dot{p}_{0,x} - v}{\|\dot{p}_{0,x} - v\|} = 0 \qquad (4.37)$$

The coefficient $\sum_{i=i}^{N_i} \mu_i F_{i,z}$ is a always positive number. Thus, the only solution for the force balance equation is $(\dot{p}_{0,x} - v)/\|\dot{p}_{0,x} - v\| = 0$, which is obviously impossible. The numerical solver will also end with some meaningless results in terms of both this example case and those cases that has small leg velocities at contact. Meanwhile, if our composited model is adopted, the force balance is as follows:

$$\sum_{i=1}^{N_i} F_{i,x} = \sum_{i=1}^{N_i} \mu_i F_{i,z}(\dot{p}_{0,x} - v) = 0 \qquad (4.38)$$

which results in the correct solution $\dot{p}_{0,x} = v$. Through this simple example, it is apparent that the friction model in the form of Equation 4.36 can also predict the motion with holonomic constraints from nonslip gaits.

Although we can estimate the performance of each friction model based on first principle analysis, the final evaluation about whether a friction model is adequate for our model structure is determined by comparing the system simulation motion with experiment ground truth motion. The key function of a friction model is to determine how the tangent forces are distributed among the supporting legs based on XY planar force and moment balance. The friction coefficients $\{\mu_j\}$ are hyper-parameters in friction models. Because of the force/moment balance, the absolute values of $\{\mu_j\}$ do not matter, while the ratios between each other really do affect the planar motion computation. The experiment summary that BigAnt steering gait achieves very similar ang/cyc on different friction surfaces in Figure 3.13 actually verifies this argument. For our robots, contact regions of the legs are symmetric in terms of material and geometric dimensions. So, we usually assume $\mu_j = 1$ for robot simulation. For cockroach simulation, we may tune $\{\mu_j\}$ as different values for different leg pairs.

4.6   Model based simulation

Based on the spring supported model structure and Coulomb-viscous combined friction model, we perform simulations for multi-legged systems in this section. The systems to be tested include BigAnt, Multipod, Mechapod and cockroach. Their leg trajectories in the body frame collected during experiments are used as both shape and shape velocity inputs for simulation. The prediction results of body motion are then compared with ground truth experiment data.

4.6.1 Model tests on BigAnt

To test the model performance on BigAnt, two trials of BigAnt experiment motions are simulated. The first trial is from the steering gait I that is introduced in Figure 3.13 and Figure 4.1. The robot motion predicted from simulation is depicted in Figure 4.14. It shows that the simulation result captures many key features of body velocity, especially for the angular velocity $\dot{\theta}$ in this trial. The translational body velocities V_{Bx} and V_{By} from simulation match most of the oscillation patterns of the experiment ground truth albeit they exhibit smaller amplitudes at some peak points.

The integrated motion variables ($[x, y, \theta]$) for these 4 gait cycles of simulation are also presented in Figure 4.14. The orientation angle θ accumulates errors as motion proceeds. We found that this model always predicts less rotation than the real experiment result for test trials that have large orientation changes during locomotion. By adding a constant offset bias to angular velocity $\dot{\theta}$ for correction, we could, trivially, cancel the error in total angular change over the trial. Using such a correction brought the heading angle and its fluctuations to closely correspond with the observations (see Figure 4.14). Such angular drift issues are common in odometry and are often corrected using some absolute heading measurement. The geometric characteristics also makes these computations much easier since gait frequency does not need to be considered.

To further check the performance of this model when applied to BigAnt robot, the second trial of test is simulated. This trial of motion is BigAnt turning left adopting a different steering gait (steering gait II) as introduced in Section 3.5.1.2 and Figure 3.11. The corresponding simulation result is presented in Figure 4.15 and also captures most of ground truth motion. For these two simulation examples, the stiffness of leg springs is hand-tuned with the assumption that the 4 legs from the front leg pair and back leg pair share the same stiffness k_1, while the 2 middle legs share another stiffness k_2. Thus, there are only two stiffness hyperparameters that have been tuned during the simulations.

To investigate whether the hyperparameter k does represent some physical essence of the real system and can be extended to different gaits for the same robot platform, we simulated all the 20 trials of steering tests (steering gait II) as depicted in Figure 3.11 with the same leg stiffness parameters k_2 for the middle legs, and k_1 for all the other legs. This test is also a systematic check of the performance of our proposed model structure applied to BigAnt robot. The simulated motions are demonstrated in Figure 4.16. The quantitative performance evaluation for predicting geometric properties dist/cyc and ang/cyc is also reported in Table 4.6.

We can see that most of the raw prediction errors come from the rotational motion. The simulation always predicts less turning than the ground truth and has larger error for trials with larger turning angles. The correction by adding constant offset to angular velocity does improve the prediction performance and greatly reduces the error of the predicted rotational motion. The absolute RSME of all ang/cyc after correction is under 2 degrees. The angular velocity correction only

125
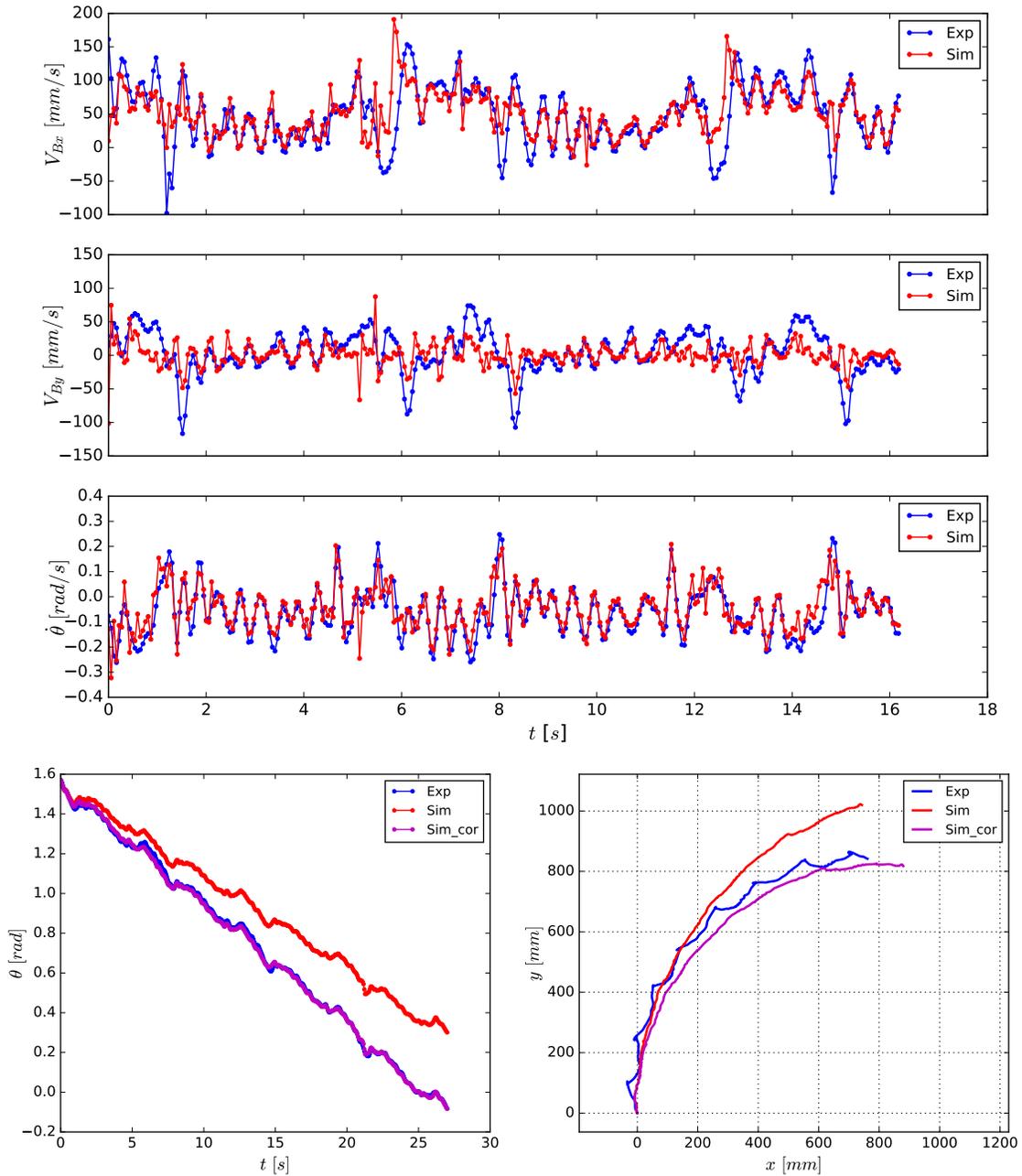
Figure 4.14: The BigAnt simulation result for 4 cycles of steering gait I with steering parameter $s = 0.75$ and gait frequency $f = 0.14 Hz$: Body velocity prediction (top), orientation prediction (bottom left) and prediction of body frame origin trajectory in the world frame (bottom right). The corrected simulation results (magenta lines) in the bottom two plots are from the operation of adding a constant offset to the raw predicted angular velocity $\dot{\theta}$.

changes the CoM trajectory curvature but does not change its length. That is why the RMSEs of dist/cyc do not show much change after the correction. With the relative RMSE around 6%
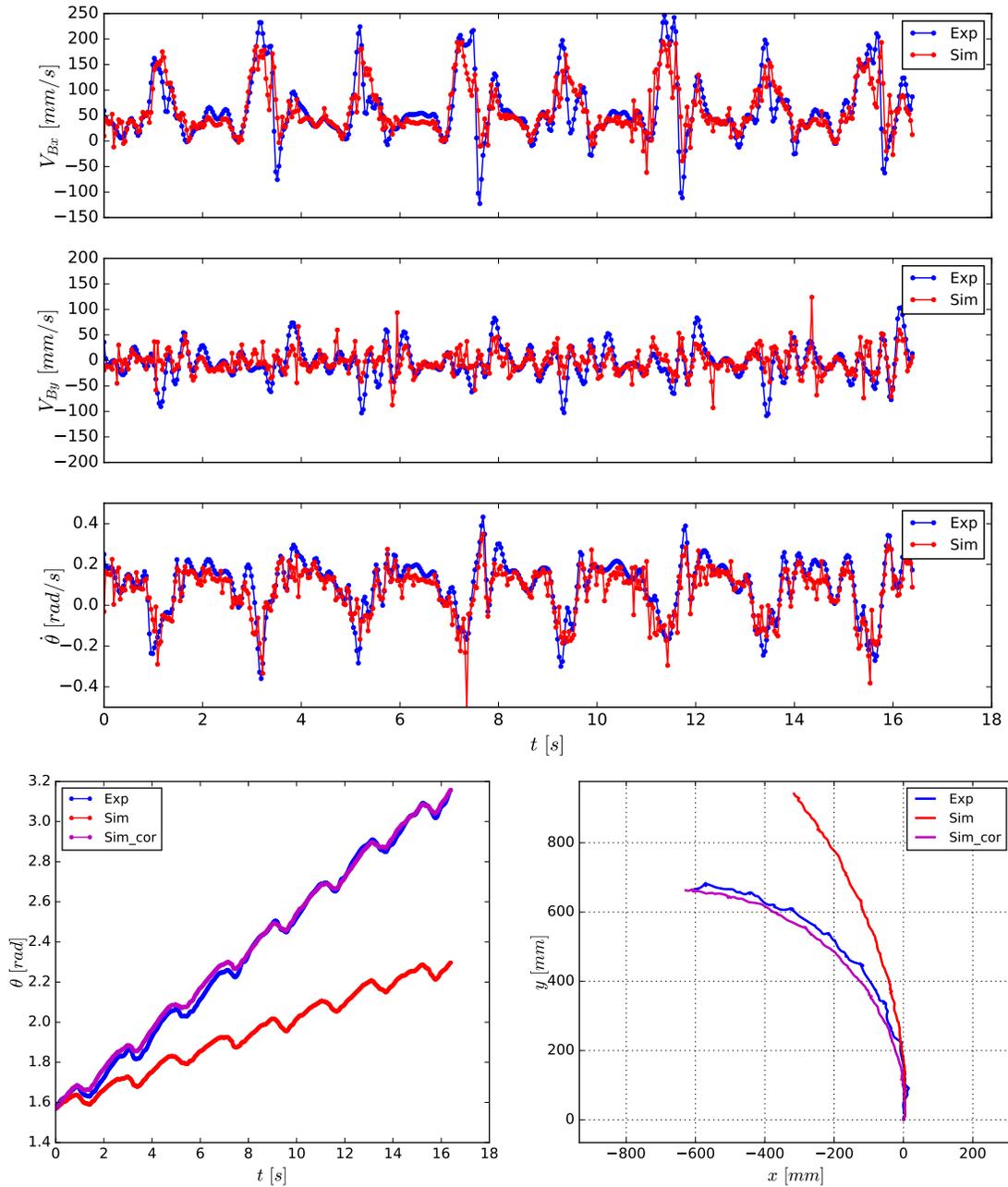
Figure 4.15: The BigAnt simulation result for 4 cycles of steering gait II with steering parameter $s = -0.2$ and gait frequency $f = 0.24Hz$: Body velocity prediction (top), orientation prediction (bottom left) and prediction of body frame origin trajectory in world frame (bottom right). The corrected simulation results (magenta lines) in the bottom two plots are from the operation of adding a constant offset to the raw predicted angular velocity $\dot{\theta}$.

on average, the raw prediction of tranlational motion itself is closer to ground truth than that of rotational motion.
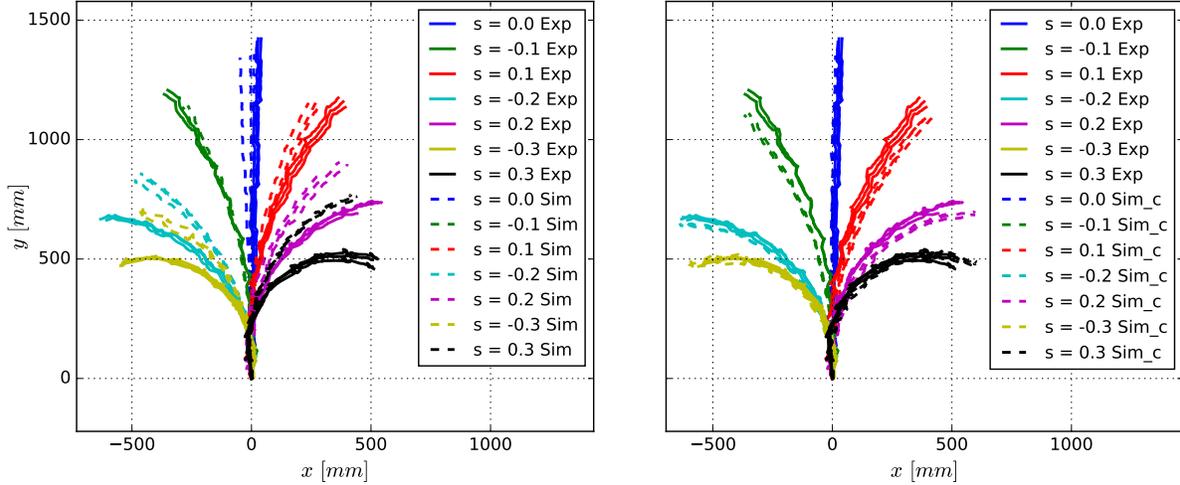
Figure 4.16: The BigAnt simulation result (dashed lines) for 20 trials of steering gait II tests: Raw prediction of body frame origin trajectory in the world frame (left); corrected prediction of body frame origin trajectory in the world frame (right). The corrected simulation results are from the operation of adding a constant offset to the raw predicted angular velocity $\dot{\theta}$.

The simulation for each test trial takes 274 ± 13 milliseconds to finish the calculation of 500 time steps (4 gait cycles) with the Python code running on one PC core, which is at least x50 faster than real-time robot motion. Thus, this model can be easily embedded into BigAnt on-board computation architecture to assist real-time planning and control.

In the following sections, we test our spring supported multi-legged model by simulating the motion of Multipod, Mechapod and Cockroach. One or two simulation examples of each system will be presented to show the motion prediction result. Systematic simulation analysis on these systems for different gaits is similar to the above BigAnt analysis and will be performed in the future.

4.6.2 Model test on Multipod

In this section, we simulated 12-legged Multipod walking with anti-phase alternating gait. The Multipod in this case has symmetric contact leg layout and also incorporate many legs, so all the leg springs are assumed to share the same stiffness parameter k which is then tuned by hand. The simulation result is exhibited in Figure 4.17. The prediction of body velocity V_{Bx} provides a good match with the experiment ground truth. V_{By} prediction captures the low frequency patterns of lateral oscillation but misses some higher frequency patterns. Unlike other systems, Mulipods are operated to walk only straight forwards or backwards with no steering command. The real angular velocity $\dot{\theta}$ is just little oscillations around 0, while the predicted $\dot{\theta}$ has some different small

Table 4.6: RMSE (root-mean-square error) of dist/cyc and ang/cyc predicted by BigAnt simulation for different steering inputs s. The absolute RMSEs for dist/cyc and ang/cyc are in units of [mm] and [deg] respectively. The relative RMSE (noted as R-RMSE) is calculated by dividing absolute RMSE by the mean value of dist/cyc or ang/cyc in the sample set.

Steering input	$s = -0.3$	$s = -0.2$	$s = -0.1$	$s = 0$	$s = 0.1$	$s = 0.2$	$s = 0.3$
Dis/cyc RMSE	18	8	22	17	16	9	18
Dis-c/cyc RMSE	17	8	22	17	16	9	17
Dis/cyc R-RMSE	9.0%	4.0%	6.8%	4.8%	5.0%	3.7%	8.4%
Dis-c/cyc R-RMSE	8.6%	4.1%	6.9%	4.8%	5.0%	3.6%	7.8%
Ang/cyc RMSE	8.4	5.6	2.5	1.1	3.8	8.8	11.8
Ang-c/cyc RMSE	1.9	1.3	1.0	0.8	1.2	0.9	1.6
Ang/cyc R-RMSE	31.6%	34.2%	23.6%	N/A	33.3%	38.5%	36.8%
Ang-c/cyc R-RMSE	7.2%	7.6%	10.0%	N/A	10.3%	4.0%	5.1%

oscillation patterns around 0. No further offset correction on $\dot{\theta}$ is implemented for this straight walking case. The combination of V_{By} and $\dot{\theta}$ imprecision leads to the error in the integrated body frame origin trajectory. A low pass filter on angular velocity would improve the prediction CoM trajectory.

4.6.3 Model test on Mechapod

The Mechapod motion we simulated in this section is from the steering gait introduced in Section 3.6.2 and Figure 3.23. The simulation result is shown in Figure 4.18. Similar to Multipod, the prediction of body velocity V_{Bx} provides a good match with the experiment ground truth. The predictions of V_{By} and $\dot{\theta}$ are in the same oscillation scale with the ground truth signal, but the signal patterns do not provide a good match. The combination of V_{By} and $\dot{\theta}$ imprecision again leads to the error in the integrated body frame origin trajectory.

4.6.4 Model test on cockroach

Although the tested cockroach motions were not proved to be geometric or at least geometric on average from the analysis in Section 4.3.3, we are still curious to check how our spring-supported multi-legged model would perform when simulating cockroach locomotion. Two trials of cockroach experiment motions with different turning rates and transnational speeds are simulated as examples in this section. The simulated results are demonstrated in Figure 4.19 and Figure 4.20.

In the first example, the predictions of all the 3 body velocities have both higher frequency and higher amplitude compared with the real cockroach motion. They are bad matches in terms of
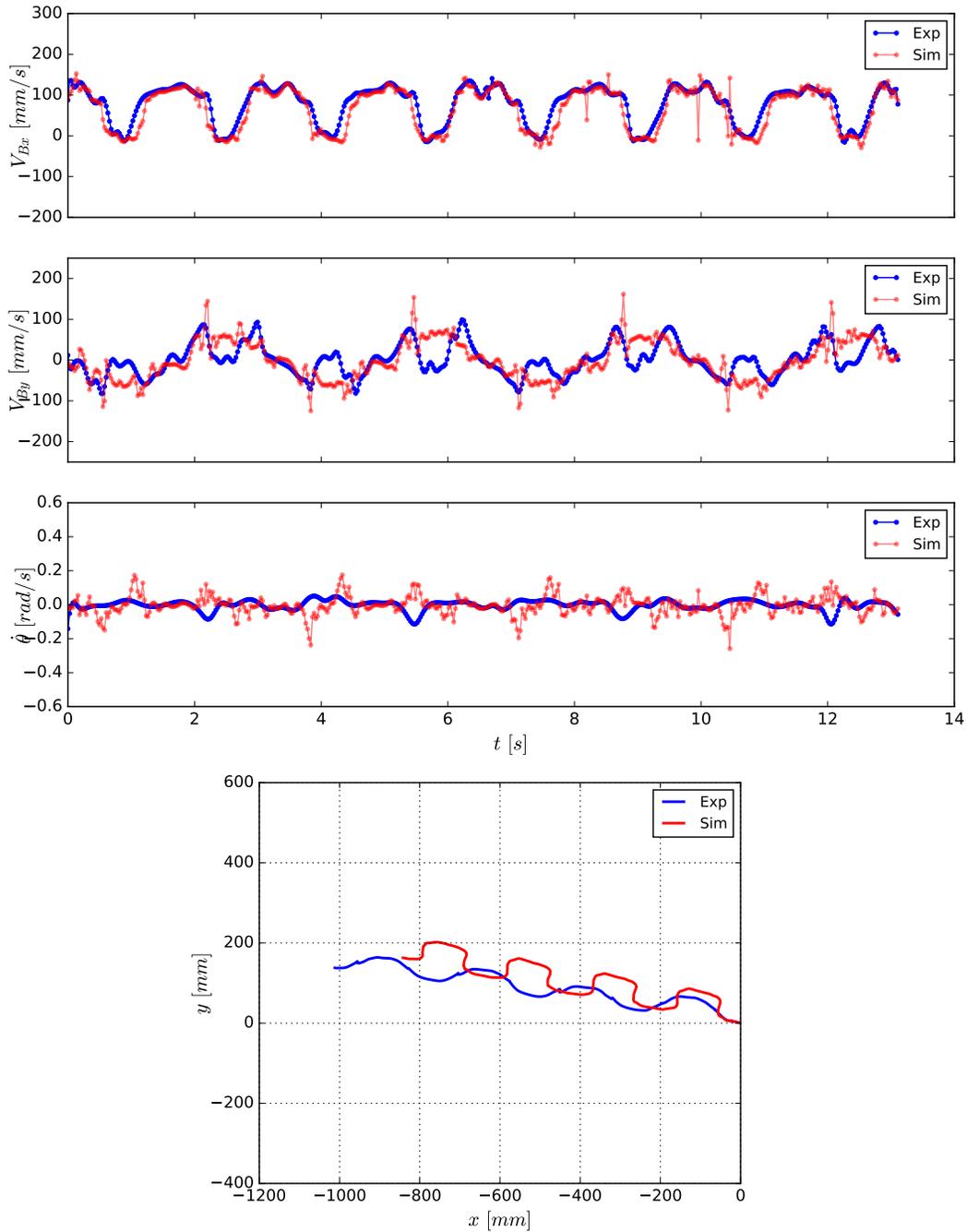
Figure 4.17: The 12-legged Mutlipod simulation result for 4 cycles of undulatory gait with phase offset $\Delta\phi = \pi$ and gait frequency $f = 0.3Hz$: Body velocity prediction (top); prediction of the body frame origin trajectory in the world frame (bottom).

instantaneous velocity. However, the integrated motion after adding constant offset to angular velocity for correction offers a surprisingly good match with the ground truth motion. This indicates that the difference between the average motion of the corrected prediction and the ground truth is
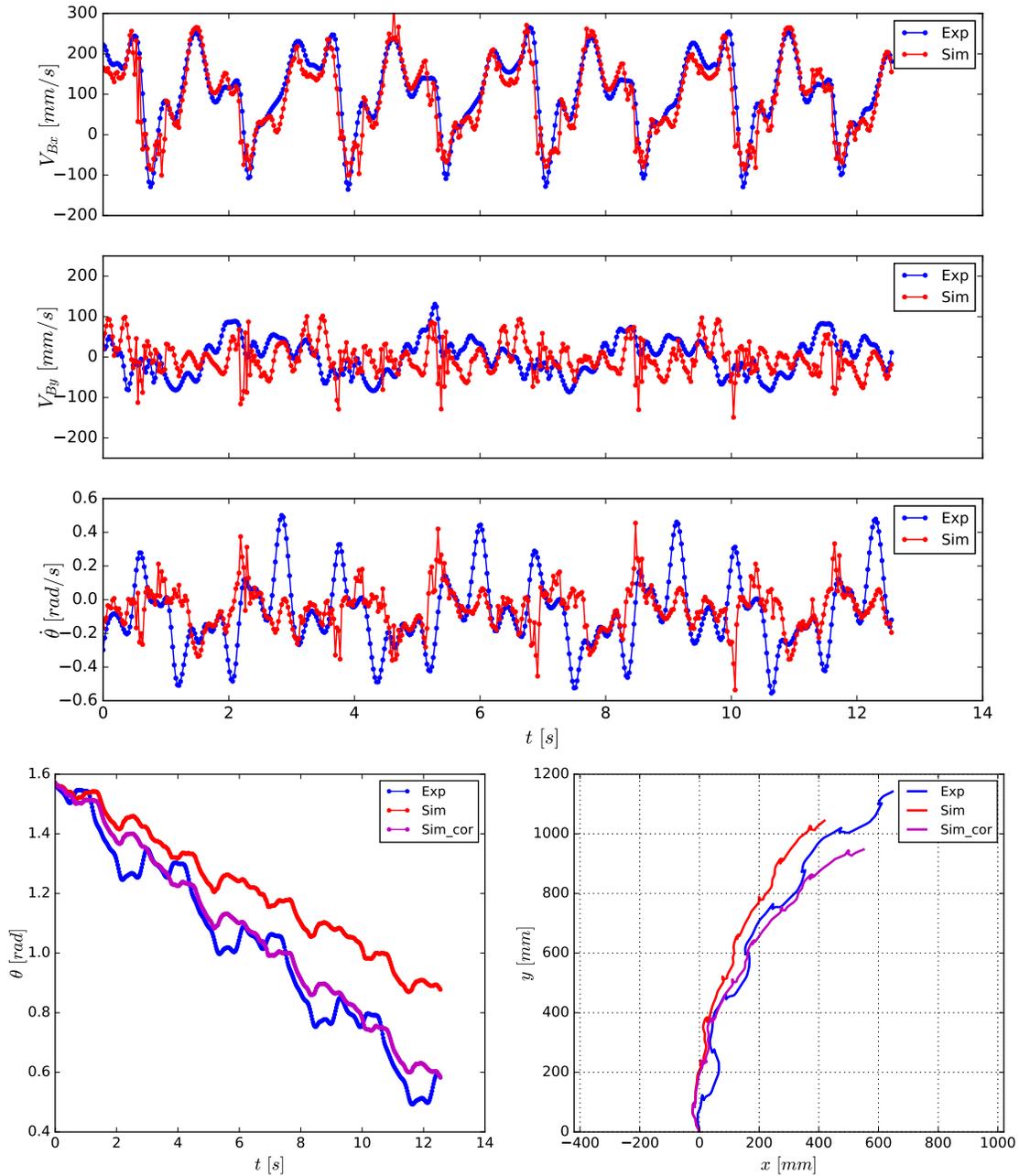
Figure 4.18: The Mechapod simulation result for 4 cycles of slipping steering gait with steering parameter $s = 20$ and gait frequency $f = 0.33Hz$: Body velocity prediction (top), orientation prediction (bottom left) and prediction of the body frame origin trajectory in the world frame (bottom right). The corrected simulation results (magenta lines) in the bottom two plots are from the operation of adding a constant offset to the raw predicted angular velocity $\dot{\theta}$.

not as large as that for the instantaneous velocity profile. The second example which offers a larger rotation compared to the first example. Its V_{Bx} prediction has similar oscillation frequency as does

the ground truth, but with larger amplitude. V_{Bx} and $\dot{\theta}$ predictions do not offer a good match with ground truth as they present higher frequency errors. In terms of the body frame origin trajectory, the raw simulation result matches the correct turning direction but again predicts less rotational motion. By applying the angular velocity correction, the final orientation and location is close to the ground truth but the middle part of the trajectory still has a clear mismatch.

In summary, the cockroach simulation results from the above two examples exhibit worse prediction if compared to the robot simulations, but these results still capture some motion features of the experiment tests. This observation aligns with our intuition that the mechanism of cockroach motion is more complicated than our proposed model and the tested cockroach behaviors are more dynamic, especially in terms of large turning motions.

4.7 Conclusion and discussion

In this chapter, we extended our preliminary observation of multi-legged steering being geometric in Chapter 3, and explored for strategies to model multi-legged locomotion with slipping based on its geometric characteristics we discovered. In this section, we discuss more details about the methods we proposed and the analysis/simulation results we achieved. The results from different sections are also connected to draw more comprehensive conclusions about each robot platform or multi-legged locomotion in general. Moreover, potential future plans follow these discussions.

To strictly check the geometric characteristics of a given periodic behavior for a given system, we proposed the methods of instantaneous geometric analysis and average geometric analysis, which can be used to describe different levels of being geometric for scientific checking and engineering applications. For the average geometric analysis, the average geometric properties we focused on using are dist/cyc and ang/cyc for checking translation and rotation respectively. These two properties are enough to assist robot motion planning with the steering gaits we tested on our robots, since the direction change of system CoM per-cycle displacement vector between two consecutive gait cycles is equal to the body frame orientation change after a gait cycle. The CoM trajectory can be predicted by dist/cyc and ang/cyc at any full-cycle time step. However, there exists some other gaits that have decoupled translation and rotation, in which case, the CoM moving direction does not match the body frame orientation change. For an example on a 2D plane, the system CoM moves along $[-1, 1]$ diction within a gait cycle while the body frame turns 30 degrees clockwise. Then the CoM trajectory cannot be predicted only by dist/cyc and ang/cyc. We need to replace the distance travelled per cycle by the displacement moved per cycle which is a 2D vector $[D_x/cyc, D_y/cyc]$ w.r.t the body frame of reference, for more general cases.

Two data driven models are associated with these two kinds of geometric analysis. One is a phase driven model from the instantaneous geometric analysis and the other is a mean value model
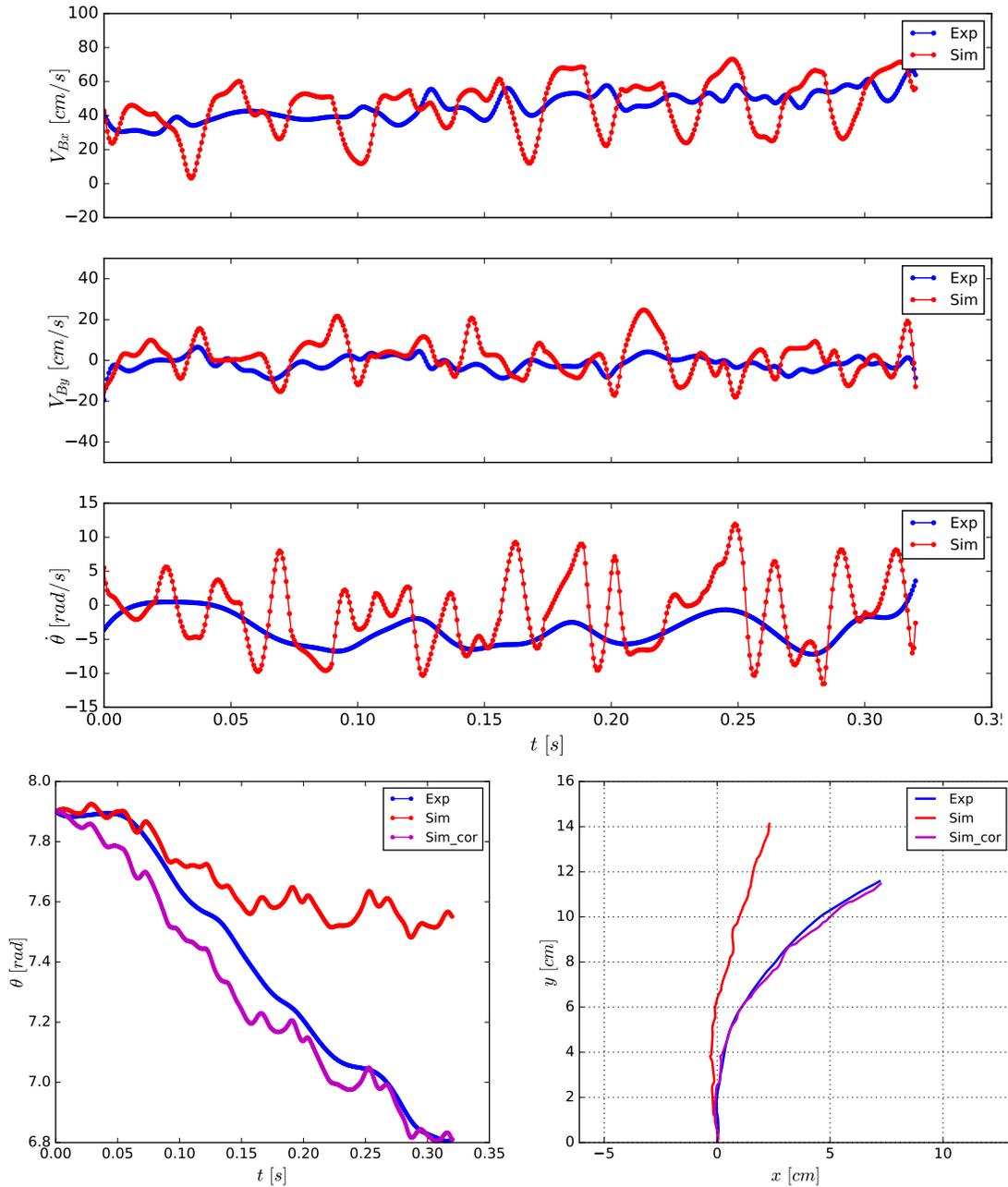
Figure 4.19: Cockroach simulation result example 1: Body velocity prediction (top), orientation prediction (bottom left) and prediction of the body frame origin trajectory in the world frame (bottom right). The corrected simulation results (magenta lines) in the bottom two plots are from the operation of adding a constant offset to the raw predicted angular velocity $\dot{\theta}$.

from the average geometric analysis. The average geometric analysis and mean value model can only be applied to periodic behavior exclusively, while the instantaneous geometric analysis and phase driven model can be extended to non-periodic behavior by regarding the whole time series
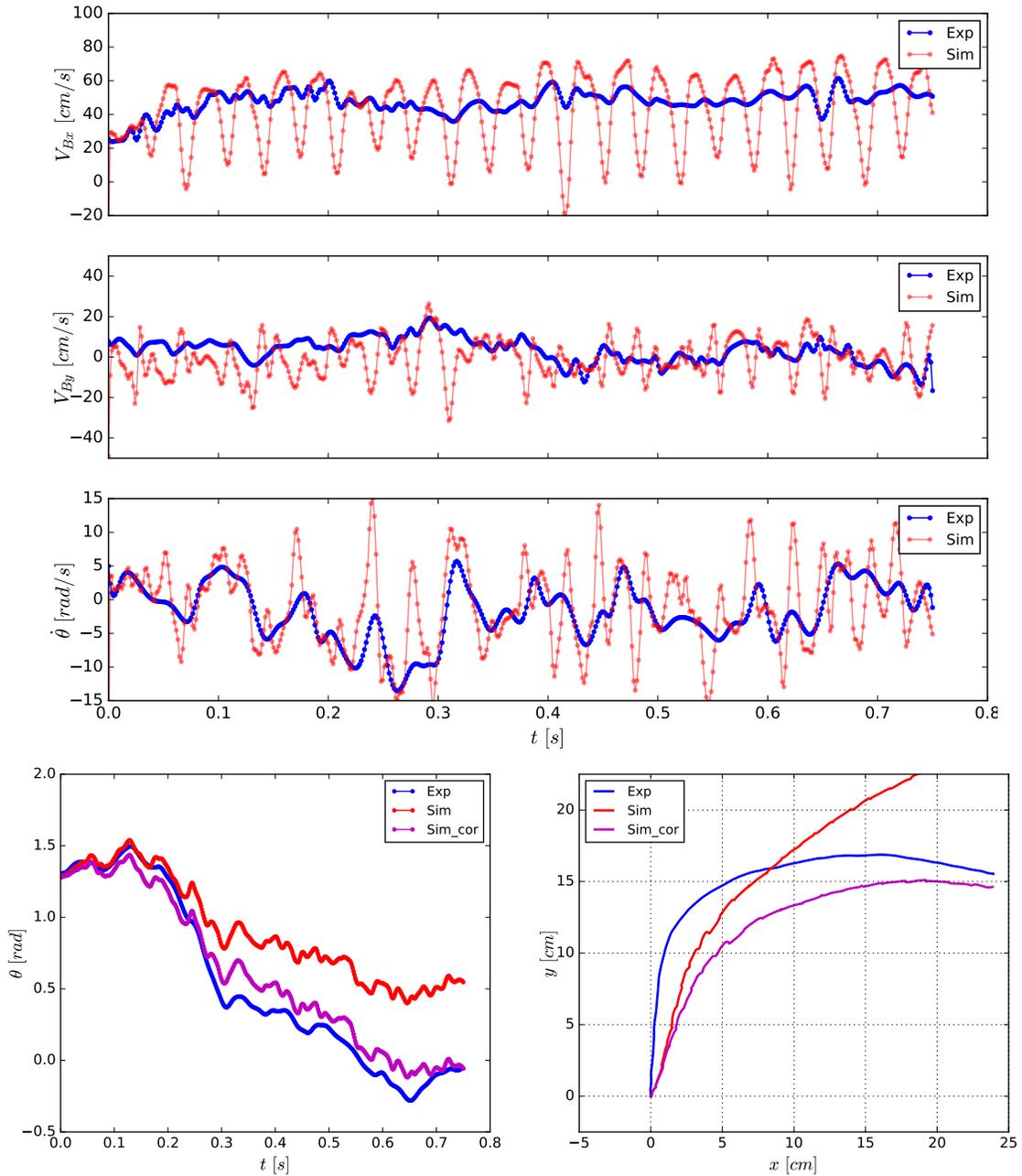
Figure 4.20: The Cockroach simulation result example 2: Body velocity prediction (top), orientation prediction (bottom left) and prediction of the body frame origin trajectory in the world frame (bottom right). The corrected simulation results (magenta lines) in the bottom two plots are from the operation of adding a constant offset to the raw predicted angular velocity $\dot{\theta}$.

signal as one cycle of motion. The experiment motion from real robot platforms cannot be perfectly geometric, because of the residual dynamic effect, the motion sensing noise, and the environment that is not perfectly symmetric. The data driven models provide the option to quantitatively check

how geometric the experiment motion is by assessing the model prediction errors. When the prediction errors from these data driven models are smaller than some thresholds, we regard the tested motion to be geometric.

By the thorough geometric analysis, we verified that multi-legged locomotion with slipping can be geometric. The tested BigAnt steering gait is proved to be both geometric on average and instantaneously geometric within the tested gait frequency range. The Multipod result is more complicated because of the large span of data set parameters: 4 numbers of legs, 5 gait frequencies and 26 kinds of undulatory gaits. The geometric analysis across the whole data set suggests that different Multipod robots (numbers of legs) with different undulatory gaits have different levels of capability for being geometric. In some cases, the geometric motion can be expanded into a wider frequency range, while for others, the geometric motion can only be achieved within a reduced frequency range. This agrees with our earlier intuition, that the geometric on average motion is easier to achieve than the instantaneously geometric motion, and is observed in a wider range of Multipod motion parameters With more legs, the Multipod locomotion is more close to being geometric in terms of both averagely and instantaneously, and can keep such a geometric characteristic in a larger frequency range. Infinite contact legs would make the Multipod robot become a snake which is a classic geometric system. We then conclude a hypothesis that with more legs contacting with environment, the multi-legged system is closer to being geometric even with slipping. The mechanism behind this could be that the system is easier to achieve the friction dominated condition by more contact with the environment. More research about this hypothesis can be performed in the future. We also performed geometric analysis on the animal counterparts of our robots: cockroaches. Although the tested cockroach motion turned out to be not even geometric on average, we still provided a paradigm about how to implement geometric analysis on animal systems.

After some system or system behavior is proved to be geometric, we can apply the data driven models to assist robot planning and control. The key advantage of being geometric is that the constructed models can be applied to different gait frequencies (operational speeds). For these multi-legged robots, we can run some calibration trials to build data driven models of certain behaviors and determine their corresponding feasible gait frequency range. The planning modules only need to do path planning by selecting the behavior patterns without concerns about the motion speed. Thus the planning and control of these multi-legged robots can be decoupled in the same way as wheeled mobile robots. In contrast, motion planning and control for bipedal and quadrupedal robots are always coupled since their motions are highly dynamic. These robots usually cannot speed up their locomotion only by scaling the speed profiles of their actuation joints. Any speed change of CoM motion needs a new control input profile to guarantee stability. In a nutshell, being geometric can make the planning of multi-legged locomotion much easier.

The geometric analysis we implemented on BigAnt and Multipod is behaviorwise. The mean value model and phase driven model are always for some given gait (shape input) pattern $r(\phi)$ which is a 1-dimensional manifold in shape space. For other gait patterns, new data driven models need to be constructed. We can build a unit motion table to collect the data driven models of different gaits for motion planning. The data driven model can be improved by the regression method developed by Bittner et al. [2018] to predict system motions from a family of gait patterns instead of just one. For example, it could be able to model a steer gait with different steering parameters. The generated data driven model will then have two dimensions: variation long system phase and variation long the steering parameter. This is a future plan for implementing more complicated data driven models on our robots.

After confirming that multi-legged locomotion with slipping can be geometric, it is significant how the physics leads to such phenomena. Meanwhile, we are also pursuing a model that is systemwise and can predict system motion from any gaits. With these two motivations, we proposed the friction dominated assumption and the spring supported multi-legged model structure. The friction dominated assumption provides the zero-momentum condition for multi-legged locomotion, just like the low Reynolds number condition for small swimmers. With this assumption, the inertia effect can be dissipated fast enough and the whole system motion becomes quasi-static. The spring supported multi-legged model is a structure for our goal model that can take any shape inputs and predicts system body motions. This proposed model structure together with the Coulomb-viscous combined friction model leads to an explicit geometric connection form for multi-legged locomotion. The simulation based on this model is tested for all the systems we experimentally studied: BigAnt, Multipod, Mechapod and cockroach. The consequent prediction results did capture many key features of body velocity for robot systems. Some predictions of body frame origin trajectories are very close to the ground truth after the correction by the constant angular velocity offset. We can say these model based simulation predictions are decent considering how simple the model is. This model can also be computed x50 times faster than realtime experiment on a single core PC, therefore it possesses the capability to be used as an odometry model and embedded into the on-board computation units for real time control and planning.

There are also some future plans that can further improve the simulation performance of this model structure. Currently, the hyper parameter k_i of the spring leg stiffness is only tuned by hand for these simulation examples. In future, we can perform optimizations over the leg stiffness parameters k_i to further increase the model prediction performance. The model prediction result usually has high frequency noises compared to the ground truth body velocity. That is because the system bandwidth increases in the model from the lack of inertia effect under the friction dominated condition. A low pass filter that matches the power spectrum of the prediction signal with the ground truth could potentially improve the predicted body velocity. More studies such as

checking the contact leg index, forces on the legs can also be performed on the simulation results to further improve the parameter choice and the spring-supported multi-legged model structure.

All the motion prediction results from either the data driven model or the geometric connection model based on first principle physics, are all indicators about how close the system is to being geometric. The BigAnt locomotion prediction from these models presented smaller errors compared to other systems such as Multipod, Mechapod and cockroach. Thus, the tested BigAnt motion is more geometric. This observation also provides support for the friction dominated assumption. BigAnt is lighter and its tested gait frequency is lower than that of Multipod. Thus the BigAnt inertia force to friction force ratio is smaller, making it closer to the friction dominated condition and more geometric. In contrast, the cockroach motion is much faster in terms of body length per second and its inertia effect cannot be dissipated fast enough. Since it is far from the friction dominated condition, the cockroach motion prediction is not accurate from neither the mean value model nor the geometric connection model.

Another important future direction is to experimentally investigate the force condition of multi-legged locomotion. Most of the experiment tests and analysis of multi-legged locomotion in this thesis is about motion study. Although the spring-supported model structure provides methods and modeling options for simulating normal forces and friction forces on robot legs, the final assessment criteria is still the motion check. We do not have the ground truth information for the intermediate force condition to further correct and adjust the force models in the simulation structure. This also pertains to the motivation of building force sensing BigAnt variant as introduced in Section 2.2.8. We believe that applying our proposed analysis and modeling technique combined with experimentally measured force information, we would harvest more insights and knowledge about multi-legged locomotion.

CHAPTER 5

Summary and Future Work

Low-DoF multi-legged robots have advantages derived from their morphology when compared with bipedal and quadrupedal robots, such as additional stability, exceptional maneuverability, easier-to-build structure, simpler control, and the ability to use redundant, high-mobility, lightweight legs. In this dissertation, we studied the unique characteristics of low-DoF multi-legged locomotion in terms of design, mobility and modeling. We demonstrated that there are intrinsic differences between low-DoF multi-legged robots and classical bipedal and quadrupedal robots. We proposed that the concept of "constraint level" identified the root of such differences by summarizing the combined influence of leg DoF and contact constraints. The constraint level is a trait describing the necessity of slipping and provides a new perspective for classifying legged systems.

Our design strategies and fabrication techniques of BigAnt provided approached for building low-DoF multi-legged robots for customized requirements. Our Multipod demonstrated a paradigm of using a highly modular design to study multi-legged locomotion in general. The corresponding data-set from our Multipod experiments can likely be used to obtain many other insights besides our studies here. Our proposed gait design strategies are universal for low-DoF multi-legged robots. In particular, our steering gaits can be easily applied to other robots with similar design morphology. Through the theoretical and experimental study, we presented the intrinsic connection between low-DoF multi-legged steering and slipping, and showed that slipping is beneficial for this category of robots to improve their maneuverability.

The results of our experimental tests on real robot platforms further led us to a key discovery that multi-legged locomotion with slipping can be geometric. Our proposed geometric analysis methods can be applied to check whether or how close a given periodic behavior is to being geometric. The associated data driven models also showed potential as a means for motion planning and control. To explore the physics making multi-legged locomotion with slipping being geometric, we proposed the friction dominated condition and the spring supported multi-legged model. This provides a result which has an explicitly geometric form, and offers a simulation model that reproduced many features of our data and can be computed much faster than real time. The discovery

that multi-legged locomotion with slipping can be geometric also made us realize a general principle, first articulated in [Revzen et al., 2021] – that the geometric ("Stokesian") form $g^{-1}\dot{g} = A(r)\dot{r}$ extends across many types of motion – piece-wise holonomic walking, slithering, low Reynolds number swimming, and walking with slipping. In other words, geometric ("Stokesian") models are a unifying framework applying to all locomotion where substantial contact forces exist all the time.

With these new insights come many natural follow-up questions for us and others to explore in the future. For example, how does dry friction contact between robot legs and the ground create effectively viscous performance in our tested multi-legged locomotion? We have an on-going project where we are trying to explore this topic by combining theoretical analysis with the force sensing experiment results from our force sensing BigAnt. How should we best model multi-legged locomotion with slipping that is outside the friction dominated condition when inertial effect cannot be neglected? The Multipod motion with gait frequency higher than $2.4Hz$ is more dynamic than the motions with lower gait frequencies which are still in the geometric range. Is the solution a more complete form of the reconstruction equation (Equation 4.2)? how will that further improve people's understanding of multi-legged locomotion?

Beside these high level theoretical directions, there are also many interesting engineering extensions of the work presented here. For example, new design iterations of BigAnt are continually being made. Would BigAnt's outdoor capabilities be enhanced by adding some compliance to the BigAnt legs? For Multipod outdoor locomotion, the YRP modular morphology combined with sensing based adaptive gait is a potential solution. Developing a steering gait design for Multipod robots that have more than 6 legs is also an interesting challenge, as is the question of whether a long Multipod can turn in place at all.

Low-DoF multi-legged robots and their locomotion provide an interesting, meaningful, and challenging research topic, with the potential for broad future impact. The ability to build simple yet highly effective locomotion platforms can influence virtually every aspect of our lives where robots are finding a use – be it a household vacuuming robot that could climb stairs, robots in agriculture and construction that can walk over rubble and loose packed soil, robots in search and rescue applications which can go to places humans should not venture, or robots exploring other planetary bodies whose ground contact mechanics we have no way to reliably model. Inspired by the locomotion of animals we usually scorn, multi-legged robots have a bright future ahead.

BIBLIOGRAPHY

Yasemin Ozkan Aydin, Baxi Chong, Chaohui Gong, Jennifer M Rieser, Jeffery W Rankin, Krijn Michel, Alfredo G Nicieza, John Hutchinson, Howie Choset, and Daniel I Goldman. Geometric mechanics applied to tetrapod locomotion on granular media. In *Conference on Biomimetic and Biohybrid Systems*, pages 595–603. Springer, 2017.

Brian Bittner, Ross L Hatton, and Shai Revzen. Geometrically optimal gaits: a data-driven approach. *Nonlinear Dynamics*, 94(3):1933–1948, 2018.

Anthony M Bloch, PS Krishnaprasad, Jerrold E Marsden, and Richard M Murray. Nonholonomic mechanical systems with symmetry. *Archive for Rational Mechanics and Analysis*, 136(1):21–99, 1996.

Anthony M Bloch, Jerrold E Marsden, and Dmitry V Zenkov. Nonholonomic dynamics. *Not. AMS*, 52(3):320–329, 2005.

Hernán Cendra, Jerrold E Marsden, and Tudor S Ratiu. Geometric mechanics, lagrangian reduction, and nonholonomic systems. In *Mathematics unlimited—2001 and beyond*, pages 221–273. Springer, 2001.

Jin Dai, Hossein Faraji, Chaohui Gong, Ross L Hatton, Daniel I Goldman, and Howie Choset. Geometric swimming on a granular surface. In *Robotics: Science and Systems*, 2016.

Jay Davey, Jimmy Sastra, Matt Piccoli, and Mark Yim. Modlock: A manual connector for reconfigurable modular robots. In *2012 IEEE/RSJ International Conference on Intelligent Robots and Systems*, pages 3217–3222. IEEE, 2012.

Michael H Dickinson, Claire T Farley, Robert J Full, MAR Koehl, Rodger Kram, and Steven Lehman. How animals move: an integrative view. *science*, 288(5463):100–106, 2000.

Xingji Duan, Weihai Chen, Shouqian Yu, and Jingmeng Liu. Tripod gaits planning and kinematics analysis of a hexapod robot. In *2009 IEEE International Conference on Control and Automation*, pages 1850–1855. IEEE, 2009.

Shamel Fahmi, Michele Focchi, Andreea Radulescu, Geoff Fink, Victor Barasuol, and Claudio Semini. Stance: Locomotion adaptation over soft terrain. *IEEE Transactions on Robotics*, 36 (2):443–457, 2020.

I Fitzner, Y Sun, V Sachdeva, and S Revzen. Rapidly prototyping robots: Using plates and reinforced flexures. *IEEE Robotics Automation Magazine*, 24(1):41–47, 3 2017. ISSN 1070-9932.

Robert Franklin, William J Bell, and Rudolf Jander. Rotational locomotion by the cockroach blattella germanica. *Journal of Insect Physiology*, 27(4):249–255, 1981.

Robert J Full and Daniel E Koditschek. Templates and anchors: neuromechanical hypotheses of legged locomotion on land. *Journal of experimental biology*, 202(23):3325–3332, 1999.

Kevin C Galloway, Galen Clark Haynes, B Deniz Ilhan, Aaron M Johnson, Ryan Knopf, Goran A Lynch, Benjamin N Plotnick, Mackenzie White, and Daniel E Koditschek. X-rhex: A highly mobile hexapedal robot for sensorimotor tasks. *Technical Reports (ESE), University of Pennsylvania*, 2010.

Zhenyu Gan, Thomas Wiestner, Michael A Weishaupt, Nina M Waldern, and C David Remy. Passive dynamics explain quadrupedal walking, trotting, and tölting. *Journal of computational and nonlinear dynamics*, 11(2), 2016.

C Gong, M J Travers, H C Astley, L Li, J R Mendelson, D I Goldman, and H Choset. Kinematic gait synthesis for snake robots. *The International Journal of Robotics Research*, 35(1-3):100–113, 2016.

Robert D Gregg, Tommaso Lenzi, Levi J Hargrove, and Jonathon W Sensinger. Virtual constraint control of a powered prosthetic leg: From simulation to experiments with transfemoral amputees. *IEEE Transactions on Robotics*, 30(6):1455–1471, 2014.

Duncan W Haldane and Ronald S Fearing. Roll oscillation modulated turning in dynamic millirobots. In *2014 IEEE International Conference on Robotics and Automation (ICRA)*, pages 4569–4575. IEEE, 2014.

Ross L Hatton and Howie Choset. Geometric motion planning: The local connection, stokes' theorem, and the importance of coordinate choice. *The International Journal of Robotics Research*, 30(8):988–1014, 2011.

Ross L Hatton and Howie Choset. Geometric swimming at low and high reynolds numbers. *IEEE Transactions on Robotics*, 29(3):615–624, 2013.

Kris Hauser, Timothy Bretl, Jean-Claude Latombe, and Brian Wilcox. Motion planning for a sixlegged lunar robot. In *The Seventh International Workshop on the Algorithmic Foundations of Robotics*. Citeseer, 2006.

Katie L Hoffman and Robert J Wood. Passive undulatory gaits enhance walking in a myriapod millirobot. In *2011 IEEE/RSJ International Conference on Intelligent Robots and Systems*, pages 1479–1486. IEEE, 2011.

Katie L Hoffman and Robert J Wood. Turning gaits and optimal undulatory gaits for a modular centipede-inspired millirobot. In *2012 4th IEEE RAS & EMBS International Conference on Biomedical Robotics and Biomechatronics (BioRob)*, pages 1052–1059. IEEE, 2012.

Philip Holmes, Robert J Full, Dan Koditschek, and John Guckenheimer. The dynamics of legged locomotion: Models, analyses, and challenges. *SIAM review*, 48(2):207–304, 2006.

Aaron M Hoover, Erik Steltz, and Ronald S Fearing. Roach: An autonomous 2.4 g crawling hexapod robot. In *2008 IEEE/RSJ international conference on intelligent robots and systems*, pages 26–33. IEEE, 2008.

Devin L Jindrich and ROBERT J Full. Many-legged maneuverability: dynamics of turning in hexapods. *Journal of experimental biology*, 202(12):1603–1623, 1999.

Aaron M Johnson. Robot parkour: the ground reaction complex & dynamic transitions. *University of Pennsylvania,Departmental Papers (ESE)*, 2013.

Akiya Kamimura, Satoshi Murata, Eiichi Yoshida, Haruhisa Kurokawa, Kohji Tomita, and Shigeru Kokaji. Self-reconfigurable modular robot-experiments on reconfiguration and locomotion. In *Proceedings 2001 IEEE/RSJ International Conference on Intelligent Robots and Systems. Expanding the Societal Role of Robotics in the the Next Millennium (Cat. No. 01CH37180)*, volume 1, pages 606–612. IEEE, 2001.

Jung-Yup Kim and Bong-Huan Jun. Design of six-legged walking robot, little crabster for underwater walking and operation. *Advanced Robotics*, 28(2):77–89, 2014.

Sangbae Kim, Jonathan E Clark, and Mark R Cutkosky. isprawl: Design and tuning for high-speed autonomous open-loop running. *The International Journal of Robotics Research*, 25(9): 903–912, 2006.

Nicholas J Kohut, Andrew O Pullin, Duncan W Haldane, David Zarrouk, and Ronald S Fearing. Precise dynamic turning of a 10 cm legged robot on a low friction surface using a tail. In *2013 IEEE International Conference on Robotics and Automation*, pages 3299–3306. IEEE, 2013a.

Nicholas J Kohut, David Zarrouk, Kevin C Peterson, and Ronald S Fearing. Aerodynamic steering of a 10 cm high-speed running robot. In *2013 IEEE/RSJ International Conference on Intelligent Robots and Systems*, pages 5593–5599. IEEE, 2013b.

R Kukillaya, J Proctor, and P Holmes. Neuromechanical models for insect locomotion: Stability, maneuverability, and proprioceptive feedback. *Chaos: An Interdisciplinary Journal of Nonlinear Science*, 19(2):026107, 2009.

M Kvalheim, B Bittner, and Revzen S. Gait modeling and optimization for the perturbed stokes regime. *Nonlinear Dynamics*, 2019. doi: 10.1007/s11071-019-05121-3.

Yujiong Liu and Pinhas Ben-Tzvi. An articulated closed kinematic chain planar robotic leg for high-speed locomotion. *Journal of Mechanisms and Robotics*, 12(4), 2020.

Jerrold E Marsden and Jim Ostrowski. Symmetries in motion: Geometric foundations of motion control. *Caltech library*, 1998.

Masahiro Masuda and Kazuyuki Ito. Semi-autonomous centipede-like robot with flexible legs. In *2014 IEEE International Symposium on Safety, Security, and Rescue Robotics (2014)*, pages 1–6. IEEE, 2014.

A J McClung. *Techniques for dynamic maneuvering of hexapedal legged robots*. phdthesis, Stanford University, December 2006.

D Miller, I Fitzner, SB Fuller, and S Revzen. Focused modularity: Rapid iteration of design and fabrication of a meter-scale hexapedal robot. In *Assistive Robotics: Proceedings of the 18th International Conference on CLAWAR 2015*, pages 430–438. World Scientific, 2015. doi: 10.1142/9789814725248_0053.

James Patrick Ostrowski. *The mechanics and control of undulatory robotic locomotion*. PhD thesis, California Institute of Technology, 1996.

Jim Ostrowski and Joel Burdick. The geometric mechanics of undulatory robotic locomotion. *The international journal of robotics research*, 17(7):683–701, 1998.

J Proctor and P Holmes. Steering by transient destabilization in piecewise-holonomic models of legged locomotion. *Regular and Chaotic Dynamics*, 13(4):267–282, 2008.

J Proctor, RP Kukillaya, and P Holmes. A phase-reduced neuro-mechanical model for insect locomotion: feed-forward stability and proprioceptive feedback. *Philosophical Transactions of the Royal Society A: Mathematical, Physical and Engineering Sciences*, 368(1930):5087–5104, 2010.

Joshua L Proctor and P Holmes. The effects of feedback on stability and maneuverability of a phase-reduced model for cockroach locomotion. *Biological cybernetics*, 112(4):387–401, 2018.

Andrew O Pullin, Nicholas J Kohut, David Zarrouk, and Ronald S Fearing. Dynamic turning of 13 cm robot comparing tail and differential drive. In *2012 IEEE International Conference on Robotics and Automation*, pages 5086–5093. IEEE, 2012.

C David Remy. *Optimal exploitation of natural dynamics in legged locomotion*. PhD thesis, ETH Zurich, 2011.

C David Remy. Ambiguous collision outcomes and sliding with infinite friction in models of legged systems. *The International Journal of Robotics Research*, 36(12):1252–1267, 2017.

S Revzen, D E Koditschek, and R J Full. *Progress in motor control - a multidisciplinary perspective*, chapter Towards testable neuromechanical control architectures for running, pages 25–56. Springer Science+Business Media, LLC - NY, 2008. doi: 10.1007/978-0-387-77064-2\%5F3.

Shai Revzen. *Neuromechanical control architectures of arthropod locomotion*. University of California, Berkeley, 2009.

Shai Revzen, Dan Zhao, Glenna Clifton, Brian Bittner, and Nicholas Gravish. Bridging walking and slithering–stokesian locomotion. In *Dynamic Walking 2021*, 2021.

Matthew A Robertson, Ozdemir Can Kara, and Jamie Paik. Soft pneumatic actuator-driven origami-inspired modular robotic "pneumagami". *The International Journal of Robotics Research*, page 0278364920909905, 2020.

Shibendu Shekhar Roy and Dilip Kumar Pratihar. Kinematics, dynamics and power consumption analyses for turning motion of a six-legged robot. *Journal of Intelligent & Robotic Systems*, 74 (3-4):663–688, 2014.

Vikram Sachdeva, Dan Zhao, and Shai Revzen. Cockroaches always slip a lot. In *The Society for Integrative and Comparative Biology Annual Meeting*, 2018.

Uluc Saranli, Martin Buehler, and Daniel E Koditschek. Rhex: A simple and highly mobile hexapod robot. *The International Journal of Robotics Research*, 20(7):616–631, 2001.

J Sastra, S Revzen, and M Yim. Softer legs allow a modular hexapod to run faster. In *Climbing and Walking Robotics (CLAWAR)*, 2012.

Jimmy Sastra, WG Bernal-Heredia, Jonathan Clark, and Mark Yim. A biologically-inspired dynamic legged locomotion with a modular reconfigurable robot. In *Proc. of DSCC ASME Dynamic Systems and Control Conference*, 2008.

John Schmitt and Philip Holmes. Mechanical models for insect locomotion: dynamics and stability in the horizontal plane i. theory. *Biological cybernetics*, 83(6):501–515, 2000.

Justin Seipel and Philip Holmes. A simple model for clock-actuated legged locomotion. *Regular and chaotic dynamics*, 12(5):502–520, 2007.

Justin E Seipel, Philip J Holmes, and Robert J Full. Dynamics and stability of insect locomotion: a hexapedal model for horizontal plane motions. *Biological cybernetics*, 91(2):76–90, 2004.

Elie A Shammas, Howie Choset, and Alfred A Rizzi. Geometric motion planning analysis for two classes of underactuated mechanical systems. *The International Journal of Robotics Research*, 26(10):1043–1073, 2007.

Simon Wilshin, Michelle A Reeve, G Clark Haynes, Shai Revzen, Daniel E Koditschek, and Andrew J Spence. Longitudinal quasi-static stability predicts changes in dog gait on rough terrain. *Journal of Experimental Biology*, 220(10):1864–1874, 2017.

Robert J Wood. The first takeoff of a biologically inspired at-scale robotic insect. *IEEE transactions on robotics*, 24(2):341–347, 2008.

Robert J Wood, Srinath Avadhanula, Ranjana Sahai, Erik Steltz, and Ronald S Fearing. Microrobot design using fiber reinforced composites. *Journal of Mechanical Design*, 130(5), 2008.

Ziyou Wu, Dan Zhao, and Shai Revzen. Coulomb friction crawling model yields linear force–velocity profile. *Journal of Applied Mechanics*, 86(5):054501, 2019.

Dongwon Yun and Ronald S Fearing. Cockroach milli-robot with improved load capacity. *Journal of Mechanisms and Robotics*, 11(3), 2019.

David Zarrouk and Ronald S Fearing. Controlled in-plane locomotion of a hexapod using a single actuator. *IEEE Transactions on Robotics*, 31(1):157–167, 2015.

David Zarrouk, Duncan W Haldane, and Ronald S Fearing. Dynamic legged locomotion for palm-size robots. In *Micro-and Nanotechnology Sensors, Systems, and Applications VII*, volume 9467, page 94671S. International Society for Optics and Photonics, 2015.

D Zhao and S Revzen. Slipping helps steering in a multilegged robot. In *Dynamic Walking*, 2016.

D Zhao, C M Schaffer, and Revzen S. Steering hexapedal robots. In *Workshop on Miniature Legged Robots, Conference on Robotics Science and Systems*, 2015.

Dan Zhao and Shai Revzen. Multi-legged steering and slipping with low dof hexapod robots. *Bioinspiration & Biomimetics*, 15(4):045001, 2020.

Dan Zhao and Shai Revzen. Toward a simple model for friction dominated multi-legged locomotion. *Bulletin of the American Physical Society*, 2021.

Dan Zhao, Taesung Heo, and Shai Revzen. Modeling multilegged locomotion: the friction dominated case. In *APS March Meeting Abstracts*, volume 2018, pages B50–011, 2018.

V Zolotov, L Frantsevich, and EM Falk. The kinematics of phototactic turns in the honeybee. *J. comp. Physiol.*, 97:339–353, 1975.